Reconstruction of mechanical properties from surface-based motion data for Digital Image Elasto-Tomography using an implicit surface representation of breast tissue structure

Helen Kershaw

A thesis presented for the degree of
Doctor of Philosophy
in
Mechanical Engineering
at the
University of Canterbury,
Christchurch, New Zealand

February 2012

Abstract

There has been great interest in recent times in the use of elastography for the characterization of human tissue. Digital Image Elasto-Tomography is a novel breast cancer pre-screening technique under development at the University of Canterbury, which aims to identify and locate stiff areas within the breast that require further investigation using images of the surface motion alone. A calibrated array of five digital cameras is used to capture surface motion of the breast under harmonic actuation. The forward problem, that is the resulting motion for a given mechanical property distribution, is calculated using the Finite Element Method. The inverse problem is to find the mechanical properties which reproduce the measured surface motion through numerical simulation. A reconstruction algorithm is developed using a shape based description to reduce the number of parameters in the inverse problem. A parallel Genetic Algorithm is developed for parameter optimization. A geometric method termed Fitness Function Analysis is shown to improve the inclusion location optimization problem. The ensemble of solutions generated using the Genetic Algorithm is used to produce an optimal and a credible region for inclusion location. Successful single frequency phantom reconstructions are presented. An effective way of combining information from multi-frequency phantom data by examining the characteristics of the measured surface motion using data quality metrics is developed and used to produce improved reconstructions. Results from numerical simulation datasets and a two inclusion phantom used to test the optimization of multiple and ellipsoidal inclusions indicate that although two inclusions can be successfully reconstructed, the single inclusions assumption may suffice even in irregular, heterogeneous cases. This assumption was used to successfully locate the stiffest inclusion in a phantom containing multiple inclusions of differing stiffness based on three multi-frequency datasets. The methods developed in phantoms are applied to three *in vivo* cases for both single and multi-frequency data with limited success.

This thesis builds on previous work undertaken at the University of Canterbury. The original contributions in this work are as follows. A new reconstruction algorithm combining a genetic algorithm with fitness function analysis is developed. The most realistic tissue mimicking phantoms to date are used. An ellipsoidal shape-based description is presented, and applied to the first multi-inclusion reconstructions in DIET. This work presents the first reconstruction using meshes created directly from data using a meshing algorithm developed by Jonas Biehler. A multi-frequency cost function is developed to produce the first multi-frequency and *in vivo* reconstructions using DIET data.

Acknowledgements

First and foremost, I would like to extent my sincerest gratitude to my supervisor, Dr. Eli Van Houten, for his support, knowledge and patience. I feel privileged to have had a supervisor both kind and enthusiastic enough to work with his students even after his home and belongings became inaccessible due to the Christchurch earthquake. I will strive to reflect his extraordinary attitude in both my professional and personal life.

The research presented here would not have been possible without the work of my co-supervisor, Dr. Thomas Lotz, and his leadership in the development of the DIET prototype. His experience and helpful advice when reviewing this thesis has been immeasurable. My thanks also go to my co-supervisor, Prof. Rick Beatson, for his friendly advice, and to Dr. Mark Jermy for assuming the role of supervisor when Eli departed for Canada.

I would like to thank Amer Kashif for his patience and help with phantom construction and wish him luck with his thesis. I am indebted to all the students, past and present, who have contributed to the DIET project, most notably Dr. Ashton Peters whom, I am glad to say, I have had the pleasure of meeting.

This thesis would not have been possible without the financial support from a University of Canterbury Doctoral Scholarship, and the work of all the university staff who got the university back on its feet after the earthquakes. In particular, the staff of Bluefern, who have not only provided excellent technical support and advice over the last three years, but had the supercomputers up and running within two days of a magnitude 6.3 earthquake.

To my parents and extended family, thank you for the support and words of encouragement that have meant so much from the other side of the world. To my local 'family', thank you for making New Zealand home.

Lastly, I would like to thank my husband Matthew who, as always, has supported me through another stage in life's greatest adventure.

Contents

List of Figures

List of Tables

Nomenclature

Abbreviations

BEM	Boundary Element Method
CO	Combinatorial Optimization
DCIS	Ductal carcinoma *in situ*
DIET	Digital Image Elasto Tomography
DMA	Dynamic Mechanical Analyzer
DOI	Diffuse Optical Imaging
DOT	Diffuse Optical Tomography
EIS	Electrical Impedance Scanning
EIT	Electrical Impedance Tomography
FE	Finite Element
FEM	Finite Element Method
FFA	Fitness Function Analysis
GA	Genetic Algorithm
GD	Gradient Descent
GPGPU	General-Purpose Computing on Graphics Processing Units
GPU	Graphics Processing Units
LCIS	Lobular carcinoma *in situ*
LFE	Local Frequency Estimation
MPI	Message Passing Interface
MRE	Magnetic Resonance Elastography
MRI	Magnetic Resonance Imaging

MUMPS	Massively Parallel Multi-Frontal Solver
OCT	Optical Coherence Tomography
OM	Optical Mammography
PDE	Partial Differential Equation
PEM	Proton Emission Mammography
PET	Proton Emission Tomography
PSO	Particle Swarm Optimization
RMS	Root Mean Square
SNR	Signal to Noise Ratio
UE	Ultrasound Elastography

Greek Symbols

Γ	Correlation cost
Γ^C	Multi-frequency correlation cost
Φ	Cost weighted using ellipse uncertainty
$\overline{\Phi}$	Normalized cost
Φ^C	Multi-frequency combined normalized cost
Φ^{SQ}	Cost using squared difference between measured and calculated displacement.
$\Psi(n,p)$	Speedup achieved solving a problem of size n on p processors.
α, β, γ	Ellipsoid rotation about x,y,z axis
δ	Ellipse residual
δ_c	Centroid Difference
ϵ	Strain
ϵ^2	Ellipse uncertainty
ζ	Damping parameter
ζ_B	Background damping parameter
ζ_I	Inclusion damping parameter
η	Viscosity
θ	Parameter combination that constitutes the material model

κ	Desired credible level
λ	Lamé parameter
μ	Shear modulus
ν	Poisson's ratio
μ_A	Mean measured displacement
σ	Stress
ϕ_i	Linear basis function
τ	Cost using phase difference
χ	Coverage
ψ	Phase
ω	Frequency

Roman Symbols

$\vec{AB}$	Vector along closest edge of surface element
A	Area of surface element
AC	Ranked Cost
$\mathbf{C}$	Centroid of contour
D	Signed distance from point to plane of surface element
E	Young's modulus
E'	Storage modulus
E''	Loss modulus
E^*	Complex valued Young's modulus
E'_B	Background storage modulus
E'_I	Inclusion storage modulus
R	Inclusion radius
V_{frac}	Volume of the contour as a fraction of the true inclusion volume
$\mathbf{X}_I$	True inclusion location
$\mathbf{X}_R$	Reconstructed inclusion location
d	Total distance from point to be projected to the three nodes of a surface element.

d_{edge}	Distance from point to be projected to edge of surface element.
$\mathbf{i}, \mathbf{j}, \mathbf{k}$	Unit vectors along the x, y, z axes respectively
$\hat{l}$	Unit normal along closest edge of surface element
$\hat{n}$	Normal to the surface element
p	Point to be projected onto surface element
t	Time
$\mathbf{u_I}$	Imaginary part of motion
$\mathbf{u_R}$	Real part of motion
$\mathbf{u}_c$	Calculated motion
$\mathbf{u}_m$	Measured motion
$v_{1,2,3}$	Ellipsoid semi-axis lengths
x_c, y_c, z_c	Inclusion center
y	Projected point on surface element

Chapter 1

Background and Introduction

1.1 Breast Cancer

Breast cancer is the second most common malignancy among women, accounting for nearly 1 in 3 cancers diagnosed among women in the United States. Approximately 230,000 new cases of invasive breast cancer and 40,000 breast cancer deaths were expected to occur in women in 2011 in the United States alone [1]. Worldwide, it is estimated that more than one million women are diagnosed with breast cancer every year, and more than 410,000 will die from the disease [2].

Previously the disease was not considered prevalent enough to warrant the allocation of health care spending in low and middle income countries [3]. Already an urgent public health problem in high-income countries, breast cancer is becoming an increasingly urgent problem in low-resource regions [4]. It is now the most common cancer among women both in developed and developing regions [5].

Figure 1.1 shows a diagram of basic breast structure. The breast is a modified skin gland consisting of several duct systems. Each duct system contains numerous lobules, which are the milk-producing glands. The surrounding tissue is a combination of adipose, *i.e.* body fat, and connective tissue, along with blood vessels and lymphatic vessels.

Breast cancer, like any other cancer, is an overgrowth of abnormal cells within the body. Instead of going through the normal process of apoptosis, or cell death, cancer cells continue to grow and form new, abnormal cells. As the cancer enlarges, it can acquire the necessary mutations to move beyond the breast, spread to axillary lymph nodes and eventually to distant organs. The spread of the cancer through the body is graduated by various stages, with the stage of the cancer ranging from 0 to VI.

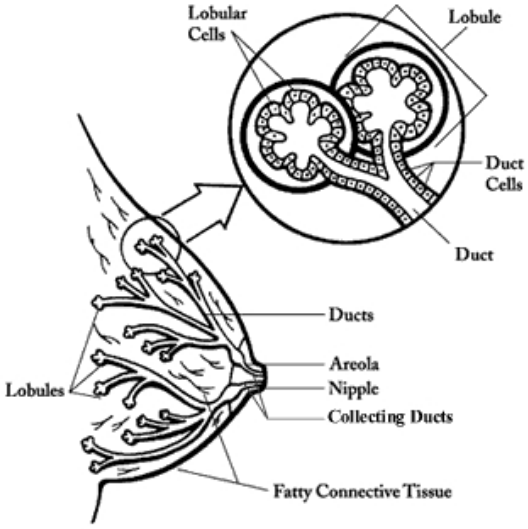

Figure 1.1: Diagram of human breast structure [6].

Stage 0 is a pre-cancerous condition where abnormal cells are found in the ducts or lobules of the breast. Ductal carcinoma *in situ* (DCIS) is a noninvasive condition in which abnormal cells are found in the lining of a breast duct. Similarly, lobular carcinoma *in situ* (LCIS) is a condition in which abnormal cells are found in the lobules of the breast. Carcinoma *in situ* will not necessarily develop into invasive cancer, in fact, most LCIS and some DCIS will not become invasive cancer. However, at the present time, it is not known how to predict which carcinoma *in situ* will become invasive.

The stages I to IV describe the spread of the cancer to lymph nodes and surrounding tissue, and/or increasing tumor size. Stage I is when an invasive cancer has formed. By stage IV the cancer has spread to other organs in the body, most often the bones, lungs, liver or brain. Once this proliferation occurs the survival rate drops significantly, as can be seen in Table 1.1.

1.1.1 Breast Cancer Screening

The rationale behind breast cancer screening is to detect breast cancer at a smaller size and earlier stage than would be detected by the patient or otherwise, and therefore reduce the number of women who die from breast cancer. Michaelson *et al.* found that the survival of patients with invasive breast carcinoma was a direct function of tumor size, independent of the method of detection [8]. For the 15 year survival rates found in the Van Nuys Breast Center population [9] the survival rate increased from 53% for tumors 26-35 mm in diameter to 86% for tumors 10-14 mm in diameter [8] [10].

Stage	5-year Survival Rate (%)
0	93
I	88
IIA	81
IIB	74
IIIA	67
IIIB	41
IIIC	49
IV	15

Table 1.1: Breast cancer 5 year survival rates by stage from the American Cancer Society and the National Cancer data base [7].

X-ray mammography is the current gold standard for breast screening, but it has several disadvantages [11]. The physical property measured in mammography, x-ray radio-density, exhibits a relatively low (5%-10%) contrast between healthy and cancerous tissue [12]. This creates difficulties in patients with higher density breast tissue [13]; a recent study shows mammography sensitivity in women with dense breasts is only 60% [14]. High density breast tissue is found in about 30% of women over the age of 50 and in about 50% of women aged 50 and younger [15]. These women are at a higher risk of developing breast cancer, but the development of tumors may be masked in mammography. This is due to the cancer exhibiting the same x-ray attenuation properties as fibroglandular tissue in breasts with extensive mammographic density [16]. In addition, young women are not routinely screened because of concerns of x-ray over-exposure.

A high non-compliance rate in mammography screening programmes is observed due to the expected and/or experienced discomfort associated with the required breast compression [17] [18]. Davy details the many studies of breast pain during mammography and the limited options available for alleviating it [19]. Manual palpation does not involve severe breast compression, but is not recommended for screening in the Western world due to poor performance and its high dependence on operator skill and experience [20].

In areas of the world were health care costs are prohibitive, more accurate diagnostics such as Ultrasound or MRI are too costly [21]. Limited access to screening in remote or rural areas, even in developed countries, has been associated with suboptimal screening rates and late-stage diagnosis of breast cancer [22].

There are no other modalities currently recommended for screening, but there is a need for a portable, low cost alternative that is less painful than mammography and more effective in women

with dense breasts.

1.1.2 Alternative and Emerging Breast Imaging Modalities

Nover *et al.* give a review of both modern breast cancer detection methods and the experimental techniques that show promise, but require widespread clinical trials to determine their potential for breast cancer detection [23].

Tomosynthesis is an extension of standard mammography. Multiple images are obtained using Full Field Digital Mammography (FFDM) with the x-ray at various angles thus allowing the creation of 3D images [24]. It requires a significant amount of experience to read and interpret the images, but tomosynthesis may be more comfortable than conventional mammography as it requires less breast compression [25].

Proton Emission Mammography (PEM) is a Proton Emission Tomography (PET) technique specifically for breast imaging. PEM can offer high spatial resolution [26], but can encounter difficulties imaging the posterier of the breast and the technique suffers from high false-positives due to fat necrosis at prior biopsy locations [27]. Nuclear medicine techniques such as PEM and PET are expensive and expose the patient to radiation, so would be recommended for high risk patients only, rather than screening the general population.

Diffuse Optical Imaging (DOI) or Optical Mammography (OM) uses near infrared light to detect functional abnormalities in tissue [28]. Several groups are currently exploring the potential of DOI for optical breast imaging [29]. DOI can potentially reveal changes in blood volume and oxygen saturation that are specific to early stages of cancer [30] [31].

Electrical Impedance Tomography (EIT), also known as Electrical Impedance Scanning (EIS), measures multiple electrical properties of breast tissue. The conductivity and permittivity of breast tumors are known to differ significantly from those of normal breast tissues, and EIT is being studied as a modality for breast cancer imaging to exploit these differences [32]. Cherepenin *et al.* developed a three-dimensional EIT system that has shown potential for breast cancer detection [33]. Soni *et al.* applied multi-frequency EIT *in vivo* using a system developed at Dartmouth College, demonstrating its potential for breast cancer detection [34]. Choi *et al.* have developed a reconstruction algorithm for breast tumor imaging using EIT techniques and applied it in phantom studies [35].

Thermography is an imaging modality in which temperature differences in the breast are mapped using the natural infrared radiation emitted by tissue. As cancerous tumors obtain nutri-

ents through neoangiogenisis, *i.e.* the growth of new blood vessels, as well as through existing blood vessels, the local temperature of the cancerous region is generally higher than that of surrounding tissue [36]. The computerized detection of breast cancer using thermography could potentially be used in the diagnosis of breast cancer [37].

All imaging modalities are based on some contrast between diseased and healthy tissue. Ideally the contrast is both high and easy to measure. Cancerous tissue is shown to be 200-1400% stiffer than the surrounding fibroglandular or fatty tissue [38]. This high contrast in stiffness between diseased and healthy tissue is the basis for tumor detection by both manual palpation and the various imaging modalities of elastography.

1.2 Elastography

Elastography, first defined by Ophir *et al.* [39], is a promising technique for diagnosing cancerous tissue based on its elastic properties. Elastic properties cannot be measured directly, however, and thus elastography requires that some compression or vibration of the tissue be performed. The resulting changes in displacements and strains from this compression or vibration can be measured and related to the underlying elastic structure. Parker *et al.* detail the development of elastography over the last twenty years [40]. The main imaging modalities used in elastography are ultrasound and Magnetic Resonance Imaging (MRI).

Compression elastography uses a comparison of ultrasound B-scan RF information from tissue before and after a modest compression [41]. By calculating the derivative of the displacement, *i.e.* the strain, an image of relative strain can be produced. The various tissues strain according to their relative stiffness, thus the strain image can be used to identify relatively stiff areas within the breast. Quantitative estimates of tissue elasticity have been made by solving the inverse problem [42], but this is not generally adopted in clinical applications. Recent work on the real-time solution of the Finite Element (FE) problem of viscoelasticity has been applied to B-scan images in phantom [43]. The advantages of compression elastography are that it can produce an image in real time [44] and the ultrasound transducer can be hand-held, allowing highly localized compression at the region of interest. The disadvantages are that currently only a relative image of strain is produced; only a 2D plane is imaged and tissue can move out-of-plane during compression; and deeper organs can be difficult to compress [40].

In vibration amplitude sonoelastography, developed by Lerner *et al.* [45], a low frequency vibration (20-1000 Hz) and usually low amplitude (less than 0.1 mm displacement) [46] is exter-

nally applied to the breast or other tissue under investigation, while the tissue is imaged with Doppler ultrasound. Doppler detection algorithms are then applied to give a real-time vibration image. A stiff inhomogeneity within the surrounding soft tissue produces a disturbance in the normal vibration eigenmode patterns. As a result, isoechoic tumors, *i.e.* reflecting ultrasound in a similar manner to surrounding tissue, that are undetectable by conventional ultrasonography may be distinguished using sonoelasticity imaging because of their altered vibration response. Three-dimensional imaging with sonoelastography can be achieved with the acquisition of sequential tomographic slices. This, combined with image segmentation, enables the reconstruction, quantification and visualization of tumor volumes [47].

Magnetic Resonance Elastography (MRE) uses Magnetic Resonance Imaging (MRI) to measure all three spatial components of the induced tissue displacement. Fowlkes *et al.* developed a quasi-static approach to MRE that measures internal tissue strain using the saturation method [48]. Plewes *et al.* used the phase-contrast method to obtain quasi-static strain images *in vivo* and determined the biomechanical properties of previously detected lesions [49]. This group also proposed a reconstruction method which reduced the three-dimensional problem to two-dimensions by imposing approximate plane strain conditions [50].

Muthupillai *et al.* proposed a dynamic approach to MRE based on the phase contrast imaging method [51]. As with sonoelasticity imaging, the shear modulus can be computed directly from local estimates of wavelength. Accurate quantification of wavelength in complex organs such as the breast can be difficult, therefore this group computed the shear modulus by applying the local frequency estimation (LFE) technique [52] to MRE data to produce encouraging *in vivo* results [53] [54].

Two groups independently proposed a different approach to MRE that measured the mechanical properties of soft tissue under steady-state harmonic actuation. Both groups use the phase-contrast imaging method. Sinkus *et al.* proposed a direct inversion technique where the elastic properties are calculated using a system of partial differential equations in which the spatial derivatives of the measured displacements are coefficients [55]. The technique is efficient, but very sensitive to measurement noise, as the measured data must be differentiated, thus amplifying any noise. Weaver *et al.* compute the shear modulus from time-harmonic displacements using an iterative inversion technique that does not require any data differentiation, but does require the solution of the three-dimensional inverse elastography problem on a highly resolved FE mesh. This massive computational overhead was overcome by employing an overlapping sub-zone inversion

technique [56], which was implemented using parallel computing [57].

The high accuracy and precision of MRI allows for quantitative reconstruction of the mechanical properties of tissue. MRE has the potential to improve the specificity of breast cancer diagnosis by imaging various viscoelastic properties of tissue [58] [59], but the high cost is prohibitive for screening the general population.

1.3 Digital Image Elasto Tomography

Digital Image Elasto-Tomography (DIET) is a novel elastography based breast cancer screening technique under development at the University of Canterbury [60] [61] [62], which quantifies tissue stiffness from digital images of the breast under harmonic actuation. It is intended as a low-cost screening modality suitable for women with denser breasts, without the pain associated with mammography. The prototype system under development shown in Figure 1.2 is designed to be portable, thus potentially improving access to screening in remote or rural areas.

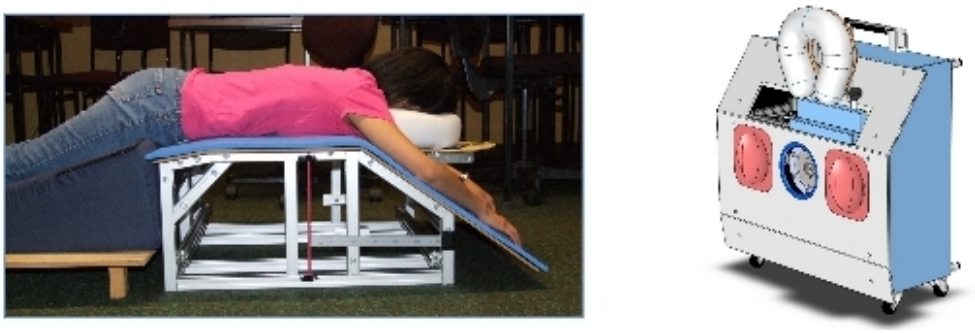

Figure 1.2: Image of the DIET prototype during ergonomic testing (left), and a sketch of the portable protoype (right).

The aim of DIET is to detect the existence and approximate location of a stiffer inclusion which would require further investigation. It is thus intended to be a pre-screening method, adjunct and complementary to mammography, particularly for those individuals who may not be eligible due to age or who do not have ready clinical access to mammography.

The imaging modality in DIET is digital imaging. In conjunction with strobe lighting, digital imaging sensors capture images of the breast surface while the breast is harmonically actuated from below. The still images of the breast in motion are converted to displacement data using image processing algorithms [63]. This displacement data is the input to a reconstruction algorithm

which produces a three dimensional representation of the internal elastic properties of the breast and thus identifies any inclusions that require further investigation. Concurrent research into various motion metrics and minimal elastographic modeling may provide greater constraint for the reconstruction algorithm [64].

The reconstruction algorithm requires solution of the forward problem, that is to calculate the resulting motion for a known actuation and given material property model. There have been two approaches to the DIET forward problem in previous work. Peters used the Finite Element Method (FEM) [61], whereas Berger *et al.* developed the Boundary Element Method (BEM) for DIET [65] [66].

This thesis is concerned with the development and application of a parallel reconstruction algorithm for DIET using FEM to solve the forward problem. A parallel reconstruction algorithm is an essential step towards producing an automated clinical system with software based diagnosis, and thus a system with low operator skill requirements that will provide wider access to breast cancer screening.

1.4 The DIET Inverse Problem

To perform a reconstruction of mechanical properties of the breast, we must solve the inverse problem. That is, for the recorded surface motion and the known actuation, what are the internal material properties of the breast? The elastography inverse problem is non-linear and ill-posed [67][68]. With a data rich modality, such as MRE, where a near full-volume motion dataset is acquired, several material properties can be optimized for at each node of an FE model using regularization techniques [69][59]. In DIET only surface motion data is available, which leads to a more difficult inverse problem to solve.

Reconstructions by Peters [61] and Beger [66] have solved for the case of a single stiff inclusion within a less stiff background. Berger used gradient descent methods to optimize for a spherical inclusion within the volume using numerically simulated data and a phantom test case [66]. The reconstructed parameters were the radius and stiffness of the inclusion and its location within the breast. Berger solved for the soft material Young's modulus by assuming that the volume was homogeneous and that any inclusion was small. This worked well for small inclusions, but less well for larger inclusions.

Van Houten *et al.* have achieved encouraging results with a reconstruction algorithm using a spherical inclusion in a cylindrical phantom [62]. The reconstruction algorithm was a hybrid

algorithm of combinatorial optimization with simulated annealing, and gradient descent for the final convergence to the best fitting solution. The reconstructed parameters were radius, stiffness, and z-position of the inclusion. Figure 1.3 shows a diagram of the phantom used. Although a successful reconstruction for such a phantom is a positive result for the DIET project, it is evident that further development is needed to progress towards a system that can produce successful reconstructions in a clinical setting.

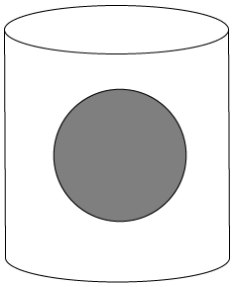

Figure 1.3: Structure of cylindrical phantom used in the reconstruction by Van Houten *et al.* [62]. Note the relatively large size of the inclusion and the rotational symmetry of the phantom.

1.4.1 Implicit Surfaces

Implicit surfaces are two-dimensional geometric shapes that exist in three-dimensional space. An implicit representation of the interface between tumor and healthy breast tissue would be an isocontour of some function. Radial basis functions (RBFs) are an example of implicit functions that have been used for reconstruction in electromagnetic tomography. Recent work by Naik et al. demonstrated the flexibility of radial basis functions in numerical studies of 2D reconstruction to converge to the correct solution of two separate objects (in their case, land mine-like objects) from an initial guess of one object [70]. This is a desirable property in the case of the DIET system as in an eventual clinical situation, multiple areas of high stiffness are a possibility.

Shape based methods use implicit algebraic surfaces such as spheres, ellipsoids and tori to describe inclusions. The feasibility of shape based methods to simplify the inverse problem in biological tissue has been demonstrated in Diffuse Optical Tomography (DOT) [71] and in vibroacoustic elastography [72], as well as in earlier phantom studies with the DIET system [62]. In an alternative approach, Olsen and Throne used element based elastic moduli in 2D for a static deformation based elastography problem [73]. In the element based approach, each element of the FE mesh becomes a parameter in the inverse problem. To extend element based elastic moduli into 3D requires a large increase in the number of parameters. In contrast, shape based methods

require far fewer additional parameters to move from 2D to 3D. Even complex three dimensional geometries can be described with a small number of shape parameters [74].

"Blobby" or "metaball" models are a blend of several implicit surfaces, usually spheres and ellipsoids. They were first proposed by Blinn [75] and are used extensively in computer graphics to design smooth, complex, organic-appearing shapes [76]. Blobby models consist of a number of source points in 3D space. The field function $D(r) = \frac{1}{r^2}$ gives the field strength, where r is the distance from the source. The total field strength at any point in space is the sum of the field strengths due to all sources within the volume. An isocontour of field strength can be drawn through this space, which results in a 3D surface. There are various blending methods that can be applied to give smooth surfaces which are of great interest in computer graphics [76]. Blobby models using ellipsoids have been used successfully as a coarse level approximation to fit a surface to point cloud data in 3D [77]. In the case of the DIET project, blending of surfaces is not critical as the surface will be used inside a mesh of discrete nodes.

The level set approach was first introduced by Osher and Sethian [78]. The idea behind level sets is rather than parameterize the curve (in 2D) of the inclusion, the curve becomes the intersection of a surface and the xy plane. In this way, a curve propagating in the plane is replaced by the problem of a two-dimensional surface evolving in three dimensions. This approach does not include any *a priori* assumptions about the geometry, which is advantageous as it allows the boundary of an inclusion to separate into two inclusions. Ameur *et al.* used the level set method for the two-dimensional inclusion problem for linear elasticity [79], which preformed well for 2D numerical case studies with various shaped single inclusions, but with less success for the two inclusion case.

1.4.2 The Genetic Algorithm

Once the model, *i.e.* the the forward problem parameter description, has been decided upon, the optimal values for the model parameters need to be discovered. Peters *et al.* exposed the limited value of using standard gradient techniques in the DIET inverse problem and the need for stochastic methods to avoid local minima [80]. The potential of the Genetic Algorithm (GA) in elastography has been demonstrated by Zhang *et al.* [81]. Olsen and Throne used a GA with success in a 2D numerical study of breast elastography [73]. In cardiovascular elastography, Khalil *et al.* developed a theoretical technique that combines FEM with a GA for characterization of atherosclerotic plaques in diseased arteries [82]. They concluded that a FEM/GA may serve as

an effective low-resolution initial guess for discrete inverse formulations. This is the desired level of reconstruction for a DIET inversion algorithm, identifying regions of high stiffness. Karami *et al.* extended the FEM/GA to estimate nonlinear elastic properties of vascular tissue [83]. The imaging modality used in both studies was Optical Coherence Tomography (OCT). This differs from the surface motion imaging of DIET, however, a combined FEM/GA can be applied to the DIET inverse problem.

1.4.3 Geometric Methods

Gradient descent methods such as Gauss Newton or the conjugate gradient method are based on the geometry of the objective function, or *cost surface*, and use the gradient of the objective function to descend down to the minimum. These methods converge quickly, but can become trapped in local minima. Genetic algorithms can avoid local minima, but do not converge quickly on the global minimum [84]. A brute force search would solve both these problems and identify the global minimum with certainty, however, for DIET, the high computational cost of each FE solution makes an efficient parameter search desirable.

Many problems have computationally expensive forward solutions. Response surfaces, that is multivariate approximations of the computationally expensive function to be optimized, have been used as a computationally inexpensive way to identify potential minima [85] [86]. Jones *et al.* [87] fitted a response surface to data collected by evaluating the objective and constraint functions at a few points and used this surface to predict optimum values. When searching the parameter space for a geophysical problem, Sambridge alternates between fitting a surface to the cost function and evaluating the forward problem [88]. In this work, a different approach to the problem is presented, termed Fitness Function Analysis (FFA), which makes assumptions about the geometry of the cost surface and uses these assumptions to generate parameter predictions for use in the GA.

1.5 Rationale for this Research

There have been major improvements in the DIET imaging system since previous reconstruction work by Peters *et al.* [89], Berger [66], and Van Houten *et al.* [62]. Previous work on phantom elasticity reconstruction used axisymmetric cylindrical phantoms with the associated FE meshes constructed from measurements of the phantoms [62] [89]. Only axisymmetric phantom recon-

structions were possible due to the limited surface coverage provided by the two cameras used for image capture. The DIET prototype now has five cameras, which allows greater surface coverage; hundreds rather than tens of fiducials can be tracked on each phantom/breast. Greater surface coverage allows a patient specific FE mesh to be constructed from the tracked data points [90]. More realistic tissue-mimicking phantoms, including anti-axissymmetric phantoms and phantoms with small (5 mm radius) inclusions and Young's moduli comparable to breast tissue, have been created. In addition, the DIET prototype has been developed to take multi-frequency datasets and the first *in vivo* data have been acquired with the DIET prototype.

The improvement in data capture and the the requirement to deal with the added complexities of multi-frequency and *in vivo* data drives the need for an improved reconstruction algorithm.

1.6 Objectives

- The nature of the DIET problem is ill-posed, and so a reconstruction method that uses as few parameters as possible while still being flexible enough to locate an inclusion is optimal.

- As the aim of the DIET project is that it will be used in a clinical setting, specificity as well as sensitivity is important. The algorithm needs to be flexible enough to produce a positive result for single inclusions, multiple inclusions, and clearly indicate the case of no inclusions present.

- The reconstruction algorithm should not be dependent on the initial guess. It should be rapid, i.e. it should take less time to run than an exhaustive search.

- The material properties of human breast tissue are variable from person to person, so the algorithm should be able to get a first estimate for the background parameters, storage modulus and damping ratio, from the motion data.

- Concurrent research into characterizing the surface motion may indicate which area of the breast an inclusion is located in [64]. The algorithm should therefore be able to accept constraints from a user as to where to restrict the inclusion location optimization.

1.7 Thesis Structure

- Chapter 2 describes the construction of the breast phantoms used in this thesis, the collection of data with the DIET prototype and the forward modeling of the breast motion.
- Chapter 3 describes the reconstruction method developed and applied in this work.
- Chapter 4 details a single frequency phantom study using the reconstruction algorithm. The phantoms have a storage modulus of approximately 3 kPa, the most realistic phantoms used in DIET to date. The sensitivity to *a priori* assumptions is examined for three phantom cases. The selected *a priori* assumptions are applied to successfully locate inclusions in two further phantoms. The optimal and credible regions for inclusion locations are described.
- Chapter 5 describes the use of the first application of a reconstruction algorithm to DIET multi-frequency datasets. Two methods of creating multi-frequency cost are examined, resulting in a recommendation for multi-frequency cost to be used in reconstructions. Successful phantom multi-frequency reconstructions are presented.
- Chapter 6 details a numerical study of the reconstruction algorithm after it has been developed to incorporate ellipsoidal and multiple inclusions with recommendations for model selection. The algorithm is applied to a phantom containing two 'cancerous' inclusions and to a phantom containing multiple inclusions, one of which represents cancer.
- Chapter 7 details the first *in vivo* reconstruction results in DIET for single and multi-frequency data. There are three patient datasets. For each patient, both the breast containing a cancerous mass and the healthy breast were imaged.
- The conclusions are given in Chapter 8 with recommendations for future work given in Chapter 9.

Chapter 2

Experimental and Forward Simulation Methods

2.1 Phantom Construction

The phantoms used in this thesis are made from a mix of silicone fluid and A-341 silicone from Factor II, Inc. A-341 is a unique two component platinum room temperature vulcanization (RTV) silicone gel and has a wide variety of uses, from prosthetics, special effects and GFAs^{TM} (gel filled appliances) to various manufacturing applications [91]. By adding various amounts of silicon fluid to the A-341, the elasticity of the silicone can be adjusted gradually. The phantoms were constructed to be tissue-mimicking and as such their Young's modulus was based on tissue elasticity measurements by Samani *et al.* [38]. Samani *et al.* have developed specialized techniques to measure tissue elasticity of normal breast tissues and tumor specimens and applied them to 169 fresh *ex vivo* breast tissue samples including fat and fibroglandular tissue as well as a range of benign and malignant breast tumor types. The results are reproduced in Table 2.1.

Breast tissue type	**Number of samples**	**Young's modulus (kPa) mean ± STD**
Normal fat	71	3.25 ± 0.91
Normal fibroglandular tissue	26	3.24 ± 0.61
Fibroadenoma	16	6.41 ± 2.86
Low-grade IDC	12	10.40 ± 2.60
ILC	4	15.62 ± 2.64
DCIS	4	16.32 ± 1.55
Fibrocystic disease	4	17.11 ± 7.35
Intermediate-grade IDC	21	19.99 ± 4.2
High-grade IDC	9	42.52 ± 12.47
IMC	1	20.21
Fat necrosis	1	4.45

Table 2.1: Breast tissue characteristics from Samani *et al.* [38]

The phantoms are constructed as follows:

- The silicone is mixed to produce the desired stiffness. The various mixtures are given in Table 2.2. The Young's moduli are known from previous material testing [61].
- The liquid silicone is degassed in a venturi vacuum chamber, shown in Figure 2.1, to avoid air bubbles forming in the silicone as it cures.
- The silicone is cured for several hours, producing solid silicone, Figure 2.2, which is then shaved into inclusions, Figure 2.3. The 'cancerous' inclusions are carved from type 1 silicone, with a Young's modulus of 27 kPa, thus giving the 'cancer' an approximately ten times contrast from the background stiffness. The inclusion material used in this thesis is the same composition as the background material for phantoms used in previous work [62]. The type 2 inclusions are used to provide varying material properties, *i.e.* not a completely homogeneous background within phantom, with their material properties comparable to breast tissue with a Young's modulus ≈ 7 kPa.
- The inclusions are suspended in the breast mold, Figure 2.4, while the background silicone is poured into the mold to form the phantom. The wires are removed once the silicone is cured.
- The final step is to pour a 10 mm layer of type 1 silicone on to the phantom to attach a plastic plate containing metal bolts, shown in Figure 2.5. This is a practical necessity which allows the phantom to be attached to the DIET acquisition system.
- The finished phantom is shown in Figure 2.6 together with the breast mold.

Type	**Silicone**		**Young's modulus (kPa)**	**Tissue**
	A-341 (%)	**Silicone Fluid (%)**		
1	100	0	27	Invasive carcinoma
2	75	25	7	Fibroadenoma and low-grade IDC
background	50	50	3	Normal fat and fibroglandular tissue

Table 2.2: The composition of silicone used in the phantoms with the Young's modulus and tissue it is used to represent.

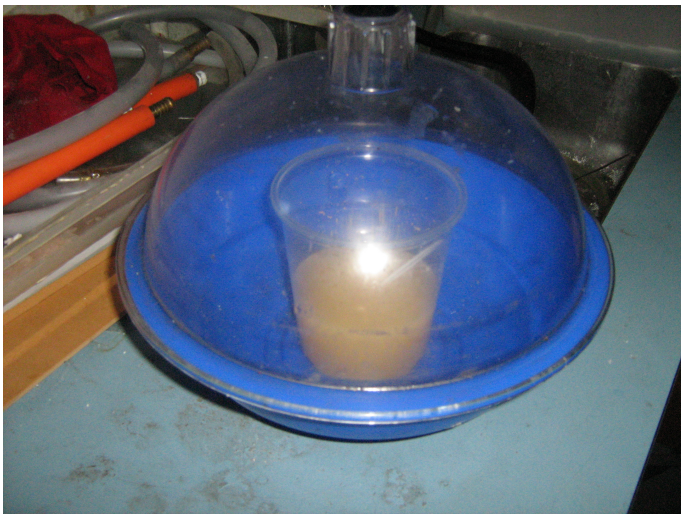

Figure 2.1: Degassing of the liquid silicone. The silicone is placed in a venturi vacuum chamber for 20 minutes to remove any air bubbles from the silicone.

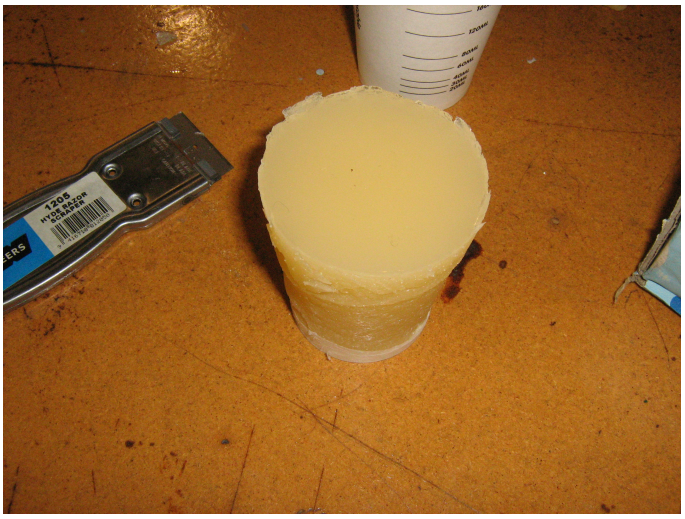

Figure 2.2: The silicone before it is shaved to form inclusions.

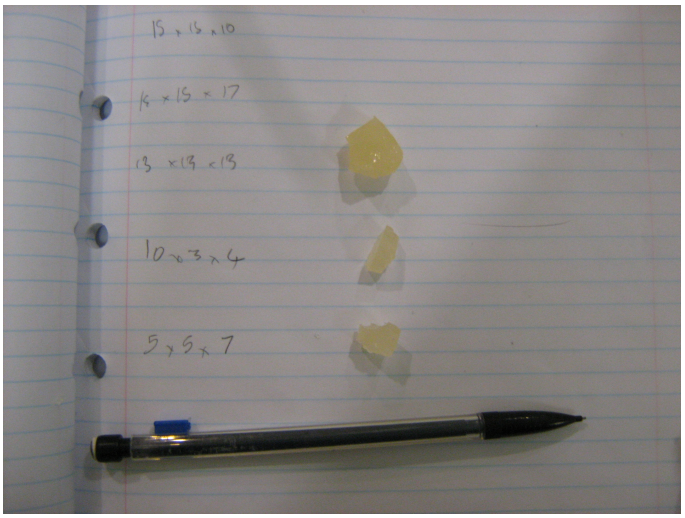

Figure 2.3: A sample of the inclusions.

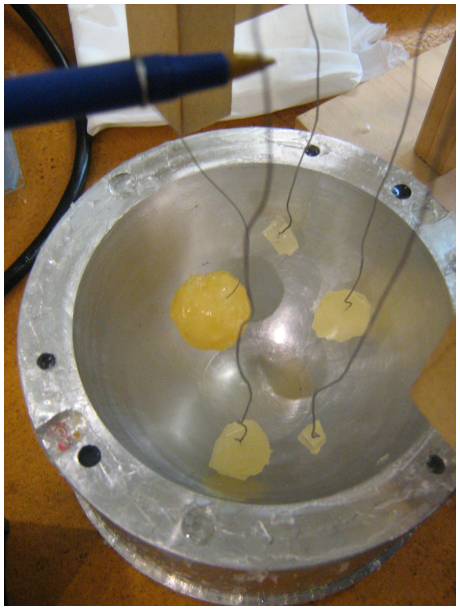

Figure 2.4: Inclusions suspended in the breast mold.

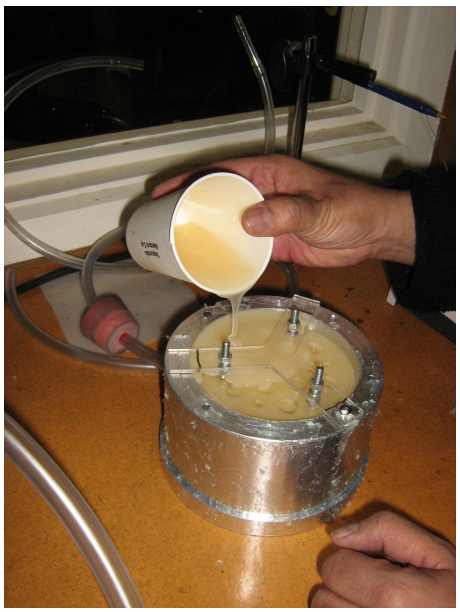

Figure 2.5: Final stage of phantom construction. Silicone is poured over a plastic plate with attached bolts. The bolts allow the phantom to be attached to a metal plate and placed in the DIET prototype.

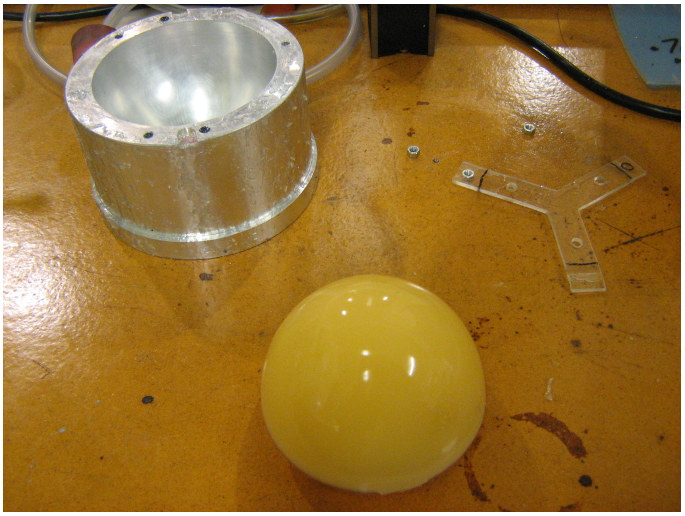

Figure 2.6: Finished phantom together with the breast mold.

2.2 Data Collection

All data in this thesis, with the exception of numerically simulated data, were acquired using the DIET prototype system, detailed in Lotz *et al.* [92]. Figure 2.7 shows a schematic of the DIET acquisition system together with a photograph of the interior of the DIET prototype. The patient lies on the DIET table with one breast hanging pendant through a hole and making contact with the actuator. The actuator is used to induce steady-state vibrations in the breast. An array of five digital cameras captures images of the steady-state oscillating breast surface using a synchronized strobe lighting system [93]. Randomly placed, colored fiducial markers are applied to provide robust tracking of the surface motion [94]. Calibration of the camera system is performed prior to breast imaging using a specially developed calibration object [63] allowing the still images of the fiducials to be converted into three dimensional point locations. Figure 2.8 shows an image collected using the DIET prototype. The red, green and blue dots are the fiducials used to track the motion of the breast surface.

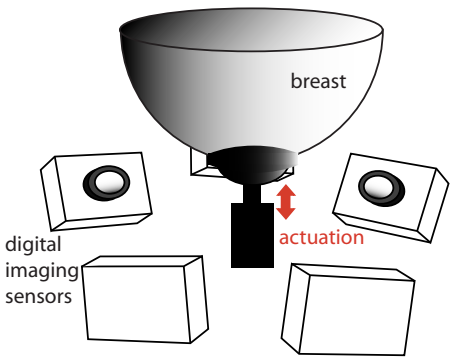

(a) Schematic of DIET acquisition system.

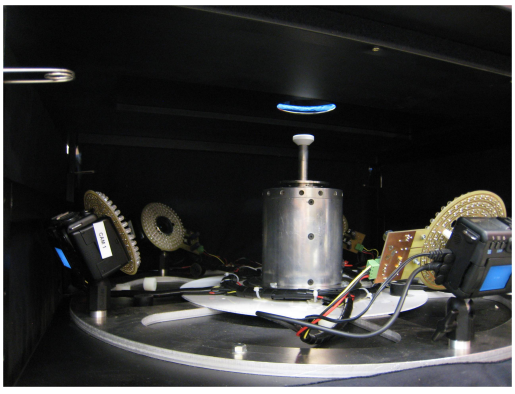

(b) Photograph of the interior of the DIET prototype.

Figure 2.7: Schematic of DIET acquisition system. The breast is harmonically actuated from below. Calibrated digital imaging sensors together with strobe lights are used to capture the surface motion of the breast.

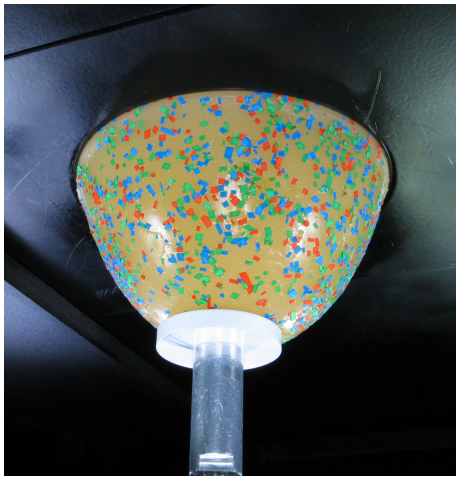

Figure 2.8: Image collected during DIET data acquisition. The red, blue and green dots are colored paper, which serve as fiducials to track the surface motion. The phantom imaged here is in motion, but the image is not blurred due to the synchronization of the strobe lights and actuator.

2.3 Finite Element Model

The reconstruction algorithm requires solution of the forward problem, that is to calculate the resulting motion for a known actuation and given material property model.

Assuming a homogeneous, isotropic, linearly elastic medium, the displacement and elastic properties are related by the following equation,

$$\nabla \cdot \mu \nabla \mathbf{u} + \nabla(\lambda + \mu) \nabla \cdot \mathbf{u} = \rho \frac{\partial^2 \mathbf{u}}{\partial t^2} \tag{2.1}$$

where μ and λ are the lamé parameters, $\mathbf{u}$ is the displacement, and body forces, such as gravity, have been assumed to be negligible.

There are several shortcomings of using a linear isotropic model for human tissue, which is hyperelastic, anisotropic and inhomogeneous. The static deformation due to gravity will change the tissue response from place to place due to the non-linearities in the tissue. It is assumed in this work that gravitational loading generates an initial set of large, static deformations, after which the light vibrations applied to the tissue are assumed to produce a small, linearly viscoelastic response around the deformed geometry. This relative difference in mechanical properties is the basis for the DIET reconstruction algorithm.

Skin is anisotropic and hyperelasitc [95], but can be successfully approximated by an isotropic and linear elastic model [96] provided that the strain does not exceed 50% [95], [97]. Elastography using MRI as an imaging modality has been shown to produce successful reconstructions for both

breast [98] and brain [99] tissue assuming a linearly viscoelastic, isotropic model. The linear, isotropic model is also used in Ultrasound Elastography [100] [101]. In DIET we must be cautious of introducing extra parameters without any gain in solution resolution because of the already poorly posed problem of reconstructing elastic properties from surface motion. Thus, following the previously mentioned MRE and ultrasound elastography methodology, a linearly viscoelastic material model is assumed in this thesis.

To solve Eq. 2.1, the problem is converted to a Finite Element problem, and a simple viscoelastic model using springs and dashpots is used to model the lossy nature of biological tissues. The nearly incompressible model is used for the forward simulations in this thesis. Peters found that a Poisson's ratio, ν, of 0.45 produced acceptable forward simulation results [61], thus Poisson's ratio is fixed at 0.45 for the forward simulations, with the shear modulus, μ and Lamé parameter λ related to the Young's modulus, E by

$$\mu = \frac{E}{2(1+\nu)} \tag{2.2}$$

and

$$\lambda = \frac{2\mu\nu}{1+2\nu} \tag{2.3}$$

The viscous response of a dashpot introduces a time varying term into the constituent equations. For DIET, the forward problem is time harmonic and so this time varying term is implemented by assuming a frequency-dependent and complex valued Young's modulus, E^*.

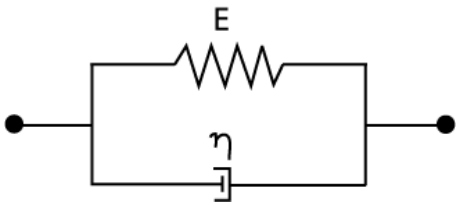

Figure 2.9: Schematic illustration of a Voigt element, a purely viscous damper and purely elastic spring connected in parallel.

To illustrate a complex valued Young's modulus, consider the Voigt model, shown in Figure 2.9 consisting of a linear spring with Young's modulus, E, and a dashpot with viscosity, η. Because the two components of the model are in parallel the strains, ϵ, must be equal,

$$\epsilon = \epsilon_1 = \epsilon_2. \tag{2.4}$$

The total stress, σ is the sum of the stresses in each component,

$$\sigma = \sigma_1 + \sigma_2 \tag{2.5}$$

which, using the stress-strain relationships for a spring and a dashpot, can be expressed as,

$$\sigma = E\epsilon + \eta\dot{\epsilon} \tag{2.6}$$

In the DIET forward problem the stress and strain are time harmonic, so assuming linear behavior strain and stress become,

$$\epsilon = \bar{\epsilon} sin(\omega t) \tag{2.7}$$

$$\sigma = \bar{\sigma} sin(\omega t + \delta) \tag{2.8}$$

where $\bar{\epsilon}$ and $\bar{\sigma}$ are the amplitude of strain and stress respectively, t is the time, ω is the angular frequency, and δ is the phase difference between stress and strain. The storage modulus, E', is a measure of the stored energy, representing the elastic property of the element, where

$$E' = \frac{\bar{\sigma}}{\bar{\epsilon}} cos(\delta). \tag{2.9}$$

The loss modulus, E'', is the energy dissipated as heat, which represents the viscous property of the element, where

$$E'' = \frac{\bar{\sigma}}{\bar{\epsilon}} sin(\delta). \tag{2.10}$$

The dynamic modulus E^*, is a complex number combining the storage and loss moduli,

$$E^* = E^{'} + iE^{''}. \tag{2.11}$$

where $E^{'} = E$ and $E^{''} = \omega\eta$. The equivalent of Eq. 2.6 for the time-harmonic case then becomes

$$\bar{\sigma} = E^*\bar{\epsilon}. \tag{2.12}$$

Similarly, the complex versions of the moduli in Eqs. 2.2 & 2.3 are given by

$$\mu^* = \frac{E^*}{2(1+\nu)} \tag{2.13}$$

and

$$\lambda^* = \frac{2\mu^*\nu}{1+2\nu} \tag{2.14}$$

It is important to note that the Voigt model described here is used purely as an illustration of the concept of complex moduli, and that in this work no direct comparison to any rheological model is made. The phantoms and tissue material properties in this work are characterized by the storage modulus E', and the damping parameter ζ, where

$$E'' = \zeta E'. \tag{2.15}$$

The basic Finite Element code used for all forward simulations in this thesis was written by Peters and Berger. A description of the Finite Element Method is given in Appendix A. The code was modified to become a parallel subroutine of the reconstruction algorithm presented here.

2.3.1 Mesh Generation and Boundary Conditions

In order to solve Eq. 2.1 using FEM, a mesh of the breast must be created. Biehler used a surface fitting technique to create a mesh from the tracked fidicuals on the breast surface [90]. The surface fitting is done using the FASTRBF$^{\text{TM}}$ toolbox from Farfield Technology [102] for fitting and evaluating radial basis functions. This development allows a patient specific mesh to be created for each dataset, an important step for the DIET project as it removes the requirement to measure the breast geometry, or to use a standardized breast mesh for all patients. All the meshes used in this thesis are composed of linear tetrahedral elements.

The boundary conditions are applied at the actuator and the chest wall. Figure 2.10 shows the location of boundary nodes used in various numerical, phantom and *in vivo* experiments. Note the meshes in Figures 2.10b and 2.10c, created from phantom and *in vivo* datasets respectively, are inverted because the DIET fiducial positioning is with the z axis positive downwards. The applied motion is the boundary condition at the actuator and the nodes at the chest wall are considered fixed. The chest wall boundary condition is a simplification of what is occurring *in vivo*. Samani *et al.* approximated the chest wall by fitting a third-order polynomial to MRI data and assuming zero displacement at the fitted surface. [103]. Bhatti & Sridhar-Keralapura constrain displacement

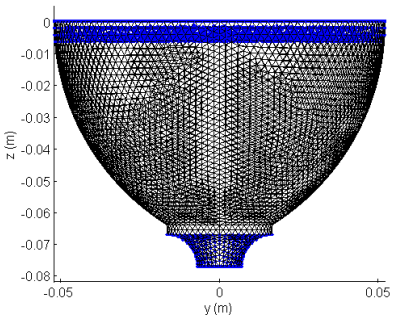

(a) The mesh used for numerical validation of GA and FFA.

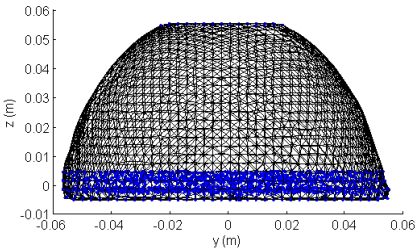

(b) A mesh used in phantom reconstructions

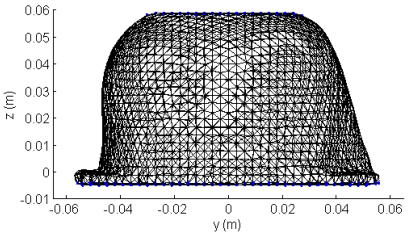

(c) A mesh used in an *in vivo* reconstruction.

Figure 2.10: Location of the boundary conditions for the numerical, phantom and in vivo FE simulations. The location of the nodes with boundary conditions are indicated in blue. The nodes at the actuator have the displacement from the actuator applied. The nodes at the chest wall have zero displacement applied.

to zero in all directions on the chest wall boundary in their software phantom for biomechanical modeling of elastography [104]. The same Dirichlet boundary condition of zero displacement at the chest wall is assumed in this work, however, at this stage in DIET development the chest wall is approximated by a flat surface. More sophisticated methods of modeling chest wall topography are used in other imaging modalities, for example, Rajagopal *et al.* customized finite element models by automatically fitting geometrical models to segmented data from breast MRIs [105].

Chapter 3

Reconstruction Methods

The reconstruction algorithm developed for this work, which aims to solve for internal material properties from external surface motion, consists of five parts:

1. A shape based parameter description to simplify the inverse problem
2. Projection of the measured data onto a Finite Element mesh
3. Comparison of measured motion to simulated motion using a cost function
4. Optimization of parameters
5. Image reconstruction

Sections 3.1 to 3.6 detail each part of the algorithm. The computational implementation and validation of the parameter optimization algorithm is described in section 3.7.

3.1 Model Selection

In DIET, motion data is available only on the surface, yet the reconstruction of material properties is desired throughout the whole volume. To produce a solution, the inverse problem must be simplified to identifying areas of high stiffness within the breast. This simplification is satisfactory, as DIET is not intended to be a standalone diagnostic tool, but an initial screening technique used to identify any stiff areas within the breast that require further investigation.

In order to choose a description of the model to optimize in the DIET reconstruction problem, one must assess what is required. Level sets and radial basis functions potentially offer a large array of complex geometries for relatively few parameters. The goal of DIET is to identify any

stiff areas within the breast where the level of detail required for the boundary of this area need not be high. Given that the priority of the DIET system is centroid location rather than geometric accuracy, spherical and ellipsoidal inclusion models were chosen for the reconstruction, as these are a reasonable approximations to a breast mass. At the present time, only the location and approximate shape and stiffness of an inclusion is required, so a simple algebraic surface of a sphere or ellipsoid will be used in the reconstruction algorithm, rather than blobby models.

The model (θ) used to describe the breast tissue is the collection of material parameters together with an algebraic surface describing the inclusion. In this thesis the terminology *background* refers to those parameters which describe the material properties of the tissue outside the inclusion. The term *inclusion* is used to refer to both phantom inclusions and *in vivo* breast masses. The model parameters are:

- E'_B Background storage modulus
- ζ_B Background damping parameter
- x_c, y_c, z_c Inclusion center
- R Inclusion radius (spherical inclusion)
- E'_I Inclusion storage modulus
- ζ_I Inclusion damping parameter
- $v_{1,2,3}$ The three semi-axes lengths of an ellipsoidal inclusion
- α, β, γ Inclusion rotation about the x, y, z axes (ellipsoidal inclusion)

The model for a spherical inclusion, $\theta(E'_B, \zeta_B, x_c, y_c, z_c, R, E'_I, \zeta_I)$, or an ellipsoidal inclusion $\theta(E'_B, \zeta_B, v_1, v_2, v_3, x_c, y_c, z_c, \alpha, \beta, \gamma, E'_I, \zeta_I)$, is implemented into the Finite Element equation by testing each node within the mesh. Nodes are classified as inside or outside the inclusion and their material property values are allocated accordingly. Node i lies within a spherical inclusion if

$$(x_i - x_c)^2 + (y_i - y_c)^2 + (z_i - z_c)^2 \leq R^2 \tag{3.1}$$

for an inclusion of radius R and center (x_c, y_c, z_c).

Nine parameters are required to describe an ellipsoidal inclusion in three-dimensional space: three parameters to describe the center of the ellipsoid, three for the length of each semi-axis, and

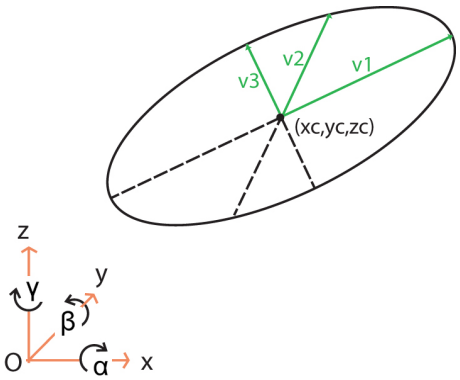

Figure 3.1: Parameters used to describe an ellipsoid in 3D space: center, axis length, and rotation.

three for the rotation of the ellipsoid about the x, y, z axes. A diagram of the nine parameters is given in Figure 3.1. A point in 3D space, $\mathbf{x}$, lies inside the ellipsoid when

$$(\mathbf{x}-\mathbf{c})^T R^T V^{-1} R(\mathbf{x}-\mathbf{c}) \leq 1, \tag{3.2}$$

where $\mathbf{c}$ is the location of the center of the ellipsoid (x_c, y_c, z_c), and the square of the semi-axis lengths, v_1, v_2, v_3, comprise the matrix V,

$$V = \begin{bmatrix} v_1^2 & 0 & 0 \\ 0 & v_2^2 & 0 \\ 0 & 0 & v_3^2 \end{bmatrix}, \tag{3.3}$$

and R is the rotation matrix combining rotations, α, β, γ about the three axes.

$$R_x(\alpha) = \begin{bmatrix} 1 & 0 & 0 \\ 0 & cos(\alpha) & sin(\alpha) \\ 0 & -sin(\alpha) & cos(\alpha) \end{bmatrix} \tag{3.4}$$

$$R_y(\beta) = \begin{bmatrix} cos(\beta) & 0 & -sin(\beta) \\ 0 & 1 & s0 \\ sin(\beta) & 0 & cos(\beta) \end{bmatrix} \tag{3.5}$$

$$R_z(\gamma) = \begin{bmatrix} cos(\gamma) & sin(\gamma) & 0 \\ -sin(\gamma) & cos(\gamma) & 0 \\ 0 & 0 & 1 \end{bmatrix} \tag{3.6}$$

For multiple ellipsoidal inclusions, each node is tested using Eq. 3.2, with the appropriate values of $x_c, y_c, z_c, v_{1,2,3}, \alpha, \beta, \gamma$.

3.2 Projection of point data onto the mesh

The data acquisition process uses intentional aliasing to capture steady state motion over several cycles [93]. This is a practical necessity as the commercial-grade cameras used in the DIET system cannot achieve high enough imaging rates to accurately capture time-harmonic motion within a single cycle.

The steady state oscilation of a point about an origin, such as the motion of a fiducial in DIET, can be expressed using a time-harmonic displacement vector, defined at any time t as

$$\bar{\mathbf{u}}(t) = \Re\left\{\mathbf{u}e^{i\omega t}\right\}, \tag{3.7}$$

where ω is the frequency of the system, and the amplitude $\mathbf{u}$ is complex, $\mathbf{u} = \mathbf{u_R} + i\mathbf{u_I}$. The motion of the fiducial can also be described using a real-valued amplitude, $\tilde{\mathbf{u}}$, and phase, ψ,

$$\bar{\mathbf{u}}(t) = \Re\left\{\tilde{\mathbf{u}}^{i(\omega t+\psi)}\right\} \tag{3.8}$$

.

Eq. 3.8 can be converted to the format of Eq. 3.7 by relating the real-valued amplitude, $\tilde{\mathbf{u}}$, and phase, ψ, to a complex amplitude $\mathbf{u}$, as follows

$$\begin{aligned} \Re(\mathbf{u}e^{i\omega t}) &= \Re(\tilde{\mathbf{u}}e^{i(\omega t+\psi)}) \\ \Re(\mathbf{u}e^{i\omega t}) &= \Re(\tilde{\mathbf{u}}e^{i\omega t}e^{\psi}) \\ \mathbf{u} &= \tilde{\mathbf{u}}e^{i\psi} \\ \mathbf{u_R} + i\mathbf{u_I} &= \tilde{\mathbf{u}}cos(\phi) - i\tilde{\mathbf{u}}sin(\psi) \end{aligned} \tag{3.9}$$

The measured complex displacement expressed in Eq. 3.9 is in now the same format as the complex displament output at each node of the FE simulation, $\mathbf{u}_c$,

$$\mathbf{u}_c = \Re(\mathbf{u}_c) + \Im(\mathbf{u}_c)i \tag{3.10}$$

A patient specific mesh is created from each dataset, thus the surface of the mesh is a best-fit

surface through the location of all the tracked fiducials in 3D space. The node locations, where the motion is simulated, and the fiducial locations, where the motion is measured, do not coincide. To compare the simulated with the measured motion, the centre of the fitted ellipse is projected onto the mesh. The nodal motions are then interpolated to the location of the projected point on the mesh. The projection of point data onto the mesh surface was simplified from previous work [61] to improve calculation time. The algorithm is as follows:

1. Find the nearest surface element to the center of the ellipse.

2. Project the center of the ellipse onto the mesh using the normal to the plane passing through the three nodes of the surface element.

3. Calculate the basis functions needed to interpolate from the nodes to the projected point.

4. Confirm the data point is correctly projected. If not, go to next nearest element and repeat steps 2-4 until either the point is correctly projected, or 10 surface elements have been checked.

5. If point cannot be projected onto an element, project onto the closest edge.

3.2.1 Projection onto a surface element

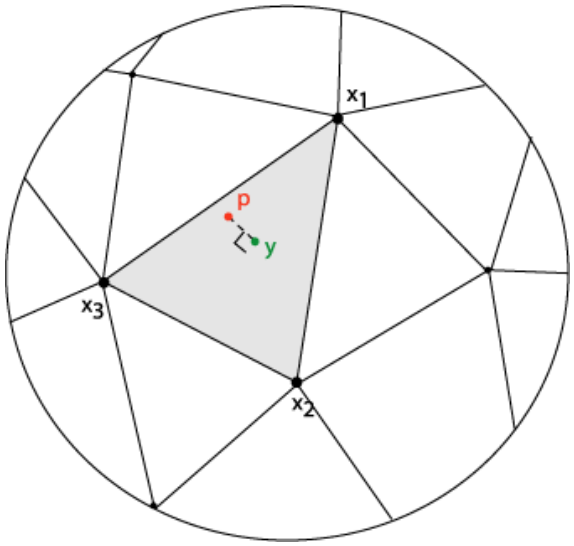

Figure 3.2: Diagram of a point projected onto a surface element. $\mathbf{p}$ is the point to be projected, $\mathbf{y}$ is the projected point on the element shaded in gray and $\mathbf{x}_1, \mathbf{x}_2, \mathbf{x}_3$ are the three nodes of the surface element.

Figure 3.2 illustrates the point, $\mathbf{p}$, to be projected onto a surface element. The nearest surface element to the point is found by finding the total distance d between $\mathbf{p}$ and the three nodes $\mathbf{x_1}, \mathbf{x_2}, \mathbf{x_3}$ associated with each surface element.

$$d = \sqrt{(\mathbf{x}_1 - \mathbf{p})^2 + (\mathbf{x}_2 - \mathbf{p})^2 + (\mathbf{x}_3 - \mathbf{p})^2} \tag{3.11}$$

The nearest surface element is assumed to be the one with the smallest value of d. The projected point $\mathbf{y}$ on the element is found using

$$\mathbf{y} = \mathbf{p} + D \cdot \hat{\mathbf{n}} \tag{3.12}$$

where $\hat{\mathbf{n}}$ is the unit normal vector from the plane passing through the three nodes,

$$\hat{\mathbf{n}} = \frac{(\mathbf{x}_2 - \mathbf{x}_1) \times (\mathbf{x}_2 - \mathbf{x}_1)}{|(\mathbf{x}_2 - \mathbf{x}_1) \times (\mathbf{x}_3 - \mathbf{x}_1)|} \tag{3.13}$$

and D is the perpendicular distance from $\mathbf{p}$ to the surface element,

$$D = \hat{\mathbf{n}} \cdot (\mathbf{p} - \mathbf{x_i}) \tag{3.14}$$

where $\mathbf{x}_i$ is any of the nodes of the surface element. Figure 3.3 shows the three triangles created from the projected point. The basis functions are calculated using

$$\phi_i = \frac{a_i}{A} \tag{3.15}$$

where a_i is the area of the basis and A is the area of the surface element.

If $\sum_{i=1}^{n} \phi_i > 1$ the projected point lies outside the surface element. There are two reasons for this occurring: the nearest surface element found by the three closest nodes may not be the correct element as illustrated in Figure 3.4a; or the point is above an edge as illustrated in Figure 3.4b. If the closest nodes do not provide the correct element, this is rectified by looping around the 10 closest surface elements until $\sum_{i=1}^{n} \phi_i = 1$.

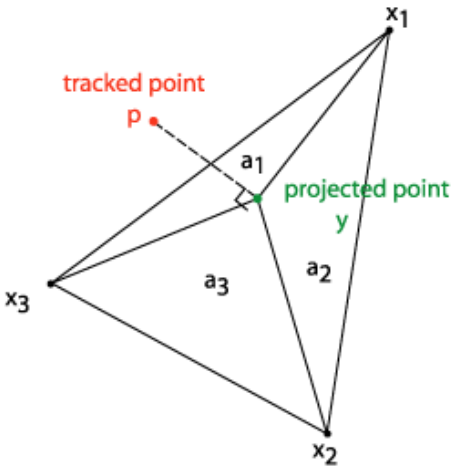

Figure 3.3: Calculation of basis functions for the projected point. The basis function is calculated using $\phi_i = \frac{a_i}{A}$, where a_i is the area of the each triangle and A is the area of the surface element.

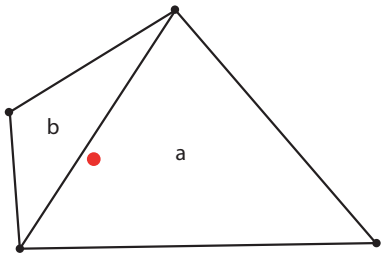

(a) The tracked point, shown in red, appears closer to the smaller element, b, than element a, when using total node distance to identify the closest element. This is rectified by looping around the ten closest elements until $\sum_{i=1}^{n} \phi_i = 1$.

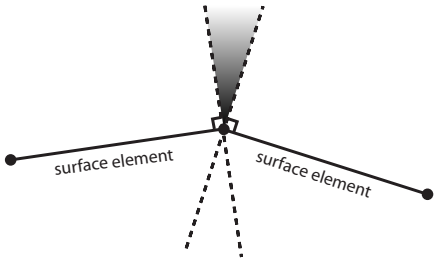

(b) Cross-sectional view of the part of the mesh surface. A point lying within the shaded region can not be projected to lie within either element, so is projected onto the edge between the two elements.

Figure 3.4: Reasons why $\sum_{i=1}^{n} \phi_i > 1$, i.e. the point is projected onto an incorrect surface element

3.2.2 Projection onto an element edge

If a closest element cannot be found, it is because the point lies in the shaded area illustrated in Figure 3.4b. The closest edge has the smallest value of d_{edge}, where

$$d_{edge} = \frac{|(\mathbf{m} - \mathbf{n}) \times (\mathbf{m} - \mathbf{p})|}{|\mathbf{m} - \mathbf{n}|} \tag{3.16}$$

Figure 3.5 illustrates the point, $\mathbf{p}$, projected onto a surface element edge, $\mathbf{mn}$.

The point is projected onto the closest edge using

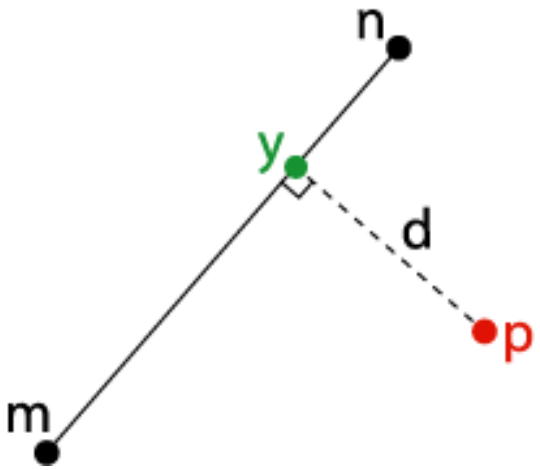

Figure 3.5: Diagram of a point projected onto a surface element edge. **p** is the point to be projected, **y** is the projected point on the element edge, and **m**, **n** are the nodes associated with the edge.

$$\mathbf{y} = \mathbf{m} + \hat{\mathbf{l}} \cdot |\vec{\mathbf{my}}| \tag{3.17}$$

where

$$|\mathbf{my}| = \sqrt{(m_1 - p_1)^2 + (m_2 - p_2)^2 + (m_3 - p_3)^2 - d_{edge}^2} \tag{3.18}$$

and $\hat{\mathbf{l}}$ is the unit vector along the closest edge, simply

$$\hat{\mathbf{l}} = \frac{(m_1 - n_1)\mathbf{i} + (m_2 - n_2)\mathbf{j} + (m_3 - n_3)\mathbf{k}}{|(\vec{\mathbf{mn}})|} \tag{3.19}$$

where $\mathbf{i}, \mathbf{j}, \mathbf{k}$ are the unit vectors in the x, y, z directions respectively. The basis functions are used to interpolate the calculated nodal motions, $\mathbf{u}_c^i$ to motion at the projection point, $\mathbf{u}_c^p$

$$\mathbf{u}_c^p = a_1\mathbf{u}_c^1 + a_2\mathbf{u}_c^2 + a_3\mathbf{u}_c^3 \tag{3.20}$$

3.3 Cost Function

In optimization, the function to be optimized is generally termed the *objective function*. In genetic algorithm terminology the function to be optimized is commonly known as the *cost function* or simply *cost*, or *fitness* of the model. In this work *cost* or *fitness* is used to refer to the function to be optimized. There are four cost functions used in this thesis to assess the quality of the fit

between the model (θ) and the data:

- Squared difference, $\Phi^{SQ}(\theta)$
- Weighted squared difference, $\Phi(\theta)$
- Correlation cost, $\Gamma(\theta)$
- Phase difference in the z direction, $\tau(\theta)$

The squared difference, $\Phi(\theta)^{SQ}$, between measured motion, $\mathbf{u}_m$ and calculated motion, $\mathbf{u}_c$, is given by

$$\Phi^{SQ}(\theta) = (\mathbf{u}_m - \mathbf{u}_c) * \overline{(\mathbf{u}_m - \mathbf{u}_c)}. \tag{3.21}$$

Expressed for the three components of motion, x, y, z for the n tracked fiducials gives,

$$\Phi^{SQ}(\theta) = \sum_{i=1}^{n} \sum_{j} (u_{ij} - f(\theta)_{ij}) * \overline{(u_{ij} - f(\theta)_{ij})}, j = x, y, z \tag{3.22}$$

where u_{ij} is the measured motion, $f(\theta)_{ij}$ is the calculated motion at fiducial i, in dimension j. Introducing the uncertainty in the ellipse fit, to give weighted cost,

$$\Phi(\theta) = \sum_{i=1}^{n} \sum_{j} \frac{(u_{ij} - f(\theta)_{ij}) * \overline{(u_{ij} - f(\theta)_{ij})}}{\epsilon_{ij}^2}, j = x, y, z \tag{3.23}$$

where and ϵ_{ij}^2 is the uncertainty of the ellipse fitting at fiducial i, in dimension j. The calculation of ϵ^2 is described in section 3.3.1.

Correlation is a measure of how similar two distributions are and is normalized to be in the interval $[-1, 1]$. In a gradient method, it would be desirable to have an analytic derivate of cost, which can be calculated for squared error, to speed up the iterations. There is no requirement for the objective function in DIET to be squared error because the optimization is performed using a Genetic Algorithm which does not require differentiation of the cost function. The cost function must be able to be minimized, so correlation over the interval $[-1, 1]$ can not be simply employed as a cost function. The correlation, *corr*, between two variables is given by,

$$corr(X, Y) = \frac{cov(X, Y)}{\sigma_X \sigma_Y} \tag{3.24}$$

where σ is the variance and *cov* the covariance of the variables X and Y. To create an objective function Γ, that can be minimized,

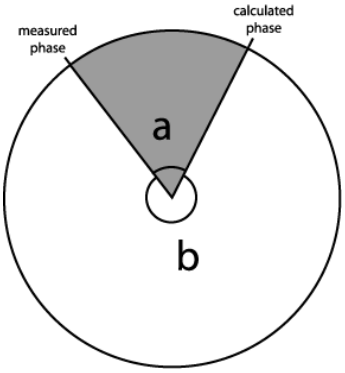

Figure 3.6: Illustration of how the phase difference is calculated. The smaller of angle a or b is the phase difference.

$$\Gamma = \Sigma_i^n 1 - corr(\mathbf{u}_i^m, \mathbf{u}_i^c) \tag{3.25}$$

where $\mathbf{u}^m$ is the measured motion and $\mathbf{u}^c$ is the calculated motion of the n data points.

Concurrent research has found the phase difference in the z component of motion may indicate in which segment of the breast the inclusion is located [64]. The phase, ϕ, is calculated from the real and imaginary parts of the displacement, u, by

$$\phi = tan^{-1}\left(\frac{\Im(\mathbf{u})}{\Re(\mathbf{u})}\right) \tag{3.26}$$

The phase difference is calculated as the smaller of angle a and b, illustrated in Figure 3.6, giving a cost τ

$$\tau = \Sigma_i^n \phi_i^m - \phi_i^c \tag{3.27}$$

where ϕ^m is the measured phase and ϕ^c is the calculated phase of the n data points.

3.3.1 Motion Model Uncertainty

The motion of each tracked fiducial over the motion cycle is modeled as ellipse in 3D space. The motion of the fiducial is described by Eq. 3.9. The fitted motion comprises an amplitude and phase for the ellipse in each dimension, x, y, z and a location for the center of the ellipse. Figure 3.7 shows an example of a high quality and low quality ellipse fit. The uncertainty of the ellipse fit compares the motion of the fiducial marker to the fitted ellipse. The uncertainty, ϵ^2, of the ellipse fit for each tracked fiducial in each direction (x, y, z) is calculated using

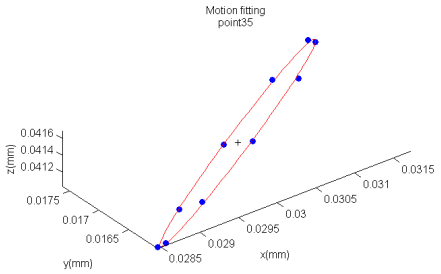

(a) Good ellipse fit. $\epsilon_x^2 = 0.2054 \times 10^{-5}, \epsilon_y^2 = 0.1221 \times 10^{-5}, \epsilon_z^2 = 0.3421 \times 10^{-5}$.

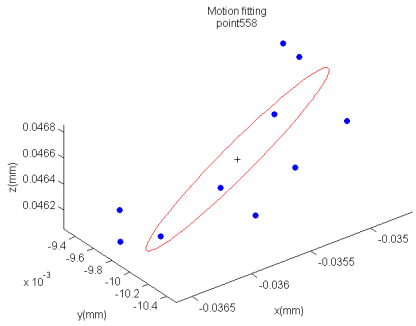

(b) Poor ellipse fit. The fiducial is either not following an elliptical path, or is not well tracked. $\epsilon_x^2 = 0.0191 \times 10^{-3}, \epsilon_y^2 = 0.1390 \times 10^{-3}, \epsilon_z^2 = 0.0422 \times 10^{-3}$.

Figure 3.7: Two examples of best-fit ellipses and the fiducials used to generate them. The ellipse in Figure 3.7a is more reliable because the tracked points lie closer to the fitted ellipse. The ellipse in Figure 3.7b will contribute less to the cost, Φ because it has a larger uncertainty, ϵ^2.

$$\epsilon_i^2 = \frac{\sum_{j=1}^{k} (\delta_{ij})^2}{(n-3)}, i = x, y, z \tag{3.28}$$

where δ is the absolute difference between each of the k tracked motion points and the corresponding location on the fitted ellipse. The measured motion, $\mathbf{u_m}$, thus has an uncertainty in each direction x, y, z given by Eq. 3.28.

3.3.2 Data Quality Metrics

The benefits of examining the frequency characteristics of the phantoms are two fold: troublesome frequencies must be identified and removed from the inverse problem in order to achieve successful reconstructions, and the information obtained is used to create a combined weighted cost function using multiple frequencies using Eq. 3.35. Measures of data quality that may be examined include: mean displacement, signal to noise and coverage. The mean displacement, μ_A, of N ellipses is calculated simply as

$$\mu_A = \frac{\sum_{i=1}^{N} \bar{u}_i}{N}, \tag{3.29}$$

where $\bar{u}_i$ is the magnitude of the displacement for the i^{th} fitted ellipse.

The signal to noise ratio, SNR, for each ellipse is calculated as

$$SNR_{ellipse} = \frac{\bar{u}}{\epsilon}, \tag{3.30}$$

where $\bar{u}$ is the magnitude of the displacement of the ellipse, and ϵ is the standard deviation of the distance of the tracked fiducial from the fitted ellipse as calculated in Eq. 3.28. The mean SNR is calculated over each of the N ellipses using

$$\overline{SNR} = \sum_{i=1}^{N} \frac{SNR_i}{N} \tag{3.31}$$

Signal to noise in this sense is really a measure of any non-elliptical nature of the motion at a particular point. In reality, this may be due to measurement errors in the motion tracking system, or due to non-linear elastic behavior, *i.e.* non-elliptical motion paths, in the motions themselves. In the latter case, the linearly viscoelastic FE model that underlies the DIET reconstruction algorithm would not be adequate and thus the characterization of noise really indicates data-model mismatch.

There are two measures of data coverage that can easily be quantified for a DIET dataset. The simplest is the overall number of fiducials that have been tracked successfully by the camera system. The other method is to calculate the percentage of the breast surface that contains associated motion information. The surface elements of the breast mesh already divide up the breast surface into approximately equal areas. The top of the breast and the breast area within the actuator contact can not be imaged, so these are not counted as part of the imageable area. The remaining elements can be assessed as having a measurement associated with them or not. The data coverage (χ) is then calculated using

$$\chi = \frac{\eta_{data}}{\eta_{total}} \tag{3.32}$$

where η_{data} is the number of surface elements that have at least one data point associated with them, and η_{total} is the total number of surface elements, not including those associated with boundary conditions.

3.3.3 Multi-Frequency Cost

Chapter 5 introduces the first multi-frequency DIET datasets. There has been much work on multi-objective optimization, which simultaneously optimizes multiple and sometimes conflicting objectives subject to constraints [106]. For the DIET tumor location optimization problem, the objectives are not conflicting, however some way of combining multiple cost functions is still required. Each frequency, i, has its own cost function, Φ_i. The genetic algorithm is explained in

the following section, but for clarity in describing the multi-frequency cost functions I shall define some terminology here.

Chromosome: The combination of parameters used to describe a particular model, θ.

Population: The collection of chromosomes at the current iteration of the algorithm.

There are a multitude of possible ways to combine cost functions. In this work, two multi-frequency cost functions are examined: ranking and normalizing.

Ranking of the model

In this method, the cost for each chromosome, $\Phi(\theta)$, in the population is calculated for each frequency. For each frequency, the N chromosomes are ranked from best (1) to worst (N) according to their relative cost. For example, chromosome 1 may be the best solution for 16 Hz data so would get a rank of 1 for 16 Hz, and be the 6^{th} best solution at 18 Hz so would get a rank of 6 for 18 Hz, and so on for all the frequencies. The aggregate cost (AC) for a particular chromosome across all frequencies is found using

$$AC = \sum_{i}^{l} rank(\Phi(\theta)_i) \tag{3.33}$$

where $rank(\Phi)_i$ is the rank of the chromosome for frequency i of the l frequencies.

Normalizing the Cost Functions

In order to sum the cost functions from multiple frequencies, the costs must be combined in some way that does not give bias to some datasets. Bias can arise from the data set having more data points and the displacement being larger. To compensate for these two biases, each chromosomes' (θ) cost at the i^{th} frequency, $\Phi(\theta)_i$, is normalized, $\overline{\Phi(\theta)_i}$, by

$$\overline{\Phi(\theta)_i} = \frac{\Phi(\theta)}{k\mu_A}, \tag{3.34}$$

Where μ_A is the mean displacement over the k measurement points. The combined normalized cost, $\Phi(\theta)^C$, for l frequencies is then

$$\Phi(\theta)^C = \sum_{i}^{l} \overline{\Phi(\theta)_i} \tag{3.35}$$

For Γ the cost for each frequency is already normalized as the cost is based on correlation. The combined cost, Γ^C across the l frequencies is simply,

$$\Gamma(\theta)^C = \sum_{i}^{l} \Gamma(\theta)_i \tag{3.36}$$

3.3.4 Multi-Frequency Mesh Generation

Each fiducial is projected on to a mesh created from point cloud data as described in section 3.2. The advantage of creating a mesh from the data is that each mesh is patient specific, without the need for extra measurements of the patient's breast. The disadvantage of this is that if the tracking of fiducials is weak, the mesh is affected. Meshes created from *in vivo* data highlight weaknesses in the DIET data collection system that need to be rectified in the inverse problem. Figure 3.8a shows a faulty mesh generated when there is poor motion tracking with some of the fiducials. This is an extreme example from an *in vivo* data set, MS016T, which is discussed in Chapter 7, used here to illustrate the effect poor motion tracking can have on mesh construction. From the location of projected points (red) in Figure 3.8a it is obvious that the assumptions used in the projection algorithm break down with such an ill shaped mesh. Any mesh projection calculation using the algorithm described in section 3.2 then becomes erroneous. For multi-frequency reconstructions, the same data can be projected onto a better quality mesh created from a different frequency, as shown in Figure 3.8b, or that frequency can simply be discarded in the inverse problem.

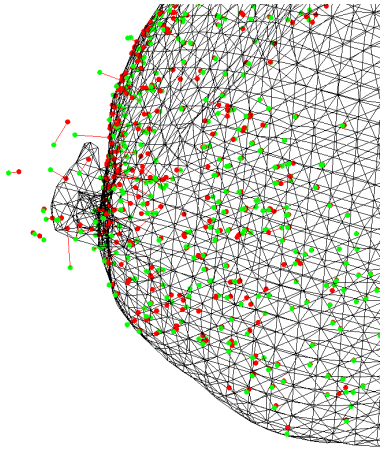

(a) Mesh using 26Hz data

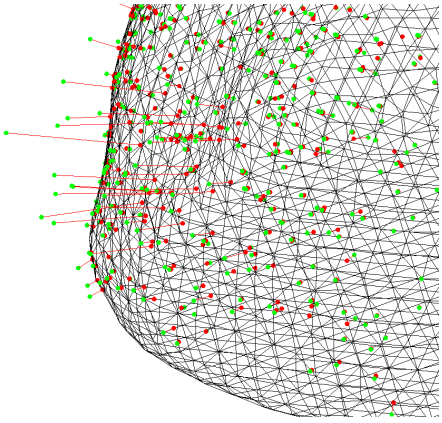

(b) 26Hz data projected on to the 20Hz mesh.

Figure 3.8: A particularly bad example of mesh generation from poorly tracked point cloud data. The data is from an *in vivo* data set (MS016T) used in Chapter 7. The green dots are the 3D tracked location of the data, the red dots are the corresponding projected data point locations. Note the erroneous projection in Figure 3.8a and how this can be corrected for by using a mesh from a different frequency dataset shown in Figure 3.8b.

3.4 Parameter Optimization

In addition to standard gradient techniques, there are a multitude of stochastic and heuristic techniques available for optimization. The are several factors to consider in determining the choice of optimization algorithm for DIET. At the time of algorithm development, only numerical simulation data were available. The shape of the phantom and *in vivo* cost surfaces were unknown and thus an algorithm with great flexibility with regard to the cost surface was desired. There is also the possibility that at some future date, a more complex cost function may be used. For example ultrasound may be combined with DIET, or a qualitative cost function such as suggesting an area for a likely tumor location may be employed.

The algorithm must not require training data because DIET is at such an early stage in terms of clinical trial development that there are few data sets for training. This discounts any algorithms which make use of a learning paradigm, such as artificial neural networks.

Local search algorithms move from solution to solution within the search space by iteratively applying local changes until a optimal solution is found, or a certain number of iterations have elapsed. [107]. The DIET optimization algorithm must be able to overcome the problem of possible multiple local minima. There are local search algorithms capable of this. Stochastic hill climbing is one such technique, where the probably of model selection varies with the 'steepness' of the uphill move. The stochastic element allows sub-optimal solutions to be accepted in order for the algorithm to avoid becoming trapped in local minima. Simulated annealing is a similar technique, where the probability of moving to a sub-optimal solution becomes increasingly unlikely as the number of iterations increase.

It is envisaged that the eventual clinical system will have standalone reconstruction software, most likely implemented on multi-core processors and possibly in combination with graphics processing units (GPUs). Although gradient methods and local search algorithms can be parallelized to the extent that multiple starting points can be used and evaluated simultaneously, they are not particularly well suited to parallelization.

Heuristic algorithms that are readily adaptable to parallelization include Particle Swarm Optimization (PSO)[108] and Genetic Algorithms [109]. In particle swarm optimization, a 'particle' is a candidate solution. Each particle searches for better positions in the search space by changing its velocity defined by a set of rules based on the behavior of schools of fish or flocks of birds. In Genetic Algorithms, the solutions are 'chromosomes' which are improved by evolutionary operators. The two classes of algorithm are similar. Both start with a randomly generated population

of solutions and then update their population using a stochastic element. The major difference between PSO and GAs is the exchange of information between solutions. In PSO the only the best particle shares its location with all the other particles, whereas in the GA chromosomes share genetic information with each other. Both PSOs and GAs are very adaptable to changes in cost function. All that is required is that there is some way of scoring models against each other; there is no requirement that the derivative of the cost function exits.

Resolution of the solution is also important in DIET, but this has to be weighed against the expense of solving the forward problem, which in DIET is a Finite Element calculation. If the cost function was trivial, a technique such as Markov Chain Monte Carlo could be employed to explore the solution space. This is not applicable to the DIET forward problem as the FEM calculation is not trivial to solve, but some indication of solution resolution is desirable. PSOs and GAs both use populations of solutions to explore the parameter space, thus they provide an ensemble of solutions across the parameter space.

A decision must be made as to the choice of algorithm for DIET. PSOs and GAs are well suited to the DIET optimization problem. Previous work showed promise using quasi-genetic operators [80] and thus the GA was selected as the optimization method. GAs do come with some disadvantages, however. They can be slow to converge, requiring more time and computational expense than gradient methods. Two approaches are taken to mitigate this, the parallelization of the algorithm to reduce overall execution time, and the development of Fitness Function Analysis (FFA) to improve the speed of convergence.

3.4.1 The Genetic Algorithm

GAs aim to mimic the process of natural selection by iteratively 'breeding' good solutions to produce better solutions. The initial population of solutions is randomly picked from the parameter space, then genetic operators are applied to iteratively improve the population to find the optimum solution. The GA is illustrated in Figure 3.9. The terminology used is described below.

- *Encoding:* The process of converting a parameter value into a form that can be used in the genetic algorithm operators.
- *Gene:* A particular parameter value once encoded.
- *Chromosome:* The combination of *genes* used to describe a particular model.

- *Natural Selection:* The sorting of chromosomes by their cost. Those that best fit the data are selected for mating.
- *Mating:* Combining *genes* from two *chromosomes* to produce new models.
- *Mutation:* The random process of altering some *genes* to produce new models.

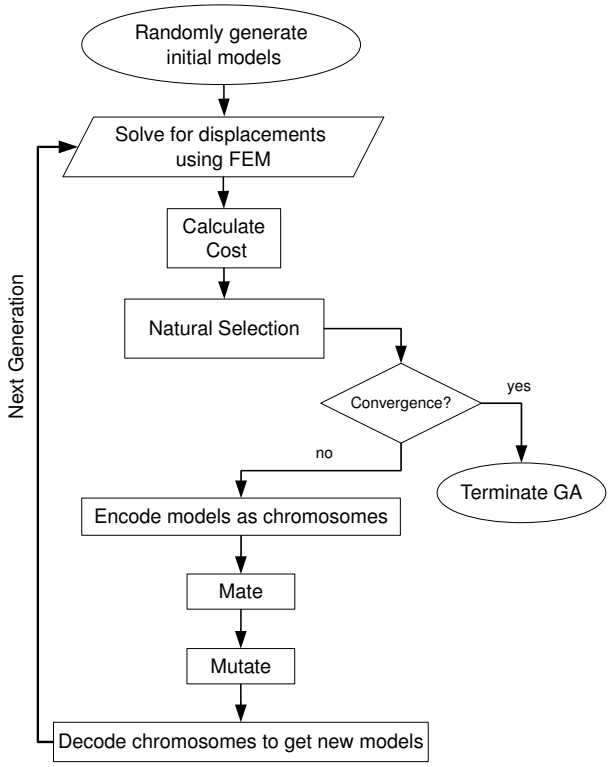

Figure 3.9: Flow chart of the Genetic Algorithm.

In nature, genes are encoded using the four DNA bases A,T,G, and C. In a GA, genes need to be encoded in some way. In this thesis, binary encoding is used for its simplicity, but other encoding methods are possible [110]. The parameter value (v) is converted to a binary gene (g) by first calculating the integer equivalent, B, given by

$$B = \mathbf{round}\left(\frac{v - v_{min}}{v_{max} - v_{min}} \times 2^N - 1\right), \tag{3.37}$$

where v is the parameter value to be encoded, v_{min} is the minimum possible parameter value, v_{max} is the maximum possible parameter value, N is the number of bits used to represent the

parameter, and 2^N is greater than or equal to the number of possible parameter values.

The number of possible parameter values depends on the choice of discretization of the problem. The gene, g is then given by

$$g = f_{conv}(B), \tag{3.38}$$

where f_{conv} is the binary conversion function. Once encoded into binary, the genes are combined together to make a *chromosome*, the combination of parameters required to describe a particular model.

The genes used in this study are material and shape parameters, in contrast to the element genes used in Olsen and Throne [73]. This gives a much shorter chromosome to optimize, as illustrated in Figure 3.10. The chromosomes are sorted according to their cost (Φ), which mimics natural selection or *survival of the fittest*.

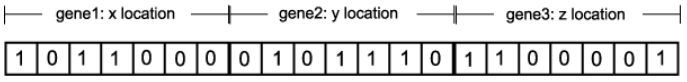

(a) An example of an inclusion location (x, y, z) encoded into a binary chromosome using 7 bits for each gene. There are 2^7 possible values for each parameter. The chromosome is 21 genes long, independent of mesh density.

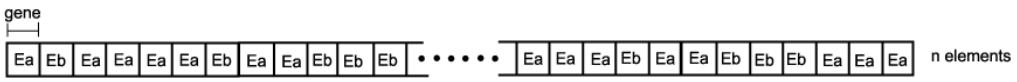

(b) An example of element based encoding. Each element can have material property Ea or Eb. A gene is required for each element of the mesh. Chromosome length is dependent on mesh density and increases drastically from 2D to 3D.

Figure 3.10: Shape based encoding versus element based encoding. The use of shape based encoding allows the number of unknown parameters to remain the same when increasing the mesh density.

The chromosomes that lie within the lowest 40% of cost scores (Φ) of each generation are selected for mating. These are the 'fittest' chromosomes, so their DNA, *i.e.* their encoded parameter values, are passed on to the next generation. The remaining chromosomes are deleted to make room for the offspring from the mating processes. The probability of a chromosome mating is inversely proportional to its cost. The probability of mating, P_m, for a particular chromosome θ is given by

$$P_m = \frac{\frac{1}{\Phi(\theta)}}{\sum_1^N 1/(\Phi_i)}, \tag{3.39}$$

where $\sum_1^N 1/(\Phi_i)$ is used to normalize the probability of mating across the N chromosomes which make up the top 40% of the population.

A random number determines which chromosome is selected for mating, known as roulette wheel weighting [84]. Pairs of chromosomes are selected until the number of chromosomes selected equals the number of chromosomes that have been deleted through natural selection. Chromosomes are not allowed to mate with themselves. If this occurs, the pairing is discarded and the selection process is repeated.

Mating is defined as combining information from two chromosomes to produce two more chromosomes. The information is combined using single point crossover, illustrated in Figure 3.11. Mutation is used to prevent early convergence on a local minimum of the cost function by introducing random information at each generation. A percentage of bits is randomly selected from the binary strings that make up the population. These bits are mutated using a bitwise *NOT*, *i.e.* if the gene is 0 it is changed to 1 and vice versa. To avoid mutating good solutions, the fittest chromosome of the population is spared from mutation. This is unlike the natural process of mutation where any gene could be mutated, but there is little to be gained by mutating the best solution of the current generation.

After the genetic operators of mating and mutation, the resulting chromosomes must be decoded back to parameter values, v, so their cost can be evaluated using Eq. 3.23. Decoding is achieved converting the binary value of the gene, g to a base 10 number, B, and then rearranging Eq. 3.37 to give,

$$v = \frac{B+1}{2^N}(v_{max} - v_{min}) + v_{min}. \tag{3.40}$$

Natural selection, mating and mutation are repeated until the algorithm is judged to have converged. In this thesis convergence is defined as the top n chromosomes of the population being identical or when a predetermined number of generations is reached.

To save computational cost, the algorithm records the parameters and associated cost for each solution generated by the GA to ensure solution evaluations are not repeated. Non-repetition of FEM calculations is critical to reducing computation time when the GA approaches convergence and identical solutions are generated. In addition, the record of solution evaluations is used both to predict good solutions using Fitness Function Analysis, described in section 3.4.2, and to construct the credible region for the inclusion location, described in section 3.6.

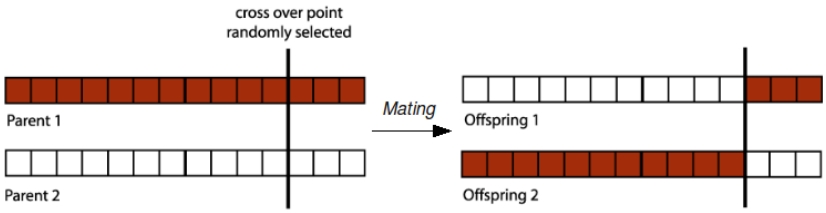

Figure 3.11: Single point crossover. A single point is selected on both parent chromosomes. The offspring are a combination of one parent before the crossover point, and the other parent after the crossover point.

3.4.2 Fitness Function Analysis

Each chromosome, θ, generated by the GA provides a point on the cost surface $\Phi(\theta)$. Just as contours on a map can be used to identify minima, Fitness Function Analysis uses the information gained from sampling the cost surface to generate predictions for the location of the global minimum.

During the genetic algorithm, a record is kept of each chromosome, θ, and its associated cost, $\Phi(\theta)$. Once more than a critical number of chromosomes have been generated, they are sorted into ascending cost. If enough of the parameter space has been sampled, the best chromosomes, *i.e.* those with the lowest cost, will surround the global minimum.

FFA is applied as follows. For the N-parameter (or *gene*) case, the best, *i.e.* lowest cost $\Phi(\theta)$, chromosomes, θ, are assumed to lie on the surface of an N-dimensional sphere. The model using the parameter values at the best-fit sphere center, θ_{bfs}, is then compared to the worst chromosome of the current generation, θ_w. If

$$\Phi(\theta_{bfs}) < \Phi(\theta_w). \tag{3.41}$$

θ_{bfs} replaces θ_w in the population. If these best solutions do truly surround the global minimum, the center of this sphere should provide a good approximation to this minimum and thus the presence of this chromosome should speed up convergence. If these best solutions do not surround the global minimum, but are instead dispersed around multiple minima, the chromosome associated with the center of this sphere will most likely have a high cost and will thus be discarded by the GA. Hence, the incorporation of the chromosome θ_{bfs} into the population will at worst have no effect on solution convergence and at best accelerate convergence towards the global minimum.

The centroid of the best solutions could be used to calculate the assumed center, however a

best-fitting sphere approximation was chosen as this is more robust when only part of the cost surface has been sampled. An example of this is when the global minimum lies close to the edge of the parameter space. Figure 3.12 illustrates this for the 2D case using the centroid and the best-fit center.

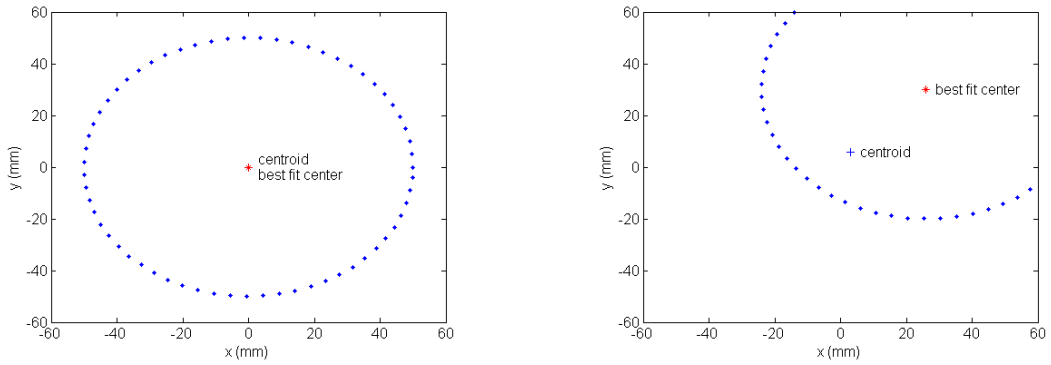

(a) Data points lie on a circle entirely within the parameter space

(b) Data points lie on a circle that is on the edge of the parameter space

Figure 3.12: Schematic to illustrate Fitness Function Analysis using the 2D case of a circle. When the points lie on a circle entirely within the parameter space, as shown in Figure 3.12a, the centroid and best-fit center both provide a good approximation to the center of the circle. Figure 3.12b illustrates the case where the data points lie on a circle that is on the edge of the parameter space. In this case the centroid is a poorer approximation to the center of the circle than that found using a best-fit center.

The center of the sphere is solved for using least squares. Any point on a sphere satisfies the equation

$$(x - x_0)^2 + (y - y_0)^2 + (z - z_0)^2 = r_0^2, \tag{3.42}$$

where x_o, y_o, z_o is the center of the sphere with radius r_o. To find the center of the sphere minimize

$$f = r_i^2 - r_0^2, \tag{3.43}$$

where $r_i = \sqrt{(x_i - x_0)^2 + (y_i - y_0)^2 + (z_i - z_0)^2}$.

Expanding Eq. 3.43 gives

$$f = -2(x_i x_0 + y_i y_0 + z_i z_0) + x_i^2 + y_i^2 + z_i^2 + \rho \tag{3.44}$$

where $\rho = (x_0^2 + y_0^2 + z_0^2) - r_0^2$ is used to linearize the equation. In matrix form this is

$$\begin{pmatrix} -2x_1 & -2y_1 & -2z_1 & 1 \\ -2x_2 & -2y_2 & -2z_2 & 1 \\ \vdots & \vdots & \vdots & \vdots \\ -2x_n & -2y_n & -2z_n & 1 \end{pmatrix} \begin{pmatrix} x_0 \\ y_0 \\ z_o \\ \rho \end{pmatrix} + \begin{pmatrix} x_1^2 + y_1^2 + z_1^2 \\ x_2^2 + y_2^2 + z_2^2 \\ \vdots \\ x_n^2 + y_n^2 + z_n^2 \end{pmatrix} = \begin{pmatrix} f_1 \\ f_2 \\ \vdots \\ f_n \end{pmatrix} \tag{3.45}$$

For the least squares solution set $(f_1, ..., f_n) = 0$. This initial estimate is used as the best fitting sphere for the data. No iteration is performed to improve the initial estimate. Figure 3.13 shows two cost isosurfaces for a numerical simulation data set used to test FFA in section 3.7.2. Figure 3.13a illustrates a cost isosurface that encloses multiple minima, a poor approximation to a sphere. The best-fit sphere solution would be discarded and the algorithm would run for further generations. Figure 3.13b illustrates a lower cost isosurface enclosing a single minima, a good approximation to a sphere. In this situation, it is proposed that using θ_{bfs} as a chromosome would cause the algorithm to reach the global minimum faster than using the GA alone.

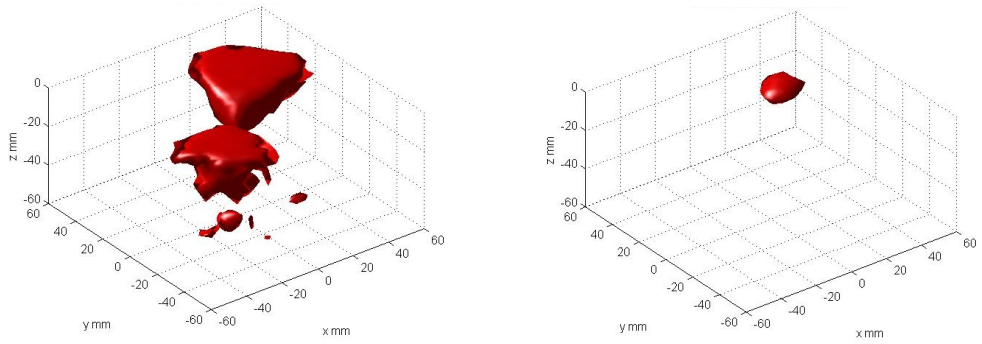

(a) Multiple minima enclosed by cost isosurface at $\Phi^{SQ} = 3.875 \times 10^{-5}$.

(b) One minimum enclosed by cost isosurface at $\Phi^{SQ} = 3.850 \times 10^{-5}$.

Figure 3.13: Cost isosurfaces for the numerical simulation data set used to test FFA.

3.5 Comparison to Previous DIET Optimization Algorithms

The optimization algorithm described in this chapter differs from the various Combinatorial Optimization (CO), gradient descent (GD), and hybrid (combination of CO and GD) algorithms that have been applied to previous cylindrical phantom reconstructions [80] [89] [62]. Figure 3.14 is an illustration of the phantom geometries used in those previous reconstructions. The phantoms were composed of a soft silicone with a Young's modulus of 25-30 kPa, and a stiffer silicone with a Young's modulus of 100-135 kPa. The points of difference between the optimization algorithm described in previous work and the optimization algorithm presented here are the method used to project data on to the mesh, the terminology used in the optimization algorithm, the encoding of parameters, the selection method, the mating of chromosomes, and the success metric used to assess the results. The following describes the differences in detail.

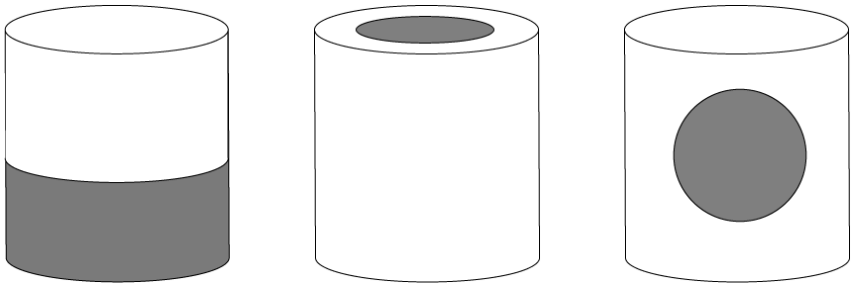

(a) Stacked geometry (b) Concentric geometry (c) Spherical inclusion

Figure 3.14: Structure of phantoms used in previous reconstructions. The grey region represents the higher stiffness material.

3.5.1 Projection of data

Details of Peter *et al.*'s method of data projection are given in [61]. The mesh is inflated along node normals until the mesh intersects the location of the data in 3D space. The data projection method used in this thesis projects the data on to the mesh along the element normal. This method is described in section 3.2 and is much faster than node normal projection. This speed increase is a necessity for the larger data sets acquired with the latest DIET prototype. Table 3.1 gives execution times on a core i7 machine running Matlab 2010b^{TM} for both element normal and node normal projection. The element normal projection method is over 35 times faster than the node normal projection method.

Projection method	Time (minutes)
node normal	67.3
element normal	1.9

Table 3.1: Comparison of node normal projection and element normal projection execution time.

3.5.2 Algorithm Terminology

Peters *et al.* used a slightly different terminology to that described in standard genetic algorithms, for instance that used in Haupt and Haupt [84]. Peters defined a *gene* as the combination of parameters used to describe a model. In this thesis standard genetic algorithm terminology is used, where a *gene* is a parameter and a *chromosome* is the combination of parameters used to describe a model.

3.5.3 Encoding of Parameters

In this thesis, all parameters are encoded using Eqs. 3.37 and 3.38 and decoded using Eq. 3.40. Peters *et al.* performed no encoding of parameters. The parameter value was merely expressed in binary form to produce a gene. This necessitates the use of simulated annealing in addition to natural selection, because mating may not produce offspring which are a combination of the parent chromosomes. For example, using the Peters *et al.* mating method to mate parameter by parameter, where the parameters to be mated are equal to 6 and 12, gives offspring equal to 14 and 4, neither of which are between 6 and 12. This is illustrated in Figure 3.15.

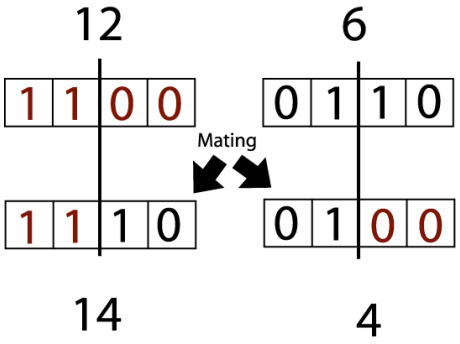

Figure 3.15: Illustration of the consequences of single parameter mating with no encoding.

3.5.4 Selection

Peters *et al.* generate a potential gene (parameter combination) G' for each G of the current generation. Whether G' replaces G is decided by the rules of Simulated Annealing (SA), first defined by Kirkpatrick *et al.* [111]. Analogous to the metallurgical process of simulated annealing, at a given temperate, T, G' replaces G if

$$e^{\frac{-\Delta}{T}} > R(0,1) \tag{3.46}$$

where Δ is the change in cost and R is a random number in the interval $[0,1]$. This stochastic element allows the algorithm to 'jump' out of local minima as high cost solutions are allowed to enter the population. The temperature is decreased as the algorithm approaches convergence so it becomes less and less likely that higher cost solutions are allowed. Figure 3.16 shows a schematic of the selection process. The next generation is composed of a mixture of original parameter combinations G and new parameter combinations $G's$. The disadvantage of this method is that no comparison is made across the population, *i.e.* G'_i is only compared to G_i rather than G_{1-n}. Essentially the algorithm consists of n simulated annealing reconstructions performed simultaneously.

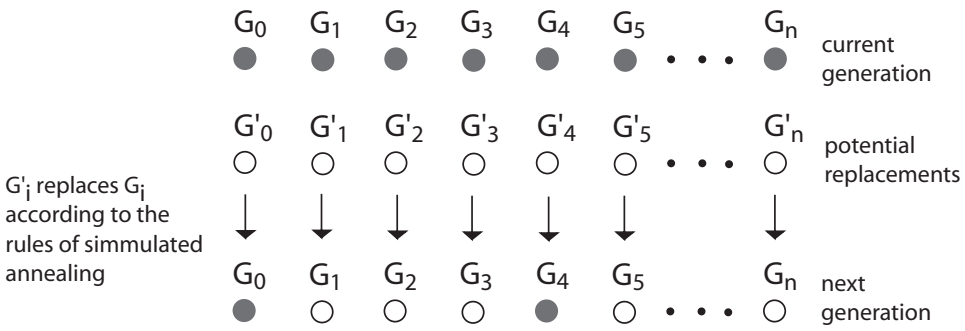

Figure 3.16: Schematic of Peters' selection method [61]. Selection compares the potential gene, G', with its current value, G. Whether the G' replaces G is determined by simulated annealing

The selection method used in this thesis is natural selection. This mimics survival of the fittest in nature, where only the fittest, *i.e.* those with the lowest cost, are selected for mating. The fittest chromosomes are allowed to survive to the next generation, and the remaining chromosomes are deleted to make room for the offspring. Thus, the population as a whole is improved each generation. As with Peters' algorithm, the number of chromosomes remains constant each

generation.

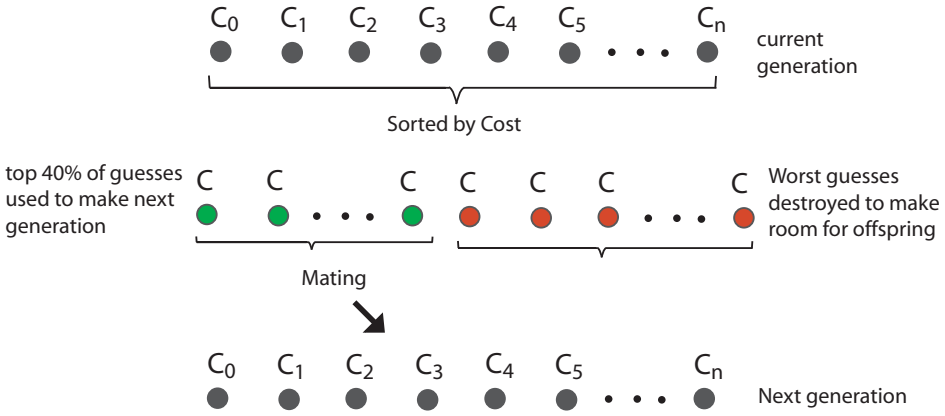

Figure 3.17: Schematic of genetic selection. The chromosomes are sorted according to their cost. The best chromosomes are kept for mating. The rest are destroyed to make room for the offspring

3.5.5 Mating

For mating, Peters *et al.* considered each parameter value separately. The single point crossover is performed on each parameter which comprises the gene. Figure 3.18 illustrates the parameter mating.

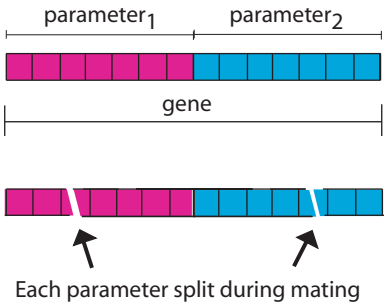

Figure 3.18: Illustration of the mating method employed by Peters. Each parameter is individually mated.

In contrast, the mating used in this thesis is across the chromosome. The single point crossover is performed on the group of parameters as a whole, illustrated in Figure 3.19. The advantage of mating using the whole chromosome is that the resulting chromosomes are a blend of successful models.

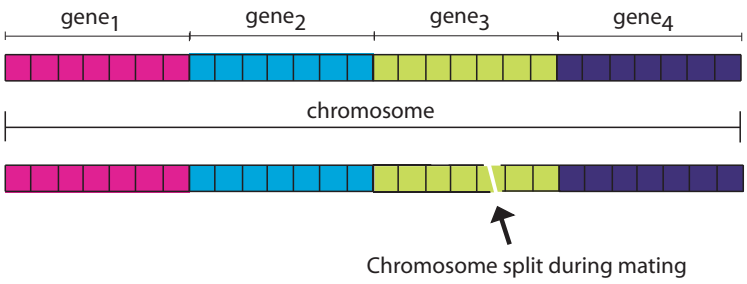

Figure 3.19: Mating using the whole chromosome. The single point crossover is performed on the group of parameters as a whole producing offspring which are a blend of successful models.

Peters *et al.* did not perform mating if the resulting new gene had parameters outside the problem domain [80]. This problem does not occur in the algorithm presented here because mating and mutation operators are performed on encoded chromosomes. Decoding the chromosome using Eq. 3.40 must give a value within the parameter space.

3.5.6 Success metric

Peters *et al.* defined a success metric to compare the various versions of their algorithm. For the two parameter case of the stacked phantom, illustrated in Figure 3.14a, where the unknown parameters are interface position P, and stiffness contrast C, the success metric Ψ was defined,

$$\Psi = 1 - \left(\frac{\sum_{i=1}^{N} ||P_0 - P_i||}{P_0} + \frac{\sum_{i=1}^{N} ||C_0 - C_i||}{C_0} \right) /2N. \tag{3.47}$$

where P_0 and C_0 are the true parameter values, P_i and C_i are the solutions produced by the i^{th} run of the algorithm, N is the total number of reconstructions performed and Ψ is expressed as a percentage.

This success metric is linked to the choice of parameter space that the algorithm is permitted explore. For example, for the case of the stacked phantom, if all runs of the algorithm converged at the edge of the parameter space, $P = 10$, $C = 100$, while the true parameter values are $P_0 = 40\%$, $C_0 = 400\%$ this would give a success metric, Ψ, equal to 25%, even though none of the reconstructions were successful. Figure 3.20 gives the Ψ values at the extremes of the parameter space used in the reconstruction. The success metric, Ψ, is acceptable for comparing variations of an algorithm applied to the same phantoms reconstructed within the same parameter space, but

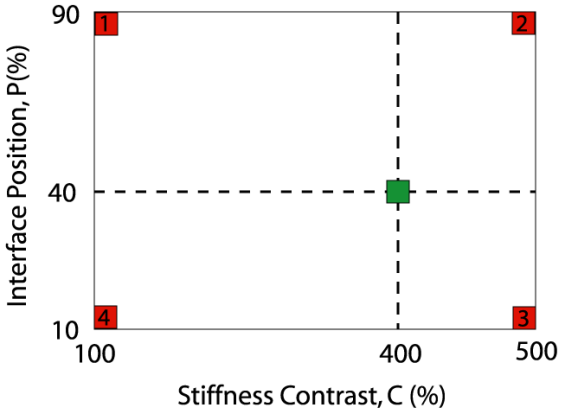

Figure 3.20: Illustration of parameter space used in the reconstruction of a cylindrical stacked phantom in [61]. The correct solution location is in green. If the algorithm converged in position 1, the success metric $\Psi = 0\%$; position 2, $\Psi = 25\%$; position 3, $\Psi = 50\%$; position 4, $\Psi = 25\%$.

it is meaningless to use it for comparison with the reconstructions presented in this thesis because the parameter spaces are different. For this reason, the success metric used by Peters *et al.* [80] and Van Houten *et al.* [62] is not used in this work. Instead, the quality of solutions is assessed by comparing each reconstruction to the true geometry of the phantom.

3.6 Image Reconstruction

The output of the GA is an optimum model for the given parameter space, together with all the cost samples found during the execution of the algorithm. In addition to finding the optimal parameter values, analysis of non-uniqueness and solution uncertainty is essential in the reconstruction of breast tissue stiffness. The genetic algorithm provides much more information on the cost surface throughout the parameter space than any gradient method. By examining the cost surface around the optimal model, multiple minima can be identified. There are four ways that the output from the GA is visualized.

1. *Minimum cost model plot.* This is the simplest visualization and shows only the optimum solution.

2. *Cost surface plot.* This provides the discovered $\Phi(\theta)$ for the models evaluated. For three parameter reconstructions both slices through $\Phi(\theta)$ and isosurfaces of $\Phi(\theta)$ can be displayed.

3. *Optimal region for inclusion location.* This method displays the solution in terms of which nodes are stiff inside the mesh. The mesh visualization uses the average E' over the best twenty models to provide an image which shows the area around the optimal solution.

4. *Credible region for inclusion location.* This provides an estimate of the resolution of the solution. Local measures, such as standard deviation, which are applied to single minima, become erroneous when applied to cost surfaces that contain multiple minima [112], common in the DIET cost surface [62]. The GA, like any Monte Carlo method, samples much more of the parameter space than a gradient optimization method and, if enough iterations are performed, can take advantage of the fact that all local likelihood maxima have been sampled [113]. Sambridge uses a Bayesian formulation for analyzing an ensemble of solutions [88]. A similar approach is used here.

3.6.1 Constructing the Credible Region

In order to construct a credible region for the location of the inclusion, the problem domain was discretized with the possible inclusion locations every 5 mm in the parameter space. This gives a finite number of possible models, each assumed to have an equal prior probability. The assumption is made that the GA has sampled enough of the cost surface so that the entire cost surface can be approximated by fitting a surface through each point generated by the GA. The credible region for the inclusion location comprises the N models that satisfy the equation,

$$\sum_{i=1}^{N} P(A|B)_i \leq \kappa \tag{3.48}$$

where $P(A|B)_i$ is the sequence of descending posterior probabilities of all models and κ is the desired credible level. Bayes theorem is used to find the posterior probability, $P(A|B)$, of the model given the data, such that

$$P(A|B) = \frac{P(B|A)P(A)}{P(B)} \tag{3.49}$$

where $P(A)$ is the prior probability of the model, $P(B|A)$ is the likelihood of the data given the model, and $P(B)$ is a the prior probability of the data, essentially used as a normalizing constant. $P(B|A)$ is found by assuming the data y_i are normally distributed about the true distribution $f(\theta)$ with variance σ_i^2,

$$p(y_1, y_2, ..., y_m|\theta, \sigma_i^2) = \prod_i^m (2\pi\sigma_i^2)^{-\frac{1}{2}} \exp(\frac{-1}{2\sigma_i^2}(y_i - f(\theta)_i)^2), \tag{3.50}$$

where m is the total number of measurements y_i, each with variance σ_i^2, and $f(\theta)$ are the motions

calculated via solution of the equations of linear viscoelasticity, Eq. 2.1, for the model θ.

Assuming identically distributed data Eq. 3.50 becomes

$$p(y|\theta,\sigma^2) = (2\pi\sigma^2)^{-\frac{m}{2}} \exp(\frac{-1}{2\sigma^2}||y - f(\theta)||^2). \tag{3.51}$$

Figure 3.21 shows a schematic of the credible region construction. The credible region for inclusion location is calculated for a reconstruction using Eq. 3.48. The posterior probability for each model θ is calculated using Eq. 3.50 where the difference between the measurement y and the motions, $f(\theta)$, is given by Φ^{SQ}, found from Eq. 3.21, and the variance of the measurement, σ^2 is given by

$$\sigma^2 = \sum_i^N \epsilon^2 \tag{3.52}$$

where ϵ^2 is the variance on each ellipse fitting found from Eq. 3.28.

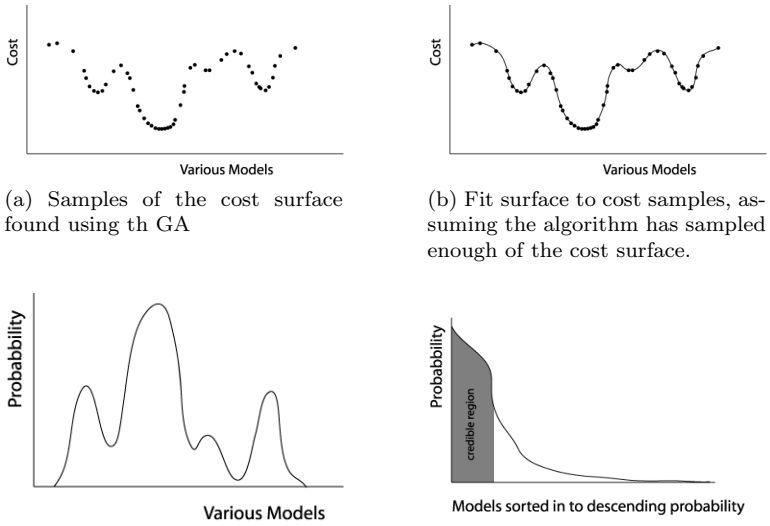

(a) Samples of the cost surface found using th GA

(b) Fit surface to cost samples, assuming the algorithm has sampled enough of the cost surface.

(c) Convert cost to probability. The sum of the probabilities of all models must equal one.

(d) Sort the models in to descending probability. Collect the models that comprise the desired credible level.

Figure 3.21: Schematic of credible region construction.

3.6.2 Quantitative Description of Reconstructed Images

The reconstructed images for both the optimal region and the credible region are created by averaging the storage modulus, E', over all models that comprise the particular region. For a quantitative description of the reconstructed image, two metrics are used:

- *Volume Fraction (V_{frac}).* The volume of the E' contour of interest as a fraction of the true inclusion volume.

- *Centroid Difference (δ_c).* The distance between the centroid of the E' contour of interest and the true inclusion location

The volume fraction, V_{frac} is calculated

$$V_{frac} = \frac{V_C}{V_I} \tag{3.53}$$

where V_C is the volume of the desired contour and V_I is the volume of the inclusion. The volume of the desired contour is calculated as follows using the example of the $E' = 25$ kPa contour. First the average storage modulus, E' over the models of interest is calculated. All elements that have three or more nodes with a $E' \geq 25$ kPa are considered inside the $E' = 25$ kPa contour. The volume of the contour, V_{total}, is given by

$$V_{total} = \sum^{m} V_{elm} \tag{3.54}$$

where the volume, V_{elm}, of each of the m elements within the contour is given by

$$V_{elm} = \frac{1}{3!}\begin{vmatrix} x_1 & y_1 & z_1 & 1 \\ x_2 & y_2 & z_2 & 1 \\ x_3 & y_3 & z_3 & 1 \\ x_4 & y_4 & z_4 & 1 \end{vmatrix} \tag{3.55}$$

where $(x_{1-4}, y_{1-4}, z_{1-4})$ are the four nodes which comprise the element. The centroid $\mathbf{C}$ of the contour is found by the centroid of N nodes, $\mathbf{x}$ within the contour,

$$\mathbf{C} = \frac{\sum_i^N \mathbf{x}_i}{N}. \tag{3.56}$$

The centroid difference, δ_c, between the true inclusion center location $\mathbf{X}_I$ and the centroid of the contour is simply

$$\delta_c = |\mathbf{C} - \mathbf{X}_I|. \tag{3.57}$$

3.7 Computational Implementation

This section describes the numerical validation of the optimization algorithm, a GA with the addition of FFA, and the parallelization of the code to run on multiple processors. The initial validation used numerical data to confirm the algorithm's performance when applied to complex cost surfaces. After this initial validation of the algorithm, the code was parallelized using the Message Passing Interface, which is no trivial task. The parallelization was required because of the computational expense of solving the inverse problem for data collected with the DIET prototype. This is the first DIET reconstruction algorithm to implement the calculation of Finite Element solutions within the reconstruction algorithm, rather than using pre-calculated solutions. In addition, this is the first DIET reconstruction algorithm to implement the mesh creation from point cloud data as implemented by Biehler [90]. Every data set is used to create a patient specific mesh, which means each data set requires its own FE calculations. For the inverse problem there is a minimum of five unknown parameters, E'_B, ζ_B, and tumor location (x, y, z). Sweeps of FE calculations such as that used in the initial validation presented here, and in previous work [61] [62] [66], are no longer practical with this number of parameters. Serial evaluation of the required FE calculations is also impractical for reconstructions presented in this thesis. Most certainly, any future large scale clinical implementation of the reconstruction algorithm will depend upon the use of parallel code.

3.7.1 Numerical Validation of the Genetic Algorithm

A serial code implementing the genetic algorithm was written in FORTRAN 90. To allow rapid testing of the algorithm, a sweep of FE simulations was pre-calculated using a breast shaped mesh composed of 2 mm linear tetrahedral elements. The sweep consisted of locating an ellipsoidal inclusion with axes of 2 mm, 4 mm and 5 mm and a storage modulus of 100 kPa every 5 mm within the parameter space. The background storage modulus was 20 kPa. The damping parameter, ζ, was fixed at 5% for both the inclusion and background. This choice of background and inclusion storage moduli was based on previous phantom material properties [62], thus the higher E' than the phantoms used in this thesis. The actuation frequency was 20 Hz with an amplitude of 0.75 mm. The solutions were spaced every 5 mm in the parameter space as this is an acceptable level of resolution for the DIET inverse problem.

To create synthetic 'measured' datasets, Gaussian random noise with a standard deviation of 5% of the root mean square displacement was added to the simulated data. Figure 3.22 shows the

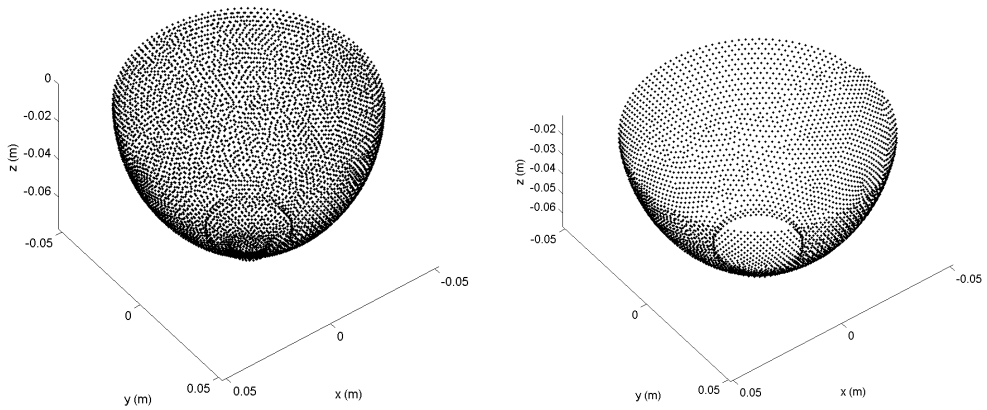

(a) All boundary nodes (b) Location of synthetic data points

Figure 3.22: Boundary nodes and location of synthetic data points used in the numerical study. The synthetic data does not include motion at the 'chest wall' nor where the actuator would make contact with the breast.

boundary nodes and the location of the synthetic data points. The synthetic data was selected to mimic the location of data acquired with the DIET prototype system, with no data at the 'chest wall' nor where the actuator makes contact with the breast. When using the reconstruction algorithm on data acquired with the DIET prototype, simulated motion is interpolated from nodal values to the measurement points. The synthetic data used in this study is obviously less complex than this, as the synthetic measurement points coincide with surface nodes. Arguably the 'inverse crime' has been committed by using the same mesh for the forward problem and the inverse problem. However, the aim of this study is not to test the material property reconstruction algorithm as a whole, only the algorithm's performance with a complex cost surface and the effect of using FFA. The synthetic data certainly provides a complex cost surface with which to test the algorithm as previously illustrated in Figure 3.13a.

Methods

Nine inclusion locations were used to test the GA's ability to locate an inclusion. Figure 3.23 shows the location of the inclusions used, with the coordinates of the center of each inclusion given in Table 3.2. The three unknowns for the reconstruction were the x, y, z location of the inclusion. Table 3.3 shows the constraints on the unknown parameters. For each inclusion location the algorithm was applied 1000 times. 32 chromosomes were used, with a mating rate of 40% and a mutation rate of 10%. The algorithm was run until convergence, the top five chromosomes being the same, or when the algorithm reached 200 generations. Φ^{SQ}, calculated using Eq. 3.22, was

used as the cost because there is no motion ellipse fitting for the synthetic data.

For each run of the algorithm, the distance, D, between the reconstructed inclusion location *i.e.* that found by the algorithm, $\mathbf{X}_R$, and the true inclusion location, $\mathbf{X}_I$, is calculated,

$$D = |\mathbf{X}_R - \mathbf{X}_I|. \tag{3.58}$$

Due to the presence of noise, the minimum Φ^{SQ} may not coincide with the true inclusion location, $\mathbf{X}_I$. An optimization algorithm can do no better than locating the minimum cost. As the purpose of this study is to assess the algorithm's ability to find the minimum Φ^{SQ}, the results are also assessed using

$$D = |\mathbf{X}_R - \mathbf{X}_{min}| \tag{3.59}$$

where $\mathbf{X}_{min}$ is the location where the minimum Φ^{SQ} occurs.

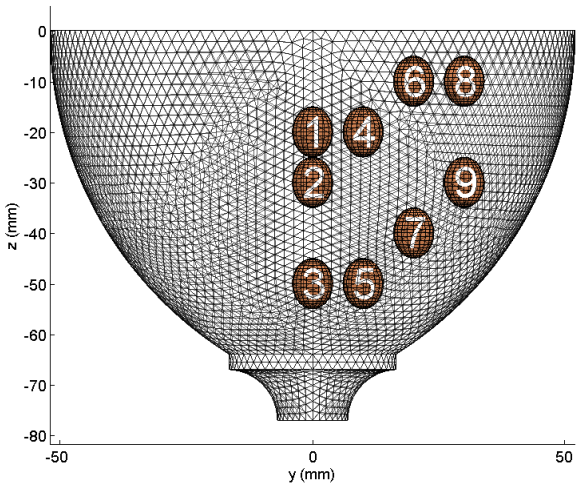

Figure 3.23: Locations of the inclusions used in the numerical validation of the Genetic Algorithm.

Inclusion	**Location**		
	x	**y**	**z**
1	0	0	-20
2	0	0	-30
3	0	0	-50
4	10	10	-20
5	10	10	-50
6	20	20	-10
7	20	20	-40
8	30	30	-10
9	30	30	-30

Table 3.2: Center of inclusion locations used in numerical validation of the GA.

Parameter		**Constraint**		
		Lower	**Upper**	**Increment**
Inclusion Location	$x(mm)$	-60	60	5
	$y(mm)$	-60	60	5
	$z(mm)$	-80	0	5

Table 3.3: Constraints on reconstructed parameters.

Results

The results using Eq. 3.58 are given in Table 3.4. For locations 4 to 9 the algorithm is very successful, with over 98% of the reconstructions locating the tumor within 5 mm of $\mathbf{X}_I$. For inclusions 1 and 2 the algorithm is less successful at locating the inclusion, but over 99% of the reconstructions were within 10 mm of $\mathbf{X}_I$ for location 1 and over 99% of the reconstructions were within 15 mm of $\mathbf{X}_I$ for location 2. The reconstructions for location 3 are the least successful, with 7.9% of reconstructions within 5 mm of $\mathbf{X}_I$. The results calculated using Eq. 3.59 are given in Table 3.5. Over 98% of all reconstructions locate $\mathbf{X}_R$ within 5 mm of $\mathbf{X}_{min}$, with the exception of location 3, for which there are two $\mathbf{X}_{min}$ locations at $(-5, 0, -50)$ and $(10, 25, -50)$.

	Distance from true tumor location (% of runs)		
Location	**0-5 mm**	**6 - 10 mm**	**11-15 mm**
1	0	99.5	0
2	0	0	99.8
3	7.9	35.4	0
4	100	0	0
5	98.6	0	0
6	98.3	0	0
7	100	0	0
8	98.4	0	0
9	100	0	0

Table 3.4: Results of the numerical validation of the GA for the true inclusion location $\mathbf{X}_I$. The algorithm was run 1000 times for each inclusion location.

Location	Distance from minimum cost location (% of runs)		
	0-5 mm	**6 - 10 mm**	**11-15 mm**
1	99.5	0	0
2	99.8	0	0
3 $(-5, 0, -50)$	35.4	7.9	0
3 $(10, 25, -50)$	54.2	2.5	0
4	100	0	0
5	98.6	0	0
6	98.3	0	0
7	100	0	0
8	98.4	0	0
9	100	0	0

Table 3.5: Results of the numerical validation of the GA calculated for the minimum cost location $\mathbf{X}_{min}$. The algorithm was run 1000 times for each inclusion location.

Conclusions

Inclusions 1-3 are located on the central axis of the phantom. The reduced signal from inclusions located here, *i.e.* deep within the breast, is more susceptible to being obscured by the noise in the surface motion. The true inclusion location in these cases does not coincide with the minimum Φ^{SQ}, *i.e.* $\mathbf{X}_I \neq \mathbf{X}_{min}$. For inclusion 1 $\mathbf{X}_{min}$ is at $(0, 5-15)$, for inclusion 2 $\mathbf{X}_{min}$ is at $(0, 0, -20)$, and inclusion 3 has two equal $\mathbf{X}_{min}$ at $(-5, 0, -50)$ and $(10, 25, -50)$.

In terms of the percentage of solutions located within 5 mm of the minimum Φ^{SQ}, the performance of the algorithm for inclusions 1 and 2 using $\mathbf{X}_{min}$ is comparable to the success rates for inclusions 4-9. The algorithm has successfuly located $\mathbf{X}_{min}$ in over 98% of all reconstructions, except for location 3, in which 89% of solutions converged on one of the two $\mathbf{X}_{min}$ locations: 35% of runs converged on one minimum, 54% converged on the other. The value of Φ^{SQ} is the same at both these locations, thus there are two global minimums. It is therefore valid that the algorithm would produce either solution as the optimum parameter values. It is of note that with complex cost surfaces, the models close to the minimum cost should be examined.

3.7.2 Numerical Validation of FFA

Methods

The aim of this validation study was to test whether FFA can be used to introduce better solutions into the population earlier than using the GA alone. Thus, this validation study was based on two experiments:

Experiment 1: Test when the correct solution was introduced into the population.

Experiment 2: Test the number of generations taken to reach convergence, judged as the top 5 chromosomes in the population being identical.

For each experiment, the algorithm was run 1000 times with and without FFA, using an initial population of 64 chromosomes. A inclusion location of $(20, 20, -10)$ was chosen as a test case as the cost surface contains multiple minima as shown in Figure 3.13a. The constraints on the reconstructed parameters were the same as those used in the numerical validation of the GA, given in Table 3.3.

Results

Table 3.6 shows the results of both experiments. FFA causes the correct guess to be introduced earlier, and the algorithm to converge in fewer generations. Using a one-tailed Student's t-test to test the statistical significance of the sample mean with FFA being smaller the sample mean without FFA, gives a p value of less than 0.0001 for both the experiment 1 and experiment 2, thus the differences are statistically significant. The 95% confidence interval for the difference in means is 3.78 to 4.77 generations. This average gain of 4.27 generations equates to 273 fewer solution evaluations needed to introduce the correct guess into the population when using FFA. The 95% confidence interval for the difference in mean generations taken to converge is 8.67 to 11.05 generations. This average gain of 9.86 generations equates to 630 fewer solution evaluations needed to converge using FFA.

	Correct Solution Introduced *(# generations)*		**Convergence Reached** *(# generations)*	
	μ	σ	μ	σ
Without FFA	13.61	6.88	31.38	14.63
FFA used	9.34	3.99	21.32	12.42

Table 3.6: Comparison of the algorithm with and without FFA, where μ is the mean and σ the standard deviation of the generations elapsed.

Discussion and Conclusions

FFA increases the chance of introducing the global minimum solution into the population earlier in the algorithm. This is advantageous if the acceptable cost level is known, as the algorithm can be terminated as soon as the desired cost level is reached. The DIET project is not at the stage where a desired cost level is known, so a convergence criteria must be defined. In this study the convergence criteria was the top 5 chromosomes being identical. The algorithm with FFA outperformed the genetic algorithm alone in this study, but there are other factors that influence convergence of the genetic algorithm, for example mutation rate, and the geometry of the cost surface. The numerical study has demonstrated the effectiveness of the FFA in the DIET inclusion location problem, where the assumption that the best chromosomes lie on a sphere around the global minimum is acceptable.

The numerical study provides evidence for using FFA as part of the GA. Better guesses are more likely to be introduced into the population earlier, and for the only additional computational expense of one extra FEM evaluation. The use of FFA to introduce fitter guesses into the algorithm earlier provides an increase in confidence, particularly when the number of generations is limited by computational cost. The numerical study demonstrates the algorithm's ability to perform well with the complex cost surfaces found in the synthetic inclusion location problem.

3.7.3 Parallel Performance of the Algorithm

The algorithm developed for this study has two levels of parallelization. The solution evaluations (FEM calculations) are performed in parallel using MUMPS, a parallel sparse matrix solver [114] [115], with an option to select the number of processors to use. A second layer of parallelism is added so multiple solution evaluations are performed simultaneously. Figure 3.24 illustrates the parallel structure of the algorithm.

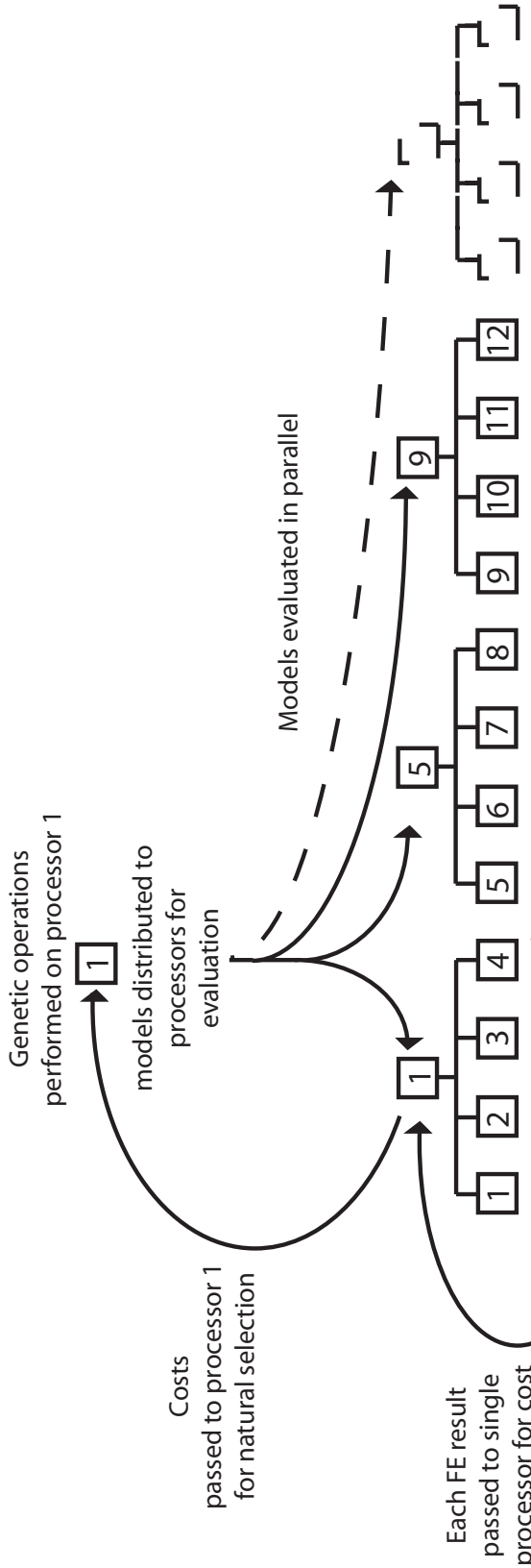

Figure 3.24: Parallel structure of the genetic algorithm.

The algorithm was written in Fortran 90 using the Message Passing Interface (MPI) and was run on both the Bluefern® IBM p575 and a Beowulf cluster. The parallel performance of the algorithm was assessed for *speedup* and *efficiency* on the IBM p575.

Speedup is defined as

$$\text{Speedup} = \frac{\text{Sequential execution time}}{\text{Parallel execution time}} \tag{3.60}$$

Operations in a parallel algorithm can be put in to the three following categories [116].

1. Computations that must be performed sequentially. For the GA this is the natural selection, mating and mutation.

2. Computations that can be performed in parallel. This is the FE calculation for to find the cost for each chromosome. These calculations have no dependence on each other.

3. Parallel overhead (communication operations and redundant computations).

The efficiency of a parallel program is a measure of processor utilization, defined as

$$\text{Efficiency} = \frac{\text{Sequential execution time}}{\text{Processors used} \times \text{Parallel execution time}}. \tag{3.61}$$

3.7.4 MUMPS performance on the DIET forward problem

The effectiveness of parallelizing the matrix inversion used to perform the forward solve depends on the size of the forward problem. In this thesis 2mm and 3mm mesh resolutions were used, so a test of the forward problem was run on various numbers of processors for a standard DIET geometry, using MUMPS with centralized matrix storage. Table 3.7 shows the results for an FE simulation using a 2mm linear tetrahedral mesh and a 3mm linear tetrahedral mesh. As can be seen from the table, there is no advantage in having multiple processors perform the forward solve for problems of this size using centralized matrix storage. In fact, the increased communication overhead with the increased processors causes an overall increase in computation time.

Number of Processors	2mm mesh Time(s)	3mm mesh Time(s)
1	9.86	56.73
2	10.06	58.94
3	10.28	58.47
4	10.75	59.38
5	11.38	60.61
6	12.12	61.12
7	12.83	61.74
8	15.58	63.28

Table 3.7: Time taken for a single FEM calculation using MUMPS for various numbers of processors on the Blufern® IBM p575

3.7.5 Genetic Algorithm Parallel Performance

Non-trivial algorithms have a computation component that is a decreasing function of the number of processors used and a communication component that is an increasing function of the number of processors. At some point, the increased cost of communication or redundant calculations outweighs the increase in the number of processors.

The algorithm was run with an initial population of 32 and 64 chromosomes for various number of processors. From the previous experiments using MUMPS to calculate the forward solution, one mumps processor was used for each FE calculation. The algorithm was limited to 10 generations, that is eleven sets of solution evaluations including the evaluation of the initial models, to avoid issues of convergence in timing the algorithm. Figure 3.25 shows the speed up for the algorithm averaged over 5 executions of the algorithm for 2 to 64 processors. Figure 3.26 shows the corresponding efficiency. An interesting feature to note is that speed up can fall because of the random nature of the GA where identical solutions can be generated. The algorithm was designed so FE evaluations are not repeated to save computational cost. As can be seen in Figure 3.26 the efficiency levels off at 16 processors for both the 32 and 64 chromosome population size. Therefore to use the shared resource of Bluefern® efficiently, 8 or 16 processors were used for the reconstructions in this thesis.

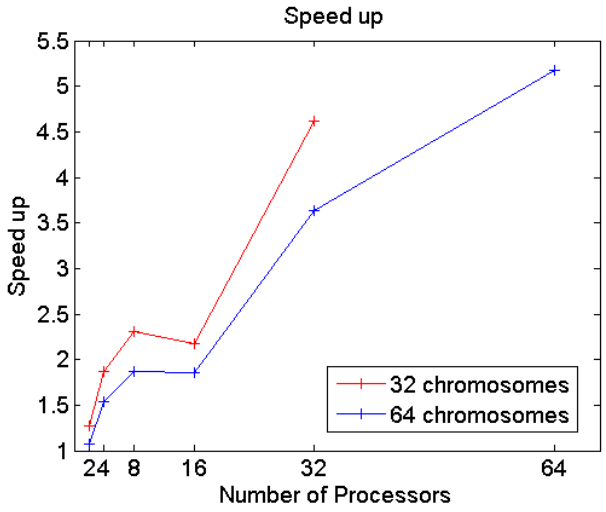

Figure 3.25: Speed up of the parallel genetic algorithm over ten generations.

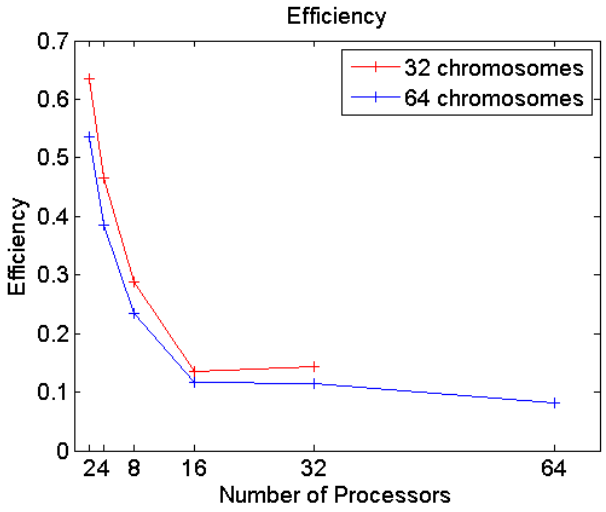

Figure 3.26: Efficiency of the parallel genetic algorithm over ten generations.

Chapter 4

Single Frequency Phantom Study

The aim of this chapter is to apply the reconstruction algorithm described in Chapter 3 to phantom data acquired with the DIET prototype. There are three breast-shaped, tissue-mimicking phantoms used in the initial phantom study: phantom Tr10, which contains a 10 mm radius inclusion; phantom Tr5, which contains a 5 mm radius inclusion; and phantom H, which has no inclusions and represents the 'healthy' case. The phantoms are constructed as described in section 2.1, with an inclusion contrast of approximately nine times the background material stiffness. The phantoms are less stiff than previous phantoms used in Van Houten *et al.* [62], which had a background $E' \approx 27$ kPa. The phantoms used in this thesis are closer to the Young's modulus of breast tissue as measured by Samani *et al.* [38], on the order of 3 kPa. A two step reconstruction approach is adopted: optimizing for background parameters, E'_B, ζ_B and then reconstructing inclusion location, $\mathbf{X}_I$, given an assumed inclusion radius and stiffness. The sensitivity to the *a priori* inclusion assumption is examined. The chosen *a priori* assumptions are applied to successfully reconstruct inclusion location for two further phantoms. The image reconstruction results are summarized in section 4.4.

4.1 Data Collection

The phantoms used in this chapter are detailed in Table 4.1. The data were acquired using an actuation frequency of 26 Hz with an amplitude of 0.5 mm. Approximately 1200 fiducials were used on each phantom. The fiducial markers are small, on the order of a couple of millimeters. They consist of pieces of colored paper which are applied to the phantom by rolling the phantom on a surface covered in the markers.

The position of the fiducial was recorded with the origin at the 'chest wall' and the z axis positive downwards. Thus both data and reconstructions are displayed with the actuator contact at the top of the image, although the data is actually collected with the breast hanging pendant. Figure 4.1 shows the tracked fiducials for phantom H together with a plot of the displacement interpolated over the phantom surface.

Phantom	**Inclusion radius**	**Inclusion location**
H	no inclusion 'healthy case'	-
Tr10	10 mm	$(0, -20, 30)$
Tr5	5 mm	$(0, -25, 25)$
R05H25V40	5 mm	$(0, 25, 40)$
R10H35V25	10 mm	$(0, 35, 25)$

Table 4.1: Phantoms used in this chapter.

The ellipse fitting of Eq. 3.8 is applied to each fiducial to produce the measured motion, $\mathbf{u}_m$ at each point, which is then compared to simulated motion on the FE mesh. Figure 4.2 shows the measured motion and an example of simulated motion for phantom Tr10. Note that the gap in data at the top of the phantom shown in Figure 4.2a is where the actuator makes contact with the breast phantom.

A much richer data set could be acquired if the DIET prototype were not limited to 1D actuation. Future prototypes may be developed which allow multiple modes of actuation, however, to allow data collection, any future actuator design must work within the constraint of having a line of sight between the cameras and the breast.

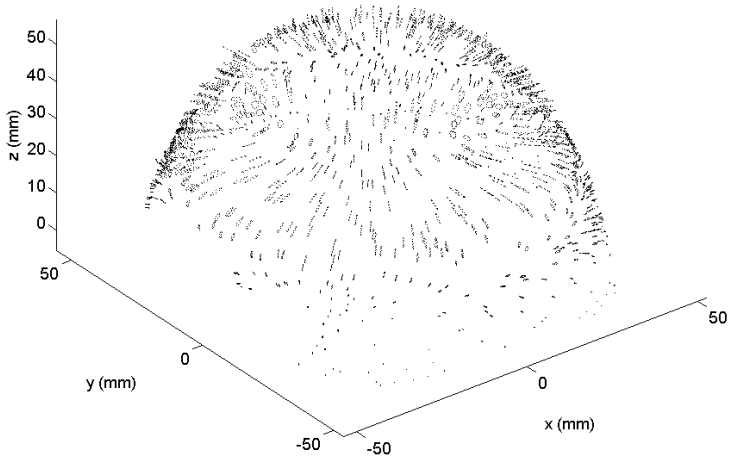

(a) Tracked fiducials

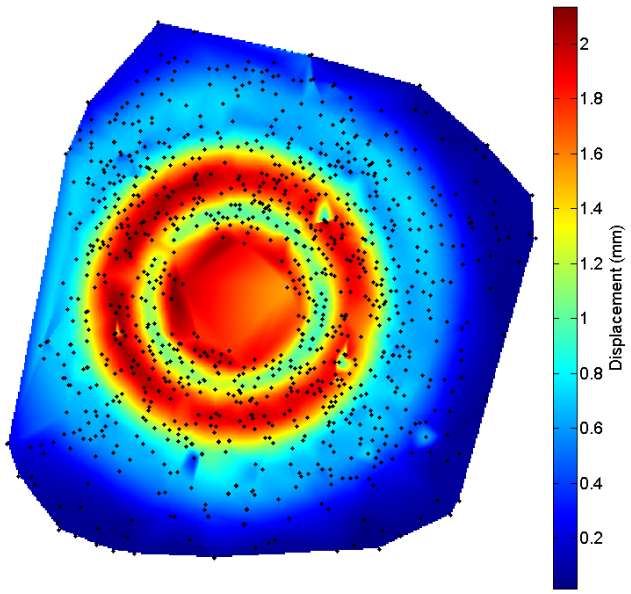

(b) Interpolated measured displacement for phantom H. The black squares indicate measurement locations.

Figure 4.1: Tracked fiducials for phantom H (4.1a) and the corresponding plot of displacement interpolated over the surface and projected flat (4.1b).

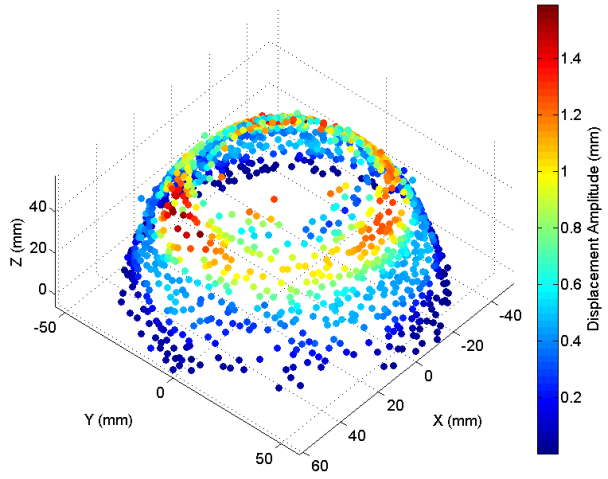

(a) Real part of displacement data, $\Re(\mathbf{u}_m)$, collected using the DIET prototype.

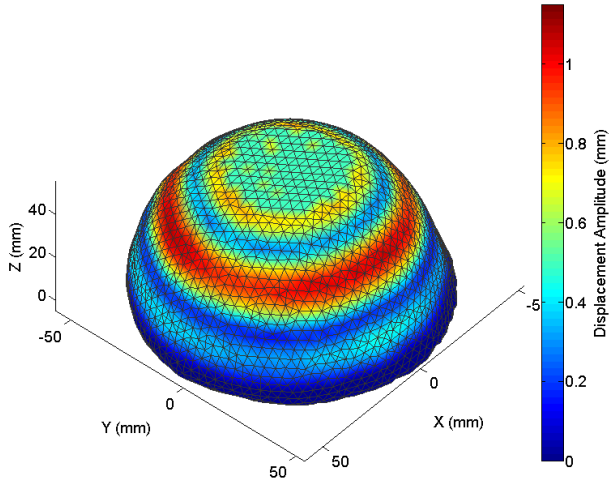

(b) Real part of simulated displacement, $\Re(\mathbf{u}_c)$, calculated using FE.

Figure 4.2: Real part of measured displacement for phantom Tr10 (4.2a) and the real part of the simulated displacement on the mesh (4.2b). Note that both figures are rotated so the gap in data at the actuator contact is visible. The height of the phantom is 65 mm.

4.2 Reconstruction Approach

The assumption was made that there is a stiff spherical inclusion of fixed radius at an unknown position within a less stiff background material. This is the so called 'contradictive' approach adapted by Peters *et al.* [89], with the addition that there is no restriction on the inclusion to remain within the breast volume. The rationale behind allowing the inclusion to move outside the breast is to allow homogeneous solutions to be generated while maintaining the assumption of an inclusion. The optimization was performed in two steps, using the algorithm described in Chapter 3 with the cost, Φ, calculated by Eq. 3.23.

1. Optimize for background parameters, storage modulus, E'_B, and damping parameter, ζ_B.
2. Fix the background parameters at the values found in step 1 and optimize for the inclusion location, $\mathbf{X}_I$.

The inclusion radius, R, and material properties, storage modulus, E'_I, and damping parameter, ζ_I are fixed at *a priori* values for each reconstruction. The motivation behind this is to reduce the number of unknown parameters in the inverse problem, as DIET is chiefly concerned with the identification and location of cancerous masses. In a clinical setting, these *a priori* values would be unknown, only an estimate of the typical cancerous material properties can be assumed and a desired inclusion size required to be identified or excluded must be decided upon. Thus the sensitivity of the reconstructions to the *a priori* assumptions is examined.

4.2.1 *A priori* Inclusion Sensitivity

Methods

To examine the reconstruction algorithm's sensitivity to the *a priori* values, ζ_I, E'_I, and R, for the phantom case, the following tests were performed:

- ζ_I: The forward problem was solved for the phantom Tr10 case with the correct inclusion size and location and E'_I fixed at 30 kPa. ζ_I was varied from 1 to 10%. The range in cost found with varying ζ_I was compared to the range in cost found with varying $\mathbf{X}_I$ throughout the parameter space using the correct inclusion size and with $\zeta_I = 10\%$.
- E'_I: Reconstructions were performed on the three phantoms with E'_I, varied between 20, 30 and 40 kPa. This provides a stiffness contrast ranging between approximately 6 to 12 times the background storage modulus, E'_B.

- R: Reconstructions were performed with R varied between 5 mm, 10 mm and 15 mm.

Table 4.2 gives the parameters and their constraints for the reconstructions. Note that there is no restriction on the inclusion to stay within the breast. The reconstruction was considered complete when the GA converged, judged as the top ten of thirty-two chromosomes being equal, or when the algorithm has reached 200 generations.

Parameter		**Constraint**		
		Lower	**Upper**	**Increment**
Background	Storage Modulus $E'_B(kPa)$	1	5	0.1
	Damping ratio $\zeta_B(\%)$	1	10	1
Inclusion Location	$x(mm)$	-60	60	5
	$y(mm)$	-60	60	5
	$z(mm)$	-60	60	5
Inclusion radius R (mm)		*Fixed at 5, 10 or 15*		
Inclusion Storage Modulus $E'_I(kPa)$		*Fixed at 20, 30 or 40*		
Inclusion Storage Damping $\zeta_I(\%)$		*Fixed at 10*		

Table 4.2: Constraints on reconstructed parameters.

Results

Table 4.3 shows the variation in cost due to ζ_I compared to the variation in cost due to $\mathbf{X}_I$ for a fixed $\zeta_I = 10\%$. The range of cost for $\mathbf{X}_I$ is two orders of magnitude higher than the range in cost for ζ_I. ζ_I was thus fixed at 10% for phantom reconstructions. The reconstruction results for the various R and E'_I *a priori* assumptions are summarized in Table 4.4.

Parameter	$\mathbf{\Phi^{SQ}}$ range	$\mathbf{\Phi}$ range
ζ_I	3.11×10^{-6}	5.86×10^{3}
$\mathbf{X}_I$	3.80×10^{-4}	8.45×10^{5}

Table 4.3: ζ_I cost range compared to $\mathbf{X}_I$ cost range.. The range of cost for $\mathbf{X}_I$ is two orders of magnitude larger than the range of cost for ζ_I for both Φ^{SQ} and Φ.

Phantom	**E′(kPa)**	**Reconstructed Inclusion Center (x, y, z) mm**	**Distance from True Center (mm)**
		R = 5 mm	
H	20	(-15,5,10)	-
	30	(30,25,25)	-
	40	(30,25,25)	-
Tr10	20	(0,-30,25)	11
	30	(0,-30,30)	10
	40	(0,-30,25)	11
Tr5	20	(5,-10,55)	34
	30	(0,-10,45)	25
	40	(0,-5,40)	25
		R = 10 mm	
H	20	(-15,5,5)	-
	30	(30,45,30)	-
	40	(30,40,30)	-
Tr10	20	(5,-30,30)	11
	30	(5,-30,30)	11
	40	(5,-30,30)	11
Tr5	20	(5,0,40)	30
	30	(10,-35,40)	20
	40	(5,-5,40)	32
		R = 15 mm	
H	30	(-10,50,50)	-
Tr10	30	(0,-45,30)	15
Tr5	30	(5,-10,30)	16

Table 4.4: Summary of various *a priori* R and E' sensitivity results. Note the distance from the *true* inclusion center for phantom H is undefined as phantom H does not contain an inclusion.

Conclusions

As stated previously, ζ_I was found to have much less of an effect on Φ than inclusion location, $\mathbf{X}_I$, and was thus fixed at 10% for phantom reconstructions to remove one of the unknowns in the inverse problem.

For phantom Tr10 there was little difference between results with $R = 5$ mm and $R = 10$ mm. The distance between reconstructed and true location changed by only 1 mm for the all three *a priori* E'_I values for $R = 5$ mm and $R = 10$ mm. Including the 15 mm *a priori* radius, all the *a priori* assumption results were within 15 mm of the true location and all located an inclusion within the breast volume. For phantom Tr5 all the *a priori* results were within 35 mm of each other and all located an inclusion within the breast. A smaller *a priori* inclusion (5 mm) has not impeded the algorithm's ability to locate a larger inclusion (10 mm). Nor the reverse, as a 15 mm *a priori* inclusion has been used to locate the 5 mm and 10 mm inclusions.

For phantom H, the inclusion was located partially outside, or fully outside, the breast volume for all *a priori* assumptions except when $E'_I = 20$ kPa. When the *a priori* E'_I was reduced to 20 kPa the presence of an inclusion within the phantom could not be discounted. Figure 4.3 shows the optimal solutions for phantom H for an inclusion radius of 10 mm and 15 mm with $E'_I = 30$ kPa. When these larger *a priori* inclusion radii are used, the phantom H reconstruction becomes completely homogeneous. This is a good result for the homogeneous case, but clinically it is desirable to exclude the smallest possible inclusion. By phrasing the reconstruction problem to identify whether there is a 15 mm radius inclusion in the phantom, we cannot discount any inclusions with a smaller radius.

In terms of specificity for the DIET system, it is desirable to pose the problem as detecting

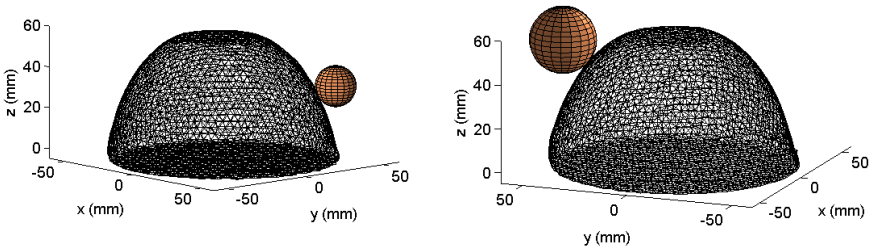

(a) $E'_I = 30$ kPa, R = 10 mm (b) $E'_I = 30$ kPa, R = 15 mm

Figure 4.3: Minimum cost solution for Phantom H for *a priori* $E'_I = 30$ kPa and $R = 10$ mm (4.3a) and $R = 15$ mm (4.3b).

the presence or absence of a small inclusion. The sensitivity study provided evidence for the use of *a priori* inclusion material properties to locate or exclude an inclusion, with the caveat that to successfully identify the 'healthy' case E'_I must be 30 kPa or higher in this phantom where $E'_B \approx 3$ kPa. This is a contrast between the inclusion and the background of approximately ten. Thus, for higher stiffness background, this would suggest that the E'_I should be adjusted accordingly. Higher contrast ratios, such as that provided by $E'_I = 40$ kPa with $E'_B \approx 3$ kPa, could be used to exclude or locate inclusions, but, as with the choice of inclusion radius, it is desirable to exclude as low a stiffness inclusion as possible. Thus, the *a priori* inclusion values were chosen to be $E'_I = 30$ kPa, $\zeta_I = 10\%$, $R = 5$ mm. The reconstruction results using these *a priori* values are detailed in the following sections.

4.3 Reconstructions Results

The homogeneous assumption results for step 1 of the optimization are shown in Table 4.5. The reconstructions using the chosen *a priori* inclusion assumption of $E'_I = 30$ kPa, $R = 5$ mm and $\zeta_I = 10\%$ results are described in sections 4.3.1-4.3.3. Section 4.3.4 details the results after manually improving the mesh for phantom Tr5. The *a priori* assumption is successfully applied to two further phantoms as detailed in section 4.3.5.

Phantom	$\mathbf{E'_B}$**(kPa)**	$\zeta_\mathbf{B}$ **(%)**
H	3.3	4
Tr10	3.4	6
Tr5	3.7	4

Table 4.5: Step 1 reconstruction results assuming a homogeneous material parameter distribution

4.3.1 Phantom H

After the optimization of the background parameters, E'_B, ζ_B, the location optimization result for the 'healthy' case converged on a solution partially outside the breast, shown in Figure 4.4a. Identifying the healthy case is an essential quality for the DIET system, which needs to identify cases where there are no stiff inclusions and thus eliminate true negatives in a screening program. Figure 4.4b shows a slice through the cost surface at z = 30 mm, with a local minimum in the center

of the breast. The algorithm successfully avoided this local minimum, indicating the functionality of the GA. Note the low cost of solutions outside the breast volume in Figure 4.4b where the mesh boundary nodes are plotted in black. The optimal region is displayed in Figure 4.5, and shows that around the optimum solution are solutions that breach the surface of the mesh.

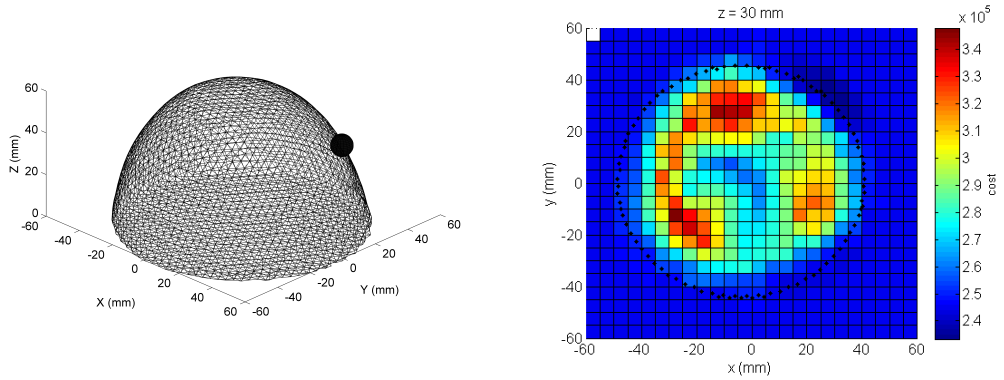

(a) Minimum cost result for the 'healthy' case, phantom H. The inclusion is partially outside the breast.

(b) Slice through the cost surface for the 'healthy' case, phantom H at z = 30 mm. Boundary nodes indicated in black.

Figure 4.4: Minimum cost result for the 'healthy' case assuming a 5 mm radius inclusion with $E'_I = 30$ kPa (4.4a) and a slice through the cost surface at z = 30 mm (4.4b).

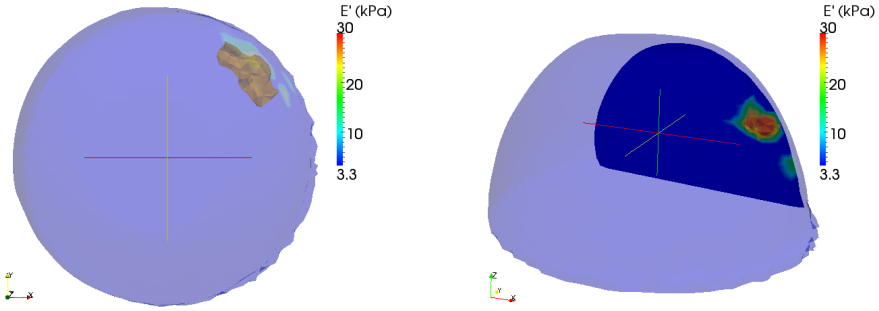

(a) Top view

(b) Slice through phantom

Figure 4.5: Optimal region for a 5 mm radius inclusion with $E'_I = 30$ kPa for phantom H. The contour is 25 kPa.

4.3.2 Phantom Tr10

Figure 4.6a shows the reconstruction result for phantom Tr10 of $(0, -30, 30)$ which is 10 mm away from the true inclusion location of $(0, -20, 30)$. The optimization has successfully identified that there is an inclusion within the breast, and placed the inclusion 10 mm away from the true location. The slice through the cost surface in Figure 4.6b shows the minimum in the correct area of the breast. The cost surface of phantom Tr10 is in contrast to that of phantom H shown in Figure 4.4b, with solutions outside the breast mesh having a high cost. The optimal region shown in Figure 4.7 shows the stiff nodes located close to the true inclusion location.

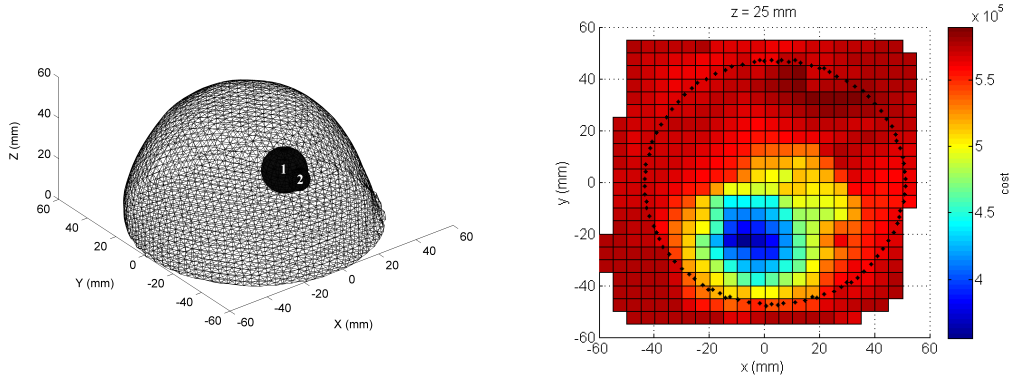

(a) Minimum cost result for phantom Tr10. 1 is the true inclusion location. 2 is the reconstructed location.

(b) Slice through the cost surface at z = 30 mm for phantom Tr10. Boundary nodes indicated in black.

Figure 4.6: Minimum cost result for phantom Tr10 assuming a 5 mm radius inclusion with $E'_I = 30$ kPa (4.6a) and slice through cost surface at z = 30 mm (4.6b).

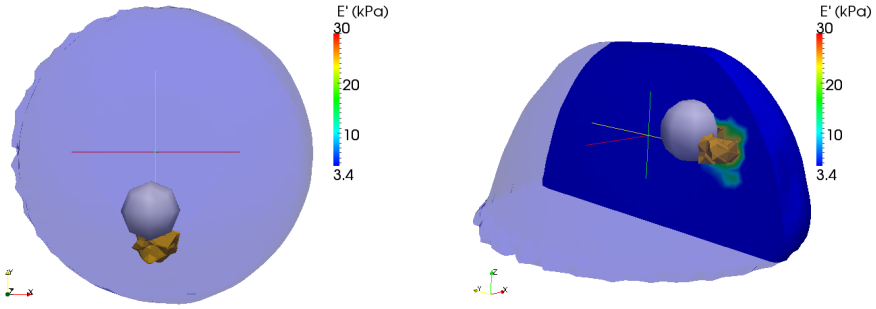

(a) Top view

(b) Slice through phantom

Figure 4.7: Optimal region for a 5 mm radius inclusion with $E'_I = 30$ kPa for phantom Tr10. The contour is 25 kPa. The true inclusion is shown in grey.

4.3.3 Phantom Tr5

Figure 4.8a shows the reconstruction result for phantom Tr5 and the true inclusion location. The reconstruction algorithm has placed the inclusion 25 mm away from the true location. There is a clear global minimum that lies at $(0, 10, -45)$, shown in Figure 4.8b that the reconstruction algorithm has converged on. Figure 4.8c shows a slice through the cost surface at z = 25 mm, which is the z location of the true inclusion. Figure 4.9 shows a 3D image of isocontours of the cost surface at the cost level of the true inclusion location compared to a lower cost isocontour that encloses the global minimum. The optimal region in Figure 4.10 shows the location of the best models, which are located 25 mm from the true inclusion location.

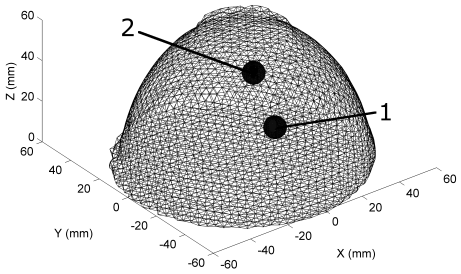

(a) Minimum cost result for the phantom Tr5. 1 is the true location of the inclusion. 2 is the reconstructed location.

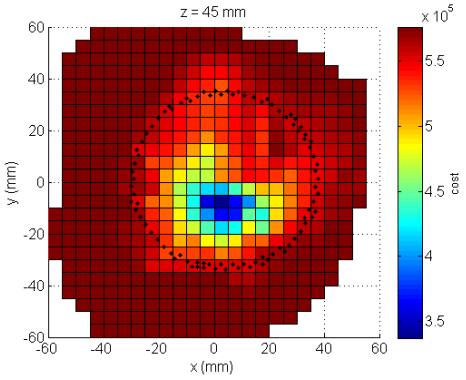

(b) Slice through cost surface at z = 45 mm for phantom Tr5. Boundary nodes indicated in black.

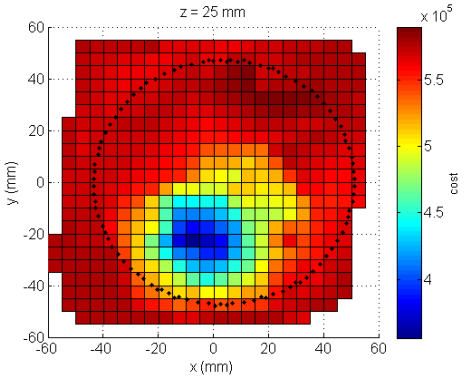

(c) Slice through cost surface at z = 25 mm for phantom Tr5. Boundary nodes indicated in black.

Figure 4.8: Minimum cost result for phantom Tr5 (4.8a) assuming a 5 mm radius inclusion with $E'_I = 30$ kPa, $E'_I = 30$ kPa, and $zeta_I = 10\%$. Slices thought the cost surface at z = 45 mm (4.8b) and z = 25mm (4.8c). The cost at z = 45 mm is lower than at true inclusion location at z = 25mm.

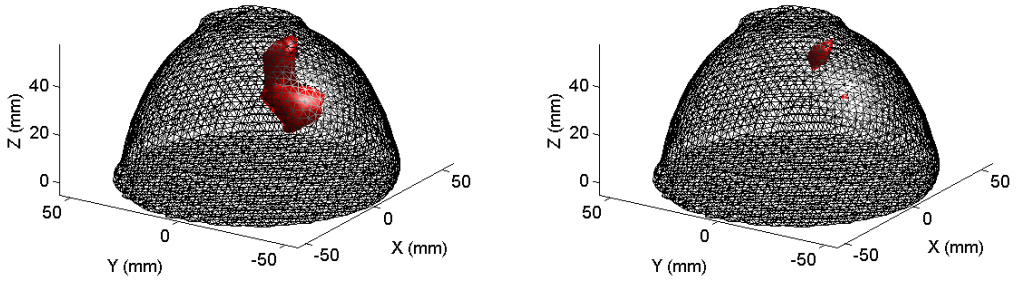

(a) Isocontour at $\Phi(\theta) = 3.84 \times 10^5$, the cost at the true inclusion location.

(b) Isocontour at $\Phi(\theta) = 3.50 \times 10^5$

Figure 4.9: Three dimensional view of isocontours of the cost surface for phantom Tr5. Figure 4.9a is the isocontour of the cost at the true inclusion location. Figure 4.9b shows a lower cost isocontour.

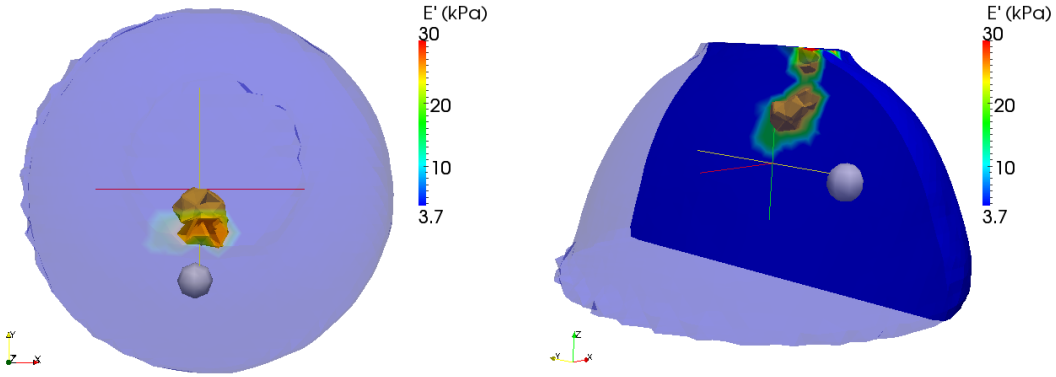

(a) Top view

(b) Slice through phantom

Figure 4.10: Optimal region for a 5 mm radius inclusion with $E'_I = 30$ kPa for phantom Tr5. The true inclusion is shown in grey.

4.3.4 Phantom Tr5 with Modified Mesh

The surface fitting to provide the mesh for the DIET forward problem relies on placing a circle at the actuator and 'chest wall' to fill the gaps in data coverage at these locations. Figure 4.11 shows the point cloud data for phantom Tr5 to illustrate the gap in data coverage at the 'chest wall' and actuator. The black lines indicate where the circles must be fitted to produce a mesh of the phantom, which is done automatically by fitting a circle the size of the actuator contact to the gap in the point cloud data. As can be seen in Figure 4.11c, which is a closer view of the mesh, there is poor meshing where the phantom makes contact with the actuator. Poor meshing in this sense means that the shape of the mesh does not match the shape of the phantom. The phantoms are all the same shape and size, thus the poor match between the data-generated mesh and phantom Tr5 becomes particularly apparent when compared to the phantom H data-generated mesh shown in Figure 4.11d.

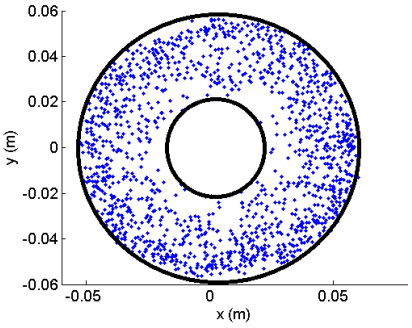

(a) Top view of the point cloud data for phantom Tr5.

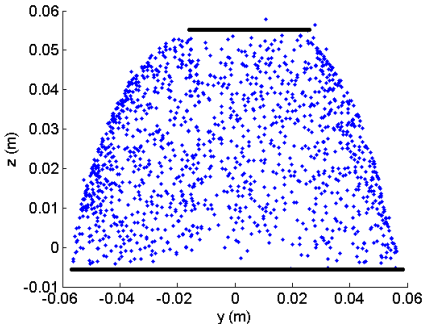

(b) Side view of the point cloud for phantom Tr5.

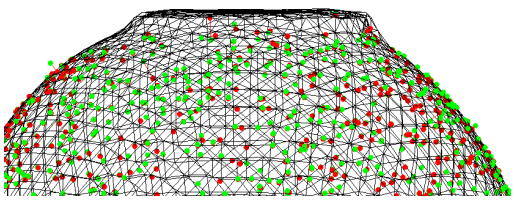

(c) Close up of poor meshing for phantom Tr5.

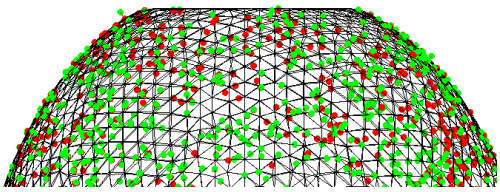

(d) Close up of meshing for phantom H.

Figure 4.11: Point cloud of data used to create mesh for phantom Tr5 (4.11a, 4.11b). The black circles complete the surface used as the basis for the mesh. Close up of the resulting poor meshing for phantom Tr5 (4.11c) with an example of meshing from phantom H (4.11d). The green circles indicate the location of the data points, the red circles indicate the projected point on the mesh.

The mesh created for Phantom Tr5 was manually corrected by adjusting the mesh at the location where the phantom meets the actuator. The step 1 optimization gave $E'_B = 4.0$ kPa and $\zeta_B = 4\%$ compared to $E_B = 3.7$ kPa and $\zeta_B = 4\%$ for the original mesh. The Canterbury Dynamic Mechanical Analyzer (DMA) machine was broken in the earthquake and thus no independent measurements of the phantom Tr5 stiffness were made. It is therefore unknown which of the fitted values of E_B is closer to the true value. However, the precise description of background stiffness is not critical in DIET, only the abilty to detect the inclusion location. Thus, it is more important to examine how well the inclusion location performed. The step 2 optimal location for the inclusion is $(0, -5, 45)$, which is still 28 mm from the true location, comparable to the 25 mm away from the true location found using the original mesh. However the optimal region result shown in Figure 4.12 shows that within the optimal region there is a better, *i.e.* closer to the true location, reconstruction when using the manually improved mesh. This change in the optimal region from Figure 4.10 to Figure 4.12 suggests that some of the data-model mismatch due to misshapen meshing has been mitigated by manually correcting the mesh. The optimal region in Figure 4.10 runs from the actuator contact to the center of the phantom. In Figure 4.12 the optimal region is split into two regions, one at the actuator contact and one close to the inclusion. Correcting the mesh has reduced the data-model mismatch, because the mesh corresponds more closely to the shape of the phantom. However, the problems of poorly tracked fiducials are two fold, affecting both the mesh generation and the actual motion data. Simply correcting the shape of the mesh has not removed the false minimum at the actuator contact.

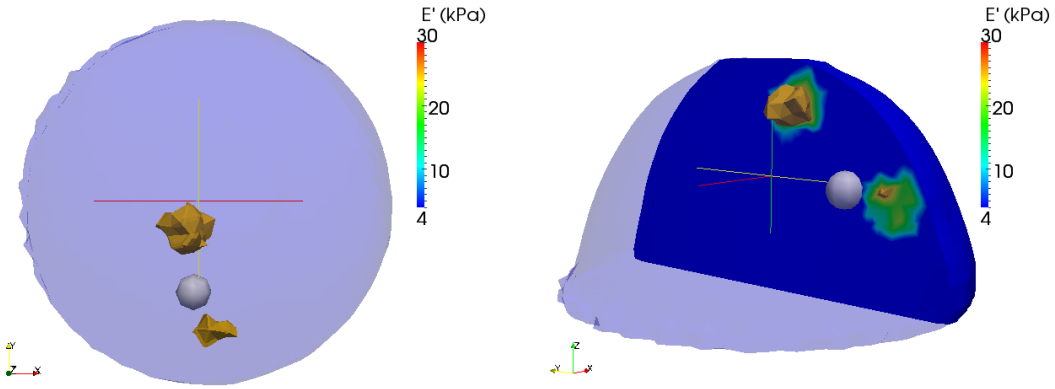

(a) Top view

(b) Slice through phantom

Figure 4.12: Optimal region for 5 mm radius inclusion with $E'_I = 30$ kPa for the manually corrected mesh. The true inclusion is shown in grey.

4.3.5 Application of selected a priori inclusion to two further phantoms

To asses the validity of the *a priori* assumption (R = 5 mm, $E'_I = 30$ kPa, $\zeta_I = 10\%$) on other datasets, the method is applied to two additional phantoms: R05H25V40, which contains a 5mm radius inclusion at $(0, 25, 40)$ and R10H35V25, which contains a 10mm radius inclusion at $(0, 35, 25)$. The step 1 homogeneous assumption results are given in Table 4.6 with the step 2 optimization results given in Table 4.7. Figures 4.13 and 4.14 show the optimal regions for the step 2 inclusion location results, both locating the inclusion in the correct location within the phantom.

Phantom	**E′(kPa)**	**damping ratio (%)**
R10H35V25	2.9	1
R05H25V40	3.0	1

Table 4.6: Step 1 reconstruction results assuming a homogeneous material parameter distribution for phantoms R05H25V40 and R05H25V40.

Phantom	**Reconstructed Location**	**Distance from True location (mm)**
R05H25V40	$(0, 20, 50)$	11
R10H35V25	$(5, 45, 15)$	15

Table 4.7: Step 2 reconstruction results with $R = 5$ mm, $E'_I = 30$ kPa, $\zeta_I = 10\%$ for phantoms R05H25V40 and R05H25V40.

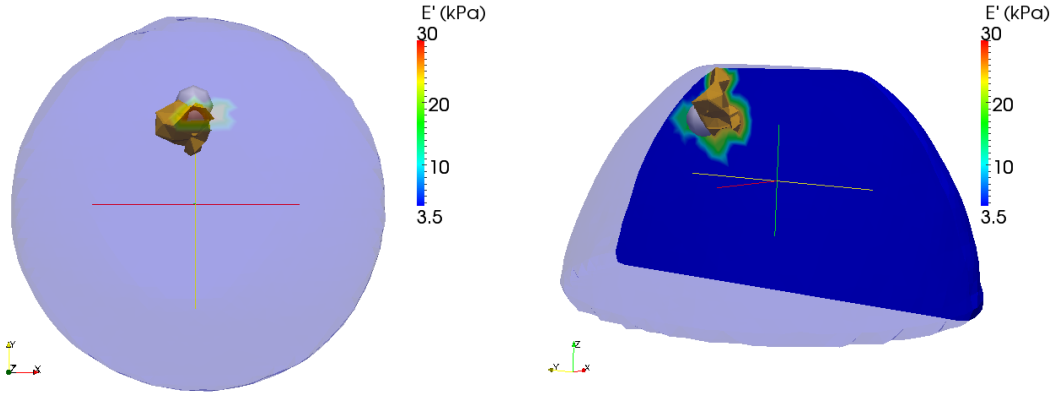

(a) Top view (b) Slice through phantom

Figure 4.13: Optimal region for 5 mm inclusion with $E'_I = 30$ kPa for phantom R05H25V40. Contour is $E' = 25$ kPa. The true inclusion is shown in grey.

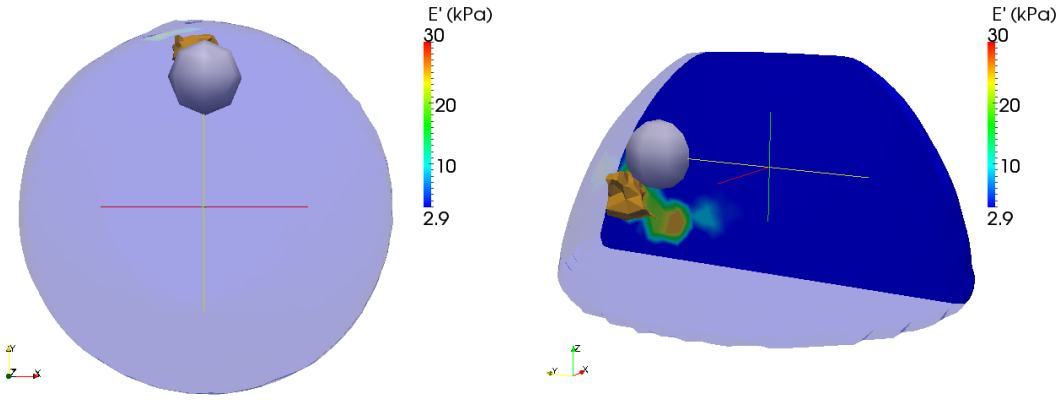

(a) Top view

(b) Slice through phantom

Figure 4.14: Optimal region for 5 mm inclusion with $E'_I = 30$ kPa for phantom R10H35V25. Contour is $E' = 25$ kPa. The true inclusion is shown in grey.

4.4 Image Reconstruction

4.4.1 Summary of Optimal Region Results

Table 4.8 gives the volume fraction and centroid difference of the $E' = 25$ kPa contour for the optimal region for each reconstruction. The volume fraction is calculated using Eqs. 3.53 and 3.54. The centroid difference is calculated using Eqs. 3.56 and 3.57. For the smaller inclusion phantoms, Tr5 and R05H25V40, the $E' = 25$ kPa contour overestimates the inclusion volume by 180% -190% the true inclusion volume. For the larger inclusions, Tr10 and R10H35V25, the $E' = 25$ kPa contour underestimates the inclusion volume, as 21%-22% of the true inclusion volume.

Phantom	**Volume Fraction**	**Centroid Difference (mm)**
Tr5	1.88	25
Tr10	0.21	12
R05H25V40	1.80	7
R10H35V25	0.23	15

Table 4.8: Quantitative description of the optimal region, where *Volume Fraction* is the volume of the 25 kPa contour divided by the volume of the true inclusion, and the *Centroid Distance* is the distance between the centroid of the credible region and the centroid of the inclusion. Note phantom H is not listed as the inclusion volume is zero and the inclusion location is undefined.

4.4.2 Credible Region Results

The measurement variance as calculated using Eq. 3.52 for each dataset is given in Table 4.9. The credible regions for each of the phantoms are shown in Figures 4.15-4.19. The credible region is colored according to the average E' of the models that comprise the credible region. A quantitative description of the credible regions, the volume fraction and the centroid difference of the $E' = 25$ kPa contour, is given in Table 4.10.

Phantom	σ^2 (m^2)
H	8.13×10^{-6}
Tr5	1.09×10^{-5}
Tr10	8.83×10^{-6}
R05H25V40	3.50×10^{-6}
R10H35V25	3.69×10^{-6}

Table 4.9: Measurement variance σ^2 for each phantom experiment.

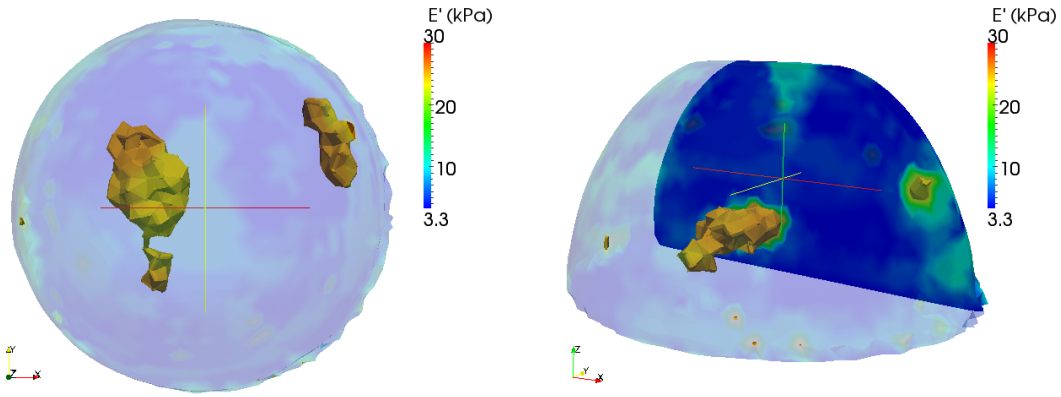

(a) Top view

(b) Slice through phantom

Figure 4.15: 90% credible region for phantom H. Contour is $E' = 25$ kPa. Note the stiff surface nodes due to models where the inclusion is located outside the phantom but makes contact with the phantom surface.

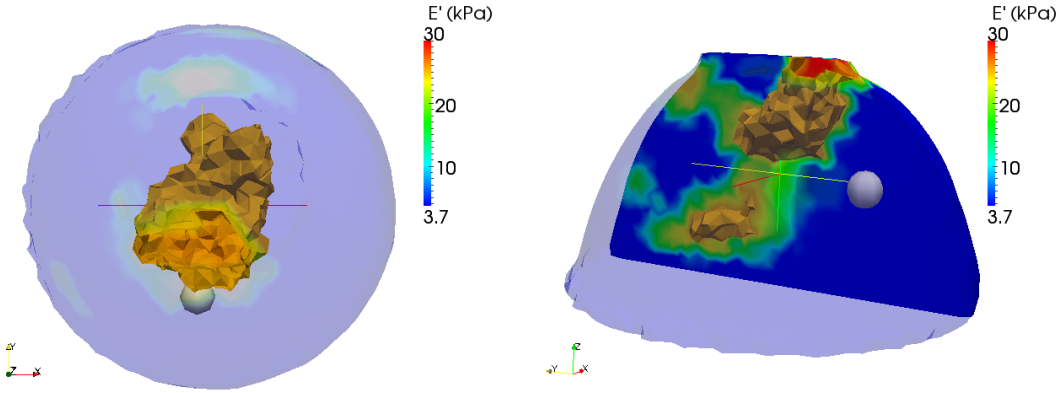

(a) Top view (b) Slice through phantom

Figure 4.16: 90% credible region for phantom Tr5. Contour is $E' = 25$ kPa. True inclusion location is shown in grey.

Phantom	Volume Fraction	Centroid Difference (mm)
Tr5	27.8	28
Tr10	4.52	14
R05H25V40	8.95	15
R10H35V25	3.13	26

Table 4.10: Quantitative description of the reconstructed 90% credible region images for the $E' = 25$ kPa contour. Note phantom H is not listed as the inclusion volume is zero and the inclusion location is undefined.

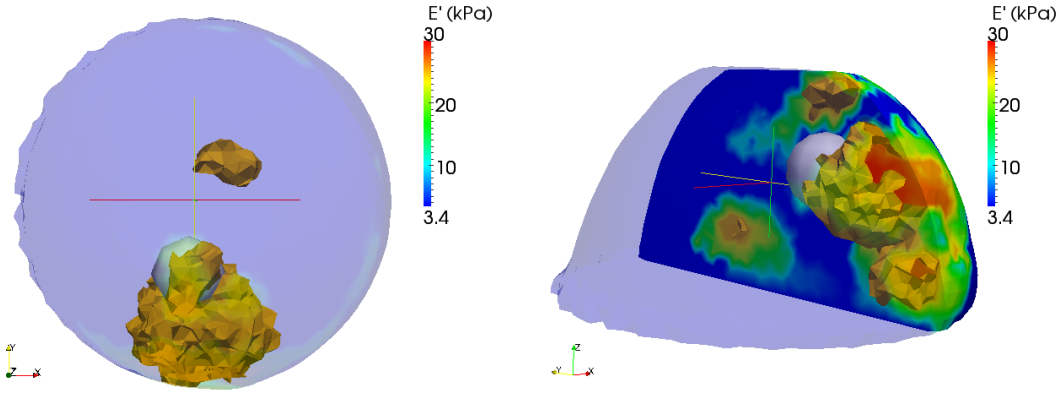

(a) Top view (b) Slice through phantom

Figure 4.17: 90% credible region for phantom Tr10. Contour is $E' = 25$ kPa. True inclusion location is shown in grey.

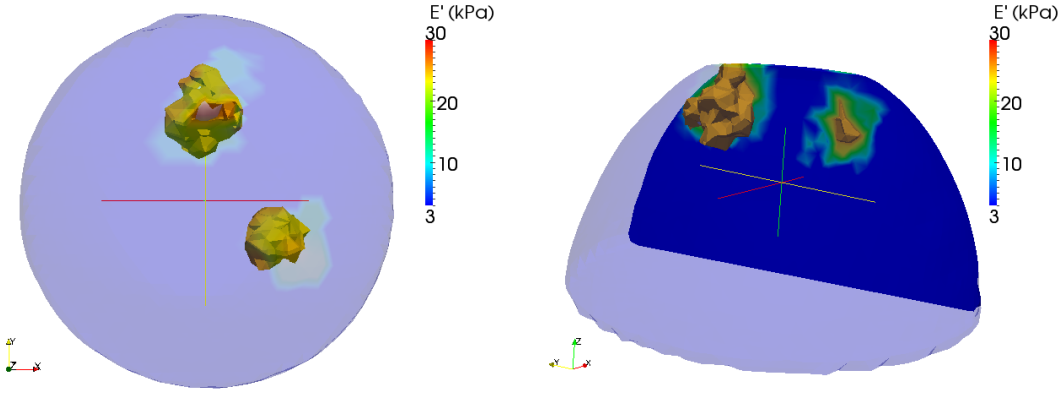

(a) Top view (b) Slice through phantom

Figure 4.18: 90% credible region for phantom R05H25V40. Contour is $E' = 25$ kPa. True inclusion location is shown in grey.

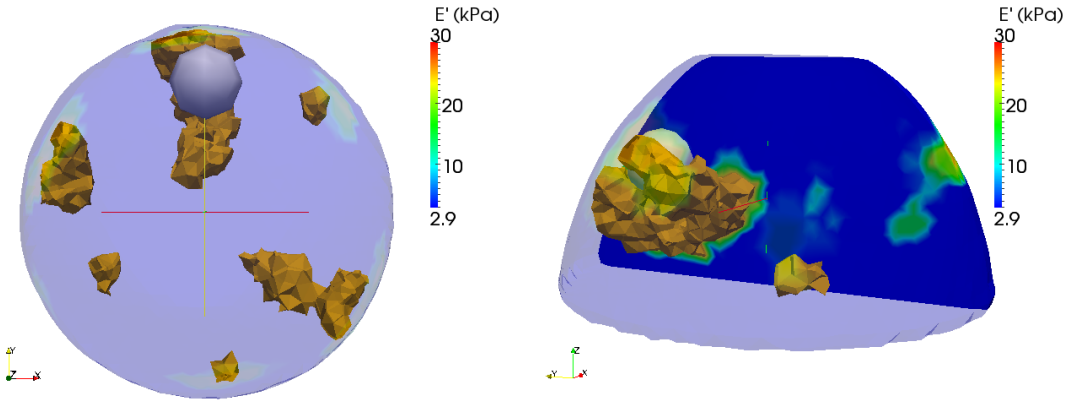

(a) Top view (b) Slice through phantom

Figure 4.19: 90% credible region for phantom R05H25V40. Contour is $E' = 25$ kPa. True inclusion location is shown in grey.

4.5 Discussion and Conclusions

The phantom H reconstruction in section 4.3.1 is encouraging, but needs improvement as the inclusion was only partially pushed outside the breast. As can be seen in Figure 4.4b, solutions outside the breast have a low cost relative to the solutions within the breast. In contrast, for a case with an inclusion, for example phantom Tr10 illustrated in Figure 4.6b, the lowest cost is clearly within the breast.

Physically, the inclusion can not breach the surface of the phantom, but for the sake of optimization these solutions are allowed. The only effect they have is on elements within the breast mesh, which can be important for the natural selection of solutions in the GA. For example, for the case illustrated in Figure 4.20a stiff elements in location 2 would be a good approximation to the true location (1) therefore the solution at location 2 should not be penalized. Figure 4.20b illustrates the effect of allowing inclusions outside the breast surface, which can lead to stiff surface nodes.

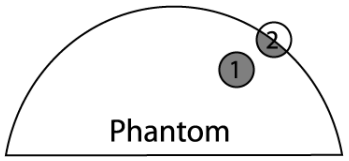

(a) Inclusion partially inside the breast at 2 will be close to the true solution at 1.

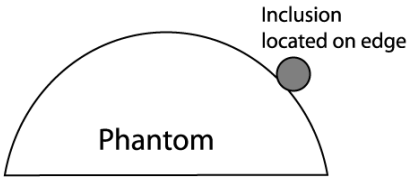

(b) Inclusions can be located on the outside of the breast, leading to stiff surface nodes.

Figure 4.20: Illustration of the rationale behind permitting the inclusion to be located outside the phantom (4.20a) and the consequences of allowing this assumption (4.20b).

The cost surface in Figure 4.4b also illustrates the need for a high signal to noise ratio to detect changes in stiffness at the deepest points within the breast. Changes in stiffness in these internal locations obviously produce a smaller change in surface motion than changes in stiffness closer to the breast surface. This is the same effect as found in the numerical validation of the algorithm in section 3.7.1. A good signal to noise ratio will allow solutions deep within the breast to be confidently accepted or discarded.

For the phantom Tr5 reconstruction in section 4.3.3, the true location of the tumor, $(0, -25, 25)$, is invisible to the reconstruction algorithm as the cost at and around the true location in parameter space is high. The global minimum occurs at $(0, -10, 45)$. The GA successfully avoided local minima, but optimization can do no better than finding the minimum cost. The reconstruction method is based on fitting the background material properties then locating the inclusion based on

any remaining anomalies. Figure 4.21 shows the location of the 100 data points with the highest Φ for phantom Tr5 assuming the best-fit homogeneous background material estimate. The location optimization fits the inclusion the anomaly remaining after the optimization of the background material properties. The clear localization of these points in a band around z = 45mm makes it no surprise that the reconstruction algorithm locates the inclusion in this region.

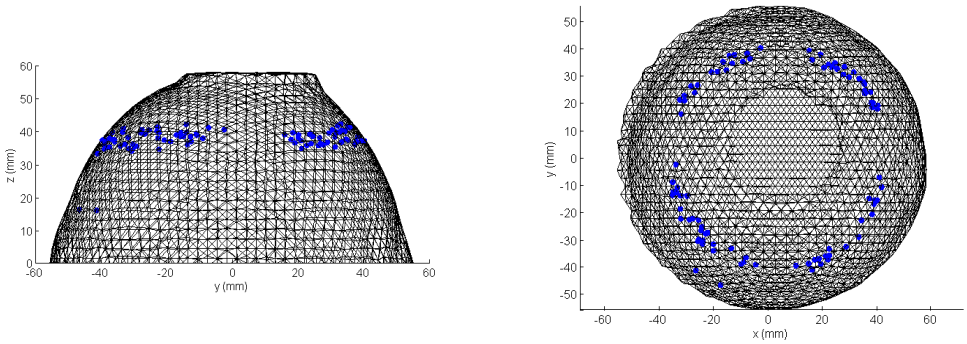

(a) Side view (b) Top view

Figure 4.21: The 100 points with the largest cost difference from the homogeneous solution for phantom Tr5. These points are the anomaly from the homogeneous solution, thus are used to locate the inclusion.

Phantom Tr5 exposes a weakness in the cost function used in this study. Figure 4.22 shows the tracked fiducials for phantom Tr5. There is poor motion tracking at the location where the actuator makes contact with the phantom, which has lead to a misshapen mesh. For comparison, the tracked fiducials for phantom H shown in Figure 4.1 do not exhibit this poor tracking at the actuator location.

The misshapen mesh for phantom Tr5 violates the assumption in the the inverse problem that the forward model provides effective simulation of the experimental process. The large error in modeling in this case may be due to the presence of poor motion tracking as a result of the large motion near the actuator. The mesh error, which is instantly identifiable to the human eye, is not accounted for in the cost function. For such a uniform geometry as the phantom, and such an obvious location at the actuator, mesh correction can be done manually. For the clinical case of a human breast, this would be a much less obvious procedure because of the non-uniform geometry and the variation in breast shape from person to person. The manual adjustment of the phantom Tr5 mesh provided a small improvement in the optimal region, but the global minimum $\theta(x_c, y_c, z_c)$ remained 28 mm from the true inclusion location. This provides evidence to support the collection of multiple frequency data because troublesome frequencies exhibiting unacceptably high surface

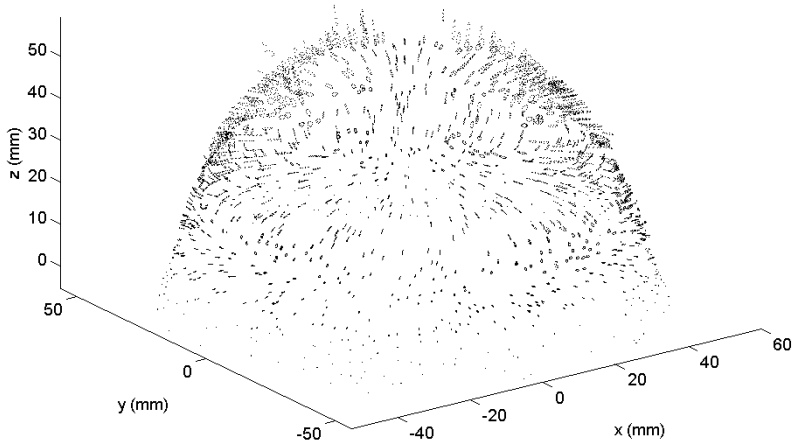

Figure 4.22: Tracked fiducials for phantom Tr5. The poorly tracked fiducials are at the actuator contact.

motion, which in the case of phantom Tr5 has caused misshaped meshing, can be discarded in the inverse problem.

In all four phantom cases containing an inclusion, the presence of an inclusion was identified. Excluding phantom Tr5, which has obvious data limitations, the inclusions were all located with 15 mm of the true inclusion location using a simple *a priori* assumption.

The large volume of the 25 kPa contour of the credible region demonstrates the uncertainty in inclusion location for each of the phantoms. The poorer quality of data for phantom Tr5 is evident in both in the larger value of σ^2 compared to the other datasets in Table 4.9 and visually in credible region, with the 25 kPa contour 27.8 times the inclusion volume. Ideally, for the eventual clinical application of the DIET system, the credible region will need to be comparable to the optimal region. Currently, the measurement variance, σ^2, is not at a level where the credible and optimal regions are comparable. For an estimate of how the measurement variance would need to be reduced to give a credible region comparable to the optimal region, Figure 4.23 shows the credible region for phantom Tr10 assuming a variance equal to half the actual measurement variance. This would alter the 25 kPa contour metrics to $V_{frac} = 1.52$ and $\delta_c = 14$ mm as calculated using Eqs. 3.53 and 3.57.

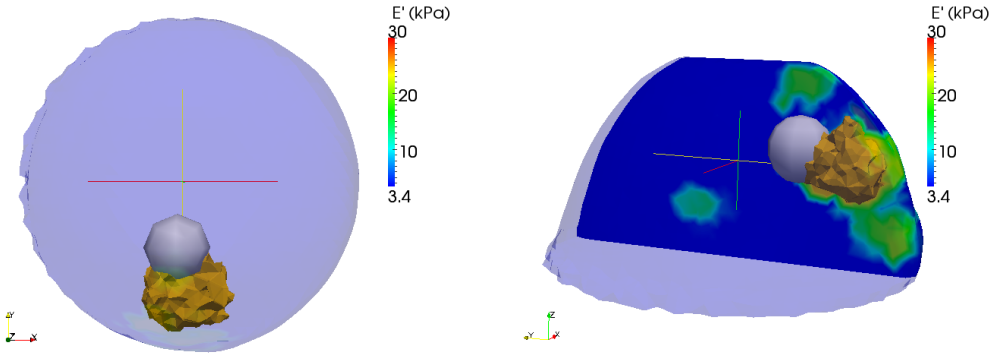

(a) Top view

(b) Slice through phantom

Figure 4.23: 90% credible region for phantom Tr10, calculated using a variance equal to half the true variance. Contour is $E' = 25$ kPa. True inclusion location is shown in grey.

The optimal region, however, is successful for all phantoms with inclusions except phantom Tr5. The success of the optimal region is encouraging as it demonstrates that the processes and algorithms developed can be successfully applied to phantoms with E' comparable to breast tissue and containing inclusions of clinically relevant size, which would be effective for cancer detection.

Chapter 5

Multi-Frequency Phantom Studies

As the dynamic response of the breast varies with different actuation frequencies, the incorporation of multiple frequencies into the inverse problem could improve overall tumor identification performance. Feng *et al.* developed an image based modal analysis system able to robustly and rapidly identify resonant frequencies in soft tissue using the DIET prototype [117]. Three images per oscillation cycle are enough to capture the behavior at a given frequency, which allows a rapid sweep over critical frequency ranges to be performed prior to imaging. The critical imaging settings of the DIET system can then be determined to optimize its image collection performance. Together with the improved DIET prototype this allows a sweep of frequency data to be collected in a time comparable to previous single frequency measurements. Typically, the data is collected between 8 Hz and 40 Hz. This provides much more information for solving the inverse problem.

The ideal DIET data set would consist of large, well tracked surface motions from phantoms or tissue exhibiting linearly elastic or linearly viscoelastic behavior. In reality, near resonant frequencies of the phantoms suffer reduced data coverage as the large motions are more difficult to track between frames [118]. This typically manifests as a reduced number of quality measurements across the tissue surface and thus reduced coverage of the data volume. Poor coverage also impacts the quality of the FE mesh which is created specifically for each patient from the motion data. As found in the initial phantom study of Chapter 4, poor meshing can affect the quality of reconstruction results. The aim of this chapter is to demonstrate an effective way of combining information from multiple frequencies to overcome the shortcomings of individual frequency datasets. There are three phantoms used in this chapter: H, Tr10 and Tr5. There is room for improvement in phantom H and phantom Tr5, and the successful reconstruction of phantom Tr10 needs to remain successful with multi-frequency data.

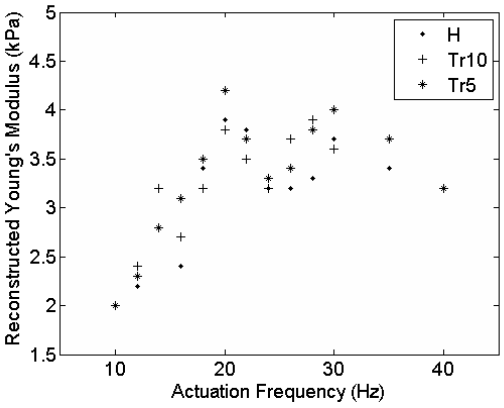

Figure 5.1: Graph showing reconstructed E'_B for phantoms H, Tr10 and Tr5.

Figure 5.1 shows the reconstructed background storage modulus, E'_B, for the three phantoms. While the homogeneous material properties, E'_B and ζ_B, may exhibit frequency dependence, the location of the inclusion will be constant with frequency. Thus, tumor location optimization can be carried out across multiple frequencies by using a combined cost function. Section 5.1 details the comparison of two multi-frequency cost functions, ranking and normalizing, defined in Eqs. 3.33 and 3.35 from Chapter 3. The best performing cost function is used to produce the first DIET multi-frequency reconstructions on phantom data in section 5.2.

5.1 Multi-Frequency Cost Function Comparison

The magnitude of the cost, Φ, from each frequency will vary due to several factors. Frequencies where more data points were tracked will have a higher total cost, equally frequencies which produce larger motions will have larger costs. If these factors are not accounted for, these frequencies will have a greater influence on a multi-frequency optimization process. Figure 5.2 shows the relative size of the costs, Φ, from each frequency for a collection of inclusion location models, $\theta(x_c, y_c, z_c)$, with $R = 5$ mm, $E'_I = 30$ kPa and $\zeta_I = 10\%$, throughout the parameter space for phantom Tr10. Note the difference in cost between 16 Hz and 18 Hz data. If these two costs were simply summed without some normalization or other weighting process, the 18 Hz data would dominate the combined cost function.

In this work, two methods of producing a combined cost function have been investigated: ranking and normalizing. These two methods were compared on a reconstruction for phantom Tr10 using multi-frequency data. Ranked cost, AC, was calculated using Eq. 3.33, while the combined normalized cost, Φ^C, was calculated using Eq. 3.35. The costs were compared using

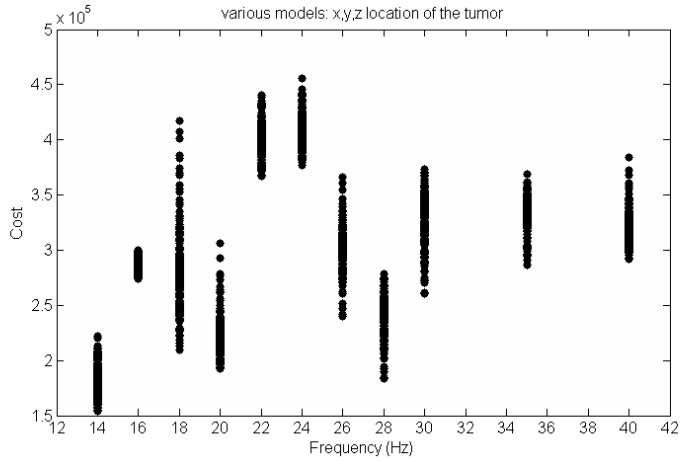

Figure 5.2: Relative size of the cost, Φ, from each frequency for phantom Tr10. The plot shows the spread of cost Φ for a collection of models for each frequency. The models are tumor locations in the parameter space.

phantom Tr10 data over the frequency range 10 to 40 Hz.

Figure 5.3 shows the cost surface for an inclusion location reconstruction of phantom Tr10 using AC as the cost. The slice is at z = 30 mm, the true z location of the inclusion. The AC cost surface provides little to no information on the location of the inclusion. Model ranking was used to eliminate the need to normalize data across the frequencies. The total cost for a model is simply the sum of its rank from each frequency. The use of ranking is thus equivalent to weighting each frequency equally. This may be why ranked cost is performing poorly in DIET. For example, data with poor coverage or low signal to noise may rank poor models highly simply because the data is insufficient to discount poor solutions. These models then get the same rank as well-fitting models from a higher quality dataset, which causes the cost surface to perform poorly. In contrast, the combined normalized cost function Φ^C performs much better. Figure 5.4 shows the cost surface at z = 30 mm for Φ^C. The true center of the inclusion is located at $(0, -20, 30)$. Φ^C puts the minimum in the correct location in parameter space, thus Φ^C was selected as the multi-frequency cost function.

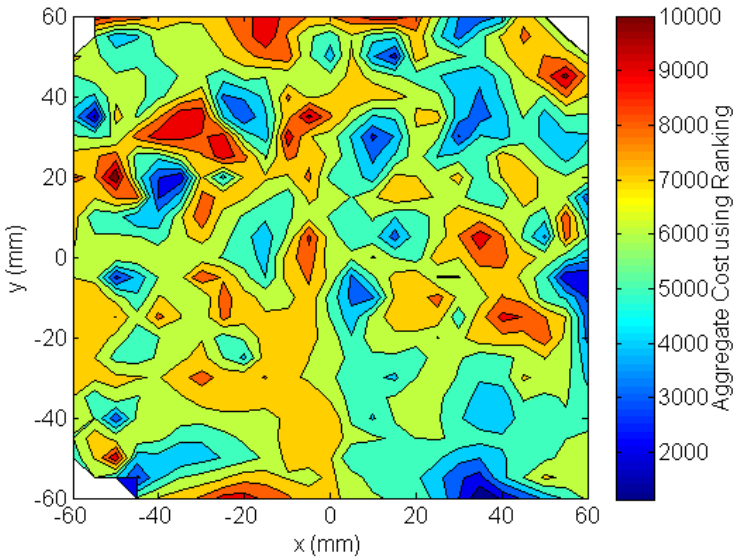

Figure 5.3: Slice through ranked cost (AC) surface for inclusion location for phantom Tr10 at z = 30 mm.

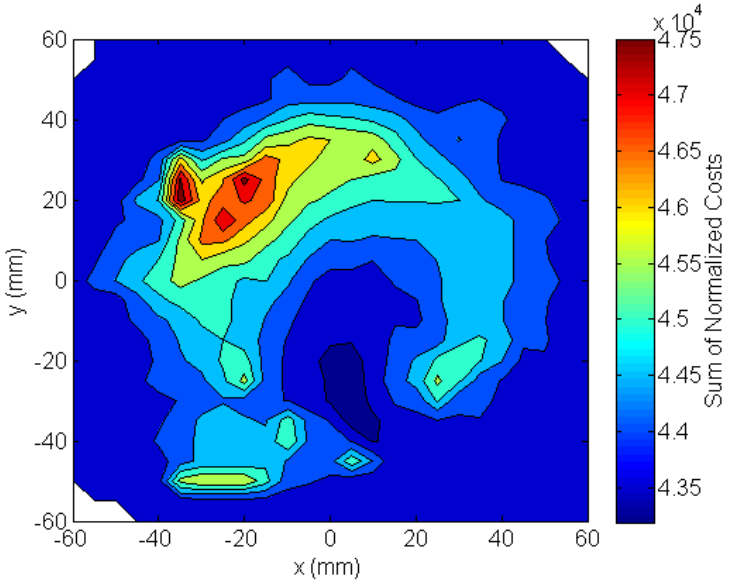

Figure 5.4: Slice through combined normalized cost (Φ^C) inclusion location surface for phantom Tr10 at z = 30 mm.

5.2 Multi-Frequency Phantom Reconstructions

The aim of this experiment is to apply the combined cost function for location optimization (Φ^C) to phantoms H, Tr10, and Tr5. There are several desired outcomes that would indicate success for the reconstruction algorithm over the single frequency reconstructions shown in Chapter 4. The 'healthy' phantom should produce a more homogeneous result, the reconstruction for phantom Tr5 needs to overcome the poor meshing at 26 Hz, and the reconstruction for phantom Tr10 must still locate the inclusion correctly. The parallel algorithm described in section 3.7.3 was modified to calculate the forward solution (FE calculation) for multiple frequencies. The background material properties, E'_B and ζ_B, were optimized for each frequency individually, then the optimal values were used in the location optimization across all frequencies.

5.2.1 Data Quality Metrics

The data quality metrics of mean displacement (μ_A), signal to noise ratio ($\overline{SNR}$) and coverage (χ) were calculated for each of the phantoms using Eqs. 3.29 to 3.32. Figure 5.5 shows the mean displacement for each frequency for the phantoms. The resonance peaks are clearly visible at approximately 16 Hz and 27 Hz for each of the three phantoms.

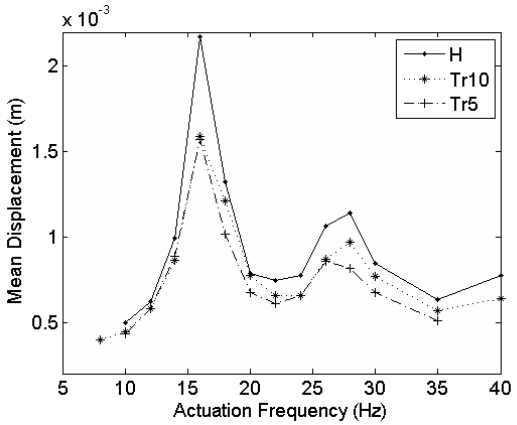

Figure 5.5: Mean measured displacement versus frequency.

Figure 5.6 shows the mean signal to noise ratio, $\overline{SNR}$ for the three phantoms. The $\overline{SNR}$ does not drop at the first resonance peak, indicating that even though the measured displacements are larger than the non-resonant frequencies the motion can be described sufficiently by Eq. 3.7, *i.e.* each fiducial follows an elliptical path. The correlation coefficient and corresponding *p value* between μ_A and $\overline{SNR}$ for each phantom is given in Table 5.1. The correlations for phantom H and Tr5 are not statistically significant using a two-tailed student's t-test, and the correlation for

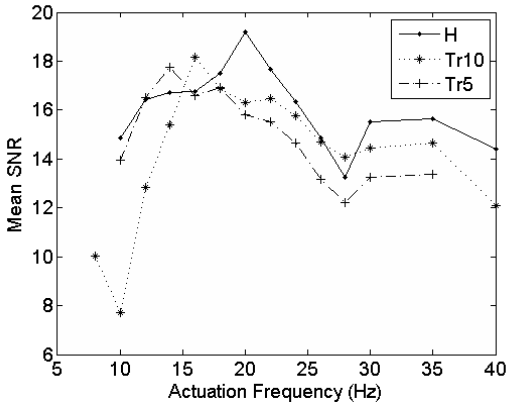

Figure 5.6: Mean signal to noise ratio versus frequency.

phantom Tr10 in fact shows a positive, statistically significant correlation between μ_A and $\overline{SNR}$. The larger motion occurring at the resonance peaks is thus not having a negative effect on $\overline{SNR}$.

Figure 5.7 shows the coverage, χ, for the three phantoms where a significant drop at the first resonant frequency 16 Hz is evident. There is also a smaller drop in χ at the second resonance peak of 27 Hz. Note that there is an inverse correlation between μ_A and χ. The correlation coefficients and corresponding *p values* are given in Table 5.1. Testing the correlations for statistical significance using a one-tailed student's t-test with a null hypothesis that the correlation is equal to zero, these correlations are all statistically significant with *p values* well below the $p = 0.05$ confidence threshold. This correlation is a consequence of the movement of fiducials becoming too large to be tracked successfully between frames [63] [118] as the actuation frequency approaches resonance. To provide a visual representation of percentage coverage, Figure 5.8 illustrates the coverage at two frequencies for phantom H.

	μ_A, $\overline{SNR}$		μ_A, χ	
Phantom	**R**	***p value***	**R**	***p value***
H	0.3884	0.8	-0.94	0.000002
Tr5	0.389	0.2	-0.90	0.00006
Tr10	0.7178	0.004	-0.89	0.00002

Table 5.1: Correlation coefficient (R) and corresponding *p value* for mean displacement(μ_A) and mean signal to noise ($\overline{SNR}$), and mean displacement and coverage (χ).

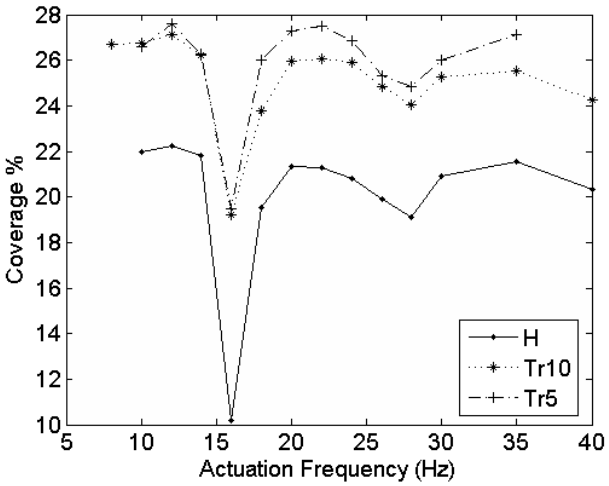

Figure 5.7: Coverage versus frequency.

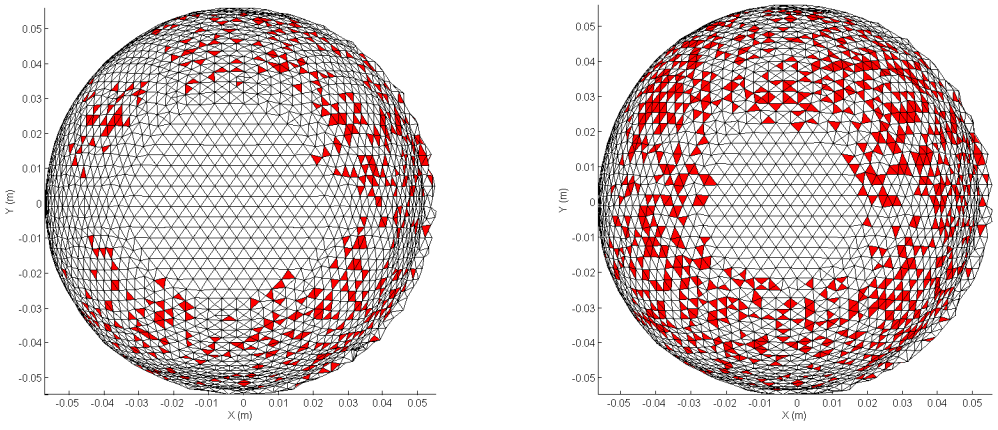

(a) Poor coverage at 16 Hz. 11% of surface elements covered.

(b) Better coverage at 18 Hz. 24% of surface elements covered.

Figure 5.8: An example of poor surface coverage compared to an example of better surface coverage to provide a visual representation of percentage coverage (χ). The surface elements colored red have one or more tracked fiducials associated with them. The data are from Phantom H.

5.2.2 Results

To visualize the results of the reconstructions the 25 kPa contour of the average E' over the optimal region is used. For qualitative description of the multi-frequency results, the volume difference, V_{frac} and the distance from the centroid of the reconstructed inclusion location to the true inclusion location, δ_c are calculated using Eqs. 3.53 and 3.56 for the $E' = 25$ kPa contour and summarized in Table 5.2. Single frequency reconstructions were performed on the individual frequency datasets to allow comparison with the multi frequency reconstructions.

Phantom	**Volume Fraction, $\mathbf{V}_{frac}$**	**Centroid Difference, δ_c (mm)**
Tr10 (all frequencies)	0.22	12
Tr5 (all frequencies)	1.96	24
Tr5 (selected frequencies)	1.83	19

Table 5.2: Quantitative description of the optimal region, where *Volume Fraction* is the volume of the 25 kPa contour divided by the volume of the true inclusion, and the *Centroid Distance* is the distance between the centroid of the credible region and the centroid of the inclusion. Note phantom H is not listed as the inclusion volume is zero and the inclusion location is undefined.

Phantom H

The multi-frequency reconstruction for phantom H, given in Figure 5.9 is a successful reconstruction result. The reconstruction is homogeneous, with only some stiff areas on the surface of the mesh where the edge of the inclusion touches the surface of the breast. This is the same effect described in section 4.5 and is due to the inclusion being allowed to move outside the breast to produce homogeneous reconstructions. Examining the individual frequency optimal regions in Figure 5.10 highlights the low sensitivity of the cost function to inclusions deep in the center of the phantom. Figure 5.10a and Figures 5.10c to 5.10f show selected single frequency reconstructions which produce an inclusion within the central column of the breast phantom. This is a red flag for the DIET reconstruction as individual frequency results would show an inclusion. By combining the information from all frequencies, the false minimums are counterbalanced.

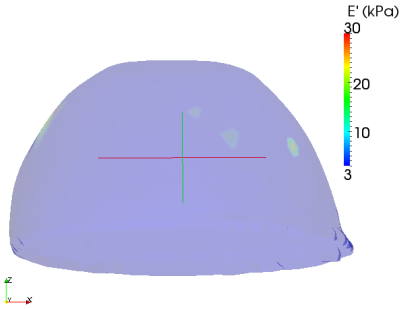

Figure 5.9: Optimal region reconstruction result using all frequencies for phantom H. The contour is $E' = 25$ kPa.

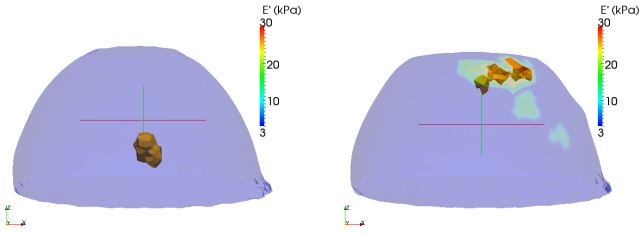

(a) 10Hz (b) 16Hz

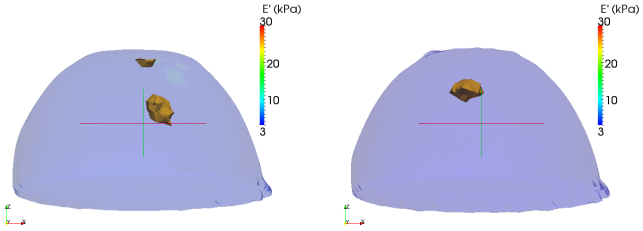

(c) 20Hz (d) 24Hz

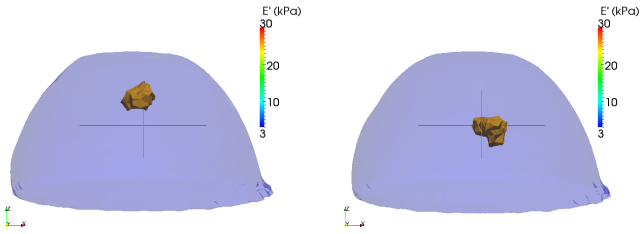

(e) 28Hz (f) 35Hz

Figure 5.10: A selection of individual frequency reconstruction results for phantom H. The contour is $E' = 25$ kPa.

Phantom Tr10

The multi frequency reconstruction for phantom Tr10 is given in Figure 5.11. The result is successful, identifying an inclusion in the correct area of the phantom, although not completely co-incidental with a centroid difference of 12 mm. Figures 5.12a to 5.12f show selected individual frequency reconstructions across the frequency range. Most of these reconstructions locate the inclusion very close to the true location. Even less successful reconstructions, such as the 16 Hz result shown in Figure 5.12b place the inclusion in the correct quadrant of the breast.

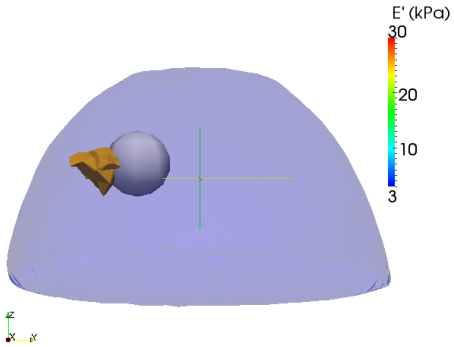

Figure 5.11: Reconstruction result using all frequencies for phantom Tr10. The contour is $E' = 25$ kPa. The true inclusion is shown in grey.

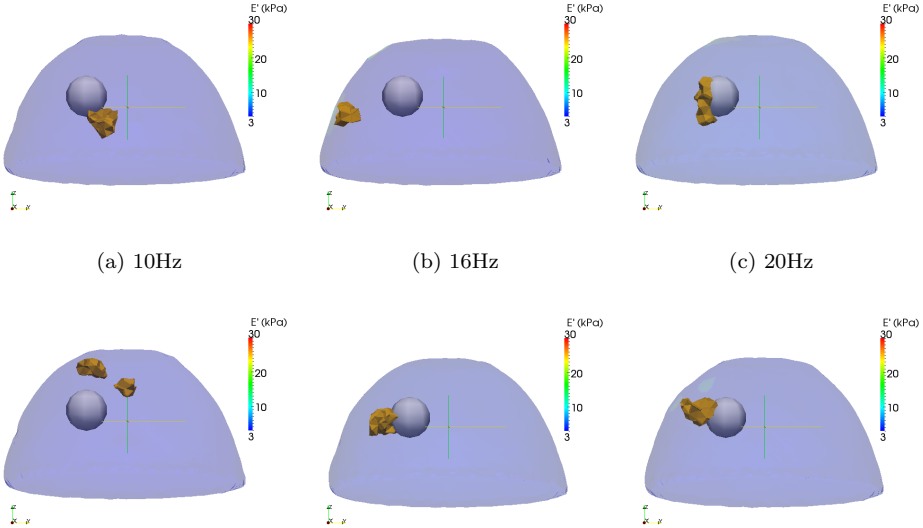

(a) 10Hz (b) 16Hz (c) 20Hz

(d) 24Hz (e) 28Hz (f) 35Hz

Figure 5.12: A selection of individual frequency reconstruction results for phantom Tr10. The contour is $E' = 25$ kPa. The true inclusion is shown in grey.

Phantom Tr5

The multi-frequency reconstruction result for phantom Tr5 is given in Figure 5.13 and is the least successful reconstruction, with the reconstructed inclusion location placed 22 mm from the true location. The single frequency results given in Figures 5.14a-5.14f show mixed results. Common to a majority of the results is placing the inclusion location close to the location of the actuator. Selecting frequencies 18-35 Hz, which lie after the first resonance peak improves the multi-frequency reconstruction producing the results given in Figure 5.15 and reduces δ_c from 24 mm to 19 mm. However, the misshapen meshing seen in Chapter 4 in the 26 Hz data where the actuator makes contact with the breast phantom can also be clearly seen in Figures 5.14a, 5.14d and 5.14f, which indicates that the high motion at the resonance peaks is not the sole cause of the poorly tracked points.

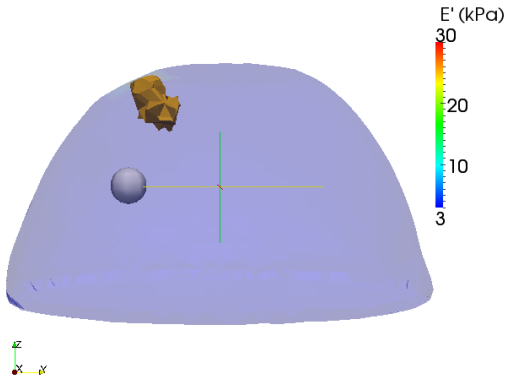

Figure 5.13: Reconstruction result using all frequencies for phantom Tr5. The contour is $E' = 25$ kPa. The true inclusion is shown in grey.

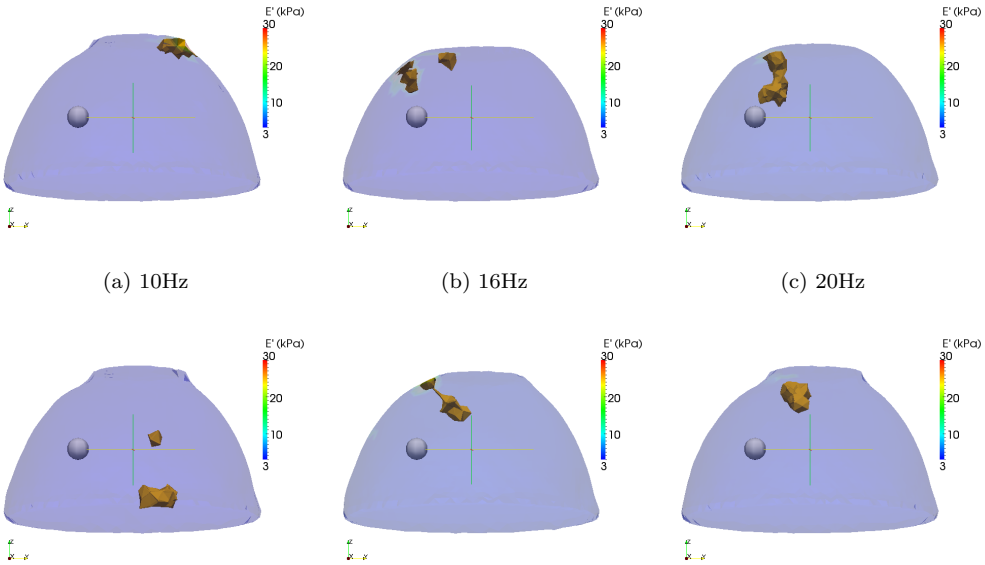

(a) 10Hz (b) 16Hz (c) 20Hz

(d) 24Hz (e) 28Hz (f) 35Hz

Figure 5.14: A selection of individual frequency reconstruction results for phantom Tr5. The contour is $E' = 25$ kPa. The true inclusion is shown in grey.

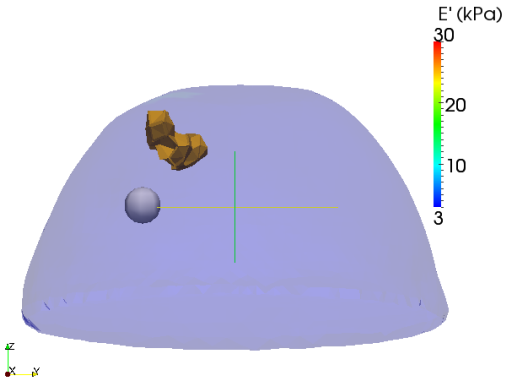

Figure 5.15: Reconstruction result using selected frequencies (18 Hz-35 Hz) for phantom Tr5. The contour is $E' = 25$ kPa. The true inclusion is shown in grey.

5.3 Single Frequency versus Multi-Frequency Reconstructions

There are two aspects to consider in the use of single frequency versus multi-frequency reconstructions: the quality of the reconstruction and the computational expense of achieving said reconstruction. The quality of the reconstruction is assessed by comparing the distance between the reconstructed inclusion location, X_R, and the actual inclusion location X_I. The computational expense is assessed by the number of model evaluations, ME, and the number of FE calculations executed during the reconstruction. For multi-frequency reconstructions multiple FE calculations are required for a single model evaluation because each frequency requires its own FE simulation.

The distance, D, between the true location of the inclusion, X_I, and the reconstructed inclusion location, X_R, is calculated by

$$D = |X_I - X_R|. \tag{5.1}$$

5.3.1 Results

ME and D for each of the single frequency reconstructions is given in Table 5.3. The mean and standard deviation of ME and D for the single frequency reconstructions is given in Table 5.4. Table 5.5 gives ME and D and the number of FE calculations for the multi-frequency reconstructions.

Frequency	H	Tr10		Tr5	
	ME	ME	D (mm)	ME	D (mm)
10	1135	943	15	1004	55
12	964	261	12	1095	22
14	1381	309	15	2575	36
16	1107	835	27	2085	22
18	488	373	17	534	24
20	1074	520	7	842	26
22	828	730	8	945	28
24	993	1214	21	324	47
26	1970	722	11	591	25
28	2647	798	11	1940	25
30	909	695	11	1185	26
35	924	575	12	1045	32
40	1658	601	16	-	-

Table 5.3: Number of model evaluations, ME, for each single frequency reconstruction. The distance, D, between the optimum solution found by the algorithm and the true inclusion location is given for phantoms Tr5 and Tr10.

Phantom	ME		D (mm)	
	Mean	STD	Mean	STD
H	1236.77	566.06	-	-
Tr10	659.69	264.85	14.27	5.42
Tr5	1180.50	678.56	31.50	10.29
Tr5 (selected frequencies)	925.88	499.28	29.57	7.60

Table 5.4: Mean and standard deviation of ME and D for the single frequency reconstructions for each phantom.

Phantom	ME	D (mm)	FE calculations
H	947	-	12 311
Tr10	737	12	9321
Tr5 (all frequencies)	705	24	8460
Tr5 (selected frequencies)	611	19	4888

Table 5.5: ME, D and the number of FE calculations for the multi-frequency reconstructions.

5.3.2 Discussion

For the single frequency reconstructions the inclusions were located with varying success across the frequency range. The largest D for phantom Tr10 occurs at the first resonance peak of 16 Hz. The large motion at the first resonance peak is the likely cause of this less successful reconstruction. However, the second resonance peak at 27 Hz has not had a negative effect on inclusion location for this phantom. The reconstructions at 26 Hz and 28 hz both produced $D = 11$ mm, which is below the mean D result. As shown in Figure 5.5, the first resonance peak is 1.5 to 2 times bigger than the second resonance peak and is thus having a greater effect on the quality of the reconstructions.

The single frequency results for phantom Tr5 exhibit a greater spread of D than those of phantom Tr10, with a standard deviation of 10.29 compared to 5.42 for phantom Tr10. In contrast to phantom Tr10, the reconstruction at the first resonance peak at 16 Hz produced the smallest value of D for phantom Tr5. The largest value of D is found at 10 Hz. This frequency is not associated with any resonance peak, which suggests that it is not simply large motions at resonance that is affecting the reconstructions. The failed reconstruction using 10 Hz data as can be seen in Figure 5.14a. The inclusion is placed at the actuator contact at the opposite side of the phantom to the inclusion. Certainly the 10 Hz data requires additional frequencies to produce a successful reconstruction. As shown in Figure 5.5, 10 Hz has the lowest displacement of all the frequencies. Any error due to motion tracking, particularly at the actuator contact as has occurred with phantom Tr5, could be assumed to be frequency independent. It would thus have a relatively larger effect on datasets with smaller displacements. This may be why the 10 Hz reconstruction produced the worst result of all the frequencies and put the inclusion at the actuator contact.

The multi-frequency reconstruction for phantom Tr10 produced a D of 12 mm, which is 2 mm smaller than the mean D of the single frequency reconstructions. The multi-frequency D for phantom Tr5 (all frequencies) is 6.5 mm smaller than the mean single frequency result. The selected frequency (18-35 Hz) result for phantom Tr5 is 12.5 mm smaller than the mean for the corresponding single frequency results. The multi-frequency reconstructions are thus performing better than their single frequency counterparts on average. This is an encouraging result for DIET as it demonstrates that the multi-frequency cost, Φ^C, can be used to overcome shortcomings in individual frequency datasets.

For phantom Tr5 the multi-frequency D is better than all the single frequency reconstructions and for phantom H, the multi-frequency reconstructions is homogeneous. However, the

multi-frequency D for phantom Tr10 is larger than or equal to 7 out of the 13 single frequency reconstructions. The multi-frequency approach is thus not necessarily an improvement over a given single frequency result, but has provided a better than average result for the phantoms in this study.

The single frequency results for phantom H and Tr5 had a greater spread in ME than phantom Tr10 with standard deviations of 566 and 678 for phantoms H and Tr5 respectively, compared to 264 for phantom Tr10. This may be because phantom Tr10 has a large inclusion that is identifiable across all frequencies. The number of model evaluations for the multi-frequency reconstructions is on a par with the single frequency reconstructions. The mean of ME of the single frequency reconstructions range from 660 for phantom Tr10 to 1236 for phantom H. The ME of the multi-frequency reconstructions range from 611 for phantom Tr5 (selected frequencies) to 947 for phantom H. The use of multi-frequency data has not lead to a large reduction in the number of model evaluations.

Although the multi-frequency reconstructions required a similar number of model evaluations, each model evaluation requires an FE calculation for each frequency. Compared to the mean single frequency computational cost, there was a 10 fold increase for phantom H (*13 frequencies*), a 14 fold increase for phantom Tr10 (*13 frequencies*), a 7 fold increase for phantom Tr5 (*all 12 frequencies*) and a 5 fold increase for phantom Tr5 (*selected 8 frequencies*). The better than average reconstructions have been achieved at an increase in computational expense of approximately n times the mean single frequency ME, where n is the number of frequencies used in the reconstruction. Interestingly, phantom Tr10, which had the best performing single frequency reconstructions on average, exhibits the largest increase in computational expense for the multi-frequency reconstructions. This could be because the single frequency reconstructions for this phantom are successful across the range of frequencies used. Thus, a single frequency cost Φ is as effective as the multi-frequency cost Φ^C and so the increase in computational expense when using multi-frequency data is approximately n times the mean single frequency cost.

5.4 Discussion and Conclusions

The comparison of ranked cost (AC) versus combined normalized cost (Φ^C) clearly indicated that AC was not suitable for the DIET reconstruction algorithm. Ranked cost as part of a more complex cost function has been used with success in other work. For example, Zhang *et al.* have had success using a ranking scheme to incorporate qualitative prior information into their cost

function for a 2D simulated inverse elasticity problem [81]. In this study, ranked cost surfaces offer little information to solve the inverse problem. A much more successful approach for DIET is to normalize the cost for each frequency and then sum them together to get a combined cost function, Φ^C.

Evaluation of the data coverage shows the need to apply fiducials to every area of the breast. For example, the 18 Hz data for phantom H as illustrated in Figure 5.8b has $\chi = 24\%$, *i.e.* only 24% of surface elements have a measurement associated with them. This is before any reduction in coverage that would occur with other frequencies closer to the resonance peak, due to the associated large motion between successive images. To acquire motion data with the current DIET imaging processing algorithm requires the application of colored fiducials to the breast surface. It is envisaged that motion tracking of natural features on the skin will become part of the DIET image processing algorithm [119]. This would allow a more complete surface motion dataset to be produced by providing information between the locations of the applied fiducial markers. Skin-feature tracking may even be sufficient to provide motion data without the need to apply fiducial markers. The drop in surface coverage at the resonance peaks could be mitigated by calculating data quality metrics in real time during data collection. Frequencies exhibiting reduced coverage could be identified and the actuation frequency adjusted accordingly to avoid resonance.

The reconstruction of Phantom Tr10 was successful, with a centroid difference of 12 mm from the true inclusion location. Although this was no improvement on the 26 Hz reconstruction of Chapter 4, which also gave a centroid difference of 12 mm, the use of multi-frequency data did not negatively impact the reconstruction. The multi-frequency reconstruction for phantom H is an improvement on the single frequency reconstruction, as it produced a homogeneous result. There are some stiff surface elements that can be seen in Figure 5.9, but no stiff elements within the breast volume. The problem was posed as locating a 5 mm radius inclusion within the parameter space, thus in interpreting the homogeneous result, one cannot exclude the possibility of smaller inclusions within the breast volume. The choice of *a priori* inclusion radius will depend upon two factors for the eventual clinical application of the DIET system: the minimum breast mass size that needs to be identified in a pre-screening method, and the smallest inclusion that can be excluded in practice with the DIET system. At this stage in the development of DIET, the exclusion of a 5 mm radius inclusion in the homogeneous case is a positive result. The reconstruction result for phantom Tr5 demonstrates that collecting a frequency sweep of data provides a more robust

dataset for solving the inverse problem, as troublesome frequencies can be discarded. However, these results also show that even with phantom data, which is undoubtedly less complex than *in vivo* data due to external effects such as patient movement, poor $\overline{SNR}$ and poor meshing have the potential to hinder the reconstruction algorithm.

Chapter 6

Ellipsoidal and Multiple Inclusions

In the reconstructions presented so far, all inclusions have been assumed to be spherical. Any reconstruction has solved for a single inclusion within the breast volume. Two modifications are made to the algorithm in this analysis: the inclusion is allowed to be ellipsoidal, and the algorithm is modified to solve for multiple inclusions. At first glance, this may seem like a small increase in the number of parameters used to describe the inclusion, but allowing the inclusion to be ellipsoidal gives 1×10^{11} possible models for inclusion shape and location. This calculation is based on inclusions spaced every 5 mm in the parameter space, and the constraints of the ellipsoid equal to those given in Table 6.1. A numerical study is performed to asses the capability of the algorithm with ellipsoidal and multiple inclusions. The *a priori* fixed radius inclusion assumption is also applied to these cases. These assumptions are then employed in reconstructions on a phantom containing two 'cancerous' inclusions. Based on the synthetic data and phantom reconstruction results, a phantom containing multiple inclusions is created, with one of the inclusions representing cancer. A positive result for the reconstruction algorithm would be to identify the *cancerous* inclusion amongst the non-homogeneous background.

6.1 Synthetic Data Study

The aim of this study is to test the performance of the reconstruction algorithm, so it is critical not to commit the inverse crime of using the same method to solve the forward problem in both the creation of synthetic data and the reconstruction. The strategy used here is to create the 'data' using a 2 mm linear tetrahedral mesh, and to solve the forward problem for the reconstruction on a 3 mm linear tetrahedral mesh.

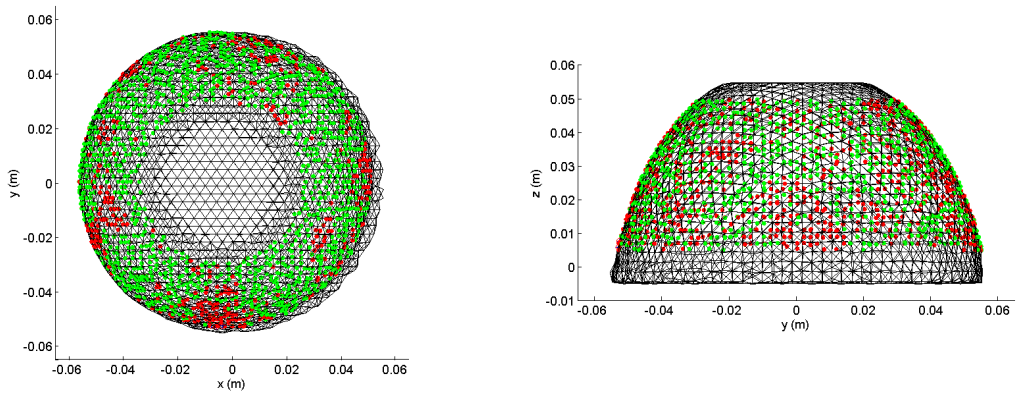

(a) Top view of synthetic data locations on the mesh. (b) Side view of synthetic data locations on the mesh.

Figure 6.1: Synthetic data projected onto the 3 mm mesh. The green dots are the 3D locations of the data, the red dots are the projection onto the mesh. Note the visibility of red or green dots in the plot is due to the data point being located just outside or just inside the surface of the mesh. There are no data where the actuator would make contact with the breast, nor at the 'chest wall'.

To create the synthetic data, a 2 mm mesh was created from the point cloud of phantom H 26 Hz data. The forward problem was solved to give the displacement at every node. Gaussian random noise with a mean of zero and a standard deviation of 5% of the RMS displacement was added to the motion. Only the nodes on the surface and visible to the cameras are used to create the 'data'. Half the nodes were removed from the data set to give 1500 fiducials, comparable to the phantom datasets used in previous chapters. To mimic the data projection, the 2 mm data is projected onto a 3 mm mesh created from a phantom H data set. The location of the synthetic data is shown in Figure 6.1. The motion and projection information comprise the synthetic data. The FE calculations used in the reconstructions were evaluated on the 3 mm mesh.

6.1.1 Experimental Setup

Two synthetic data sets were created to test the algorithm using an actuation frequency of 26 Hz and an amplitude of 0.5 mm. Dataset A was a single ellipsoidal inclusion, shown in Figure 6.2a. Dataset B contained two inclusions, shown in Figure 6.2b. The background material properties were a storage modulus of 3.4 kPa and a damping parameter of 4% for both datasets. The inclusion E' was set equal to 27 kPa, to mimic the phantoms used in Chapter 4. Because generating the data did not involve fitting of an ellipse to fiducials, the cost function used was Φ^{SQ}, as defined in Eq. 3.22 in Chapter 3. The model θ comprises the background material properties and the inclusion shape and material properties,

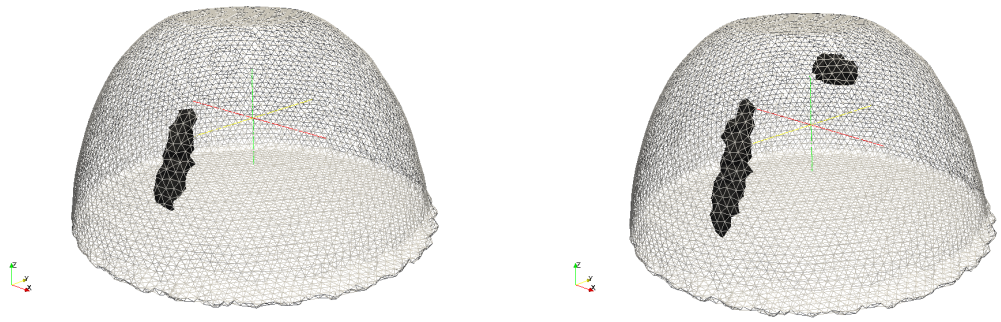

(a) Dataset A: Single ellipsoidal inclusion (b) Dataset B: Two inclusions

Figure 6.2: Inclusion locations for the two synthetic datasets.

$$\theta(E'_B, \zeta_B, v_1, v_2, v_3, x_c, y_c, z_c, \alpha, \beta, \gamma, E'_I, \zeta_I). \tag{6.1}$$

Four experiments were run to test the potential of the algorithm with more complex inclusions than the single spherical inclusions used in Chapter 4. In addition, two experiments using the *a priori* inclusion assumptions from Chapter 4 were applied to the synthetic data. As in previous experiments, there were two steps to optimization; background material properties were solved for, then inclusion properties. An initial population of 128 chromosomes was used and the experiments were limited to 50 generations. Experiment 3 was then run again with a limit of 500 generations.

Experiment 1: Using data set A, solve for one ellipsoidal inclusion.

Experiment 2: Using data set B, solve for one ellipsoidal inclusion.

Experiment 3: Using data set A, solve for two ellipsoidal inclusions.

Experiment 4: Using data set B, solve for two ellipsoidal inclusions.

Experiment 5: Using data set A, solve for a spherical inclusion with $R = 5$ mm.

Experiment 6: Using data set B, solve for a spherical inclusion with $R = 5$ mm.

Experiments 1 and 2 were designed to test if an ellipsoidal inclusion could be successfully reconstructed. Obviously, in a clinical setting it is not known whether there are single, multiple, or no masses present in a breast. Experiments 3 and 4 are to test the assumption of two ellipsoidal inclusions. Experiment 3 was designed to test whether one sole inclusion could be successfully located if the problem was posed as locating two inclusions. Experiment 4 was designed to test if two inclusions could be successfully reconstructed. The constraints on the ellipsoids were the

Parameter		Lower constraint	Upper constraint	Increment
Background $E'(kPa)$		1	5	0.1
Background $\zeta(\%)$		1	10	1
Ellipsoid Center	$x(mm)$	-60	60	5
	$y(mm)$	-60	60	5
	$z(mm)$	0	60	5
Ellipsoid Axes	$v_1(mm)$	1	15	1
	$v_2(mm)$	1	15	1
	$v_3(mm)$	1	15	1
Ellipsoid Rotation	$\alpha(degrees)$	0	180	10
	$\beta(degrees)$	0	180	10
	$\gamma(degrees)$	0	180	10
Inclusion $E'(kPa)$		Fixed at 30 kPa		
Inclusion $\zeta(\%)$		Fixed at 10%		

Table 6.1: Constraints on the reconstructed parameters for Experiments 1-3.

same for Experiments 1 to 4 and are given in Table 6.1. The constraints for Experiments 4 and 5 are the same as used in Chapter 4, given in Table 4.2, with the $E'_I = 30$ kPa and $\zeta_I = 10\%$.

6.1.2 Results

The results displayed are the optimum location parameter values found using the reconstruction algorithm. The reconstructed background material properties were 3.5 kPa and 5% damping for both dataset A and B. The true values were 3.4 kPa and 4% damping. The inclusions had little effect on the background material property reconstruction. The center and volume of the inclusions were used to compare the reconstructions with the true inclusions. For inclusions completely within the mesh, the volume of the inclusion was simply the volume of the ellipsoid, V, where

$$V = \frac{4}{3}\Pi abc \tag{6.2}$$

where a, b, c are the lengths of the three principle axes of the ellipsoid. The results of each experiment are given in the following sections, with a summary of the success of the reconstructions given in Table 6.2. The computational expense for each reconstruction, *i.e.* the number of models evaluated, is given in Table 6.3.

Experiment 1: *Dataset A using one ellipsoidal inclusion*

Figure 6.3 shows the true inclusion location together with the reconstructed location for Experiment 1. The reconstruction is a good location match for the inclusion, and a good match for inclusion shape with the reconstructed inclusion similarly elongated as the true inclusion. The reconstructed inclusion is closer to the surface of the breast than the true location and the angle of the inclusion is not quite correct. The reconstructed inclusion center of $(0, -40, 15)$ is 11 mm away from the true inclusion center of $(0, -30, 20)$. The volume of the reconstructed ellipsoid is 1885 mm^3 compared with 1571 mm^3 for the true volume, thus overestimating the inclusion volume by 19%.

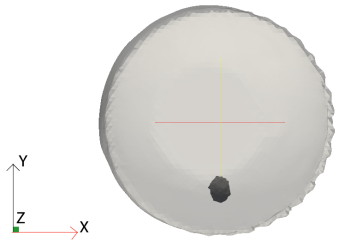

(a) True location, top view.

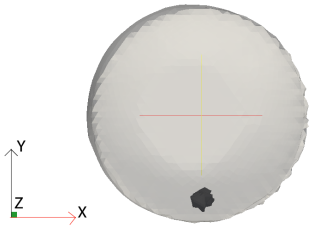

(b) Reconstructed location, top view.

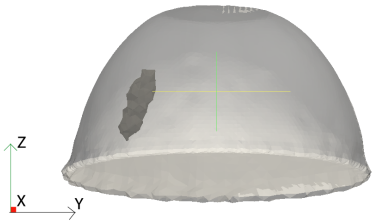

(c) True location, side view.

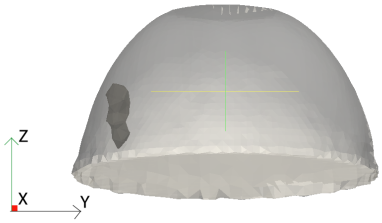

(d) Reconstructed location, side view.

Figure 6.3: Various views of the true location and reconstructed location of the inclusion for Experiment 1. Solving for one ellipsoidal inclusion with 128 chromosomes in the population and the algorithm limited to 50 generations.

Experiment 2: *Dataset B using one ellipsoidal inclusion*

Figure 6.4 shows the true and reconstructed location of the inclusion for Experiment 2. The reconstructed inclusion is located at $(0, -35, 20)$, only 5 mm away from the actual location of the larger inclusion at $(0, -30, 20)$. The volume of the reconstructed inclusion is 900 mm^2, which is 42% of the true inclusion volume of 2094 mm^2. The reconstructed inclusion is elongated in two dimensions, compared to the elongation in one dimension of the true inclusion. The side view of the reconstruction in Figure 6.4d shows that the angle of the inclusion has not matched that of the true inclusion, shown in Figure 6.4c.

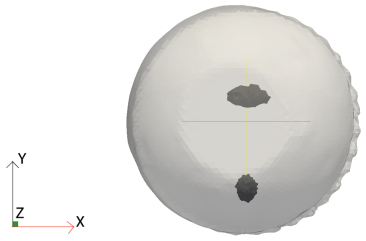

(a) True location, top view.

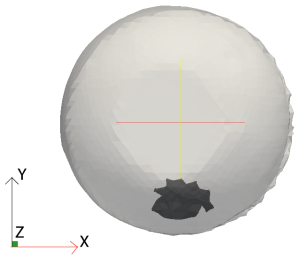

(b) Reconstructed location.

(c) True location, side view.

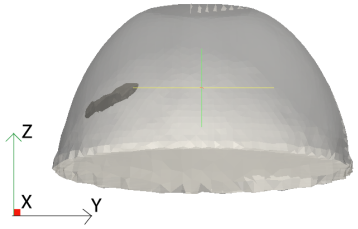

(d) Reconstructed location, side view.

Figure 6.4: Various views of the true location and reconstructed location of the inclusions for Experiment 2. Solving for one ellipsoidal inclusion with 128 chromosomes in the population and the algorithm limited to 50 generations.

Experiment 3: *Dataset A using two ellipsoidal inclusions*

Figure 6.5 shows the true and reconstructed location of the inclusion for Experiment 3. The reconstruction is not as successful as the results of Experiment 1 in terms of reconstruction inclusion shape. One inclusion is placed at $(0 - 30, 25)$, 5 mm away from the true inclusion location of $(0, -30, 20)$. but is not as good a match for the shape of the inclusion, with a volume of of 1005 mm^3, 64% of the true inclusion volume. The second inclusion is pushed up towards the actuator leaving stiff surface nodes, rather than completely out of the breast. For an ideal reconstruction, the second inclusion would be entirely outside the breast.

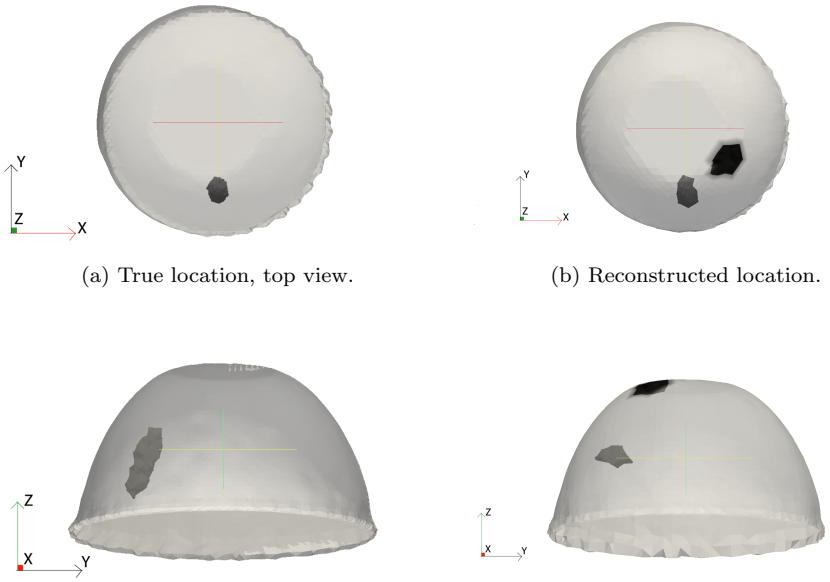

(a) True location, top view.

(b) Reconstructed location.

(c) True location, side view.

(d) Reconstructed location, side view.

Figure 6.5: Various views of the true location and reconstructed location of the inclusions for Experiment 3. Solving for two ellipsoidal inclusions with 128 chromosomes in the population and the algorithm limited to 50 generations.

Experiment 4: *Dataset B using two ellipsoidal inclusions*

Figure 6.6 shows the true location and reconstructed location of the inclusion for Experiment 4 after 50 generations. The reconstructed location of $(0, -30, 25)$ for the larger inclusion is a good match for location, 5 mm away from the true location of $(0, -30, 20)$, but not for inclusion shape. The reconstructed inclusion does not have the same elongation of the true inclusion, but the volumes are comparable, with a difference of 2% of the true volume. The true volume is 2094 mm^3, the reconstructed volume is 2052 mm^3. The smaller inclusion at $(0, 10, 40)$ is not identified in the reconstruction. Figure 6.7 shows the reconstructed location for Experiment 4 after 500 generations. The larger inclusion is still dominating the reconstruction. The reconstructed inclusion centroid is still at $(0, -30, 25)$, a good match for location, but the reconstructed volume is 1047 mm^3, 50% of the true inclusion volume.

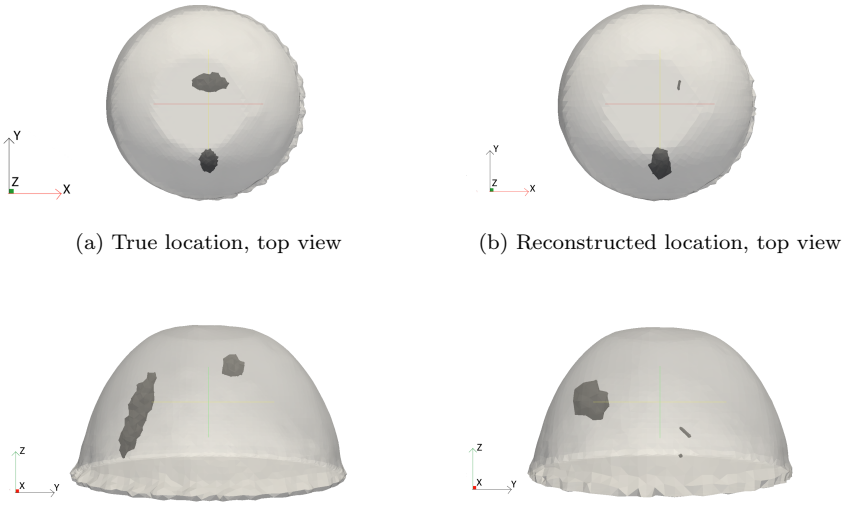

(a) True location, top view

(b) Reconstructed location, top view

(c) True location, side view

(d) Reconstructed location, side view

Figure 6.6: Various views of the true location and reconstructed location for Experiment 4. Solving for two ellipsoidal inclusions with 128 chromosomes in the population and the algorithm limited to 50 generations.

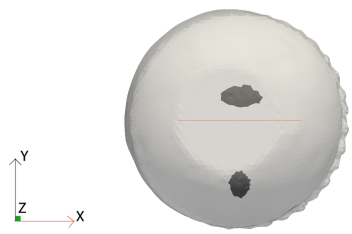

(a) True location, top view

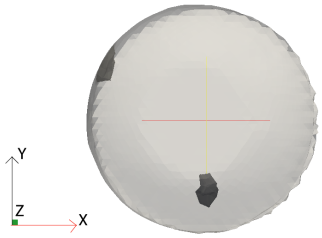

(b) Reconstructed location, top view

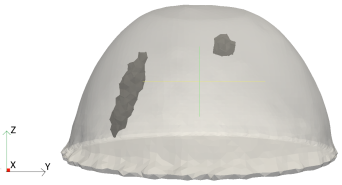

(c) True location, side view

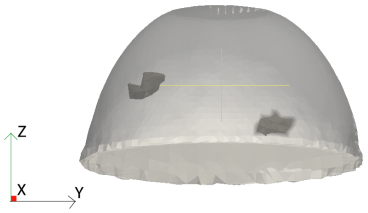

(d) Reconstructed location, side view

Figure 6.7: Various views of the true location and reconstructed location for Experiment 4 after 500 generations. Solving for two ellipsoidal inclusions with 128 chromosomes in the population and the algorithm limited to 500 generations.

Experiment 5: *Dataset A using a spherical inclusion*

Figure 6.8 shows the true location and reconstructed location for Experiment 5. Even with an *a priori* inclusion geometry that does not match the elongation of the true inclusion, the centroid of the reconstructed location, $(0, -30, 25)$, is only 5 mm away the true location. The reconstructed centroid for the spherical inclusions is 6 mm closer than the reconstructed ellipsoidal inclusion centroid of Experiment 1 and coincides with the reconstructed centroid of Experiment 3.

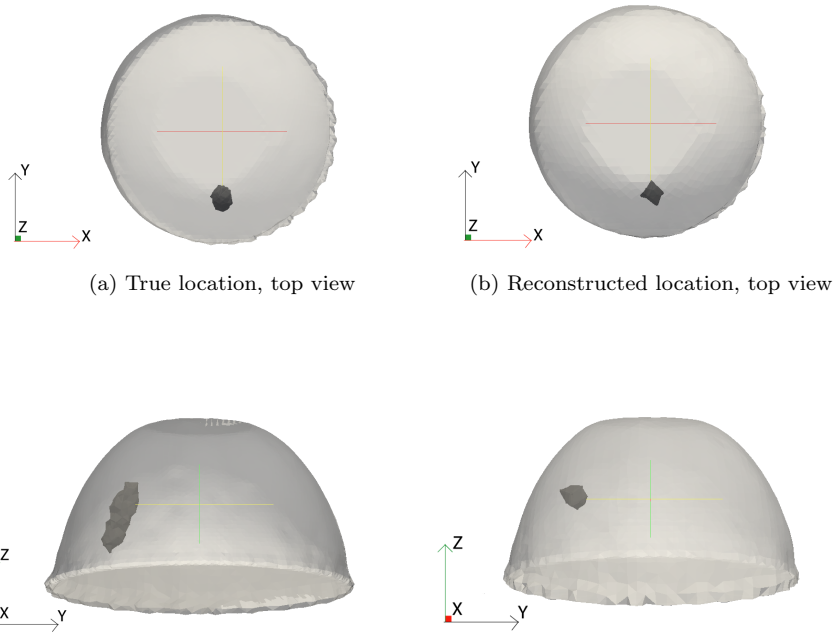

(a) True location, top view (b) Reconstructed location, top view

(c) True location, side view (d) Reconstructed location, side view

Figure 6.8: Various views of the true location and reconstructed location for Experiment 5. Solving for a 5 mm radius spherical inclusion. 128 chromosomes in the population and the algorithm limited to 50 generations.

Experiment 6: *Dataset B using a spherical inclusion*

Figure 6.9 shows the true location and reconstruction location for Experiment 6. As with Experiment 4 the larger inclusion has dominated the reconstruction. The *a priori* sphere has moved to the location of the large inclusion. The assumption of a spherical inclusion has produced a good match for inclusion location for the larger inclusion with a centroid difference of 5 mm. The reconstructed centroid for the spherical inclusion coincides with the reconstructed ellipsoidal inclusion centroid of Experiments 4 at $(0, -30, 25)$.

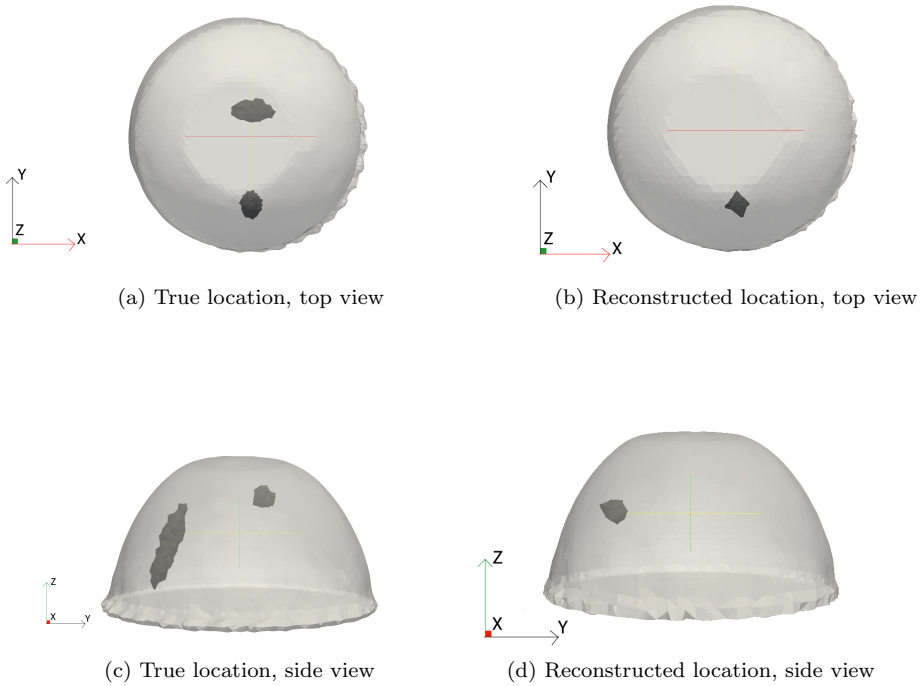

(a) True location, top view

(b) Reconstructed location, top view

(c) True location, side view

(d) Reconstructed location, side view

Figure 6.9: Various views of the true location and reconstructed location for Experiment 6. Solving for a 5 mm radius spherical inclusion. 128 chromosomes in the population and the algorithm limited to 50 generations.

Dataset	Reconstruction Assumption		
	1	**2**	**Sphere**
A			
B			

Table 6.2: Summary of synthetic data results. The reconstruction assumption is one ellipsoid (1), two ellipsoids (2), or a 5mm radius sphere. Black indicates the reconstructed inclusion shape and location was successful, grey indicates a positive result, *i.e.* at least one inclusion was located correctly but not a good shape match, and red indicates a failed reconstruction *i.e.* no inclusion was identified.

A priori	**Dataset**	**# Model evaluations**
Single ellipsoid	A	6479
	B	6041
Two ellipsoids	A	6478
	B	6472 (50 generations)
		63 612 (500 generations)
Sphere	A	3548
	B	1031

Table 6.3: Number of model evaluations for each *a priori* assumption.

6.2 Two Inclusion Phantom

A two inclusion phantom was created to apply the ellipsoidal inclusion algorithm to phantom data. The phantom was created using the method described in section 2.1 of Chapter 2, with two type one inclusions, *i.e.* $E'_I = 27$ kPa, representing two cancerous masses. The inclusions were located at $(-10, 35, 20)$ and $(-5, -30, 30)$. Both inclusions have a radius of 10 mm. The two step reconstruction approach of section 4.2 in Chapter 4 was used. As with the synthetic studies of section 6.1 various *a priori* inclusion assumptions were tested:

Phantom Experiment 1: Solve using a single ellipsoidal inclusion.

Phantom Experiment 2: Solve using two ellipsoidal inclusions.

Phantom Experiment 3: Solve using a spherical inclusion with $R = 5$ mm.

Phantom Experiment 4: Solve using two spherical inclusions both with $R = 5$ mm.

The experiments were run with the same constraints as the synthetic data experiments of section 6.1 with a population of 128 chromosomes and the algorithm limited to 50 generations. The actuation frequency was 26 Hz with and amplitude of 0.5 mm. As with the synthetic experiments, the two ellipsoidal inclusion assumption experiment was run again with the algorithm limited to 500 generations.

6.2.1 Results

Figure 6.10 shows the result for Phantom Experiment 1. The reconstruction has identified one of the inclusions. The centroid of the reconstructed stiff nodes is at $(-24, 44, 20)$, which is 16 mm from the true centroid of the inclusion at $(-10, 35, 20)$. Note that the $(-24, 44, 20)$ is the centroid of the stiff nodes within the breast volume, rather than the centroid of the ellipsoid. In this case the ellipsoid is partially inside the breast volume, hence the (x, y, z) are not necessarily multiples of five as would be expected given the constraints in Table 6.1. The reconstructed volume of 1783 mm^3 is 43% of the true inclusion volume of 4187 mm^3.

Figure 6.11 shows the result for Phantom Experiment 2 after 50 generations. One inclusion is not identified at all, with the ellipsoid completely outside the breast volume. The other inclusions is reconstructed with a volume of 45% of the true inclusion volume of 4187 mm^3 and a centroid

difference of 30 mm. This reconstruction is not as successful as the single inclusion phantom results of Chapter 4, in which even phantom Tr5 was reconstructed with a centroid difference of 25 mm. However, the reconstruction is much improved when allowed to run for 500 generations, as can be seen in Figure 6.12. Both inclusions are successfully reconstructed with a centroid difference of 19 mm for the inclusion located at $(-10, 35, 20)$ and a centroid difference of 18mm for the inclusion located at $(-5, -30, 30)$. Both reconstructed inclusions underestimate the true inclusion volume with 47% and 22% of the true volumes respectively. The reconstruction of the inclusion at $(-10, 35, 20)$ is similar to the reconstruction result of Phantom Experiment 1, shown in Figure 6.10.

Figure 6.13 shows the result for Phantom Experiment 3. The *a priori* spherical inclusion assumption has correctly located one of the inclusions. In fact, the centroid difference is 12mm, better than any of the ellipsoidal reconstructions.

Figure 6.14 shows the results for Phantom Experiment 4. Both inclusions are located successfully. One inclusion is located at $(-15, -30, 20)$, 14 mm away from the true inclusion location of $(-5, -30, 30)$. The second inclusion is located at $(-15, 40, 15)$, which is 9 mm away from the true inclusion location of $(-10, 35, 20)$.

The computational expense of each reconstruction is given in Table 6.4.

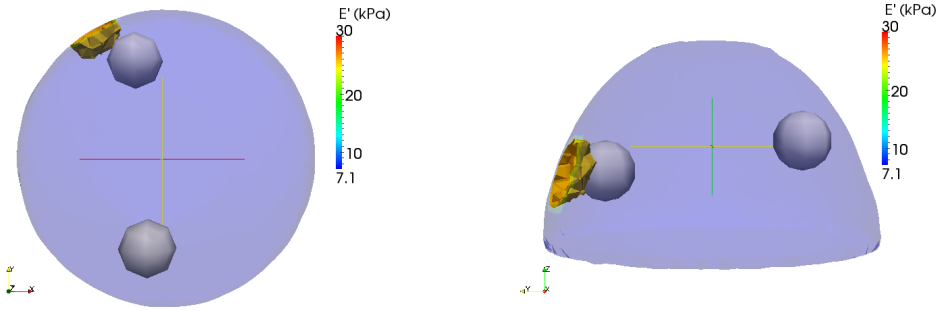

(a) Top view (b) Side view

Figure 6.10: Result for Phantom Experiment 1 assuming a single ellipsoidal inclusion. 128 chromosomes in the population and the algorithm limited to 50 generations. The true inclusions are shown in grey.

.

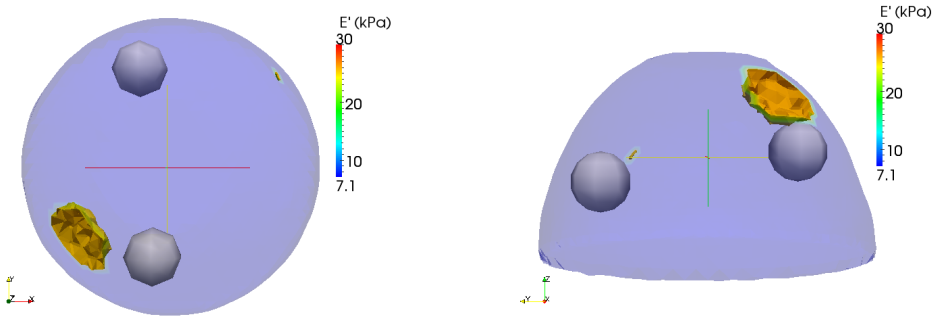

(a) Top view (b) Side view

Figure 6.11: Result for Phantom Experiment 2 assuming two ellipsoidal inclusions. 128 chromosomes in the population and the algorithm limited to 50 generations. The true inclusions are shown in grey.

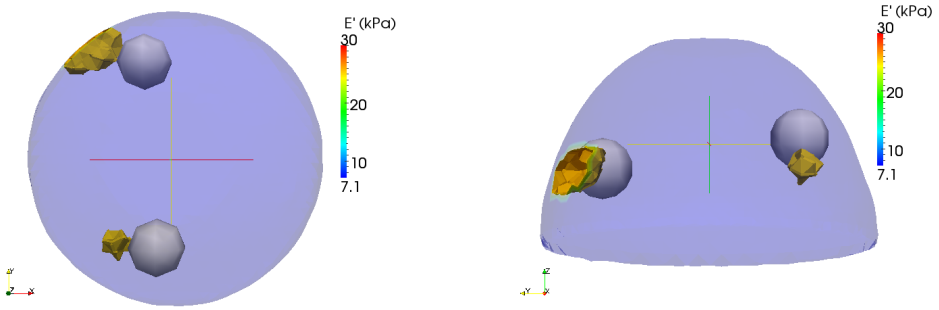

(a) Top view (b) Side view

Figure 6.12: Result for Phantom Experiment 2 assuming two ellipsoidal inclusions. 128 chromosomes in the population and the algorithm limited to 500 generations. The true inclusions are shown in grey.

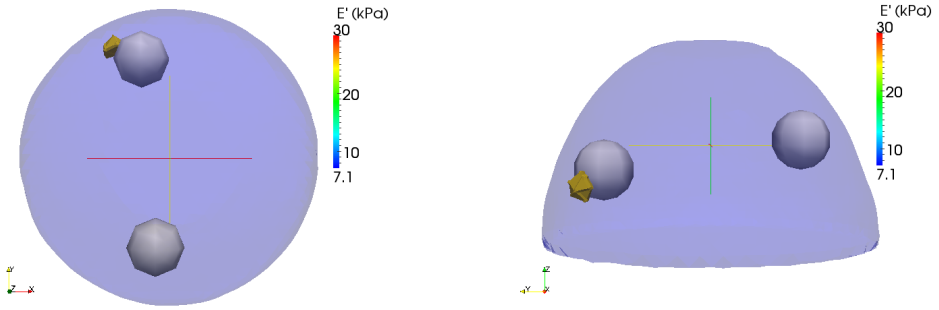

(a) Top view (b) Side view

Figure 6.13: Result for Phantom Experiment 3 assuming a spherical inclusion with $R = 5$ mm. 128 chromosomes in the population and the algorithm limited to 50 generations. The true inclusions are shown in grey.

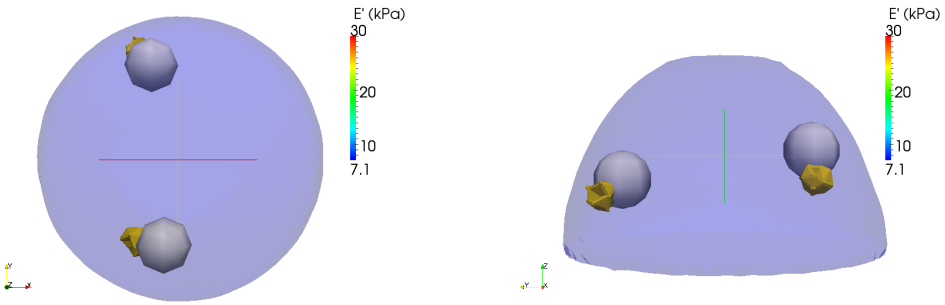

(a) Top view (b) Side view

Figure 6.14: Result for Phantom Experiment 4 assuming two spherical inclusions both with $R = 5$ mm. 128 chromosomes in the population and the algorithm limited to 50 generations. The true inclusions are shown in grey.

A priori	**# Model evaluations**
Single ellipsoid	1572
Two ellipsoids	1581 (50 generations) 15 529 (500 generations)
Single Sphere	1162
Two Spheres	1499

Table 6.4: Number of model evaluations for each *a priori* assumption.

6.3 Discussion and Conclusions

In the synthetic experiments an inclusion was identified and located in each of the reconstructions with varying success. The most successful reconstruction was that of Experiment 1, with a good match for location, volume and shape. When two ellipsoidal inclusions were assumed in Experiment 2, this reduced the success of the reconstruction by not identifying the correct inclusion shape, but the reconstructed inclusion was still located only 5 mm away from the true location. The second inclusion was moved to the outside edge of the breast at the edge of the actuator. A completely successful reconstruction would locate the second inclusion completely outside the breast volume, but in terms of a positive result for the DIET system, an inclusion was correctly identified and located and the patient would be flagged for further investigation.

For the synthetic case of two inclusions present, the largest inclusion was successfully located in Experiment 3, with a comparable inclusion volume, but the shape of the inclusion was not a good match. The second, smaller inclusion is not identified in the reconstruction. The inability to distinguish the second inclusion from the background material was apparent even after 500 generations and 63 612 model evaluations. These results support the idea of solving for a single inclusion because the largest inclusion can dominate the reconstruction. If there are multiple inclusions and DIET can be used to identify one within the breast, then DIET would be a success as a pre-screening method because further clinical investigation of the patient would take place. The largest inclusion was identified for single ellipsoid and single sphere *a priori* assumptions requiring only 6041 and 1031 model evaluations respectively. This is approximately ten to sixty times less computational expense than the two ellipsoid *a priori* result and has produced inclusion location results that are just as successful.

For the two inclusion phantom, the results were similar to the synthetic data experiments. An inclusion was correctly identified for the four inclusion assumptions *(single ellipsoid, two ellipsoids, single fixed-radius sphere, two fixed-radius spheres)*, thus a successful pre-screening result was produced. The centroid differences in phantom ranged from 12 mm to 30 mm, larger than the 5 mm found using synthetic data. This is to be expected as synthetic data can never fully replicate experimental errors. The worst result was the 50 generation result for Phantom Experiment 2. Although an inclusion was identified, it was placed 30 mm from the correct location. When the algorithm was allowed to run for 500 generations both inclusions were successfully reconstructed. This is a particularly encouraging result for DIET as it demonstrates that two inclusion reconstructions are possible in phantoms. In the 500 generation reconstruction, 15,529 models were

evaluated. The actual number of FE evaluations is less because the homogeneous solution is only calculated once, even though it can be generated with multiple parameter combinations.

The single ellipsoid, single sphere and two sphere assumptions required 1571, 1161 and 1499 model evaluations respectively. This is an approximately ten fold decrease in computational expense compared to the result using an *a priori* of two ellipsoidal inclusions. The *a priori* spherical inclusion assumption not only gave a smaller centroid difference than either of the ellipsoidal inclusion assumptions, but also required the fewest model evaluations. Similarly, the two spherical inclusion assumption produced centroid differences of 14 mm and 9 mm, better than the 19 mm and 18 mm of the two ellipsoidal inclusion assumption and for far fewer model evaluations. The obvious caveat is that the two ellipsoidal inclusion assumption produced a much better reconstruction of internal material properties, identifying both inclusions with good matches for both inclusion volume and location. Thus, the results of the two inclusion phantom demonstrate that one or more of the inclusions present can be identified and located with simple *a priori* assumptions, and that with increased computational expense reconstructions that provide inclusion location and volume are possible in phantom.

A model that can provide a positive result as a pre-screening test with as few parameters as possible is one of the main objectives for the DIET reconstruction algorithm. The reconstructions from the synthetic Experiments 4 and 5 are encouraging for the DIET reconstruction algorithm as, even with the *a priori* assumption of a spherical inclusion, the single inclusion in dataset A was located correctly and the larger of the two inclusions in dataset B was located correctly. The identification and location of one of the inclusions present was also achieved in Phantom Experiment 3. All three results would be a positive result for DIET. The much smaller parameter space associated with finding a best fit model for a spherical inclusion $\theta(E_B, \zeta_B, R, x_c, y_c, z_c)$ compared to a best fit model using one or multiple ellipsoidal inclusions $\theta(E'_B, \zeta_B, v_1, v_2, v_3, x_c, y_c, z_c, \alpha, \beta, \gamma, E'_I, \zeta_B)$, is desirable because of the reduction in the search space and therefore the number of possible FE evaluations required.

6.4 Heterogeneous Phantom Validation

Commercial breast phantoms are available for ultrasound training, allowing users to develop and practice the skills necessary to gain proficiency in using ultrasound for elastography imaging [120]. These phantoms have multiple inclusions which can be used in various separate training exercises by targeting the different inclusions individually. DIET is not a targeted imaging technique, in that the complete elastic property distribution must be reconstructed by optimizing an FE model of the breast. It is critical then, to examine the more complex phantom case.

The phantoms used in Chapter 4 and Chapter 5 consisted of a single inclusion within an otherwise homogeneous background. This material property distribution matches the assumption in the inverse problem of a single stiff inclusion within a homogeneous background. The rationale behind the heterogeneous phantom is to investigate the algorithm's performance when faced with a phantom that violates this assumption. The phantom, referred to as phantom MI, contains not only a type 1 inclusion (27 kPa) representing cancer, but four other type 2 (7 kPa) inclusions. These inclusions are stiffer than the background material, but less stiff than the 'cancerous' inclusion. The inclusion and background compositions are described in Table 2.2 in section 2.1. A successful result for the reconstruction algorithm would be to locate the stiffest inclusion within this more complex geometry. The reconstructions performed on the two inclusion phantom in section 6.2 were considered successful if one or both of the inclusions were located. For phantom MI reconstructions to be considered successful, the target 'cancerous' inclusion must be located rather than any of the other inclusions.

Phantom MI was constructed as described in section 2.1. A description of each of the inclusions in the phantom is given in Table 6.5. Figure 6.15 shows the location of the inclusions within the phantom. The 'cancerous' inclusion is located at $(10, -30, 20)$. Because the heterogeneous phantom potentially provided a more difficult optimization problem for the GA, the cost functions Φ^{SQ}, Φ, Γ and τ as defined by Eqs. 3.21-3.27, were examined for a test sweep of forward solutions with the aim of determining if Φ was acceptable as a cost function or should be replaced with an alternative. For each of the four cost functions under examination, the background cost was examined, then the location cost. This is to reflect the two step reconstructions used in this thesis. Single frequency reconstructions were then performed on phantom MI using Φ. Multi-frequency reconstructions were performed using Φ^C and Γ^C as the costs which were calculated using Eqs. 3.35 and 3.36 respectively.

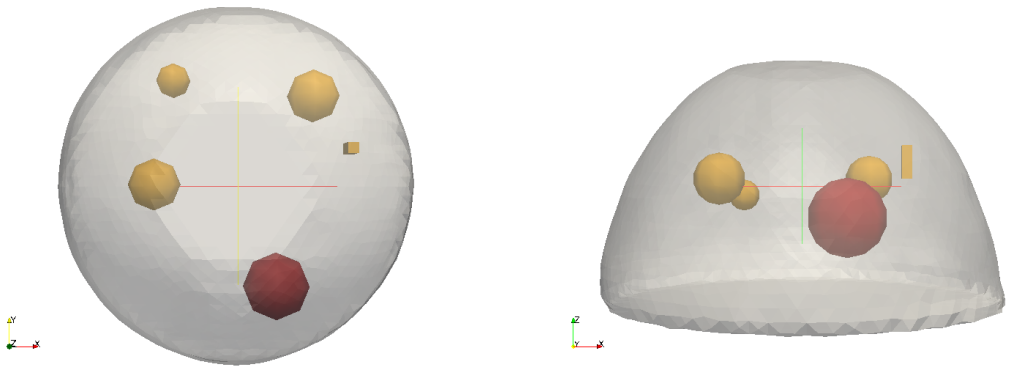

(a) Top view

(b) Side view

Figure 6.15: Visualization of the location of the inclusions within the phantom MI. The target 'cancerous' inclusion is indicated in red.

Inclusion	**Description**	**Size**
1	*Cancer* (inclusion type 1	10 mm radius
2	inclusion type 2	7.5 mm radius
3	inclusion type 2	7.5 mm radius
4	inclusion type 2	5 mm radius
5	inclusion type 2	10 mm x 3 mm x 4mm

Table 6.5: Inclusion descriptions for phantom MI

6.4.1 Cost Function Comparison

FE calculations were performed for phantom MI using an actuation frequency of 20Hz and amplitude of 0.5 mm for the range of parameters used in the reconstruction, given in Table 4.2 in Chapter 4 . The cost functions, $\Phi, \Phi^{SQ}, \Gamma, \tau$ were calculated for each of the forward solutions using Eqs. 3.21 to 3.27. Cost surfaces for the background parameters, E'_B, ζ_B, and inclusion location (x_c, y_c, z_c) were examined. For the location problem the *a priori* inclusion assumption from Chapter 4 of $R = 5$ mm, $E_I = 30kPa$ and $\zeta_I = 10\%$ was used.

Background Cost Surface

Figure 6.16 shows the background parameter cost surfaces. There is very little sensitivity to damping in all of the cost metrics in the phantom. The correlation cost, Γ, in Figure 6.16c shows most clearly the low sensitivity to damping, with the contours on the cost surface running parallel to the y axis (ζ_B) of the plot. For Φ, Φ^{SQ} and Γ the minimum $\zeta_B = 1\%$, for τ the minimum $\zeta_B = 2\%$. Φ, Φ^{SQ} and Γ produce estimates of E'_B of 6.8 kPa, 7.2 kPa and 7.2 kPa respectively, all within 0.4 kPa of each other. The minimum E'_B for τ is higher, at 7.8 kPa.

Location Cost Surface

Figures 6.17 to 6.20 show the location problem cost surfaces for phantom MI for the four metrics, Φ,Φ^{SQ}, Γ, and τ respectively. Comparing weighted cost Φ with squared error Φ^{SQ} shows that the homogeneous solution is a higher cost in Figure 6.18 than in Figure 6.17. This is an encouraging result for Φ, because it is a stronger indicator that the phantom does contain a stiff inclusion. Figures 6.18 and 6.19, for Φ and Γ respectively, both show a clear minimum in the correct area of the breast (South East quadrant of the cost surfaces), and a clear maximum in the opposite quadrant (North West quadrant of the cost surfaces). τ, shown in Figure 6.20, is the worst performing cost metric for the location optimization. τ is unsuccessful as the phase difference cost does not take into account how many cycles of phase difference there is between measured and calculated motion. As the output from the forward simulation is simply the complex displacement, $\mathbf{u}_c$, there is an ambiguity in the calculation of phase using Eq. 3.26. The calculated phase would need to be unwrapped to be compared to the measured phase for use as a cost function. However, the other three cost metrics can be used to identify tumor location without the need for phase unwrapping.

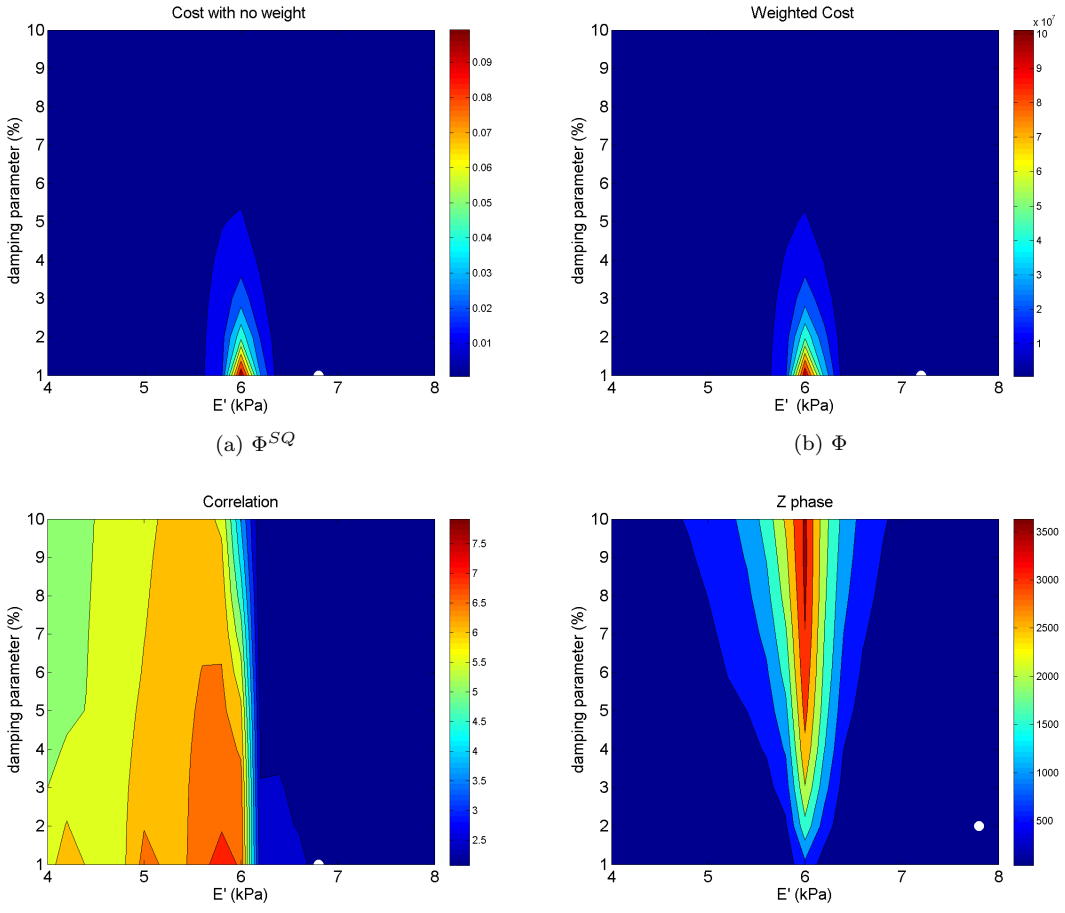

(a) Φ^{SQ} (b) Φ

(c) Γ (d) τ

Figure 6.16: Phantom MI homogeneous cost surfaces. Squared error, Φ^{SQ} (6.16a), Weighted cost, Φ (6.16b), Correlation cost, Γ (6.16c) and z phase cost, τ (6.16d). The minimum cost is indicated by a white circle.

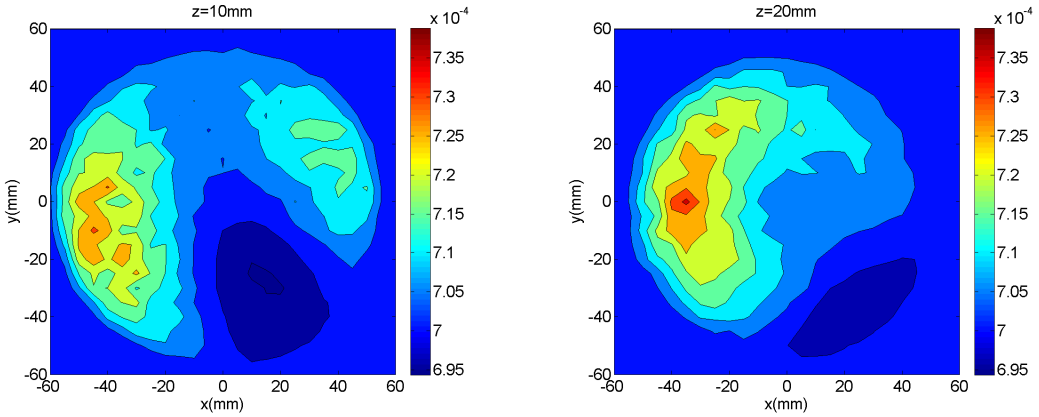

(a) slice at z = 10 mm

(b) slice at z = 20 mm

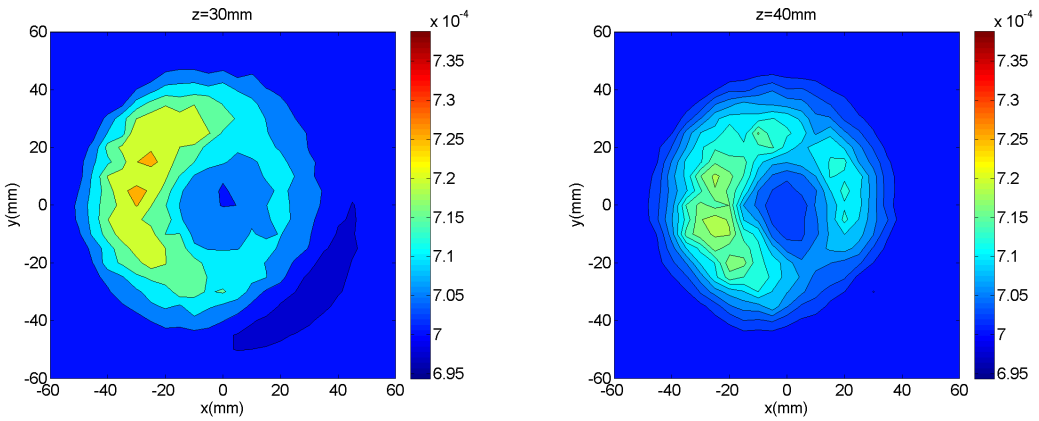

(c) slice at z = 30 mm

(d) slice at z = 40 mm

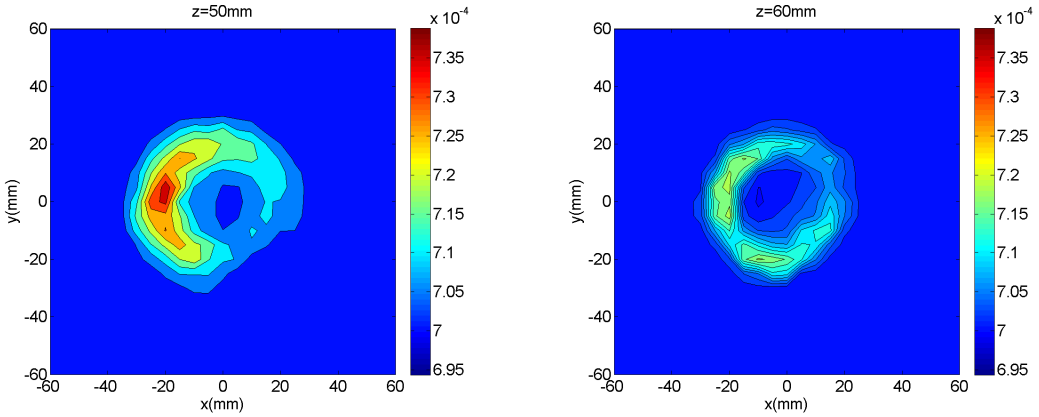

(e) slice at z = 50 mm

(f) slice at z = 60 mm

Figure 6.17: Phantom MI slices through Φ^{SQ} location cost surface.

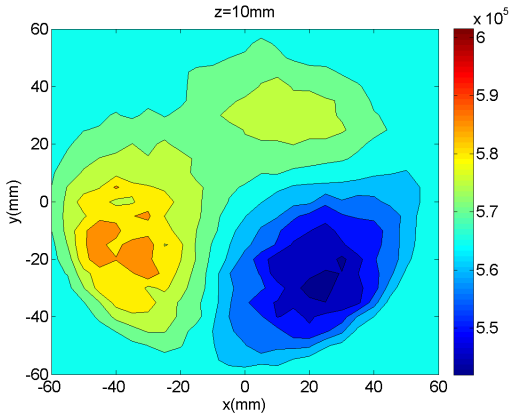

(a) slice at z = 10 mm

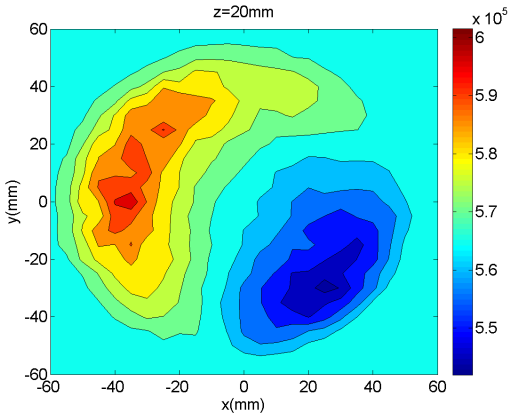

(b) slice at z = 20 mm

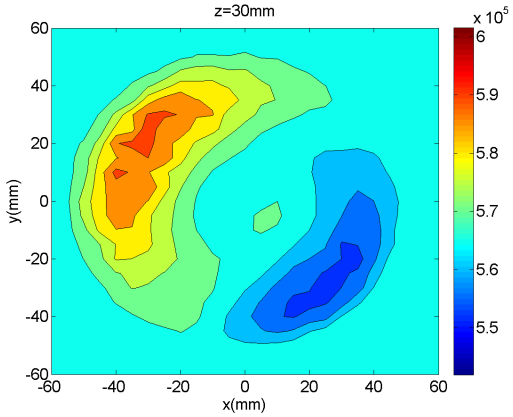

(c) slice at z = 30 mm

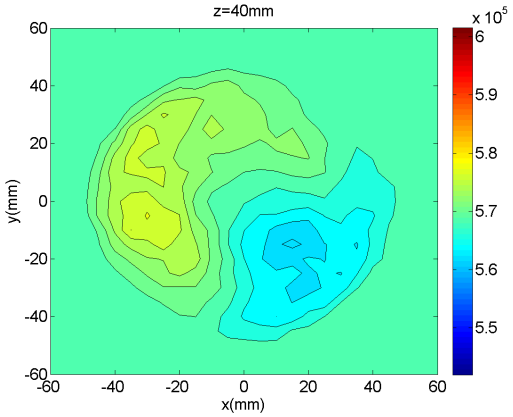

(d) slice at z = 40 mm

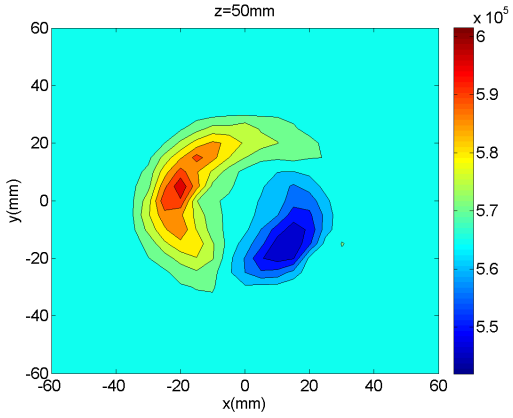

(e) slice at z = 50 mm

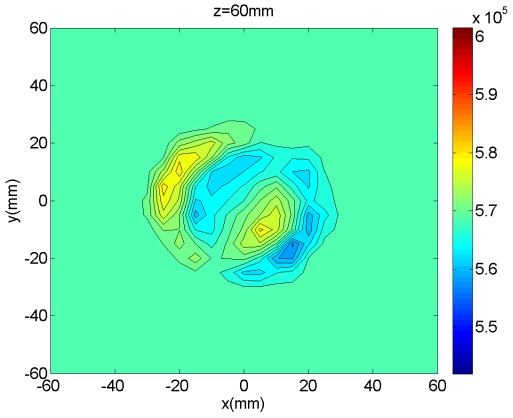

(f) slice at z = 60 mm

Figure 6.18: Phantom MI slices through Φ location cost surface.

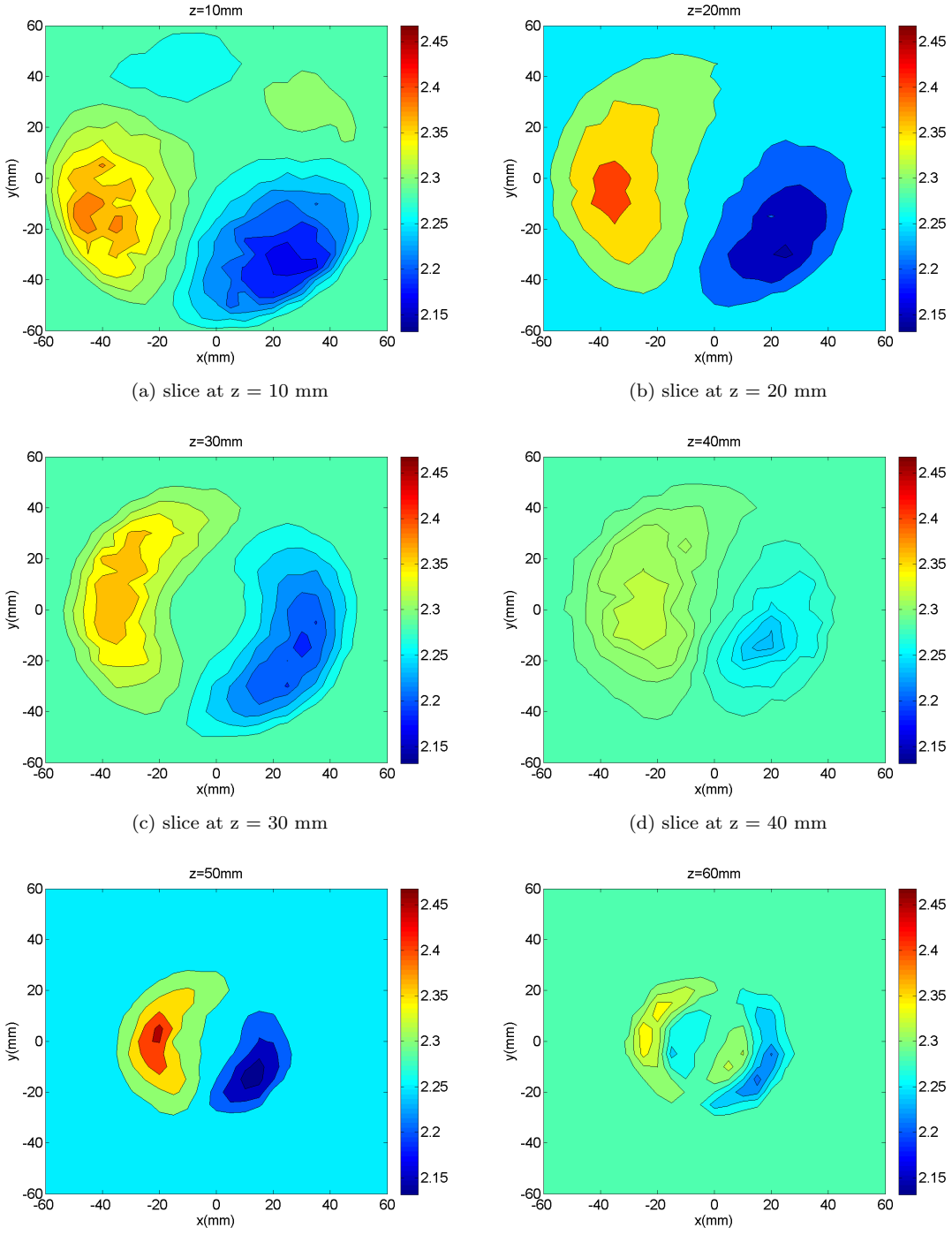

(a) slice at z = 10 mm

(b) slice at z = 20 mm

(c) slice at z = 30 mm

(d) slice at z = 40 mm

(e) slice at z = 50 mm

(f) slice at z = 60 mm

Figure 6.19: Phantom MI slices through Γ location cost surface

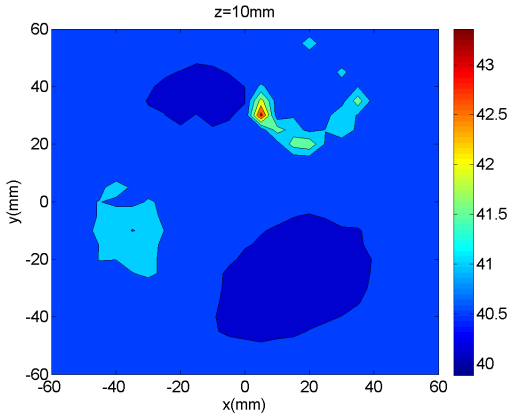

(a) slice at z = 10 mm

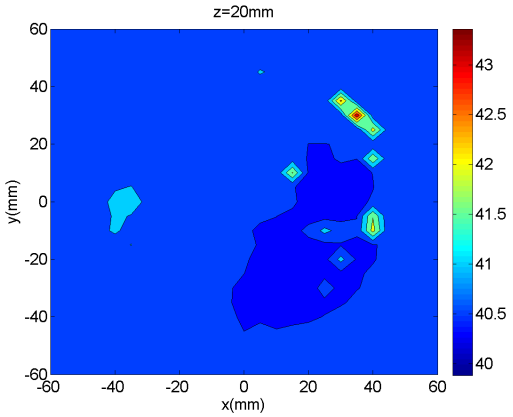

(b) slice at z = 20 mm

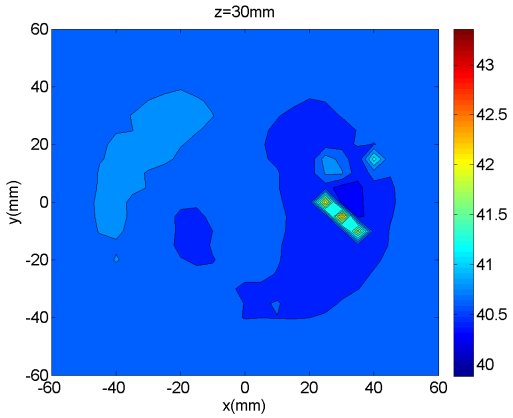

(c) slice at z = 30 mm

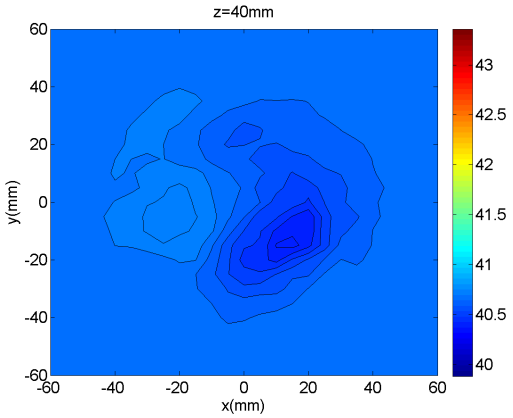

(d) slice at z = 40 mm

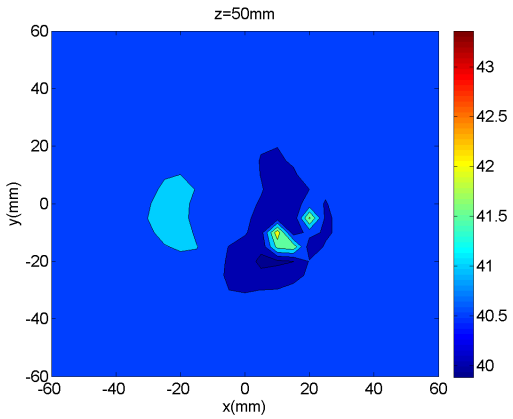

(e) slice at z = 50 mm

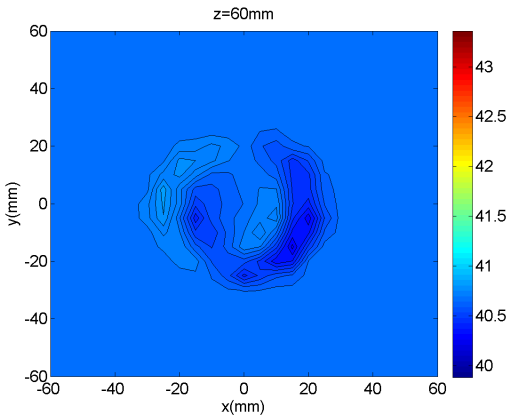

(f) slice at z = 60 mm

Figure 6.20: Phantom MI slices though τ location cost surface

6.4.2 Experimental Setup

Single frequency and multi-frequency reconstructions were performed on phantom MI. For the single frequency reconstructions, the experiments of section 6.1.1 were applied to phantom MI: *a priori* assumptions of one ellipsoidal inclusion, two ellipsoidal inclusions, and a spherical inclusion for 20Hz actuation frequency. The constraints on the reconstructed parameters were the same as those in Table 6.1 or Table 4.2 for ellipsoidal and spherical inclusions respectively.

For the multi-frequency reconstructions, a frequency sweep of data was used, with data acquired every 2 Hz from 10 Hz to 60 Hz. The method of optimization was the same as the previous multi-frequency reconstructions in Chapter 5 where the background material properties were optimized independently for each frequency and then the inclusion location was reconstructed using the combined cost function Φ^C. Three different multi-frequency reconstructions were preformed: 10 Hz to 26 Hz, 18 Hz to 40 Hz, and 42 Hz to 60Hz. The constraints on the reconstructed parameters were equal to those given in Table 4.2 in Chapter 4 with $E_I' = 30$ k Pa and $\zeta_I = 10\%$ and the inclusion radius fixed at 5 mm. In addition, a multi-frequency reconstruction was performed on the 18 Hz to 40 Hz data using the combined cost function Γ^C as defined by Eq. 3.36. The number of model evaluations for each of the reconstructions was recorded and is given in Table 6.7.

6.4.3 Single Frequency Results

Figure 6.21 shows the reconstruction result using a single ellipsoid. The reconstructed inclusion center is a reasonable match for inclusion location with a centroid difference of 18 mm. The volume of the reconstructed ellipsoid is 9 398 mm^3, overestimating the inclusion volume by 2.37 times. Figure 6.22 shows the reconstruction result assuming two ellipsoids. In this case, the reconstruction is more successful than the single ellipsoid assumption, with a centroid difference of 11 mm. Again the volume of the inclusion is overestimated, with the reconstructed volume 1.8 times the true volume. The second ellipsoid is completely outside the breast volume, which demonstrates that only the target inclusion is identified by the reconstruction algorithm. The spherical inclusion reconstruction result is shown in Figure 6.23. As with the results of section 6.1 and 6.2, the spherical inclusion provided a good match for inclusion location with a centroid difference of 11mm.

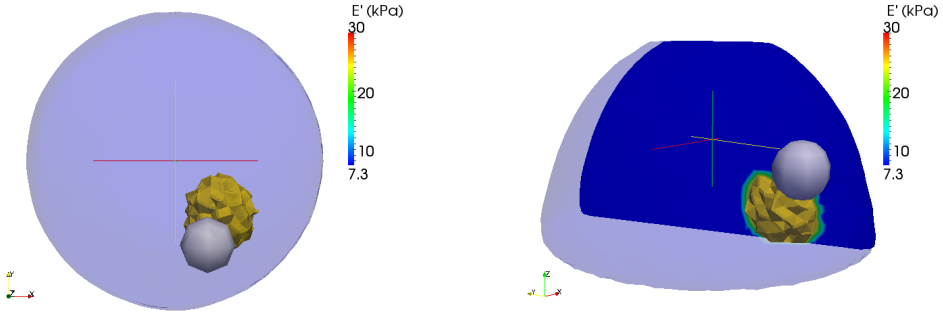

(a) Top view (b) Slice through phantom

Figure 6.21: Reconstruction result for the heterogeneous phantom using one ellipsoid. The target inclusion is shown in grey. Actuation frequency 20Hz.

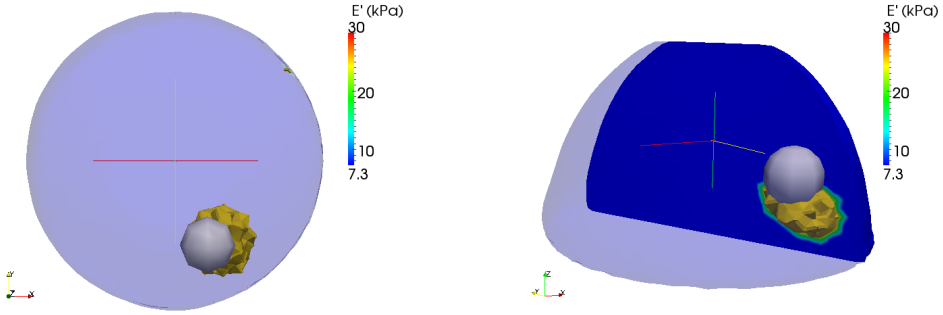

(a) Top view (b) Slice through phantom

Figure 6.22: Reconstruction result for the heterogeneous phantom using two ellipsoids. The target inclusion is shown in grey. Actuation frequency 20Hz.

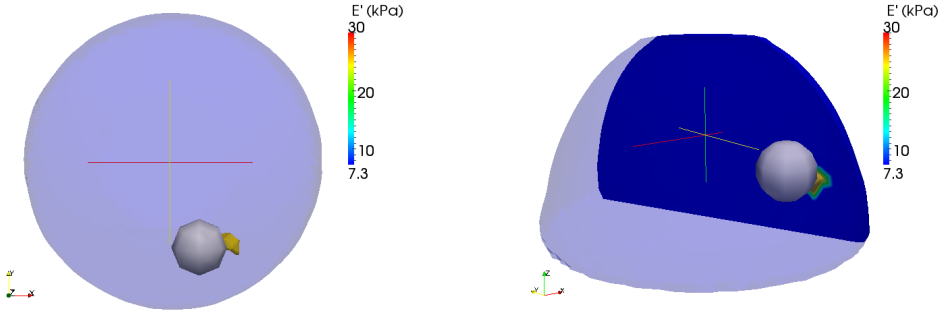

(a) Top view (b) Slice through phantom

Figure 6.23: Reconstruction result for the heterogeneous phantom using a 5 mm radius sphere. The target inclusion is shown in grey. Actuation frequency 20Hz.

6.4.4 Multi-Frequency Results

Figure 6.24 shows the $\overline{SNR}$ and the reconstructed E'_B across the frequency sweep. The lower frequencies, those below 14 Hz, have the lowest signal to noise, similar to the multi-frequency phantom experiments of Chapter 5.

The background E' results are interesting as the background silicone is the same composition as previous phantoms, but the presence of stiffer inclusions has produced a higher reconstructed background E'_B. The phantom displays the same increase in reconstructed storage modulus, but the storage modulus is higher, approximately 7 kPa rather than the 3 kPa found in Chapter 4. This is an important result for DIET which demonstrates that the homogeneous model fitting is affected by multiple stiff inclusions.

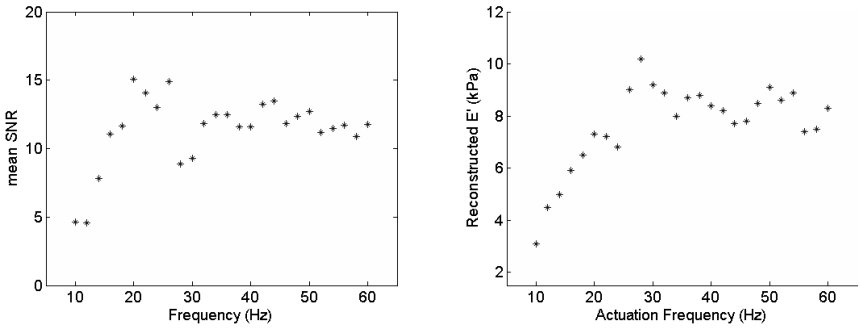

(a) Signal to noise (b) Reconstructed E'_B

Figure 6.24: Signal to noise (6.24a) and reconstructed background storage modulus, E'_B (6.24b), for phantom MI.

Figures 6.25, 6.26 and 6.27 show the optimal region for inclusion location using Φ^C as the cost. Figure 6.28 shows the optimal region for inclusion location using Γ^C as the cost. A quantitative description of the optimal region, as calculated using Eqs. 3.53 and 3.57, for each reconstruction is given in Table 6.6. All the reconstructions locate the inclusion in the correct area of the breast with centroid differences of 12 mm or less. The reconstruction for 42 Hz to 60 Hz using Φ^C as the cost provides the closest centroid difference of 8 mm. All the reconstructions similarly underestimate the inclusion volume to give a reconstructed volume ~30% of the true inclusion volume.

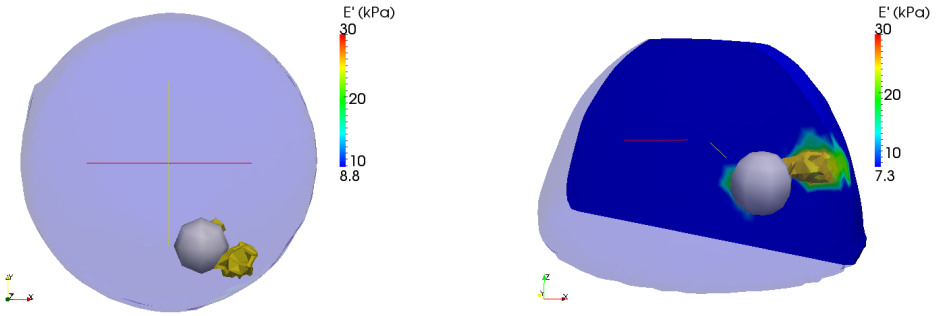

(a) Top view (b) Slice through phantom

Figure 6.25: Reconstruction result for phantom MI using 10 Hz to 26 Hz frequency data with Φ^C as the cost. The target inclusion is shown in grey.

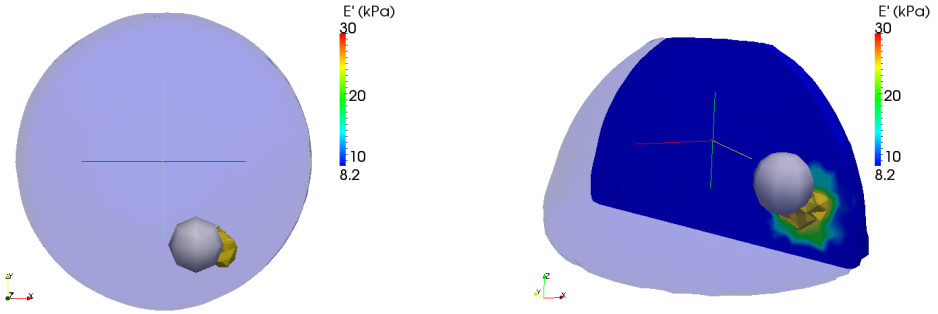

(a) Top view (b) Slice through phantom

Figure 6.26: Reconstruction result for phantom MI using 18 Hz to 40 Hz frequency data with Φ^C as the cost. The target inclusion is shown in grey.

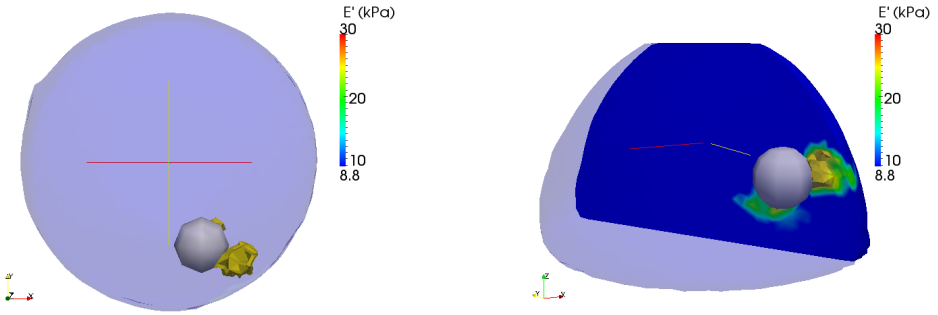

(a) Top view (b) Slice through phantom

Figure 6.27: Reconstruction result for phantom MI using 42 Hz to 60 Hz frequency data with Φ^C as the cost. The target inclusion is shown in grey.

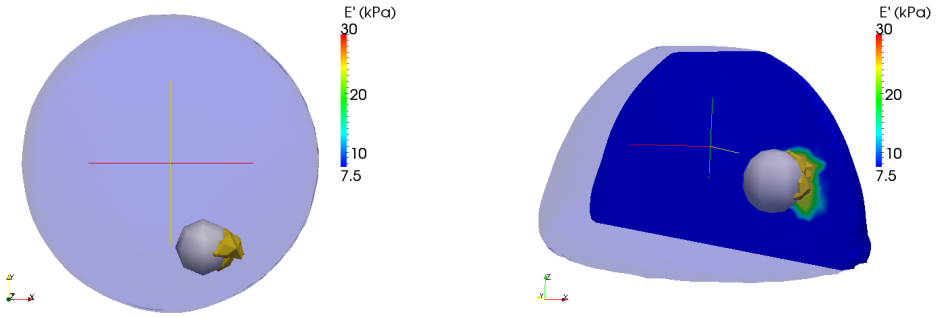

(a) Top view (b) Slice through phantom

Figure 6.28: Reconstruction result for phantom MI using 18 to 40 Hz frequency data with Γ as the cost. The target inclusion is shown in grey.

Frequency Range (Hz)	**Cost Function**	**Volume Fraction**	**Centroid Difference (mm)**
18 to 26	Φ^C	0.31	12
28 to 40	Φ^C	0.27	11
42 to 60	Φ^C	0.28	8
28 to 40	Γ^C	0.28	11

Table 6.6: Quantitative description of the optimal region, where *Volume Fraction* is the volume of the 25 kPa contour divided by the volume of the true inclusion, and the *Centroid Distance* is the distance between the centroid of the optimal region and the centroid of the inclusion.

Reconstruction		# Model evaluations
Single ellipsoid		6497
Two ellipsoids		6478
Sphere	20 Hz	3534
	18 Hz to 26 Hz	5373
	28 Hz to 40 Hz	6576
	42 Hz to 60 Hz	5650

Table 6.7: Number of model evaluations for each reconstruction.

6.4.5 Discussion and Conclusions

Each of the reconstructions for the single frequency experiments located the target inclusion and not any of the other type 2 inclusions present. As demonstrated with the synthetic data in section 6.1.2, a two inclusion assumption can be successfully used to locate a single target inclusion. The second ellipsoid in the reconstruction shown in Figure 6.22 is completely outside the breast volume. This is an important result for DIET as the other inclusions, which are not intended targets, were not present in the reconstructed material property distribution.

The single frequency *a priori* sphere reconstruction required 3534 model evaluations, the fewest of all the reconstructions. The number of model evaluations for the multi-frequency reconstructions ranged from 5373 to 6576, which is a similar number to the single frequency *a priori* ellipsoidal inclusion reconstructions. As with the single inclusions phantom results of Chapter 5 the use of multi-frequency data has not reduced the number of model evaluations required.

All the multi-frequency reconstructions are successful, locating the inclusion in the correct area of the breast even with the presence of a non-homogeneous background. The reconstruction for 42 Hz to 60 Hz using Φ^C as the cost provides the closest centroid difference of 8 mm. However, all reconstructions have a centroid difference of 12 mm or less which is comparable to the successful inclusion locations in Chapter 4 where the centroid differences ranged between 7 mm and 15 mm. These results would be satisfactory for the identification and location of a breast mass for DIET. The cost comparison using sweep data in section 6.4.1 demonstrates that Φ^{SQ}, Φ or Γ could be used as a cost function to successfully locate inclusions in the more complex phantom case. The reconstruction using Γ^C as a cost, shown in Figure 6.28, demonstrates that the Γ^C can be employed as a multi-frequency cost. For the reconstruction algorithm presented in this thesis, Φ^C was chosen as the multi-frequency cost function, but the viability of Γ^C may be of importance for future work if some modification to the cost function is required.

There are two effects that may contribute to the 42 Hz to 60 Hz Φ^C reconstruction producing the best result in terms of locating the target inclusion. These are the $\overline{SNR}$ and the wavelength of the motion. The higher frequencies exhibit a consistently high $\overline{SNR}$ of approximately 12, whereas between 10 Hz and 30 Hz the $\overline{SNR}$ varies between 5 and 15. The shorter wavelength of the higher frequencies is illustrated in Figure 6.29, which displays 20 Hz and 50 Hz data side by side for comparison. The shorter wavelength of the measured motion may provide a more distinctive anomaly for the reconstruction algorithm. However, the reconstructions using each of the three frequency ranges located the 'cancerous' inclusion within the complex geometry of phantom MI. The trade off is an over estimation of the background material properties, which in this case has not affected location optimization.

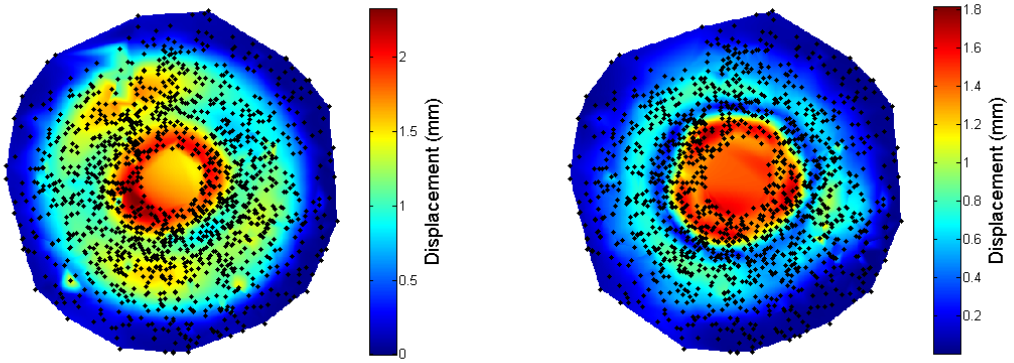

(a) Measured displacement at 20 Hz (b) Measured displacement at 50 Hz

Figure 6.29: Measured displacement at 20 Hz (6.29a) and 50 Hz (6.29b) for phantom MI. The black squares indicate measurement locations. The data is interpolated to cover the surface and projected flat.

The reconstructed background E' displays the same frequency dependence exhibited by the phantoms in Chapter 5. The frequencies below 20 Hz show an increasing E'_B with frequency which levels off between 20 Hz and 30 Hz. This dependence can not be attributed to the presence of an inclusion affecting the background property reconstruction adversely with decreasing frequency, because the homogeneous phantom reconstruction of Chapter 5 exhibits the same behavior. A possible cause is the actuation for frequencies up to 20 Hz not being sufficiently sinusoidal, *i.e.* if there was some additional undesired motion in the actuation. This data-model mismatch would account for the lower $\overline{SNR}$ and the frequency dependence of the reconstructed E'_B. However it is clear from Figure 6.30 that both low and high frequencies are exhibiting sinusoidal motion. The observed frequency dependence of the reconstructed background E' may be the result of low $\overline{SNR}$

combined with fewer wavelengths with which to compare measured and simulated motion. These two effects may have led to an incorrect E_B having the lowest cost at the lower frequencies. In terms of DIET reconstruction the absolute value of E'_B is not critical, it is only required that an inclusion can be distinguished, which has been accomplished in each of the reconstructions in this Chapter.

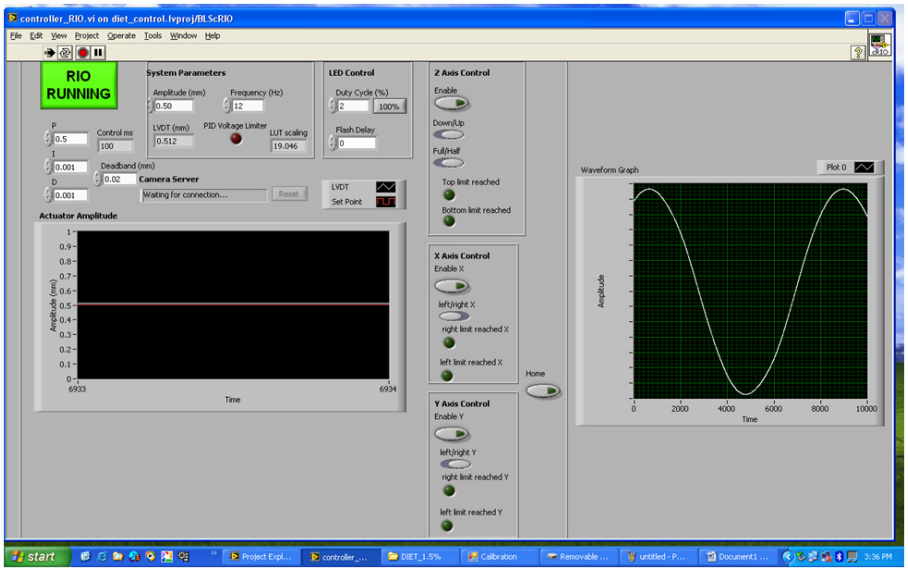

(a) Screenshot of actuator at 12 Hz

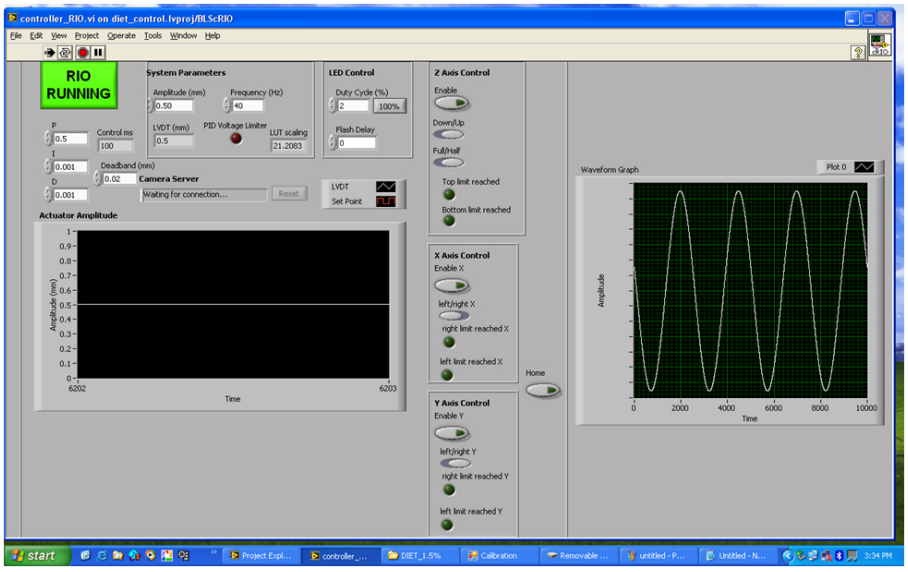

(b) Screenshot of actuator at 40 Hz

Figure 6.30: Screenshots of actuation at 12 Hz and 40 Hz. Both the low frequency (6.30a) and high freqeuncy (6.30b) actuation are sinusoidal.

Chapter 7

In Vivo Experiments

This chapter is concerned with the application of the reconstruction algorithm to *in vivo* data collected with the DIET prototype. There are three patients in the study, referred to as patient KF004, KS003, and MS016. Both breasts of each patient were imaged. To distinguish the healthy breast from the breast containing the tumor an H or a T is appended to the name of the dataset. For example, KF004T is the breast of patient KF004 which contains the tumor. The description of each tumor is given in Table 7.1. Note the location of the tumor is described clinically using the clock position as illustrated in Figure 7.1. The clock position location is the same for either breast.

Patient Dataset	**Tumor Location**
KF004T	11 mm diameter tumor at 10:30.
KS003T	30 mm diameter tumor 15mm from the nipple between 1 and 2 o'clock.
MS016T	15 mm diameter tumor at 3 o'clock.

Table 7.1: Description of tumor size and location for the three patients.

The data were collected using the DIET prototype system during an ongoing clinical pilot validation study. The actuation frequency and amplitude used for each patient dataset in the single frequency reconstructions is given in Table 7.2. The multi-frequency actuation parameters are given in Table 7.3. The fiducials are the same material as used in the phantom experiments of Chapter 4-6 and are applied to the breast using a light adhesive. The breast motion is imaged as described in section 2.2, the same method as the phantom data acquisition in previous chapters, with the patient lying prone and the breast making contact with the actuator. An example of

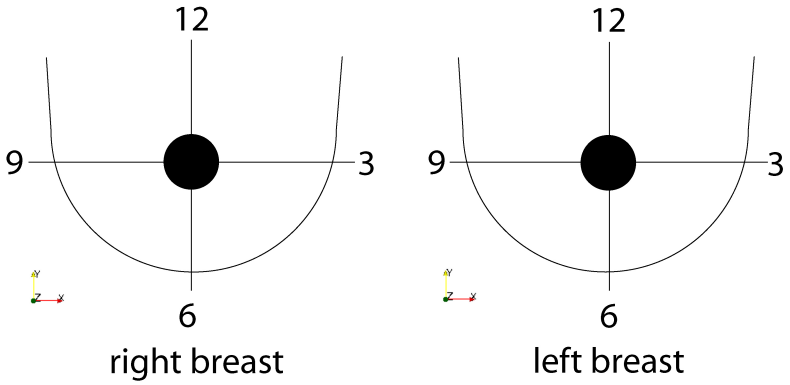

Figure 7.1: Diagram of the location convention for breast tumors.

tracked fidicuals is given in Figure 7.2 which shows the data collected from patient MS016T. The data is projected on to a patient specific mesh using Eqs. 3.11 to 3.19. The interpolation from simulated nodal motions to the measurement points is calculated using Eq. 3.20. The sensitivity to the *a priori* ζ_I was examined for KF004T. As with the heterogeneous phantom MI in section 6.4, the cost functions Φ^{SQ}, Φ, Γ, and τ were examined for patient MS016T to assess their potential for tumor location. Based on these results, the reconstruction algorithm was applied to the three patients for single frequency and multi-frequency reconstructions with the constraints on the parameters given in Table 7.4.

Patient	**Actuation Frequency (Hz)**	**Actuation Amplitude (mm)**
KF004	20	0.5
KS003	30	0.7
MS016	20	0.5

Table 7.2: Actuation frequency and amplitude for single frequency *in vivo* experiments.

Patient	**Actuation Frequencies (Hz)**	**Actuation Amplitude (mm)**
KF004	10,15,18,20,25,30,40	0.5
KS003	20,30,50	0.7
MS016	16-50 every 2Hz	0.5

Table 7.3: Actuation frequency and amplitude for multi-frequency *in vivo* experiments.

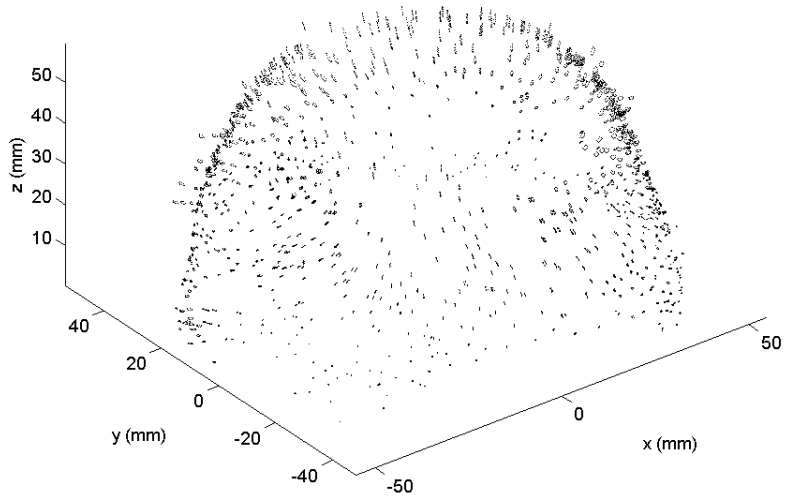

Figure 7.2: Tracked fiducial markers for patient MS016T.

Parameter			Constraint		
			Lower	**Upper**	**Increment**
Background	Storage Modulus $E'_B(kPa)$		2	10	0.1
	Damping ratio ζ_B *(%)*		10	200	10
	Inclusion Location	$x(mm)$	-60	60	5
		$y(mm)$	-60	60	5
		$z(mm)$	0	80	5
Inclusion radius (mm)			*Fixed at 5*		
Inclusion Storage Modulus E'_I (kPa)			*Fixed at 30*		
Inclusion Damping ζ_I (%)			*Fixed at 60*		

Table 7.4: Constraints on reconstructed parameters *in vivo*.

7.1 *A priori* Inclusion Properties

For the phantom experiments in Chapters 4-6, ζ_I was fixed at 10% after it was discovered that the change in Φ^{SQ} in response to a change in ζ_I was two orders of magnitude less than the change in Φ^{SQ} in response to tumor location. The damping parameter in tissue is much higher than in the silicone phantoms used in this work, so the *a priori* sensitivity to ζ_I *in vivo* was examined. A

sweep of forward solves was calculated for KF004T with an inclusion location of $(-30, 30, 30)$, the approximate tumor location, and an inclusion radius of 5mm, the approximate tumor size, with ζ_I varied from 10% to 150% and an actuation frequency of 20 Hz. The variation in Φ^{SQ} over this range is shown in Figure 7.3. This was compared to the range in Φ^{SQ} for inclusion location for a 5 mm radius inclusion with a fixed $\zeta_I = 60\%$, shown in Table 7.5. As found in the phantom case, the variation in ζ_I had much less of an effect on Φ^{SQ} than inclusion location thus ζ_I was fixed at 60% for all *in vivo* reconstructions.

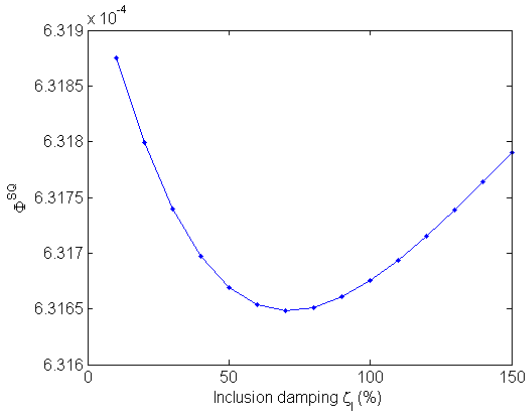

Figure 7.3: Variation in Φ^{SQ} with ζ_I.

Parameter	$\mathbf{\Phi^{SQ}}$ range
ζ_I	2.27×10^{-7}
Location	2.82×10^{-5}

Table 7.5: Inclusion damping cost range compared to location Φ^{SQ} range. The range of Φ^{SQ} for location is two orders of magnitude larger than the range of Φ^{SQ} for inclusion damping.

7.2 Cost Function Comparison

The cost functions Φ, Φ^{SQ}, Γ, and τ were calculated for a sweep of FE calculations throughout the parameter space using 20Hz data for MS016T using Eqs. 3.21 to 3.27 from Chapter 3. Cost surfaces for the background parameters, E'_B, ζ_B, and location (x_c, y_c, z_c) were examined. For the location problem, the *a priori* inclusion assumption of $R = 5$ mm, $E_I = 30$ kPa and $\zeta_I = 60\%$ was used with the solutions spaced every 5mm in the parameter space.

7.2.1 Background Parameters Cost Surface

Figure 7.4 shows the cost surfaces for each of the metrics for the MS016T breast. The major point to note is how much damping is present in the *in vivo* case compared to the $\zeta_B \approx 5\%$ exhibited in the phantom results of Chapters 4-6. The storage modulus of the silicone phantoms used in this thesis is representative of breast tissue stiffness, but the damping is not. The minimum combination of storage modulus and damping for Φ^{SQ}, Φ and Γ is found between 2.4 and 2.6 kPa and 40 to 70 % damping. The τ minimum cost is found at a higher stiffness, 3.4 kPa, and lower damping, 10 %. Figure 7.5 shows profiles through the minimum cost for each of the cost surfaces. The Hessian,

$$H = \begin{bmatrix} \frac{\partial^2 f}{\partial x^2} & \frac{\partial^2 f}{\partial x \partial y} \\ \frac{\partial^2 f}{\partial y \partial x} & \frac{\partial^2 f}{\partial y^2} \end{bmatrix} \tag{7.1}$$

where x the storage modulus E' and y is the damping parameter ζ, was evaluated numerically for each of the cost surfaces. The eigenvalues at the minima for the respective cost functions are given below.

$$eig(H_{\Phi^{SQ}}) = 1.0 \times 10^{-4} \begin{pmatrix} 0.0013 \\ 0.9107 \end{pmatrix} \tag{7.2}$$

$$eig(H_{\Phi}) = 1.0 \times 10^{4} \begin{pmatrix} 1.7673 \\ 0.0007 \end{pmatrix} \tag{7.3}$$

$$eig(H_{\Gamma}) = \begin{pmatrix} 0.0001 \\ 0.6813 \end{pmatrix} \tag{7.4}$$

$$eig(H_{\tau}) = 1.0 \times 10^{3} \begin{pmatrix} 3.2180 \\ -0.0009 \end{pmatrix} \tag{7.5}$$

As indicated by the negative eigenvalue in Eq. 7.5 and can be seen in the profile in Figure 7.5h the minimum value z phase within the parameter space is a point of inflection. It is unlikely that the damping parameter is less than 10 % *in vivo* [59] thus the minimum location in the τ is most likely a consequence of phase ambiguity in the data.

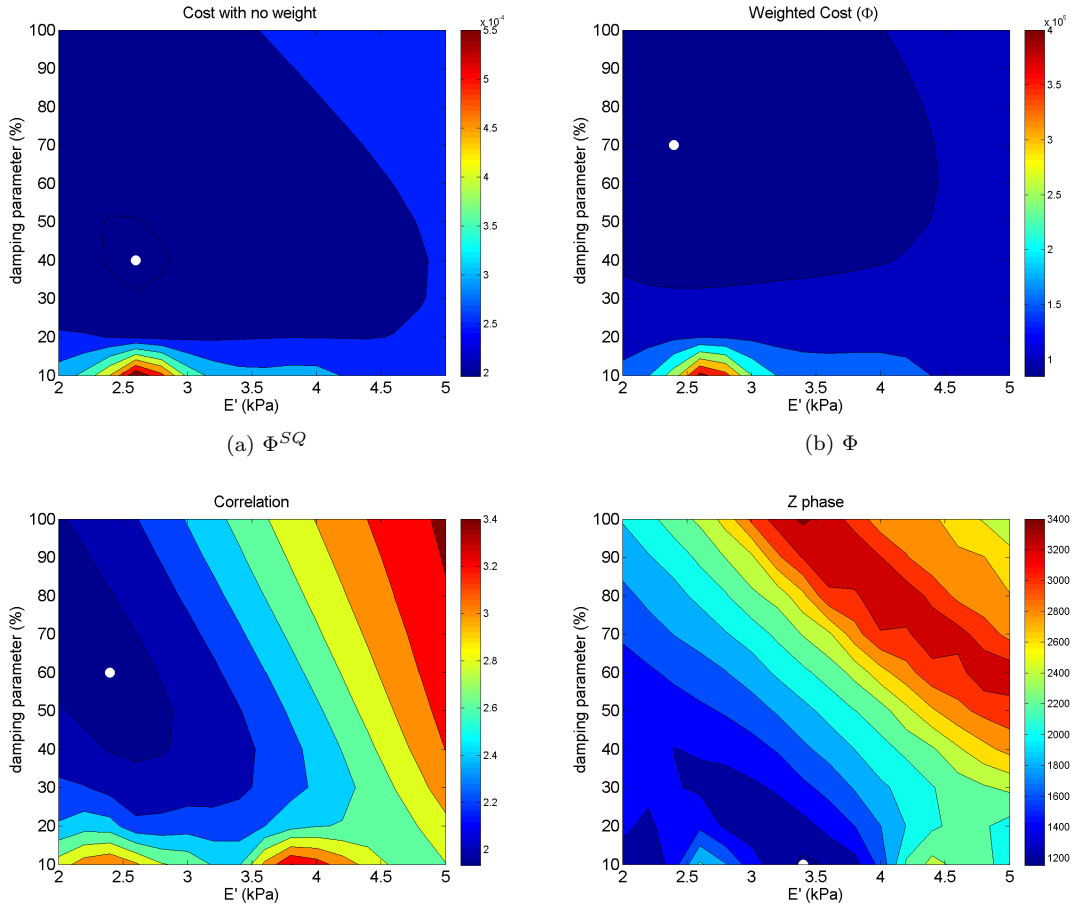

(a) Φ^{SQ} (b) Φ

(c) Γ (d) τ

Figure 7.4: MS016T homogeneous cost surfaces. Squared error, Φ^{SQ} (7.4a), Weighted cost,Φ (7.4b), Correlation cost, Γ (7.4c) and z phase cost, τ (7.4d).The minimum cost is indicated by a white circle.

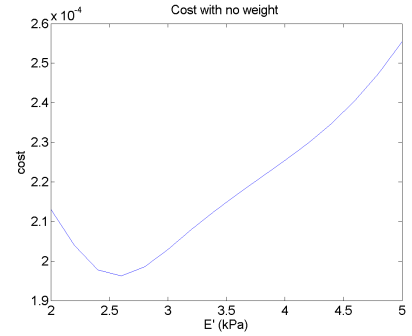

(a) Φ^{SQ} at 40% damping

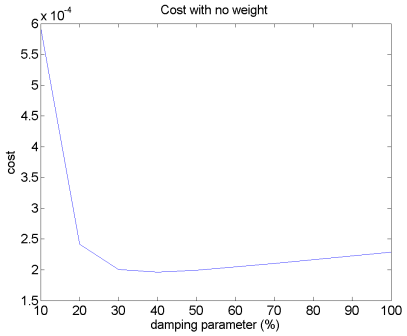

(b) Φ^{SQ} at $E' = 2.6kPa$

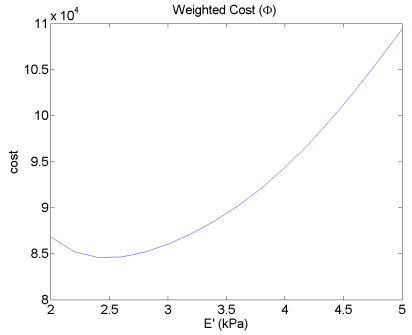

(c) Φ at 70% damping

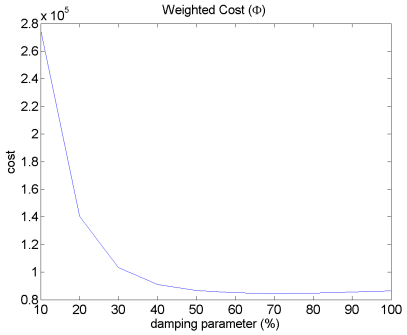

(d) Φ at $E' = 2.4kPa$

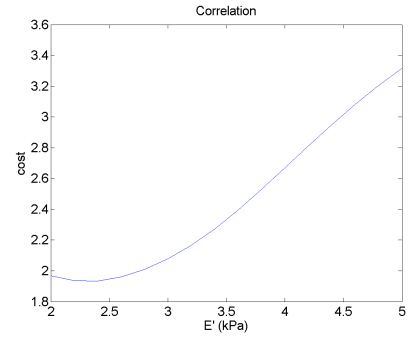

(e) Γ at 60% damping

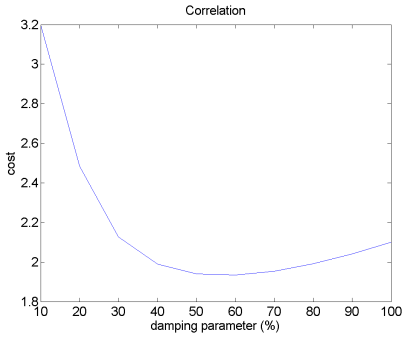

(f) Γ at $E' = 2.4kPa$

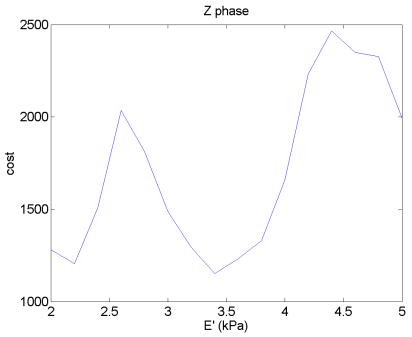

(g) τ at 10% damping

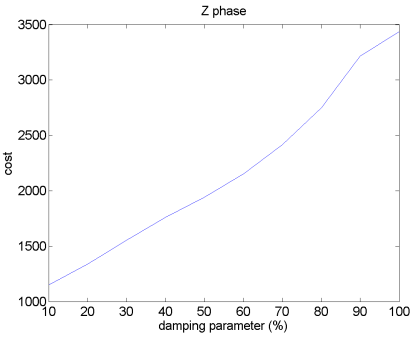

(h) τ at $E' = 3.4kPa$

Figure 7.5: Profiles though the minima of MS016T homogeneous cost surfaces. The profiles run parallel to the axes of the plots in Figure 7.4. Squared error, Φ^{SQ} (7.5a, 7.5b), Weighted cost,Φ (7.5c, 7.5d), Correlation cost, Γ (7.5e, 7.5f) and z phase cost, τ (7.5g, 7.5h).

7.2.2 Location Cost Surface

Figure 7.6 to 7.9 show the inclusion location cost surfaces for MS016T. The most striking difference between the *in vivo* and the phantom MI cost surface shown in Figures 6.17 to 6.20 in Chapter 6 is the complexity of the cost surface. For example, Figure 7.6d shows three minima at $(0, 40, 40)$, $(20, 0, 40)$,and $(-15, 15, 40)$. As found with the phantom MI, in section 6.4.1, τ is unsuccessful as a cost function, most likely due to phase ambiguity in the calculation of phase using Eq. 3.26. However, the tumor is located in the correct position at 3 o'clock using Φ^{SQ}, Φ and Γ.

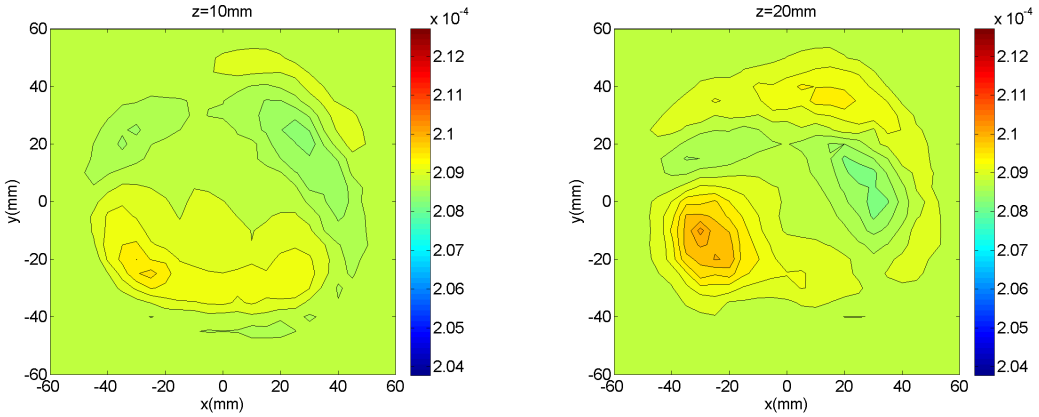

(a) slice at z = 10 mm

(b) slice at z = 20 mm

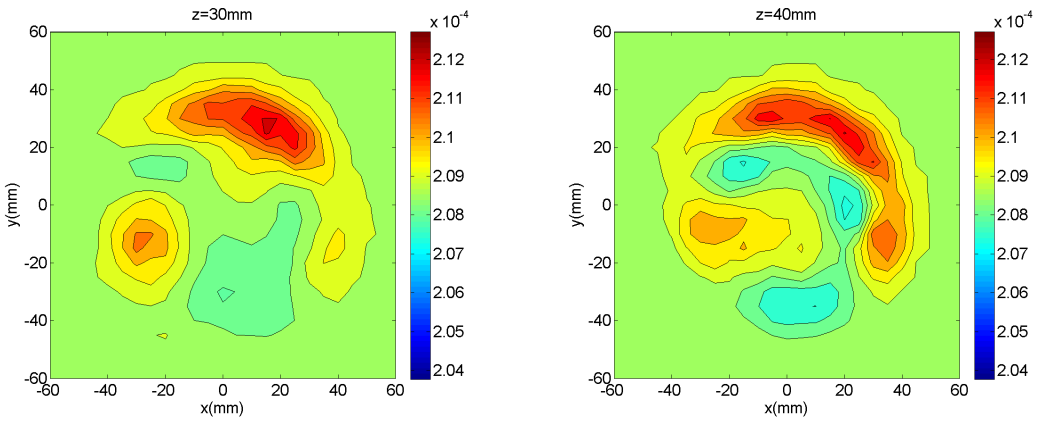

(c) slice at z = 30 mm

(d) slice at z = 40 mm

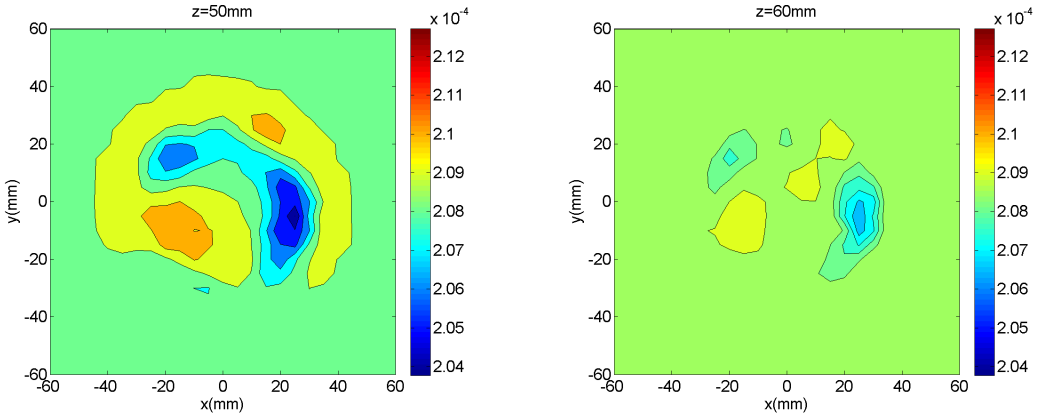

(e) slice at z = 50 mm

(f) slice at z = 60 mm

Figure 7.6: MS016T slices through Φ^{SQ} location cost surface.

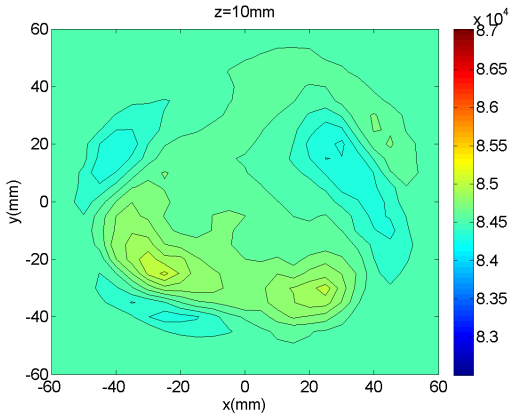

(a) slice at z = 10 mm

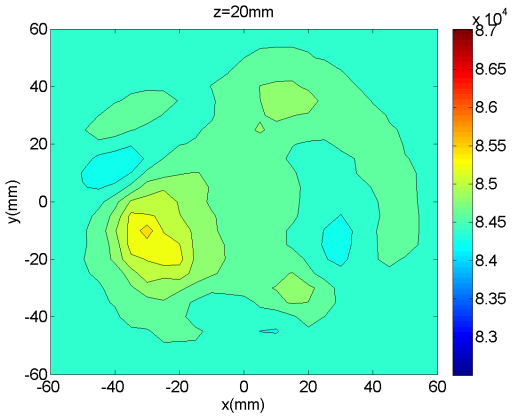

(b) slice at z = 20 mm

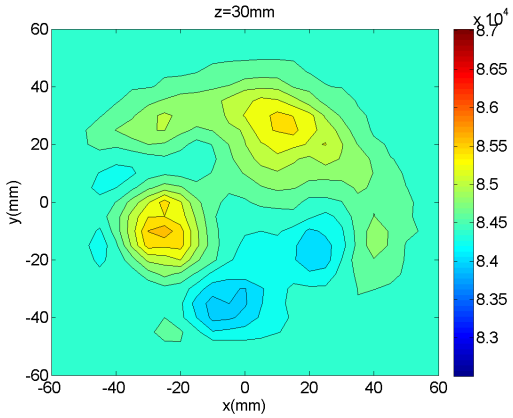

(c) slice at z = 30 mm

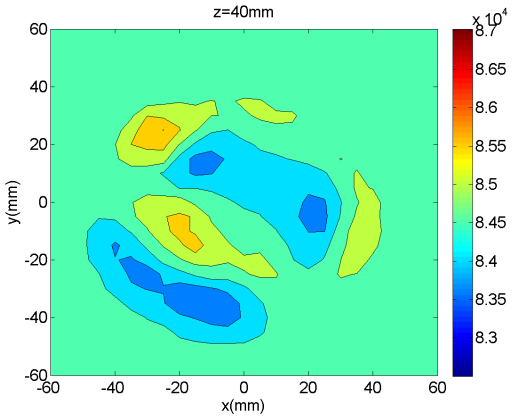

(d) slice at z = 40 mm

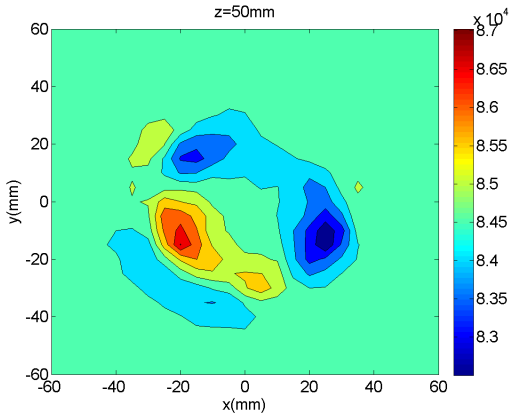

(e) slice at z = 50 mm

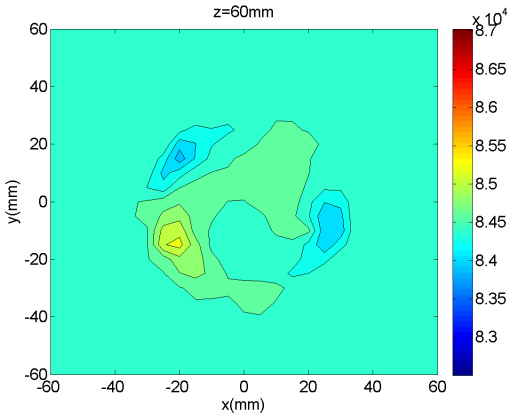

(f) slice at z = 60 mm

Figure 7.7: MS016T slices through Φ location cost surface.

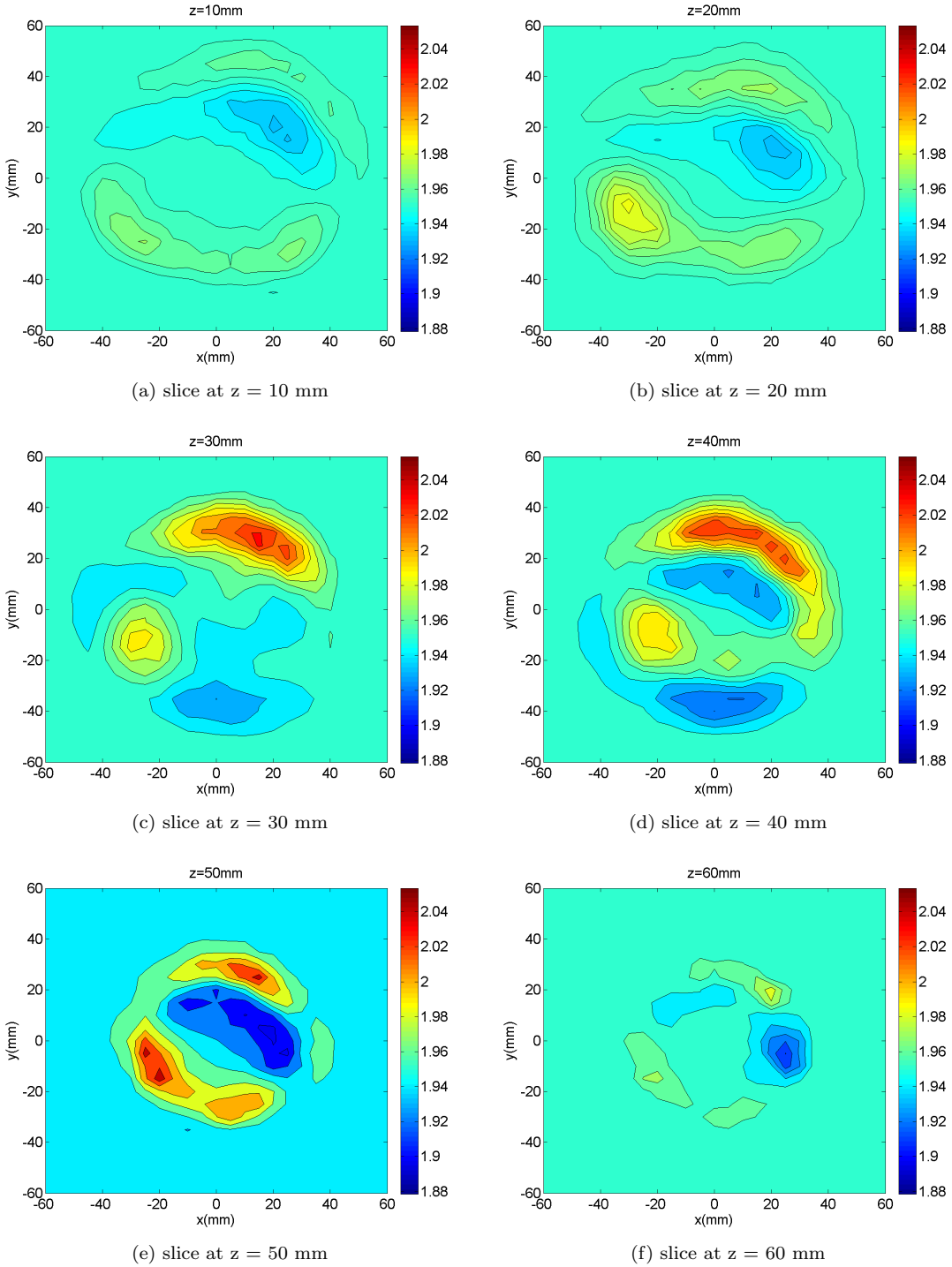

(a) slice at z = 10 mm

(b) slice at z = 20 mm

(c) slice at z = 30 mm

(d) slice at z = 40 mm

(e) slice at z = 50 mm

(f) slice at z = 60 mm

Figure 7.8: MS016T slices through Γ location cost surface

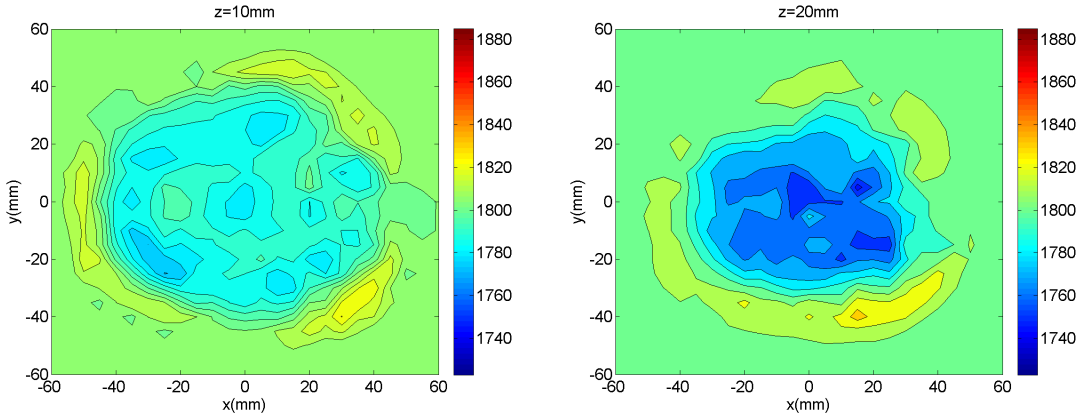

(a) slice at z = 10 mm

(b) slice at z = 20 mm

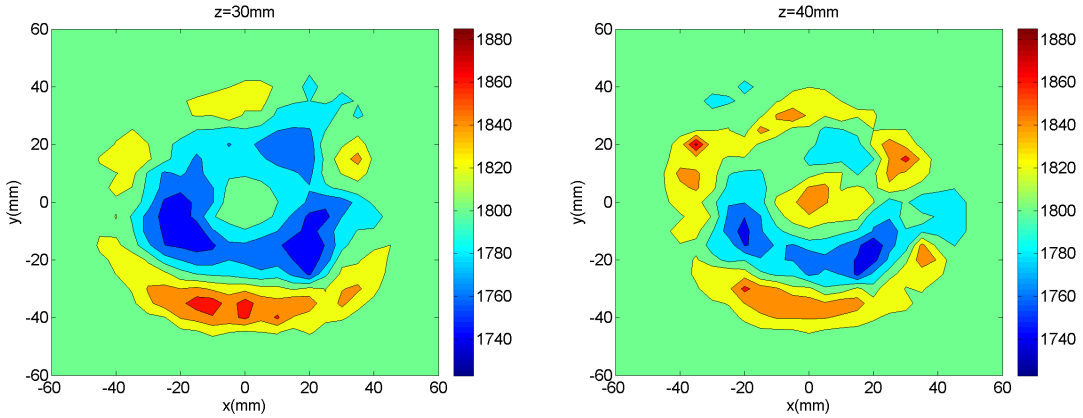

(c) slice at z = 30 mm

(d) slice at z = 40 mm

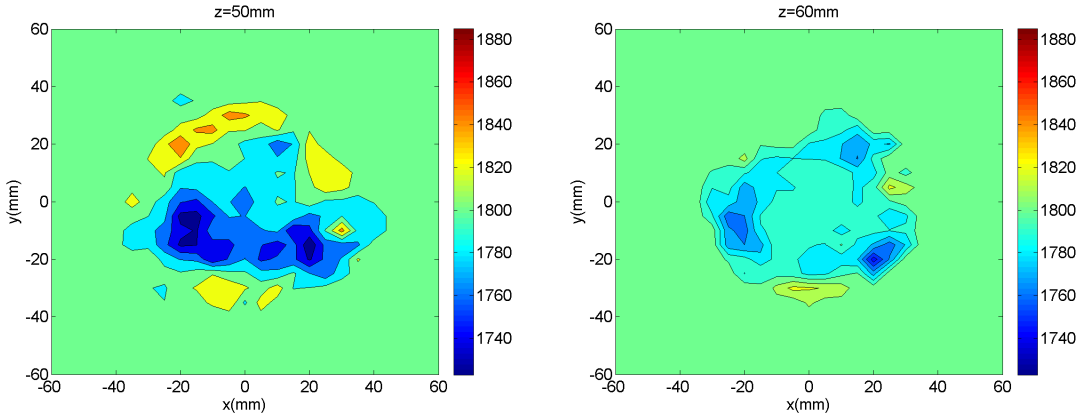

(e) slice at z = 50 mm

(f) slice at z = 60 mm

Figure 7.9: MS016T slices though τ location cost surface

7.3 Single Frequency Reconstructions

7.3.1 Tumor Location Results

Figures 7.10, 7.11 and 7.12 show a projected image of the measured displacement, $\mathbf{u}_m$, for KF004T, KS003T and MS016T respectively. For comparison, Figure 7.13 shows the same image for phantom Tr10. The motion pattern in the phantom is much more regular than that observed *in vivo*, with clear circular wave patterns extending out from the actuator. The reconstructed background parameters for the three patients are given in Table 7.6. E'_B is the same order of magnitude as the phantoms, but the reconstructed background damping parameter, ζ_B, *in vivo* is much higher, ranging from 60% to 120% for the three patients.

Patient	$\mathbf{E'_B(kPa)}$	$\zeta_\mathbf{B}(\%)$
KF004T	1.8	60
KS003T	2.9	120
MS016T	2.5	70

Table 7.6: Background parameter results for single frequency *in vivo* data.

The optimal regions for the tumor location reconstructions are shown in Figures 7.14-7.16, with the quantitative description of the optimal regions given in Table 7.7. The single frequency tumor location performed reasonably well, locating a tumor in the correct area of the breast for KF004T, MS016T and close to the correct area for KS003T. The true tumor location is between 1 and 2 o'clock for KS003T, the single frequency reconstruction placed the tumor at 12 o'clock. In terms of the optimal region, the reconstruction underestimates the size of the tumor for KS003T, with the reconstruction only 6% of the true tumor size. For KF004T the optimal region overestimates the tumor, with the optimal region 1.11 times the size of the true tumor. For MS016T the optimal region is 52% of the true inclusion size.

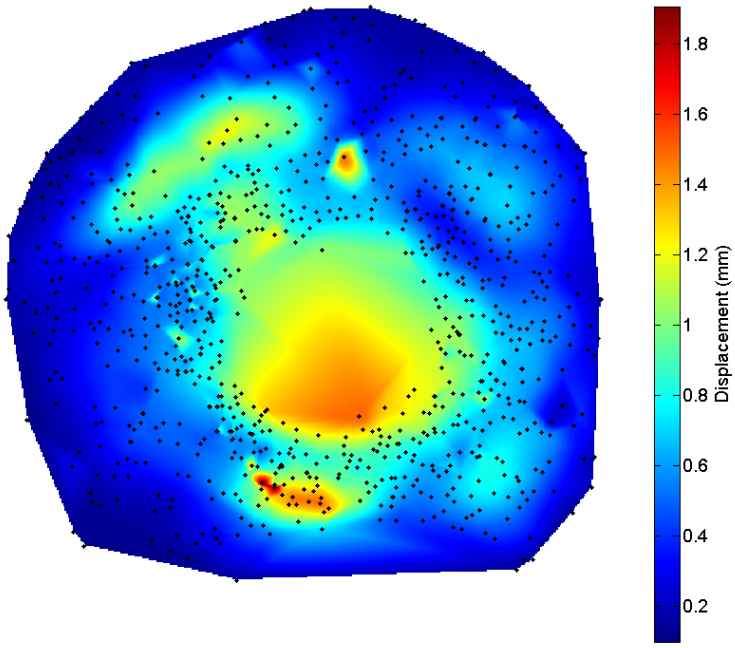

Figure 7.10: Measured displacement for KF004T with an actuation frequency of 20 Hz and amplitude of 0.5 mm. The black squares indicate measurement locations. The data is interpolated to cover the surface and projected flat.

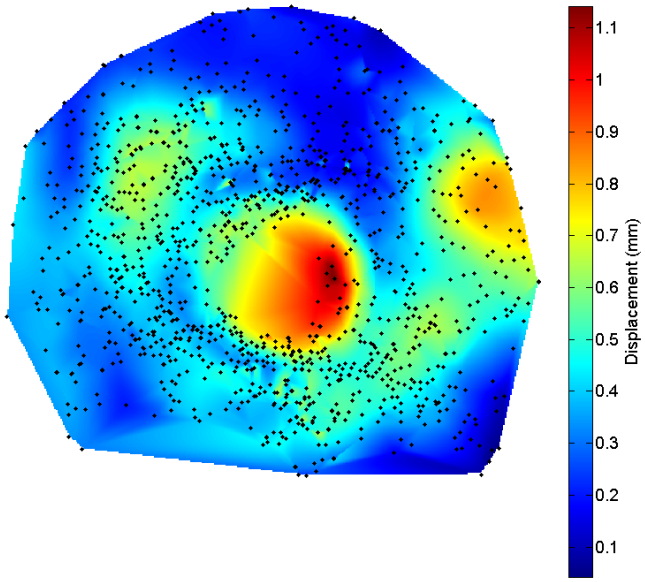

Figure 7.11: Measured displacement for KS003T with an actuation frequency of 30 Hz and amplitude of 0.5 mm. The black squares indicate measurement locations. The data is interpolated to cover the surface and projected flat.

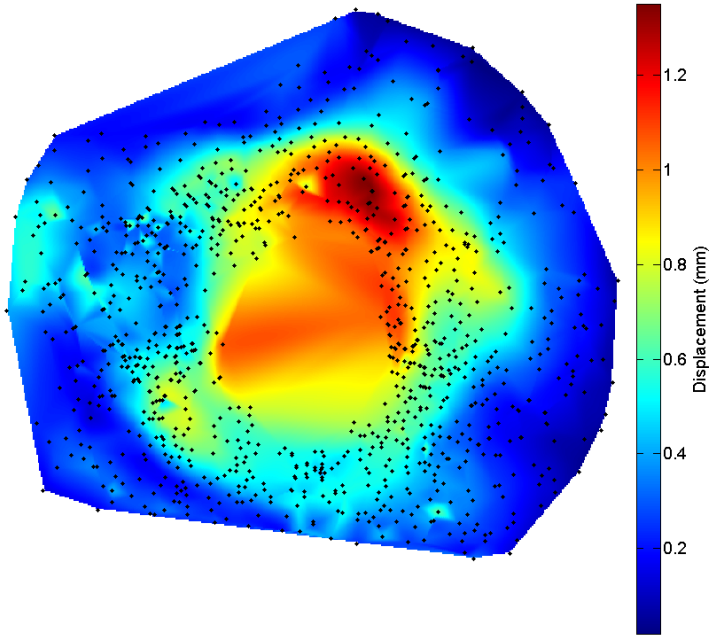

Figure 7.12: Measured displacement for MS016T with an actuation frequency of 20 Hz and amplitude of 0.5 mm. The black squares indicate measurement locations. The data is interpolated to cover the surface and projected flat.

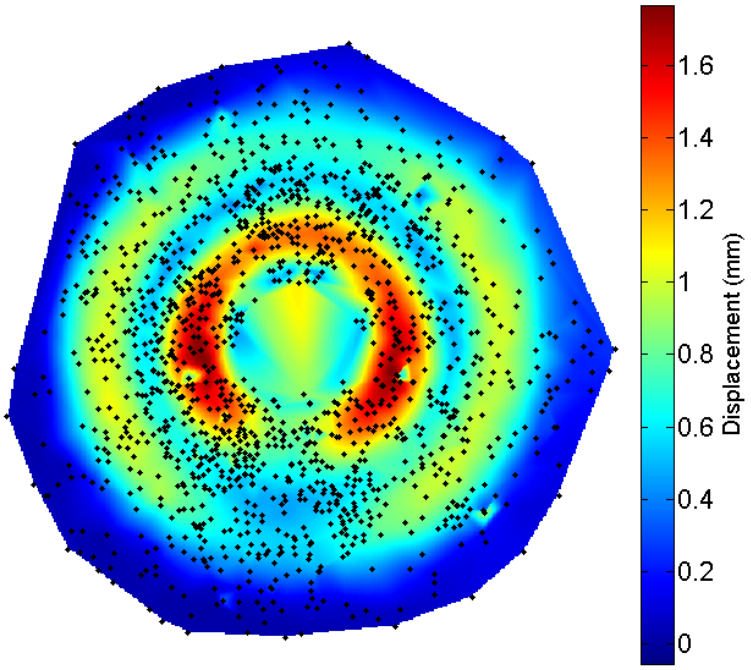

Figure 7.13: Measured displacement for phantom Tr10 with an actuation frequency of 20 Hz and amplitude of 0.5 mm. The black squares indicate measurement locations. The data is interpolated to cover the surface and projected flat. The wave pattern is much clearer to the human eye in phantom data compared to the *in vivo* datasets.

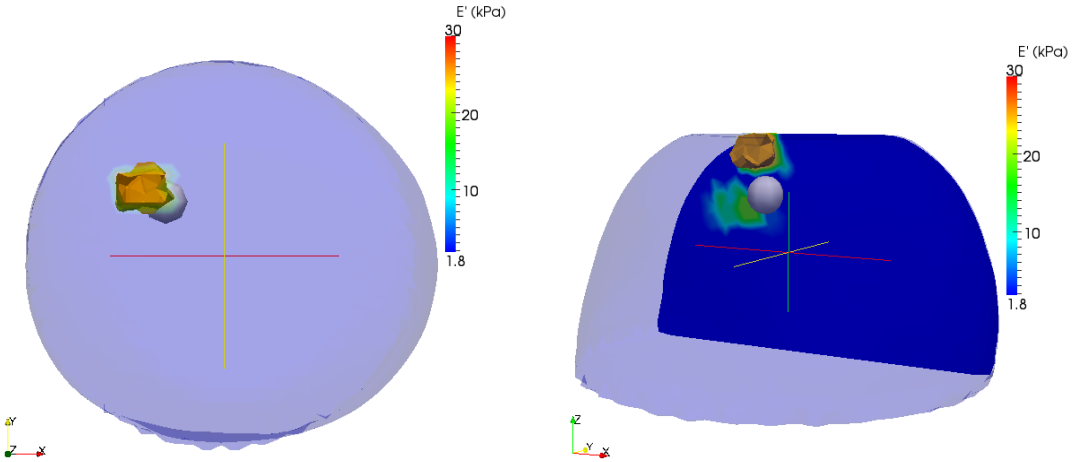

(a) Top view

(b) Slice through breast

Figure 7.14: Single frequency reconstruction for patient KF004T. The actuation frequency was 20 Hz. The true tumor is located at 10:30 and shown in gray.

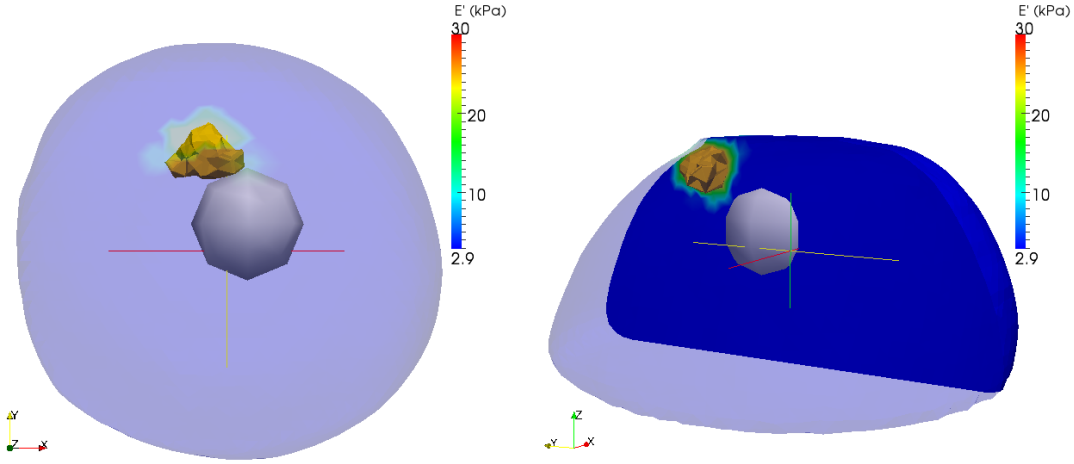

(a) Top view (b) Slice through breast

Figure 7.15: Single frequency reconstruction for patient KS003T. The actuation frequency was 30 Hz. The true tumor is located between 1 and 2 o'clock and shown in gray.

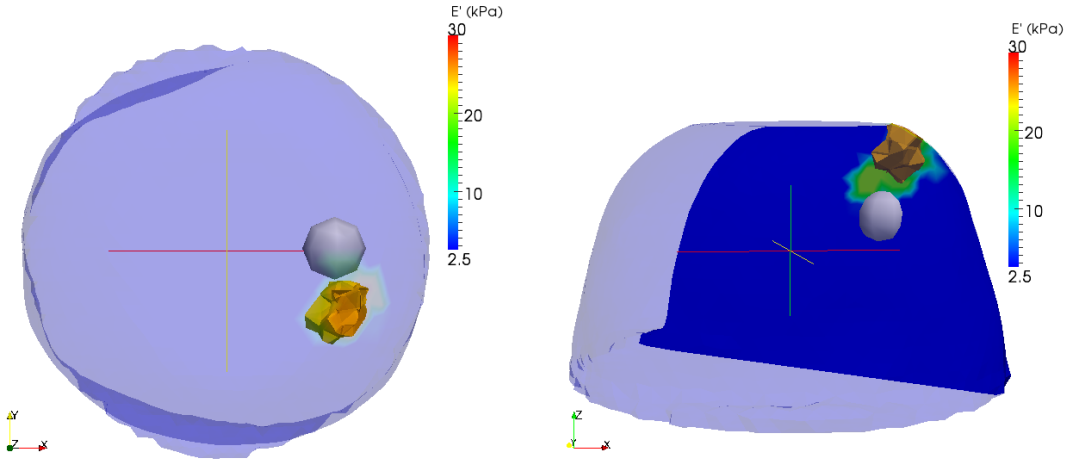

(a) Top view (b) Slice through breast

Figure 7.16: Single frequency reconstruction for patient MS016T. The actuation frequency was 20 Hz. The true tumor is located at 3 o'clock and shown in gray.

Patient	Volume Fraction
KF004T	1.11
KS003T	0.07
MS016T	0.52

Table 7.7: Quantitative description of the optimal region images for the single frequency *in vivo* reconstructions, where *Volume Fraction* is the volume of the 25 kPa contour divided by the volume of the true inclusion.

Comparison of Measured and Simulated Motion

The data quality metrics of signal to noise ($\overline{SNR}$) and coverage (χ), calculated using Eqs. 3.31 and 3.32, for the three patient datasets are given in Table 7.8. The coverage is better *in vivo* than in phantom, with close to 40% coverage for the *in vivo* data compared to 11-28% for the phantom data found in Chapter 5. This is, at least in part, due to the application of a greater number of fiducial markers *in vivo*. The *in vivo* $\overline{SNR}$, which ranges from 1.6 to 5.6, is lower than that of the phantom data in Chapter 5, which had an $\overline{SNR}$ of between 8 and 20. As stated previously, $\overline{SNR}$ is, at least in part, a measure of data-model mis-match. The simulated displacement for KF004T, KS003T and MS016T for the minimum cost background, E'_B, ζ_B, are shown in Figures 7.17a to 7.17c respectively. In all three patients, the simulated displacement is smaller than the measured displacement. The measured displacement for KS003T, shown in Figure 7.11, shows 0.8mm displacement between 1 and 2 o'clock at the chest wall. In contrast, the simulated displacement is damped to virtually zero in the same location. Although the tumor location reconstruction has performed reasonably well, it is clear from the visual comparison of simulated and measured motion that the Finite Element simulations as described in section 2.3 are not providing a good match for displacement *in vivo* near the boundary condition of the chest wall.

Patient	$\overline{\mathbf{SNR}}$	$\boldsymbol{\chi}$ (%)
KF004T	4.6	37
KS003T	1.6	39
MS016T	5.6	39

Table 7.8: Data quality metrics for single frequency *in vivo* data.

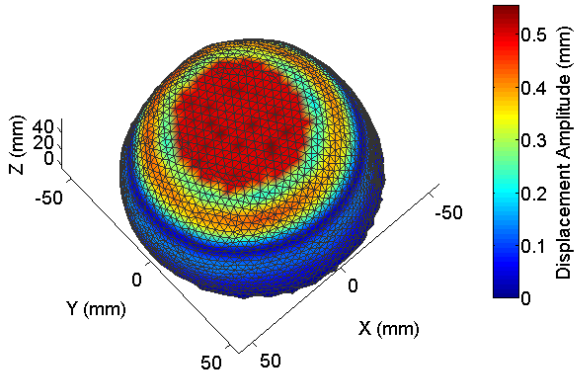

(a) Simulated displacement for KF004T.

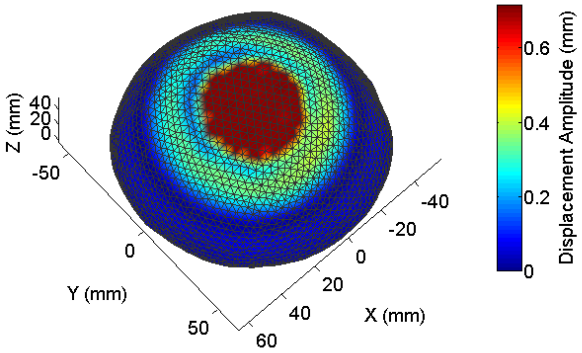

(b) Simulated displacement for KS003T.

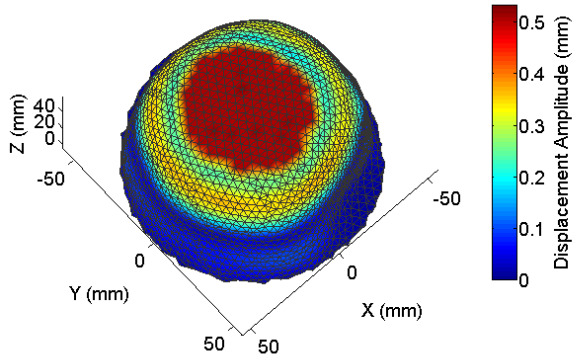

(c) Simulated displacement for MS016T.

Figure 7.17: Simulated displacement for the three patients.

7.3.2 Healthy Breast Results

For KF004H the 20Hz data has a tracking problem, which has lead to the misshapen mesh shown in Figure 7.18. Thus this frequency was discarded and the 25Hz data was used in the single frequency reconstruction of KF004H. Figures 7.19 to 7.21 show the measured displacement for patients KF004H, KS003H and MS016H respectively. Table 7.9 gives the reconstructed background parameters. The data quality metrics are given in Table 7.10. The $\overline{SNR}$ is low, ranging from 1.5 to 5 indicating that the fiducials are not following an elliptical path. The measured displacement for KS003H shows large (~0.7 mm) displacements at the chest wall at 4 o'clock, 7 o'clock and 11 o'clock. The reconstruction results are given in Figures 7.22 to 7.24. The results are unsuccessful for all patients, locating a tumor within each of the healthy breasts.

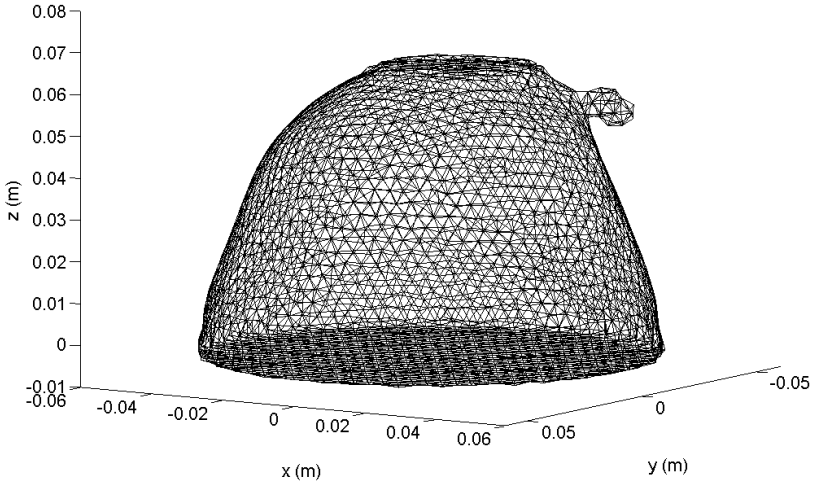

Figure 7.18: Mesh created from 20 Hz data for patient KF004H. There is an obvious motion tracking problem, thus the 25 Hz data was used instead for the single frequency reconstruction.

Patient	$\mathbf{E'_B}$**(kPa)**	$\boldsymbol{\zeta_B}$ **(%)**
KF004H	1.6	80
KS003H	1.7	150
MS016H	1.9	50

Table 7.9: Background parameter results for single frequency *in vivo* data for the healthy cases.

Patient	$\overline{\textbf{SNR}}$	χ (%)
KF004H	2.2	33
KS003H	1.5	39
MS016H	5	36

Table 7.10: Data quality metrics for single frequency *in vivo* data.

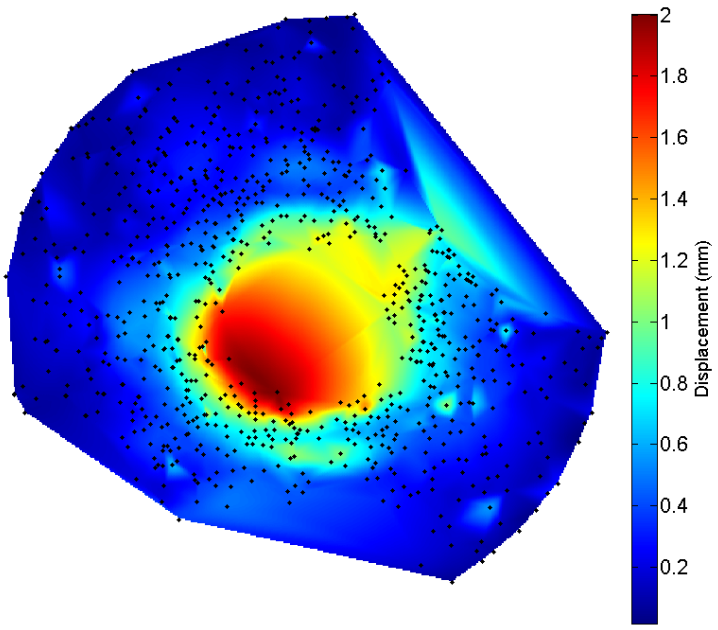

Figure 7.19: Measured displacement for KF004H with an actuation frequency of 25 Hz and amplitude of 0.5 mm. The black squares indicate measurement locations. The data is interpolated to cover the surface and projected flat.

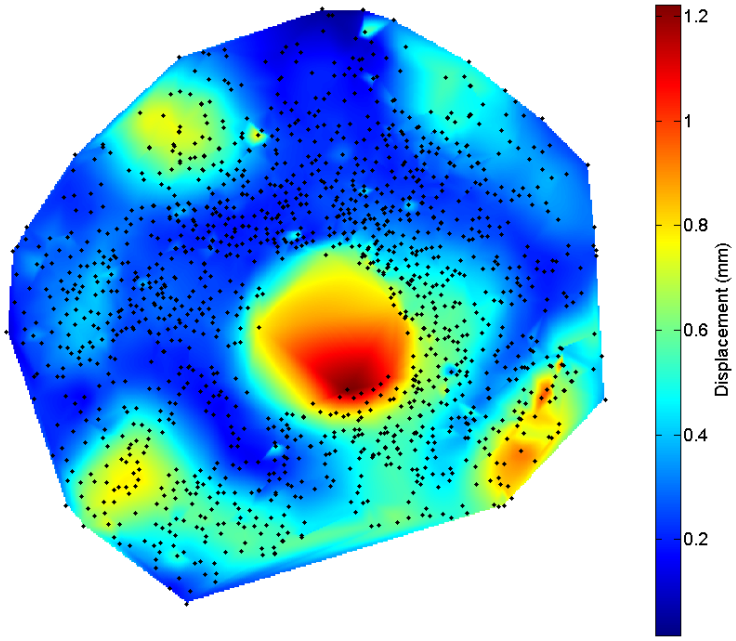

Figure 7.20: Measured displacement for KS003H with an actuation frequency of 30 Hz and amplitude of 0.7 mm. The black squares indicate measurement locations. The data is interpolated to cover the surface and projected flat.

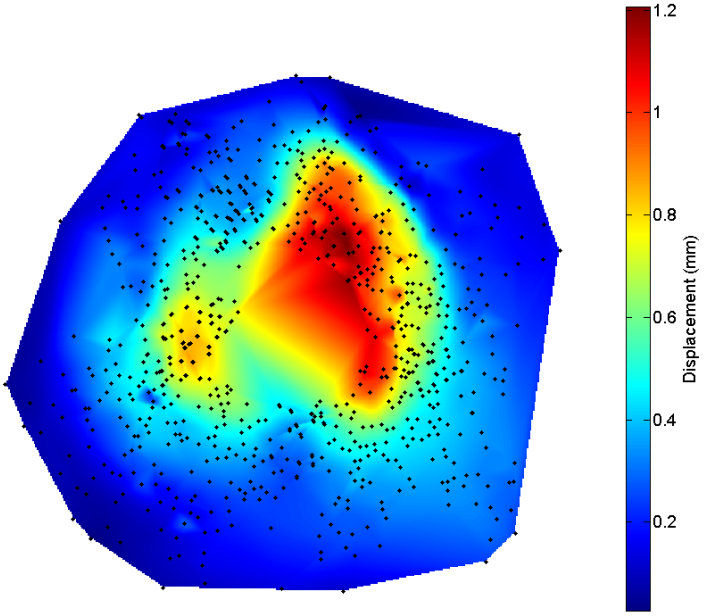

Figure 7.21: Measured displacement for MS016H with an actuation frequency of 20 Hz and amplitude of 0.5 mm. The black squares indicate measurement locations. The data is interpolated to cover the surface and projected flat.

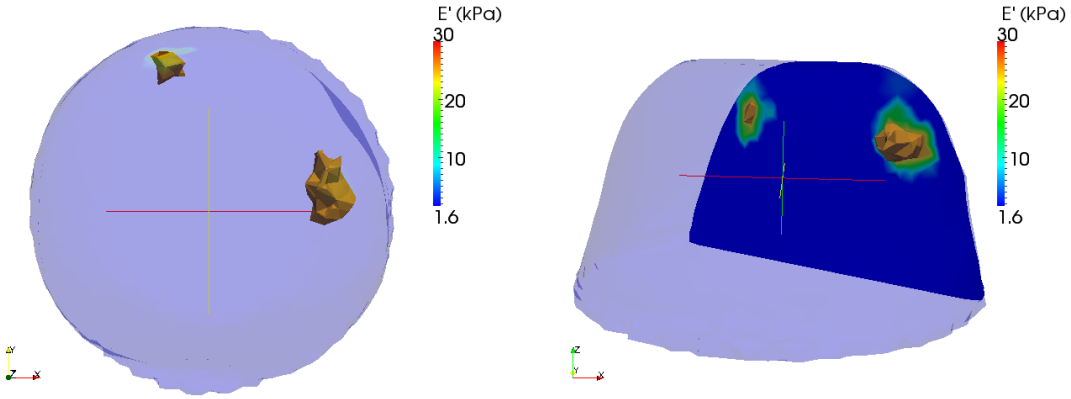

(a) Top view

(b) Slice through breast

Figure 7.22: Single frequency reconstruction for patient KF004H. The actuation frequency was 25Hz.

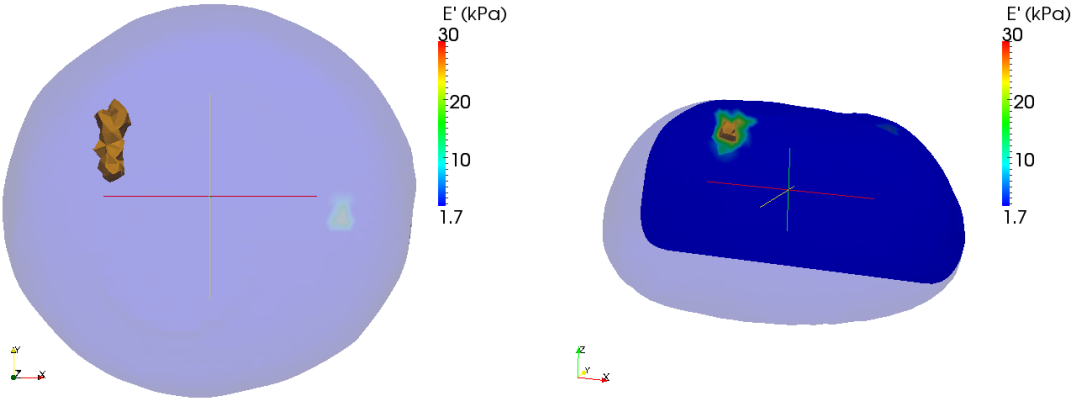

(a) Top view (b) Slice through breast

Figure 7.23: Single frequency reconstruction for patient KS003H. The actuation frequency was 30Hz.

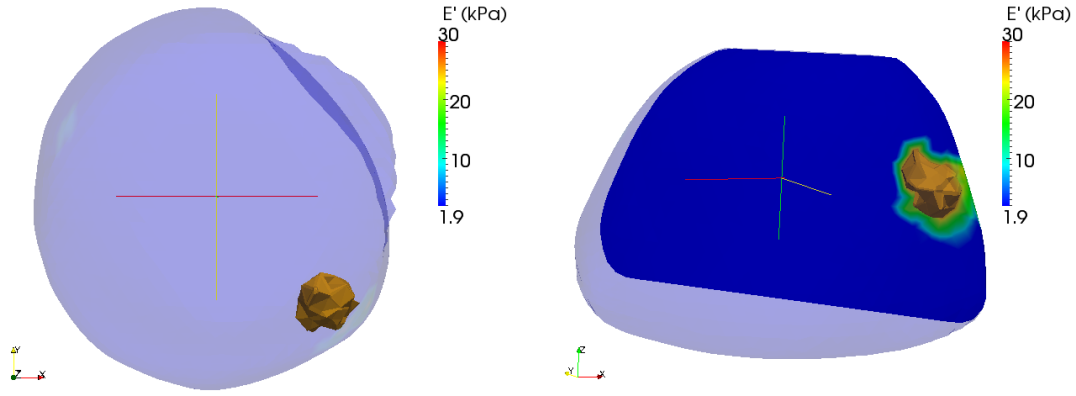

(a) Top view (b) Slice through breast

Figure 7.24: Single frequency reconstruction for patient MS016H. The actuation frequency was 20Hz.

7.4 Multiple Frequency Reconstructions

The techniques developed in Chapter 5 are applied to the three patients. The cost function used was combined normalized cost, Φ^C, as calculated in Eq. 3.35. Table 7.11 shows the frequencies used in the reconstruction of the tumor cases. Table 7.12 shows the frequencies used in the reconstruction of the healthy breast cases. Frequencies with obvious tracking problems such as 20 Hz for KF004T, shown in Figure 7.18 and 26 Hz for MS016T shown in Figure 3.8 in Chapter 3 were discarded.

Patient	**Frequencies Used**
KF004T	15, 18, 20, 25, 30
KS003T	20, 30, 50
MS016T	16, 18, 20, 22, 24, 28 30, 32, 34, 36, 38, 40, 42, 44, 46, 48, 50

Table 7.11: Frequencies used in the tumor case multi-frequency reconstructions

Patient	**Frequencies Used**
KF004H	15, 18, 20, 30
KS003H	20, 30, 50
MS016H	16, 18, 20, 22, 24, 26, 28 30, 32, 34, 36, 38, 40, 42, 44, 46, 48, 50

Table 7.12: Frequencies used in the healthy breast multi-frequency reconstructions

7.4.1 Data Quality Metrics

The data quality metrics, mean displacement, mean signal to noise and coverage calculated using Eqs. 3.29-3.32 are shown in Figures 7.25 to 7.27. The mean displacement with frequency *in vivo* does not exhibit the multiple resonance peaks within the actuation frequency range as was found in phantoms in Chapter 5, section 5.2.1. The largest motions occur at 18-20 Hz for each of the patients. The signal to noise *in vivo* is lower than that found in the phantom experiments, with the highest *in vivo* $\overline{SNR} = 6$ compared to the lowest phantom $\overline{SNR} = 8$ and the typical phantom $\overline{SNR}$ between 12 and 20. KS003 is the poorest dataset in terms of signal to noise, with $\overline{SNR}$

between 1 and 2 across all frequencies for both breasts. The coverage for the *in vivo* data ranges from 32% to 40% with no noticeable frequencies exhibiting poor coverage, unlike the phantom results of section 5.2.1, where the large displacement around the first resonant frequency caused a corresponding reduction in coverage.

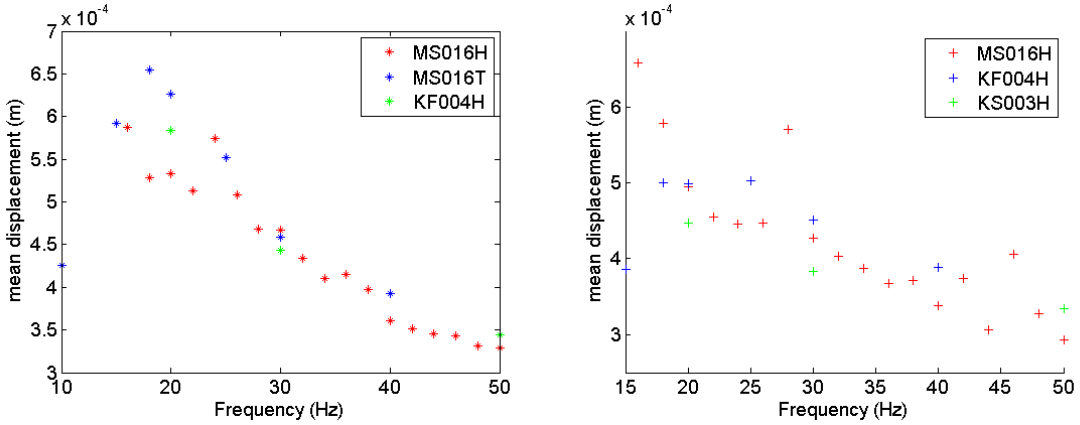

(a) Tumor case (b) Healthy case

Figure 7.25: Mean measured displacement, μ_A, against frequency.

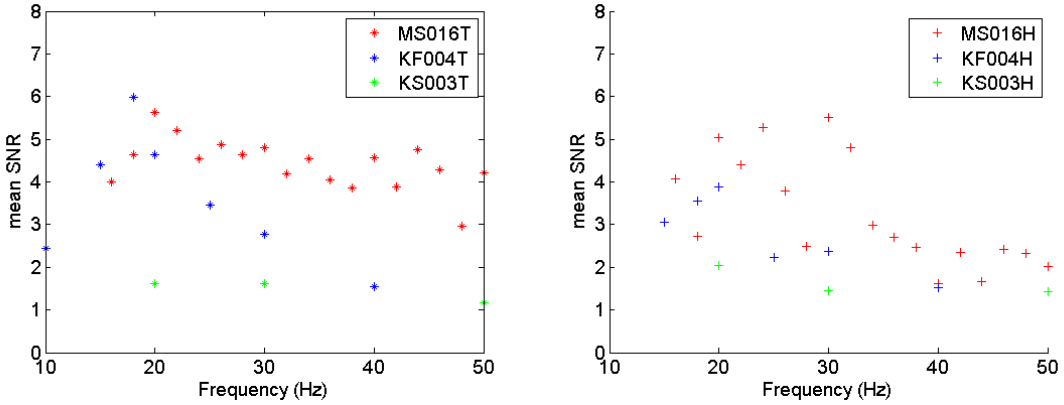

(a) Tumor case (b) Healthy case

Figure 7.26: Mean signal to noise, $\overline{SNR}$, against frequency.

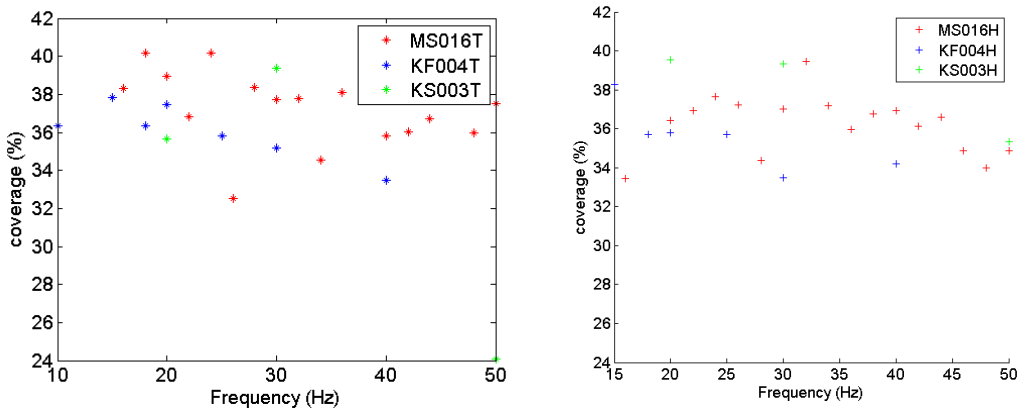

(a) Tumor case (b) Healthy case

Figure 7.27: Coverage, χ, against frequency.

7.4.2 Tumor Location Results

The multi frequency result for KF004T shown in Figure 7.28 locates the tumor in the correct area of the breast, with the optimal region providing a similar overestimation of tumor size as the single frequency reconstruction: 1.12 times the size of the tumor. For KS003T the optimal region is in the correct location between 1 and 2 o'clock. Again the 5 mm inclusion assumption has lead to an underestimation of the true tumor volume, with the optimal region 8% of the true tumor size, but has correctly identified the presence and location of the tumor. The multi-frequency reconstruction for MS016T for the lower frequencies, 16 Hz to 28 Hz, shown in Figure 7.30, locates the tumor in the correct area of the breast, at 3 o'clock. The higher frequency reconstructions, 30 Hz to 38 Hz shown in Figure 7.31, and 40 Hz to 50 Hz, shown in Figure 7.32, both locate the tumor incorrectly, placing the tumor at approximately 8 o'clock.

Patient	Volume Fraction
KF004T	1.12
KS003T	0.08
MS016T	0.54
	0.48
	0.59

Table 7.13: Quantitative description of the optimal region images for multi-frequency *in vivo* reconstructions, where *Volume Fraction* is the volume of the 25 kPa contour divided by the volume of the true inclusion. The true tumor is shown in gray.

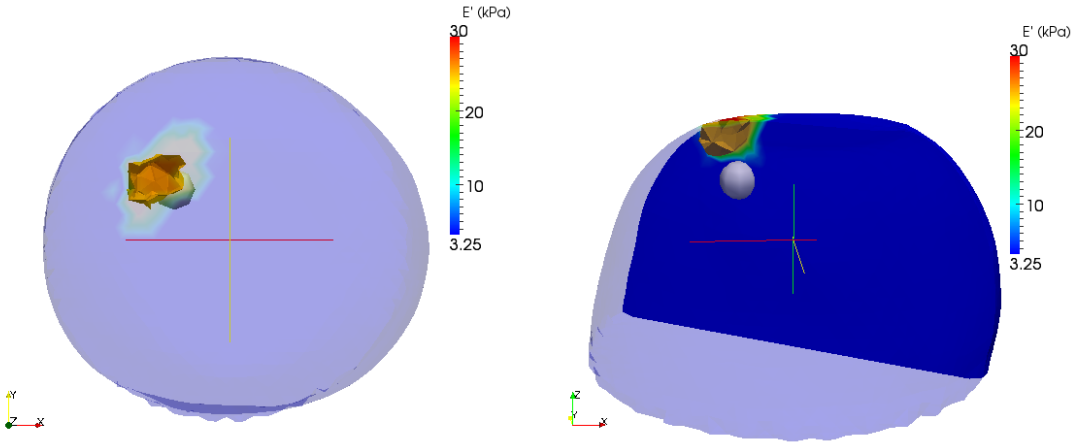

(a) Top view (b) Slice through breast

Figure 7.28: Multi-frequency reconstruction result for patient KF004T. The contour is 25 kPa. The true tumor is shown in gray.

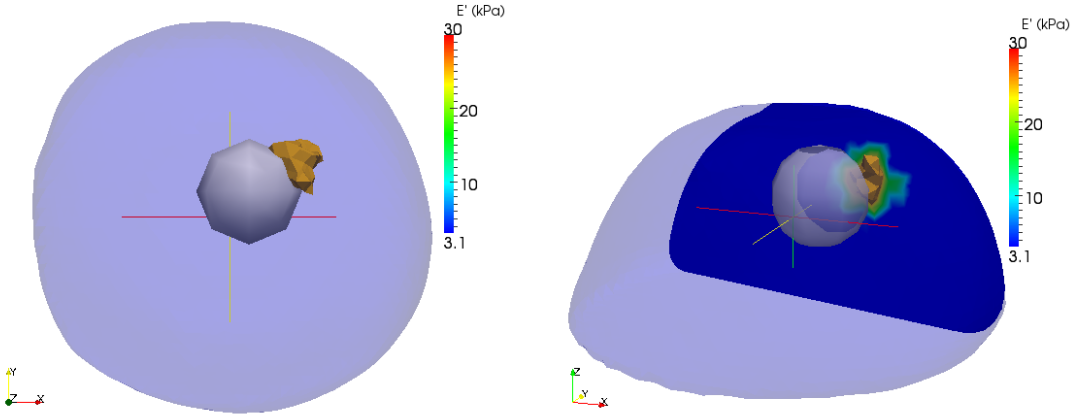

(a) Top view (b) Slice through breast

Figure 7.29: Multi-frequency reconstruction result for patient KS003T. The contour is 25 kPa. The true tumor is shown in gray.

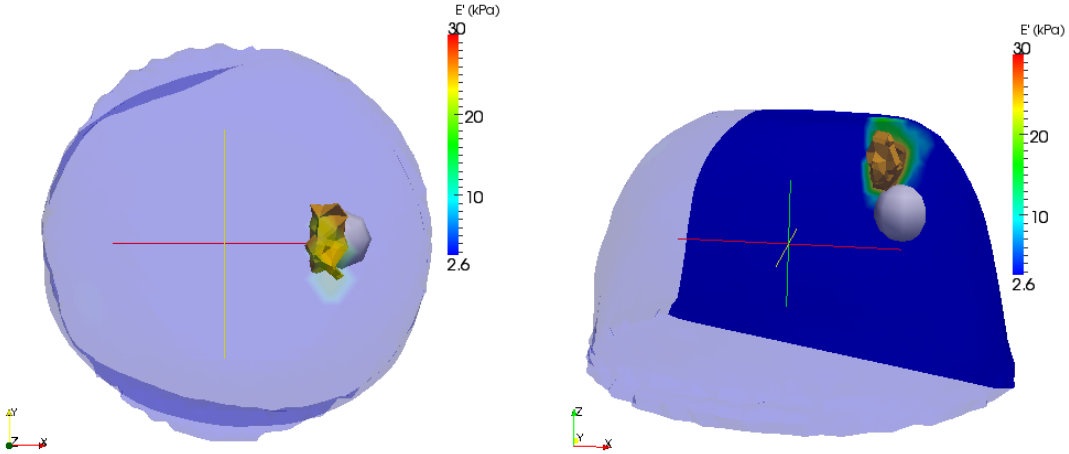

(a) Top view (b) Slice through breast

Figure 7.30: Multi-frequency reconstruction result for patient MS016T using 16 Hz to 28 Hz. The contour is 25 kPa. The true tumor is shown in gray.

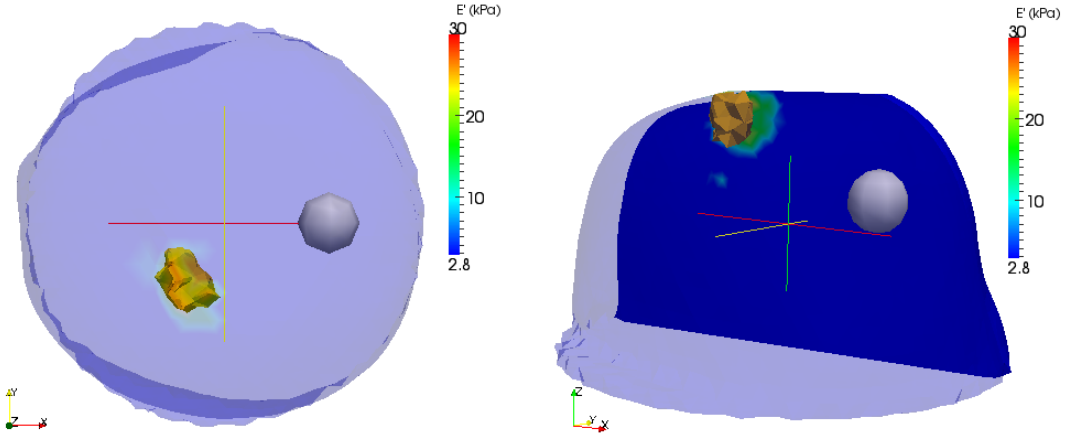

(a) Top view (b) Slice through breast

Figure 7.31: Multi-frequency reconstruction result for patient MS016T using 30 Hz to 38 Hz. The contour is 25 kPa. The true tumor is shown in gray.

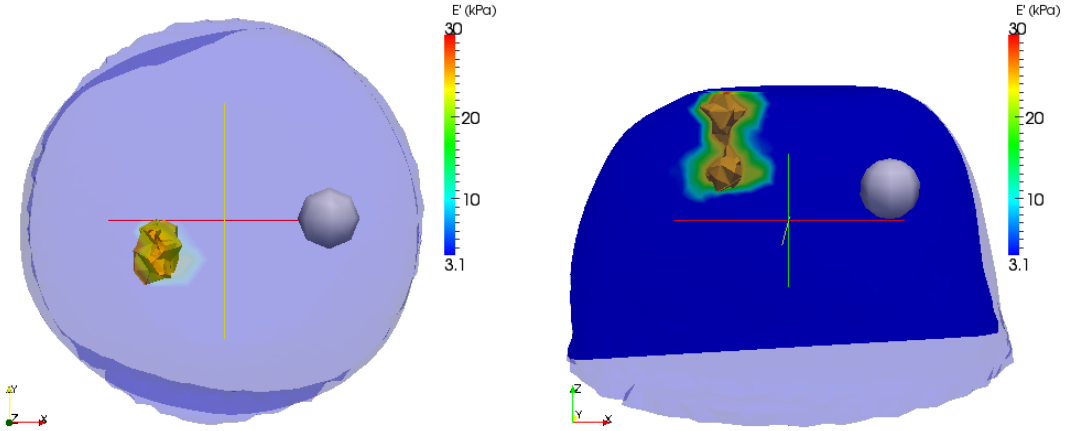

(a) Top view

(b) Slice through breast

Figure 7.32: Multi-frequency reconstruction result for patient MS016T using 40 Hz to 50 Hz. The contour is 25 kPa. The true tumor is shown in gray.

7.4.3 Healthy Breast Results

The multi-frequency result for KF004H is shown in Figure 7.28. The reconstruction result has placed a tumor at 12 o'clock. The multi-frequency reconstruction result for KS003H is shown in Figure 7.29. As with the single frequency result of Figure 7.23, the reconstruction has placed a tumor at 10 o'clock. The multi-frequency results for patient MS016H are shown in Figures 7.30 to 7.32. All three frequency range results have placed a tumor 'beneath' the actuator *(Note that the DIET motion tracking is referenced to a z axis which is positive downwards, thus, in reality, the breast is hanging pendant and actuated from below)*. In contrast, the 20 Hz single frequency reconstruction placed a tumor at 4:30 at the edge of the breast. The combination of multi-frequency data has removed this tumor at the edge of the breast, but still the reconstruction algorithm is unable to discount solutions 'beneath' the actuator.

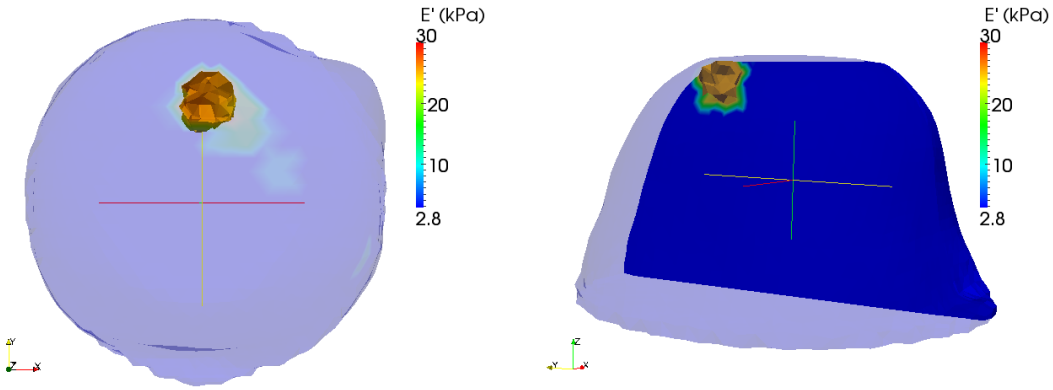

(a) Top view (b) Slice through breast

Figure 7.33: Multi-frequency reconstruction result for patient KF004H. The contour is 25 kPa.

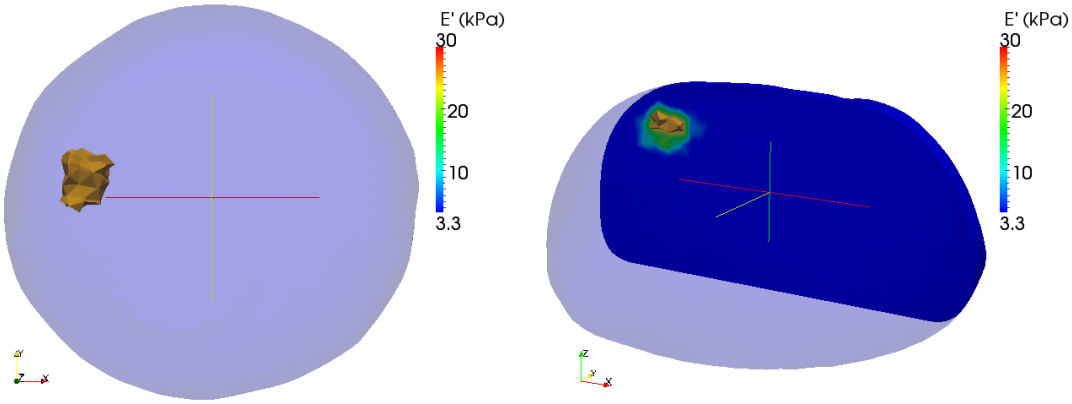

(a) Top view (b) Slice through breast

Figure 7.34: Multi-frequency reconstruction result for patient KS003H. The contour is 25 kPa.

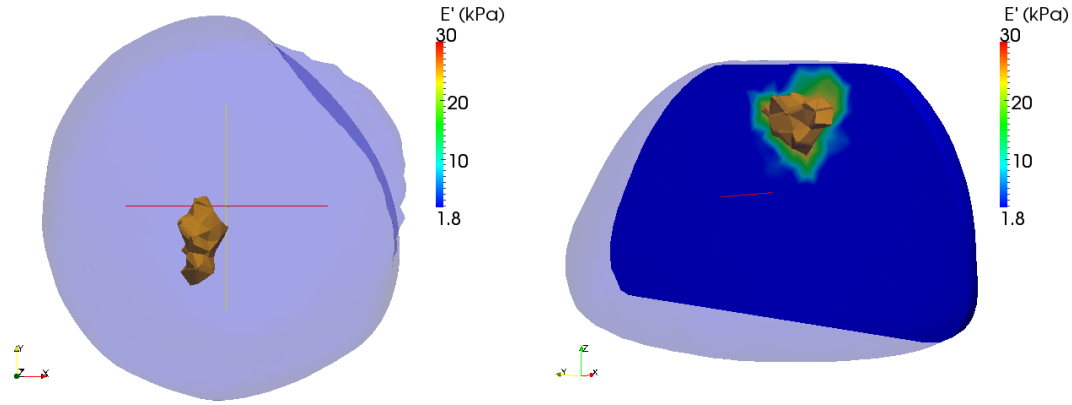

(a) Top view (b) Slice through breast

Figure 7.35: Multi-frequency reconstruction result for patient MS016H using 16 Hz to 28 Hz. The contour is 25 kPa.

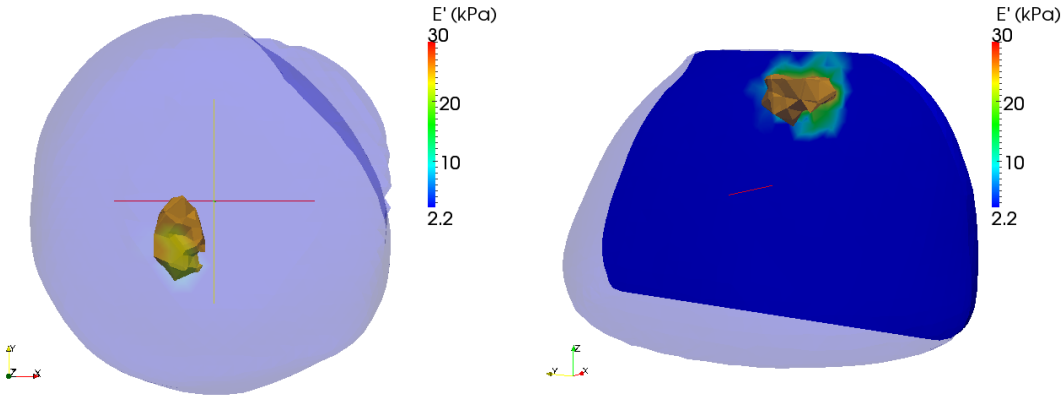

(a) Top view (b) Slice through breast

Figure 7.36: Multi-frequency reconstruction result for patient MS016H using 30 Hz to 38 Hz. The contour is 25 kPa.

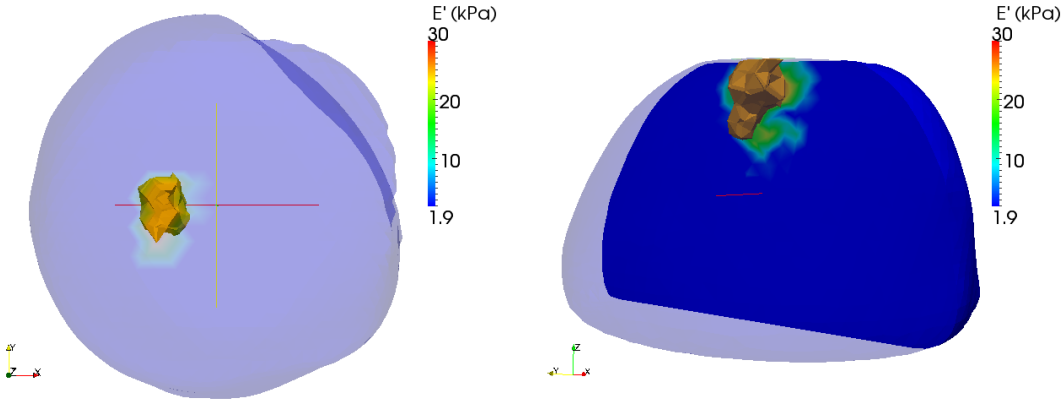

(a) Top view (b) Slice through breast

Figure 7.37: Multi-frequency reconstruction result for patient MS016H using 40 Hz to 50 Hz. The contour is 25 kPa.

7.5 Discussion and Conclusions

The single frequency tumor location results are encouraging, as for KF004T and MS016T the tumor was correctly located. Even with the low $\overline{SNR}$ of KS003T, the tumor location was reasonable, 12 o'clock versus the true location between 1 and 2 o'clock. This is most likely due to the large, 15 mm radius tumor of KS003T having a large effect on motion even in the presence of low signal to noise. For instance, in the measured displacement for KS003T in Figure 7.11, an anomaly in the motion pattern between 12 and 2 o'clock can be observed.

For the multi-frequency tumor location, the KF004T and KS003T reconstructions were successful, identifying and locating the inclusion correctly in each case. The reconstruction results for MS016T were mixed, with the lower frequencies, 16 Hz to 28 Hz providing a successful reconstruction, while the higher frequencies, 30 Hz to 38 Hz and 40 Hz to 50 Hz were unsuccessful at locating the tumor. In contrast, the phantom MI reconstructions in section 6.4.4 were successful across all frequencies from 10 Hz to 60 Hz.

One possible reason for the failure of the MS016T reconstruction at the higher frequencies is the acquisition time. Patient MS016 had seventeen acquisition frequencies compared to three for KS003 and seven for KF004. This would require patient MS016 to remain prone on the DIET prototype for upwards of 30 minutes. The data is collected from low to high frequency so the later, higher frequencies may have been affected more by patient movement than the earlier, lower frequencies as the patient becomes uncomfortable. In phantoms, there is obviously no such problem with 'patient' discomfort. The next DIET prototype will feature higher specification cameras which will allow data from each frequency to be collected in seconds, thus reducing the time required for data acquisition.

The major observation from the *in vivo* results is that although the tumor location has proved somewhat successful, there is a mis-match between measured and simulated displacement. Two possible reasons for this occurring are: the FE model may not suffice for breast tissue, or the boundary conditions applied to the FE model do not match what is occurring in reality. From the plots of measured displacement in Figures 7.10-7.12 and 7.19-7.21 it can be seen that the observed motion is more complex than that observed in the phantom case, for example that of phantom Tr10 shown in Figure 7.13 and that of phantom H shown in Chapter 4, Figure 4.1b. This is both evident visually in the plots, and in the $\overline{SNR}$ of the *in vivo* data. KS003T has the lowest $\overline{SNR}$ and is the dataset with the largest amplitude of actuation, 0.7 mm, compared to 0.5 mm for the other datasets. The $\overline{SNR}$ is low for all three acquisition frequencies for KS003T and KS003H

ranging from 20 Hz to 50 Hz. There is large motion at KS003T at 3 o'clock at the chest wall that cannot be accounted for with the FE forward simulation used in this thesis. From only the two amplitudes used on three patients in this thesis, it is not possible to tell whether it is the increased amplitude of actuation that is applied to KS003 that caused the lower observed $\overline{SNR}$. At some point, increasing the actuation amplitude will invalidate the assumption of linear viscoelasticity, but the low $\overline{SNR}$ observed in KS003 may be due to other factors, such as patient movement or poor actuator contact.

A much larger number of *in vivo* datasets will be required to determine the optimal actuation parameters of the DIET prototype with respect to adhering to the linearly viscoelastic model. It may prove that the linearly viscoelastic model is insufficient, or that it is valid only within a range of actuation parameters. The former would provide a much greater challenge for reconstruction because of the increased cost of simulation for non-linear elastic properties, the latter would no doubt be preferable for any reconstruction algorithm involving numerical simulation of motion.

There is a large difference in material response from the phantom to the patient studies. The model is not performing well with *in vivo* data, but it is much more successful with phantom data. Material assumptions about linearity, isotropy and homogeneity which may be satisfactory for silicone may be problematic for breast tissue. Certainly the silicone does not exhibit the amount of damping observed *in vivo.* More phantom studies are needed to improve the DIET methodology. As with all phantom design, it is critical for the phantom to exhibit the physical properties of interest. For example, in optical tomography, the optical properties of the phantom are key [121], whereas in microwave imaging, the chief concern is the dielectric properties of the phantom [122]. A sensible next step in DIET would be to create a phantom with a skin layer of differing stiffness to better match the mechanical properties human breast.

All three *in vivo* datasets show large displacements at the actuator, compared to the simulated motion which uses the applied actuation of 0.5 mm or 0.7 mm displacement in the z-direction only. This boundary condition assumes that there is no motion in the x or y direction at the contact with the actuator. The current DIET prototype does not have the ability to move the actuator vertically to improve contact with the breast. The prototype under development has this feature, which will allow a compression of the breast for a better contact with the breast and thus less x-y motion at the actuator contact. Figure 7.38 shows the mesh created for the MS016T 20Hz data. As this figure illustrates, the breast is smaller than the hole through which the breast is placed for data collection. As the DIET prototype is developed, more patient-customizable features will

allow the hole to be more finely adjusted for patient size and thus reduce the capacity for patient movement.

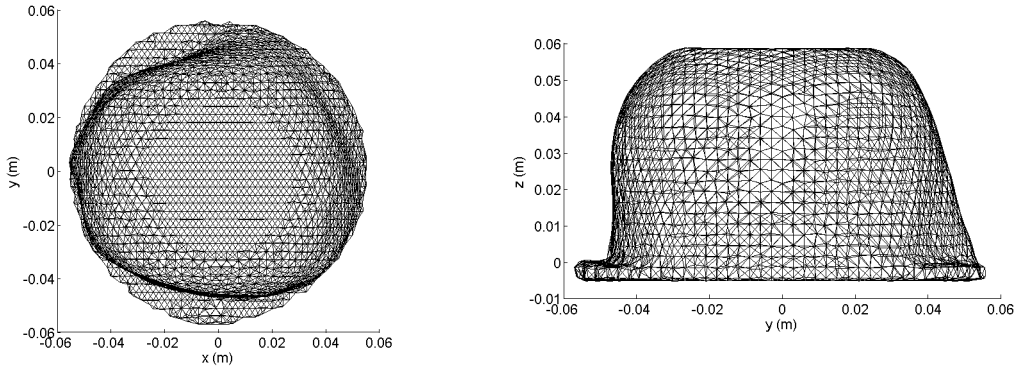

(a) Top view

(b) Side view

Figure 7.38: Mesh for MS016T using 20 Hz data. Note the breast is smaller than the hole through which the breast is placed during data acquisition.

The success with the homogeneous phantom multi-frequency reconstructions of Chapter 5 has not translated to success with *in vivo* data. None of the healthy *in vivo* reconstructions returned a homogeneous 'healthy' reconstruction. The model, $\theta(E'_B, \zeta_B, x_c, y_c, z_c, R, E'_I, \zeta_B)$, assumes that the breast can be approximated by a homogeneous background with the absence or presence of a stiff inclusion to be determined. The phantom MI experiments in Chapter 6 demonstrated that this assumption could be used in more complex phantom geometries to locate a 'cancerous' inclusion. The *in vivo* tumor location results shown in this chapter are encouraging, because they demonstrate that for *in vivo* tumor location this simple assumption can be also used successfully. For the healthy *in vivo* cases examined in this chapter, the assumption is not adequate.

The weakness is in optimizing the background parameters E'_B, ζ_B, which stems from minimizing the cost between the model and the measured data. The presence of a tumor in the three cases examined has provided enough motion difference to be identified as a tumor. The absence of a tumor requires a much stricter adherence to the background model to reject any models that locate tumors within the breast. The MS016H reconstructions shown in Figures 7.35 to 7.37 all locate a tumor 'beneath' the actuator. There is no motion information at the actuator contact, only the applied boundary conditions which *in vivo* may not be correct, a considerable obstacle to correct FE motion simulation.

To explain why solutions 'beneath' the actuator are providing a better fit to the data than the homogeneous solution, let us examine two cases: an inclusion located some distance from the

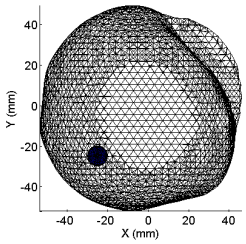

(a) Inclusion location, top view

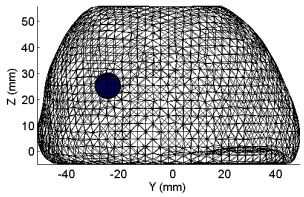

(b) Inclusion location, side view

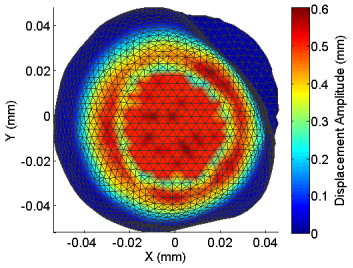

(c) Inclusions FE solution (1).

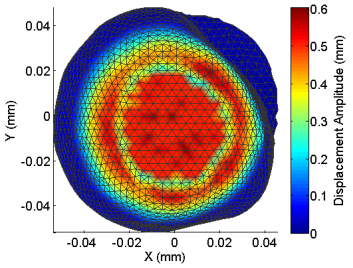

(d) Homogeneous FE solution (2).

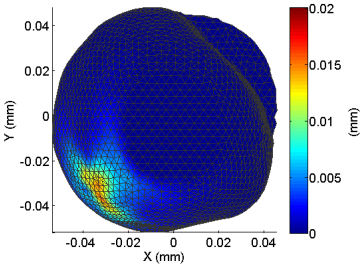

(e) Difference between solutions 1 and 2.

Figure 7.39: Inclusion some distance from the actuator (7.39a, 7.39b). Forward simulations with (7.39c) and without (7.39d) the inclusion, and the difference between the forward simulations (7.39e).

actuator and an inclusion beneath the actuator. For both cases, the FE mesh is that of MS016H with an actuation frequency of 30 Hz. Figure 7.39 illustrates the case of an inclusion that is some distance from the actuator. Figures 7.39a and 7.39b show the location of the inclusion. Figure 7.39c is an FE simulation with the inclusion present and Figure 7.39d shows the homogeneous FE simulation. Figure 7.39e is the difference between 7.39d and 7.39d, *i.e.* the anomaly due to the inclusion. The anomaly is localized around the inclusion.

The case of an inclusion that is 'beneath' the actuator is illustrated in Figure 7.40. Figures 7.40a and 7.40b show the location of the inclusion and Figure 7.40c is an FE simulation with the inclusion present. For ease of visual comparison, the homogeneous FE simulation is plotted again in Figure 7.40d. Figure 7.40e shows the difference between the simulations shown in Figures 7.40c and 7.40d. Here the anomaly is at the edge of the actuator. For reconstructions from DIET data, any error in the boundary conditions, such as neglecting x-y motion, which may be common across all frequencies, or noise at the actuator contact, would appear as misfit to the homogeneous solution and thus be interpreted as an inclusion beneath the actuator. This creates a blind spot beneath the actuator from which inclusions cannot be discounted with the available data.

A more serious possibility for the failure of the *in vivo* healthy case reconstructions is that the

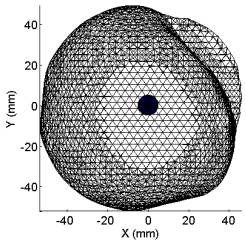

(a) Inclusion location, top view

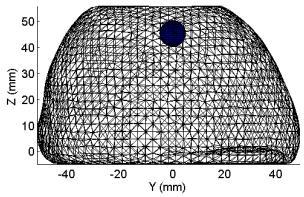

(b) Inclusion location, side view

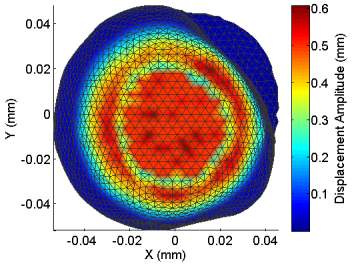

(c) Inclusions FE solution (1).

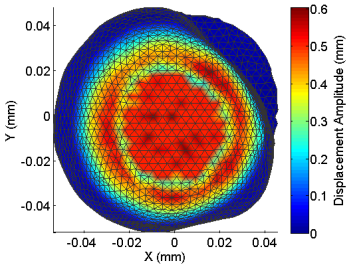

(d) Homogeneous FE solution (2).

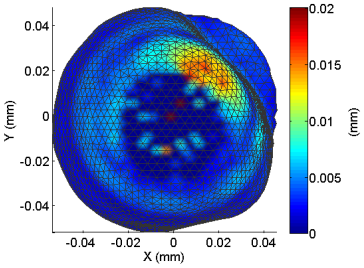

(e) Difference between solutions 1 and 2.

Figure 7.40: Inclusion 'beneath' the actuator (7.40a, 7.40b). Forward simulations with (7.40c) and without (7.40d) the inclusion, and the difference between the forward simulations (7.40e).

model may be too simple to be applied *in vivo*. The homogeneous background does not take into account any viscoelastic effects of skin nor the variation of tissue within the breast. Such effects may need to be incorporated in to the FE model in order to successfully reject tumors within the breast volume. There is, however, much room for improvement in both data collection and FE modeling, so as yet, the approach of assuming a tumor until rejected should not be discarded.

Chapter 8

Conclusions

A parallel reconstruction algorithm for the DIET system has been presented. The optimization algorithm developed and employed here has been shown to be successful for tumor location in numerical simulation, in phantoms and *in vivo*. As demonstrated in the numerical validation of the GA in section 3.7, the algorithm is not dependent on the initial guess. The initial population was randomly generated for each run of the algorithm. For each of the cases where there was a single global minimum, the algorithm located the inclusion at the minimum cost or within 5 mm of the minimum cost solution more than 98% of the time.

The parallelization of the algorithm was essential for the reconstructions of this thesis and has allowed the reconstruction of viscoelastic properties using patient specific meshes and without the requirement for pre-calculated sweeps of FE solutions. In the clinical application of DIET, parallelization is critical for this or any other reconstruction algorithm which requires the evaluation of the forward problem.

FFA was developed to take advantage of the sampling of the cost surface by the GA. FFA was shown to introduce the correction solution earlier into the population, and to improve convergence of the algorithm in the test case of section 3.7.2. The relatively small increase in computational expense of one extra FE calculation per generation is negligible compared to the potential benefits of introducing the optimum solution at an earlier stage in the algorithm. Certainly if the DIET system is developed to a point where the tolerance in motion error is well defined, *i.e.* there is a known minimum cost level at which a solution can be identified as correct, FFA could be very effective. FFA may also be applied to other problems, and is not limited to use with the GA. Any algorithm which samples the cost surface sufficiently could be combined with FFA.

The element projection method employed in this thesis is faster than the node normal projection

used in earlier work [61] [62]. For the ~10 fiducials used in those previous experiments this 35 fold decrease in computation time may not have been particularly beneficial, but it becomes increasingly more important as the number of fiducial markers is increased; approximately 1000 fiducials were used in each of the experiments in this thesis.

The aim of DIET is to be a pre-screening technique which complements mammography for women who may not have access to screening because of economic or geographic reasons, or for those who are not eligible for mammographic screening due to age. As such it is required to identify and locate stiff areas within the breast that require further investigation, ideally with as few model parameters as possible.

The model of a fixed radius, fixed stiffness sphere to be located within or excluded from the breast volume has been used to locate an inclusion in phantoms and *in vivo*. In the phantom experiments of Chapter 4 the larger inclusions could be used to locate smaller inclusions and *vice versa*. *A priori* stiffnesses of 20 kPa, 30 kPa and 40 kPa could all be used to successfully locate the inclusion within a background stiffness of ~3 kPa. For the homogeneous case, the stiffer, larger inclusions could be excluded from the phantom. However, clinically, the smallest possible inclusion needs to be discounted. In phantoms, the use of multi-frequency data produced the correct result for the homogeneous case using an *a priori* radius of 5 mm and $E'_I = 30$ kPa, a contrast of nine times the background stiffness.

The credible region results of Chapter 4 demonstrate that currently the credible region for inclusion location is larger than the inclusion volume, ranging from seven to twenty-five times the inclusion volume. This shows the uncertainty in the current DIET system, however, the minimum cost solutions were a good match for the inclusion location for all phantoms, with the exception of phantom Tr5. The optimal region provides a visual representation of the minimum cost solution and the surrounding models in parameter space. With an improved data acquisition system, *i.e.* a reduction in measurement noise, it is feasible that the credible and optimal regions may be comparable.

The fixed radius, fixed stiffness sphere model was also used successfully in phantoms with more complex geometries: two 'cancerous' inclusions present, and multiple inclusions of varying stiffness with one target inclusion. The presence of multiple inclusions in phantom did not affect the algorithm's ability to identify the location of the target inclusion with a simple *a priori* assumption. In addition, the algorithm developed has the capability to reconstruct ellipsoidal and multiple inclusions if required, as demonstrated in the synthetic data reconstructions and the

successful two-inclusion phantom reconstructions in Chapter 6. Both spherical and ellipsoidal *a priori* assumptions were used to locate the two inclusions. The *a priori* assumption of two spherical inclusions achieved a reconstruction with a ten fold decrease in computation over the *a priori* two ellipsoidal inclusions. However, the two ellipsoid *a priori* provided a better match for the volume of the inclusions.

The multi-inclusion phantom experiments produced a reconstructed E'_B higher than the true value of the storage modulus of the background material. By using a single inclusion assumption, the location optimization for the 'cancer' was successful, but at the expense of the background stiffness. This highlights the inherent non-uniqueness in the DIET inverse problem and the importance of interpreting the reconstruction results in terms of the model used. When using a single inclusion, multiple stiff areas in the breast cannot be discounted. However, as a pre-screening test, the correct identification of the presence of an inclusion is a positive result.

The cost surfaces for phantom MI and patient MS016T demonstrate that the cost functions Φ, Φ^{SQ} and Γ could all be applied successfully in the DIET reconstruction algorithm. The data quality metrics, μ_A, $\overline{SNR}$ and χ have been employed to characterize multi-frequency data sets and to produce a combined cost function, Φ^C. Φ^C was found to produce a better than average reconstruction compared to the corresponding n individual frequency reconstructions at the expense of an increase in computational cost of approximately n times that of the single frequency reconstructions. Both cost functions, Φ^C, based on squared error, and Γ^C, based on correlation, have been used to produce successful reconstructions for multi-frequency data.

In vivo the presence of an inclusion was identifiable, but the absence of an inclusion was not. In phantom, using multi-frequency data, the inclusion could be excluded, but *in vivo* this was not the case. The encouraging result is that for the three patient datasets examined in this thesis, the tumor provides enough signal to be located. The tumor sizes of the patients ranged from 11 mm to 30 mm in diameter and all were successfully located. Further patient data will be required to test the model with a larger range of tumor sizes.

The weakness in the model selection of $\theta(E'_B, \zeta_B, x_c, y_c, z_c, R, E'_I, \zeta_B)$ is that the inclusion is fitted to the anomaly from the homogeneous model $\theta(E'_B, \zeta_B)$. In phantom Tr5, this caused the mis-location of an inclusion. The anomaly was due to the chain reaction of poor motion tracking, which led to poor meshing, which in turn led to the generation of a poor solution to the forward problem. For the healthy *in vivo* cases, the model does not provide a good enough approximation to the measured motion of the breast to discard all models that locate an inclusion within the

breast volume. The *in vivo* data is noisier than the phantom data, with $\overline{SNR}$ ranging from 1.41 to 5.98 compared the $\overline{SNR}$ in phantoms which ranged from 7.70 to 19.19. In addition, the chest wall boundary condition is an unknown that has been approximated by setting the motion of the nodes at the 'chest wall' equal to zero. In phantoms, this boundary condition is satisfactory. *In vivo*, the presence of muscle and ribs behind the breast may have an effect on the motion that is not mimicked in the construction of the phantoms used in this study.

Samani *et al.* used a zero displacement chest wall boundary condition [103]. However, they approximated the chest wall topography using a third-order polynomial. In this work the chest wall is approximated by a flat surface. When using MRI as an imagining modality, image segmentation can be used on a patient by patient basis to locate the chest wall [105]. Recent developments have produced algorithms for automatic segmentation of the chest wall [123]. There is no interior imaging of the breast in DIET, thus to create patient specific chest wall topography using the current DIET system the chest wall curvature would have to be solved as an unknown in the inverse problem. This would be a non-trivial addition to the reconstruction algorithm, and there are other approaches to the problem that may be more prudent. Combining DIET with ultrasound is one possible area for development. This would give an image of the chest wall to use in the reconstruction algorithm, but would require that the chest wall imaging could be successfully automated to produce chest wall topography. Alternatively, a next step for DIET would be to develop a generic chest wall model based on typical measurements from clinical MRI data, and test this generic model's performance using phantoms with various chest wall shapes.

The phantoms also fit the current DIET prototype well and thus make good contact with the actuator. The actuator contact boundary condition of motion in the z direction only is thus appropriate in phantoms. The current DIET prototype does not include the capability to raise the actuator and thus, because of the various breast shapes *in vivo*, the actuator contact may not be as good as that exhibited in phantoms. The no-slip actuator boundary condition would be less appropriate in these cases leading to a greater data-model mismatch. By assuming an inclusion, the danger is that if the data is noisy enough, or the data-model mis-match is significant, an inclusion can be fitted to the noise. This has lead to the false positives *in vivo*.

However, this is the first *in vivo* data acquired with the DIET prototype. Certainly the tumor location results are encouraging and demonstrate the potential of current DIET prototype to locate inclusions *in vivo*. There are some obvious improvements in data collection that can be made which may allow the successful homogeneous phantom reconstruction to be translated into

successful healthy *in vivo* reconstructions. The further development of the DIET prototype and how this affects the reconstruction results in a larger clinical trial is the next goal for the DIET project.

In summary the original contributions presented in this thesis are as follows:

- A new reconstruction algorithm combining a genetic algorithm with fitness funciton analysis was developed.
- An ellipical shape based description of inclusions was developed, and multiple inclusions were reconstructed for the first time.
- Building on the work of Jonas Biehler, which allowed meshes to be constructed directly from data without the need to measure of the phantoms, the first reconstructions using meshes created directly from DIET data were produced.
- The phantoms used in this thesis are the most realistic DIET phantoms used to date.
- A multi-freqeuncy cost function was developed to produce the first DIET multi-freqeuncy data reconstructions.
- The first *in vivo* reconstructions using DIET data are presented.

Chapter 9

Future Work

There are several areas for future work: improvement in data collection, improvement of the mechanical model of the breast and improvement of the reconstruction algorithm.

The DIET acquisition system is currently under development. The next prototype will use higher specification cameras and strobe lights which will decrease the imaging time so a frequency sweep of data can be acquired within several minutes. The *in vivo* experiments of Chapter 7, particularly the large frequency sweep of MS016, have highlighted the need for the data to be taken in as short a time as possible as this would reduce the likelihood of patient movement during data acquisition. Also, the acquisition time will need to be improved for the practical implementation of any clinical study. For phantom data, the time requirement is not of concern. The increased speed of data acquisition could allow the data quality metrics developed in this work to be calculated during data acquisition, allowing the acquisition frequencies to be tuned to the patient while still keeping short acquisition times.

The higher specification cameras planned for the next DIET prototype will also provide higher quality images. In conjunction with the capability of tracking natural features of the skin [119], this potentially could offer denser and more accurate surface coverage. The possibility of skin feature tracking without the need to apply fiducial markers to the breast is an exciting potential development for DIET. Although the application of fiducials to the breast can be achieved in a couple of minutes, it would be advantageous for the patient not to need fiducials to be applied at all. Not only would the patient need to spend less time at the screening appointment, there would be no requirement to wash the fiducials off after the imaging, thus increasing patient comfort.

Results from this work show that in some reconstructions, inclusions can be pushed towards the actuator, particularly when the motion tracking is poor at that part of the breast surface. The

poor motion tracking impacts the mesh generation, meaning the mesh is not a good match for the true geometry at the contact with the actuator. An alternative approach would be to track the actuator, make it part of the model and apply the boundary condition to the actuator itself, as a very stiff object in motion.

The boundary condition at the actuator contact is in the z direction with no motion in the x or y direction. This may not be the case in reality as the breast may slip in the x-y plane at the contact with the actuator. The ability to move the actuator contact will be available in the next prototype, which will allow a slight compression of the breast. This may provide a better contact and allow the no-slip boundary condition to be successfully employed.

The actuator in the current DIET prototype can only be used to actuate at the nipple. Actuation from multiple directions would allow the whole breast surface to be imaged at some point in the procedure, but the development of a multi-directional actuator is by no means a trivial task. As with multi-frequency data, each additional dataset, either frequency or actuation location, increases the computational expense of solving the forward problem.

The Finite Element calculations used to simulate displacement in this thesis are based on the assumption of linearly viscoelastic behavior and a very simple material property distribution of a stiff inclusion within a homogeneous background. For the *in vivo* results in this thesis this approach was used successfully for inclusion location, but not for the exclusion of a breast mass in the healthy case. It may be that the model is not sufficient for the human breast due to the linearly viscoelastic assumption, the simplicity of the material property distribution model, or a combination of both. Other groups are using hyper-elastic properties to model tissue [124] [125]. One advantage of DIET is that the multiple-frequency data acquisition allows one to chose a frequency range which best fits the model. It may be that within a certain range of actuation frequency and amplitude that the motion can be described sufficiently with a linearly viscoelastic model. Further *in vivo* studies are required to determine under what conditions the simple model can be successfully applied or whether a new mechanical model of the breast must be implemented.

The development of a more anatomically correct mechanical model of the breast is a significant undertaking, particularly when the model needs to be applied to all patients in a screening population. Incorporating anatomical features with varying elastic properties such as skin, chest wall, muscle and connective tissue in to a model that can be applied to the general patient may require a flexible generic breast model.

A major step to overcome in developing DIET into a viable clinical product is to improve the

specificity. One possibility for future work is to combine DIET with ultrasound. The benefits of this potentially are two-fold; the false positives at the actuator contact may be reduced, and ultrasound could provide an image of the chest wall to be used in reconstruction algorithm. DIET is intended to be a portable system to increase access to to screening in rural areas. Hand-held ultrasound transducers, such as the Vscan [126] developed by General Electric, are an exciting technological development that could be of use in DIET.

The reconstruction algorithm developed in this thesis was parallelized to run on the Bluefern® p575 and a Beowulf cluster. Even the simple breast models used in this thesis necessitated the use of parallel computing to produce reconstructions. The eventual clinical product for the reconstruction algorithm would be a standalone unit capable of performing reconstructions. The DIET system is intended to be low-cost and portable and obviously the current requirement for the reconstruction algorithm to have a supercomputer or parallel computing cluster is neither low-cost nor portable. Although acceptable for the DIET system in its current stage of development, the clinical application of DIET will require a highly parallelized reconstruction algorithm within a standalone device. General-purpose computing on graphics processing units (GPGUP) may provide the massively parallel processing power required [127]. GPGPU is being employed in real-time soft tissue simulation for surgical applications [128] and may be a good solution for DIET.

Appendix A

The Finite Element Method

The Finite Element Method (FEM) is a powerful procedure for obtaining discretized, approximate solutions to partial differential equations. It allows a large range of physical senarios to be modelled using computers. The following describes the Finite Element approach used to solve steady-state, time-harmonic solid mechanics problems for three-dimensional models. For an in depth review of FEM, the reader is referred to the classic text by Bathe and Wilson [129].

Weighted Residuals

The equilibrium conditions for a solid body in a static system can be expressed as a null divergence of the stress tensor,

$$\sigma_{ij,j} = 0. \tag{A.1}$$

When considering the intertial forces present in an undamped, steady-state, time-harmonic system, Equation A.1 becomes

$$\bar{\sigma}_{ij,j} + \rho\omega^2 \bar{u}_i = 0, \tag{A.2}$$

where ρ is the material density, ω is the system frequency, $\bar{u}_i$ is the motion amplitude and $\bar{\sigma}$ is the corresponding time-harmonic stress tensor. In the case where the exact displacement is not known, it is approximated as $\hat{u}$ and Eq. A.2 will have a non-zero residual term R, where

$$R = \hat{\sigma}_{ij,j} + \rho\omega^2 \hat{u}_i, \tag{A.3}$$

and $\hat{\sigma}$ are the approximate stresses given by the approximate displacements $\hat{u}$. Ideally, the residual term over the entire domain will be zero, thus any weighted integration of R should also be zero,

$$\left\langle W^k(\hat{\sigma}_{ij,j} + \rho\omega^2\hat{u}_i)\right\rangle = 0 \tag{A.4}$$

where $\langle\rangle$ means integrating over the three-dimensional domain and W^k is an arbitrarily-chosen weighting function. As the number of weighting functions, N_k, increases, the match between the approximate and exact stress solutions improves towards the limit

$$\lim_{N_k\to\infty} \hat{u} = \bar{u} \tag{A.5}$$

Interpolating Polynomials

The FE method makes use of interpolating polynomials, ϕ_k to describe the value of field variables at any position within the domain. In this work, linear interpolating functions were used, allowing a fine discritization of the domain while keeping relatively short integration times. The variable interpolation within a four-noded tertrahedral element, as used in this work and illustrated in Figure A.1, takes the form

$$\hat{u}_e = \sum_{k=1}^{4} \hat{u}_k\phi^k(x, y, z), \tag{A.6}$$

where ϕ^k is the linear interpolating function, $\hat{u}_e$ is an approximation to the displacement solution $\bar{u}$ at location (x, y, z) and $\hat{u}_k$ is the the displacement at each node.

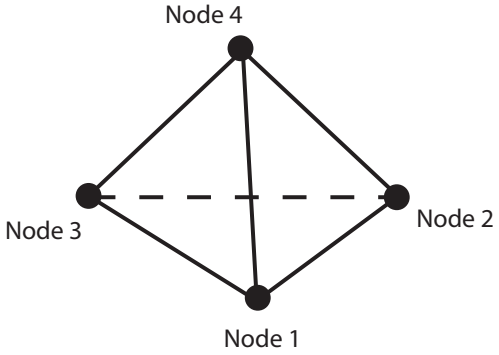

Figure A.1: A linear tetrahedral element with nodes numbered according to the right-handed convention.

The Galerkin Method

The Galerkin method is a technique where the weighting functions used in the method of weighted residuals additionally form the basis functions for the interpolating polynomials,

$$W^k = \phi^k \tag{A.7}$$

It is standard practice in FE methods to perform the integration of the weighted residual statement in Eq. A.4 using Green's theorem,

$$\left\langle \phi_i^k(\hat{\sigma}_{ij,j} + \rho\omega^2\hat{u}_i)\right\rangle = \left\langle -\phi_i^k\hat{\sigma_{ij}} + \phi_i^k\rho\omega^2\hat{u_i}\right\rangle + \oiint \phi_i^k\hat{\sigma}_{ij}n_j dS = 0 \tag{A.8}$$

where n_j is a surface normal vector. This is the 'weak' form of the weighted residual statement.

Stiffness Function Terms

Expressing the differential system provided by Eq. A.2 in terms of displacement requires a conversion from stress to strain terms. The relationship between displacements, u, and strains, ϵ, for a linear elastic material can be expressed in tensor form as

$$\bar{\epsilon}_{ij} = \frac{1}{2}(\bar{u}_{i,j} + \bar{u}_{j,i}) \tag{A.9}$$

while the corresponding relationship between strains and stress is

$$\bar{\sigma}_{ij} = \lambda\delta_{ij}\bar{\epsilon}_{kk} + 2\mu\bar{\epsilon}_{ij} \tag{A.10}$$

where λ and μ are the Lamé parameters, and $\delta_{i,j}$ is the Kronecker delta function. Substituting Eqs. A.9 & A.10 into the weighted residual in Eq. A.8 and writing out terms in full for the x-direction gives

$$\left\langle 2\mu\frac{\partial\hat{u}_x}{\partial x} + \lambda\left(\frac{\partial\hat{u}_x}{\partial x} + \frac{\partial\hat{u}_y}{\partial y} + \frac{\partial\hat{u}_z}{\partial z}\right)\frac{\partial\phi_i}{\partial x}\right\rangle + \ldots$$
$$\left\langle \mu\left(\frac{\partial\hat{u}_x}{\partial y} + \frac{\partial\hat{u}_y}{\partial x}\right)\frac{\partial\phi_i}{\partial x}\right\rangle + \left\langle \mu\left(\frac{\partial\hat{u}_x}{\partial z} + \frac{\partial\hat{u}_z}{\partial x}\right)\frac{\partial\phi_i}{\partial x}\right\rangle = -\rho\omega^2\hat{u}_x \tag{A.11}$$

To solve this equation using FEM, Eq. A.11 is reformulated as a system of equations

$$[\mathbf{k}]\{u\} = \{b\}, \tag{A.12}$$

where the stiffness matrix $[\mathbf{k}]$ contains the material property terms and $\{b\}$ contains the forcing terms arising from intertial forces or externally applied constraints. For the three-dimensional case, each node has three degrees of freedom, one for each of the three orthogonal components of diplacement. The local stiffness matrix terms are defined

$$\begin{aligned}
k_{11} &= \left\langle (2\mu+\lambda)\frac{\partial\hat{\phi}_i}{\partial x}\frac{\partial\hat{\phi}_j}{\partial x} + \mu\frac{\partial\hat{\phi}_i}{\partial y}\frac{\partial\hat{\phi}_j}{\partial y} + \mu\frac{\partial\hat{\phi}_i}{\partial z}\frac{\partial\hat{\phi}_j}{\partial z} \right\rangle \\
k_{12} &= \left\langle \lambda\frac{\partial\hat{\phi}_i}{\partial x}\frac{\partial\hat{\phi}_j}{\partial y} + \mu\frac{\partial\hat{\phi}_i}{\partial y}\frac{\partial\hat{\phi}_j}{\partial x} \right\rangle \\
k_{13} &= \left\langle \lambda\frac{\partial\hat{\phi}_i}{\partial x}\frac{\partial\hat{\phi}_j}{\partial z} + \mu\frac{\partial\hat{\phi}_i}{\partial z}\frac{\partial\hat{\phi}_j}{\partial x} \right\rangle \\
k_{21} &= \left\langle \lambda\frac{\partial\hat{\phi}_i}{\partial y}\frac{\partial\hat{\phi}_j}{\partial x} + \mu\frac{\partial\hat{\phi}_i}{\partial x}\frac{\partial\hat{\phi}_j}{\partial y} \right\rangle \\
k_{22} &= \left\langle \mu\frac{\partial\hat{\phi}_i}{\partial x}\frac{\partial\hat{\phi}_j}{\partial x} + (2\mu+\lambda)\frac{\partial\hat{\phi}_i}{\partial y}\frac{\partial\hat{\phi}_j}{\partial y} + \mu\frac{\partial\hat{\phi}_i}{\partial z}\frac{\partial\hat{\phi}_j}{\partial z} \right\rangle \\
k_{23} &= \left\langle \lambda\frac{\partial\hat{\phi}_i}{\partial y}\frac{\partial\hat{\phi}_j}{\partial z} + \mu\frac{\partial\hat{\phi}_i}{\partial z}\frac{\partial\hat{\phi}_j}{\partial y} \right\rangle \\
k_{31} &= \left\langle \lambda\frac{\partial\hat{\phi}_i}{\partial z}\frac{\partial\hat{\phi}_j}{\partial x} + \mu\frac{\partial\hat{\phi}_i}{\partial x}\frac{\partial\hat{\phi}_j}{\partial z} \right\rangle \\
k_{32} &= \left\langle \lambda\frac{\partial\hat{\phi}_i}{\partial z}\frac{\partial\hat{\phi}_j}{\partial y} + \mu\frac{\partial\hat{\phi}_i}{\partial y}\frac{\partial\hat{\phi}_j}{\partial z} \right\rangle \\
k_{33} &= \left\langle \mu\frac{\partial\hat{\phi}_i}{\partial x}\frac{\partial\hat{\phi}_j}{\partial x} + \mu\frac{\partial\hat{\phi}_i}{\partial y}\frac{\partial\hat{\phi}_j}{\partial y} + (2\mu+\lambda)\frac{\partial\hat{\phi}_i}{\partial z}\frac{\partial\hat{\phi}_j}{\partial z} \right\rangle
\end{aligned} \tag{A.13}$$

The local element stiffness matrices are assembled into a global stiffness matrix, which is sparse, symmetric, and positive definite. The global displacement field, $\hat{u}$, can then be calculated via matrix inversion.

Appendix B

Genetic Algorithm Parameters

There are two competing factors in a genetic algorithm: converging on a solution and exploring the parameter space. The aim is to explore the parameter space sufficiently to find the global minimum yet converge on the solution in a reasonable number of solution evaluations. The parameters in the algorithm that control these two competing factors are:

- K The percentage of the population to keep for mating
- M The percentage of bits to mate in the population

A sweep of forward solutions was calculated for phantom MI in Chapter 6 in order to test the various cost functions for the location optimization problem. This sweep of forward solutions was used to tune the parameter options of the GA with FFA. The algorithm was run with K varied between 10% and 80% and M varied between 5% and 20%. Thirty-two chromosomes were used with the algorithm limited to 200 generations and run 100 times for each parameter combination. Two measures of success were used:

- The percentage of runs of the algorithm that converged on the global minimum.
- The number of generations taken to converge.

The results are shown in Figure B.1. There is a clear trend in Figure B.1a where increasing M and K leads to an increase in the number of generations to converge. Figure B.1b shows the percentage of runs that converged on the global minimum. The low M, low K reconstructions are the least successful, which suggests that the algorithm is exhibiting premature convergence at these low values. There is a dip in success rate at the highest M and K. This is because the algorithm is limited to 200 generations. At high M and K the algorithm may not reach the global

minimum before 200 generations. The algorithm is not efficient at these higher values of M and K.

GAs can be very problem specific [84], so it is important not to tune the genetic algorithm too heavily to the cost surface of one dataset. For the phantom dataset presented here, $M = 40\%$ to 70 % and $K = 10\%$ to 20% are parameter choices capable of producing successful reconstructions consistently (90+% converged on correct minimum). To converge in the fewest generations M and K should be set at the lower end of these ranges.

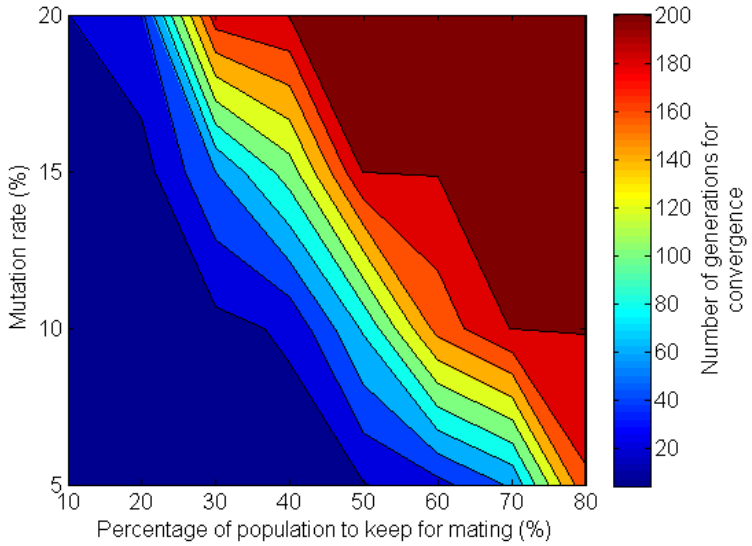

(a) Number of generations taken to converge.

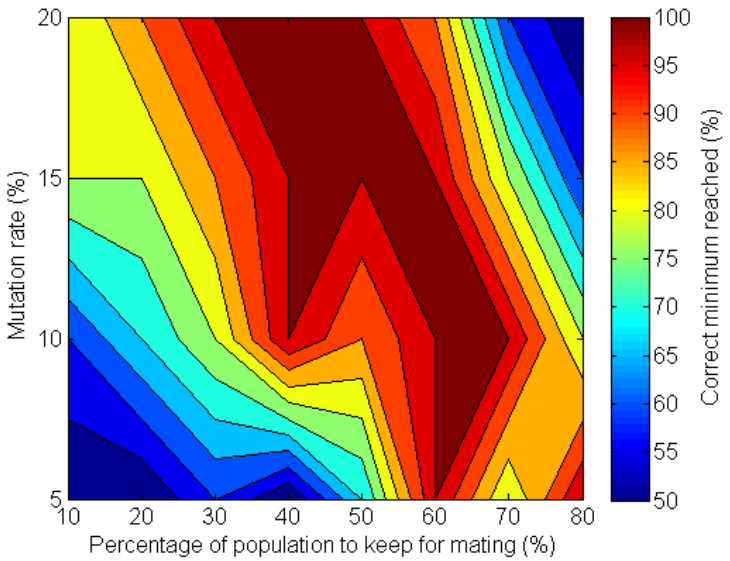

(b) Percentage of runs that converged on the correct minimum.

Figure B.1: Number of generations taken to converge (B.1a) and the percentage of runs that converged on the correct minimum (B.1b) for various values of K and M.

Bibliography

[1] C. DeSantis, R. Siegel, P. Bandi, and A. Jemal, "Breast cancer statistics, 2011," *CA: A Cancer Journal for Clinicians*, 2011.

[2] S. S. Coughlin and D. U. Ekwueme, "Breast cancer as a global health concern," *Cancer epidemiology*, vol. 33, Nov 2009.

[3] P. Porter, "Westernizing women's risks? breast cancer in lower-income countries," *New England Journal of Medicine*, vol. 358, no. 3, pp. 213–216, 2008.

[4] B. O. Anderson, C. H. Yip, R. A. Smith, R. Shyyan, S. F. Sener, A. Eniu, R. W. Carlson, E. Azavedo, and J. Harford, "Guideline implementation for breast healthcare in low-income and middle-income countries," *Cancer*, vol. 113, no. S8, pp. 2221–2243, 2008.

[5] J. Ferlay, H. Shin, F. Bray, D. Forman, C. Mathers, and D. Parkin, "Estimates of worldwide burden of cancer in 2008: Globocan 2008," *International Journal of Cancer*, 2010.

[6] Saint Francis Breast Health Services, "Breast anatomy."

[7] American Cancer Society, "Breast cancer survival by stage." http://www.cancer.org/Cancer/BreastCancer/DetailedGuide/breast-cancer-survival-by-stage.

[8] J. S. Michaelson, M. Silverstein, J. Wyatt, G. Weber, R. Moore, E. Halpern, D. B. Kopans, and K. Hughes, "Predicting the survival of patients with breast carcinoma using tumor size," *Cancer*, vol. 95, pp. 713–23, Aug 15 2002.

[9] M. Silverstein, "The Van Nuys Breast Center: the first free-standing multidisciplinary breast center.," *Surgical oncology clinics of North America*, vol. 9, no. 2, p. 159, 2000.

[10] M. Silverstein, P. Gamagami, R. Masetti, M. Legmann, P. Craig, and E. Gierson, "Results from a multidisciplinary breast center. analysis of disease discovered.," *Surgical oncology clinics of North America*, vol. 6, no. 2, p. 301, 1997.

[11] A. Sobti, P. Sobti, and L. Keith, "Screening and diagnostic mammograms: Why the gold standard does not shine more brightly," *International Journal Of Fertility And Womens Medicine*, vol. 50, pp. 199–206, Sep-Oct 2005.

[12] D. Kopans, *Breast imaging*. Lippincott Williams & Wilkins, 1998.

[13] M. Tilanus-Linthorst, L. Verhoog, I.-M. Obdeijn, K. Bartels, M. Menke-Pluymers, A. Eggermont, J. Klijn, H. Meijers-Heijboer, T. van der Kwast, and C. Brekelmans, "A brca1/2 mutation, high breast density and prominent pushing margins of a tumor independently contribute to a frequent false-negative mammography," *International Journal of Cancer*, vol. 102, no. 1, pp. 91–95, 2002.

[14] E. D. Pisano, R. E. Hendrick, M. J. Yaffe, J. K. Baum, S. Acharyya, J. B. Cormack, L. A. Hanna, E. F. Conant, L. L. Fajardo, L. W. Bassett, C. J. D'Orsi, R. A. Jong, M. Rebner, A. N. A. Tosteson, and C. A. Gatsonis, "Diagnostic accuracy of digital versus film mammography: exploratory analysis of selected population subgroups in dmist," *Radiology*, vol. 246, pp. 376–83, Feb 2008.

[15] P. Stomper, D. D'Souza, P. DiNitto, and M. Arredondo, "Analysis of parenchymal density on mammograms in 1353 women 25-79 years old," *Ajr*, vol. 167, pp. 1261–5, Nov 1996.

[16] C. Vachon, C. Van Gils, T. Sellers, K. Ghosh, S. Pruthi, K. Brandt, and V. Pankratz, "Mammographic density, breast cancer risk and risk prediction," *Breast Cancer Res*, vol. 9, no. 6, p. 217, 2007.

[17] A. Asghari and M. K. Nicholas, "Pain during mammography: the role of coping strategies," *Pain*, vol. 108, pp. 170–9, Mar 2004.

[18] S. Kashikar-Zuck, F. J. Keefe, P. Kornguth, P. Beaupre, A. Holzberg, and D. Delong, "Pain coping and the pain experience during mammography: a preliminary study," *Pain*, vol. 73, no. 2, pp. 165 – 172, 1997.

[19] B. Davey, "Pain during mammography: Possible risk factors and ways to alleviate pain," *Radiography*, vol. 13, no. 3, pp. 229–234, 2007.

[20] S. McDonald, D. Saslow, and M. H. Alciati, "Performance and reporting of clinical breast examination: A review of the literature," *CA: A Cancer Journal for Clinicians*, vol. 54, no. 6, pp. 345–361, 2004.

[21] A. Sarvazyan, V. Egorov, J. Son, and C. Kaufman, "Cost-effective screening for breast cancer worldwide: Current state and future directions," *Breast cancer*, vol. 1, pp. 91–99, Jul 2 2008.

[22] L. S. Elting, C. D. Cooksley, B. N. Bekele, S. H. Giordano, Y. C. T. Shih, K. K. Lovell, E. B. Avritscher, and R. Theriault, "Mammography capacity: Impact on screening rates and breast cancer stage at diagnosis," *American journal of preventive medicine*, vol. 37, pp. 102–8, Aug 2009.

[23] A. Nover, S. Jagtap, W. Anjum, H. Yegingil, W. Shih, W. Shih, and A. Brooks, "Modern breast cancer detection: a technological review," *Journal of Biomedical Imaging*, vol. 2009, 2009.

[24] L. Niklason, B. Christian, L. Niklason, D. Kopans, D. Castleberry, B. Opsahl-Ong, C. Landberg, P. Slanetz, A. Giardino, and R. Moore, "Digital tomosynthesis in breast imaging.," *Radiology*, vol. 205, no. 2, pp. 399–406, 1997.

[25] W. Good, G. Abrams, V. Catullo, D. Chough, M. Ganott, C. Hakim, and D. Gur, "Digital breast tomosynthesis: a pilot observer study," *American Journal of Roentgenology*, vol. 190, no. 4, pp. 865–869, 2008.

[26] F. Bénard and E. Turcotte, "Imaging in breast cancer: Single-photon computed tomography and positron-emission tomography," *Breast Cancer Research*, vol. 7, no. 4, pp. 153–162, 2005.

[27] E. Rosen, T. Turkington, M. Soo, J. Baker, and R. Coleman, "Detection of primary breast carcinoma with a dedicated, large-field-of-view FDG PET mammography device: Initial experience," *Radiology*, vol. 234, no. 2, p. 527, 2005.

[28] D. Leff, O. Warren, L. Enfield, A. Gibson, T. Athanasiou, D. Patten, J. Hebden, G. Yang, and A. Darzi, "Diffuse optical imaging of the healthy and diseased breast: a systematic review," *Breast cancer research and treatment*, vol. 108, no. 1, pp. 9–22, 2008.

[29] A. Gibson, J. Hebden, and S. Arridge, "Recent advances in diffuse optical imaging," *Physics in Medicine and Biology*, vol. 50, p. R1, 2005.

[30] L. C. Enfield, A. P. Gibson, N. L. Everdell, D. T. Delpy, M. Schweiger, S. R. Arridge, C. Richardson, M. Keshtgar, M. Douek, and J. C. Hebden, "Three-dimensional time-resolved optical mammography of the uncompressed breast," *Appl. Opt.*, vol. 46, pp. 3628–3638, Jun 2007.

[31] D. Grosenick, K. T. Moesta, H. Wabnitz, J. Mucke, C. Stroszczynski, R. Macdonald, P. M. Schlag, and H. Rinneberg, "Time-domain optical mammography: Initial clinical results on detection and characterization of breast tumors," *Appl. Opt.*, vol. 42, pp. 3170–3186, Jun 2003.

[32] Y. Zou and Z. Guo, "A review of electrical impedance techniques for breast cancer detection," *Medical Engineering & Physics*, vol. 25, no. 2, pp. 79 – 90, 2003.

[33] V. Cherepenin, A. Karpov, A. Korjenevsky, V. Kornienko, A. Mazaletskaya, D. Mazourov, and D. Meister, "A 3D Electrical Impedance Tomography (EIT) system for breast cancer detection," *Physiological Measurement*, vol. 22, no. 1, p. 9, 2001.

[34] N. Soni, A. Hartov, C. Kogel, S. Poplack, and K. Paulsen, "Multi-frequency electrical impedance tomography of the breast: new clinical results," *Physiological measurement*, vol. 25, p. 301, 2004.

[35] M. Choi, T. Kao, D. Isaacson, G. Saulnier, and J. Newell, "A reconstruction algorithm for breast cancer imaging with Electrical Impedance Tomography in mammography geometry," *Biomedical Engineering, IEEE Transactions on*, vol. 54, no. 4, pp. 700–710, 2007.

[36] T. Yahara, T. Koga, S. Yoshida, S. Nakagawa, H. Deguchi, and K. Shirouzu, "Relationship between microvessel density and thermographic hot areas in breast cancer," *Surgery today*, vol. 33, no. 4, pp. 243–248, 2003.

[37] E. Ng, S. Fok, Y. Peh, F. Ng, and L. Sim, "Computerized detection of breast cancer with artificial intelligence and thermograms," *Journal of medical engineering & technology*, vol. 26, no. 4, pp. 152–157, 2002.

[38] A. Samani, J. Zubovits, and D. Plewes, "Elastic moduli of normal and pathological human breast tissues: an inversion-technique-based investigation of 169 samples," *Physics in Medicine and Biology*, vol. 52, no. 6, p. 1565, 2007.

[39] J. Ophir, I. Cespedes, H. Ponnekanti, Y. Yazdi, and X. Li, "Elastography: a quantitative method for imaging the elasticity of biological tissues," *Ultrasonic imaging*, vol. 13, no. 2, pp. 111–134, 1991.

[40] K. J. Parker, M. M. Doyley, and D. J. Rubens, "Imaging the elastic properties of tissue: the 20 year perspective," *Physics in Medicine and Biology*, vol. 56, no. 1, p. R1, 2011.

[41] B. Garra, E. Cespedes, J. Ophir, S. Spratt, R. Zuurbier, C. Magnant, and M. Pennanen, "Elastography of breast lesions: initial clinical results.," *Radiology*, vol. 202, no. 1, pp. 79–86, 1997.

[42] P. E. Barbone and N. H. Gokhale, "Elastic modulus imaging: on the uniqueness and nonuniqueness of the elastography inverse problem in two dimensions," *Inverse Problems*, vol. 20, no. 1, p. 283, 2004.

[43] H. Eskandari, S. Salcudean, R. Rohling, and I. Bell, "Real-time solution of the finite element inverse problem of viscoelasticity," *Inverse Problems*, vol. 27, p. 085002, 2011.

[44] A. Thomas, T. Fischer, H. Frey, R. Ohlinger, S. Grunwald, J.-U. Blohmer, K.-J. Winzer, S. Weber, G. Kristiansen, B. Ebert, and S. Kmmel, "Real-time elastography - an advanced method of ultrasound: first results in 108 patients with breast lesions," *Ultrasound in Obstetrics and Gynecology*, vol. 28, no. 3, pp. 335–340, 2006.

[45] R. M. Lerner, S. Huang, and K. J. Parker, "Sonoelasticity images derived from ultrasound signals in mechanically vibrated tissues," *Ultrasound in Medicine & Biology*, vol. 16, no. 3, pp. 231 – 239, 1990.

[46] K. Parker and R. Lerner, "Sonoelasticity of organs: shear waves ring a bell.," *Journal of ultrasound in medicine*, vol. 11, no. 8, pp. 387–392, 1992.

[47] L. Taylor, B. Porter, D. Rubens, and K. Parker, "Three-dimensional sonoelastography: principles and practices," *Physics in medicine and biology*, vol. 45, p. 1477, 2000.

[48] J. Fowlkes, S. Emelianov, J. Pipe, A. Skovoroda, P. Carson, R. Adler, and A. Sarvazyan, "Magnetic-resonance imaging techniques for detection of elasticity variation," *Medical physics*, vol. 22, p. 1771, 1995.

[49] D. Plewes, J. Bishop, A. Samani, and J. Sciarretta, "Visualization and quantification of breast cancer biomechanical properties with Magnetic Resonance Elastography," *Physics in Medicine and Biology*, vol. 45, p. 1591, 2000.

[50] J. Bishop, A. Samani, J. Sciarretta, and D. Plewes, "Two-dimensional MR elastography with linear inversion reconstruction: methodology and noise analysis," *Physics in medicine and biology*, vol. 45, p. 2081, 2000.

[51] R. Muthupillai, D. Lomas, P. Rossman, J. Greenleaf, A. Manduca, and R. Ehman, "Magnetic Resonance Elastography by direct visualization of propagating acoustic strain waves," *Science*, vol. 269, no. 5232, p. 1854, 1995.

[52] A. Manduca, T. E. Oliphant, M. A. Dresner, J. L. Mahowald, S. A. Kruse, E. Amromin, J. P. Felmlee, J. F. Greenleaf, and R. Ehman, "Magnetic Resonance Elastography: Non-invasive mapping of tissue elasticity," *Medical Image Analysis*, vol. 5, no. 4, pp. 237 – 254, 2001.

[53] S. A. Kruse, J. A. Smith, A. J. Lawrence, M. A. Dresner, A. Manduca, J. F. Greenleaf, R. L. Ehman, S. A. Kruse, J. A. Smith, A. J. Lawrence, M. A. Dresner, A. Manduca, and J. F. Greenleaf, "Tissue characterization using Magnetic Resonance Elastography: preliminary results," *Physics in Medicine and Biology*, vol. 45, no. 6, p. 1579, 2000.

[54] S. Kruse, G. Rose, K. Glaser, A. Manduca, J. Felmlee, C. Jack Jr, and R. Ehman, "Magnetic Resonance Elastography of the brain," *Neuroimage*, vol. 39, no. 1, pp. 231–237, 2008.

[55] R. Sinkus, J. Lorenzen, D. Schrader, M. Lorenzen, M. Dargatz, and D. Holz, "High-resolution tensor MR elastography for breast tumour detection," *Physics in Medicine and Biology*, vol. 45, p. 1649, 2000.

[56] E. E. W. Van Houten, K. D. Paulsen, M. I. Miga, F. E. Kennedy, and J. Weaver, "An overlapping subzone technique for MR-based elastic property reconstruction," *Magnetic resonance in medicine*, vol. 42, no. 4, pp. 779–786, 1999.

[57] M. Doyley, E. Van Houten, J. Weaver, S. Poplack, L. Duncan, F. Kennedy, and K. Paulsen, "Shear modulus estimation using parallelized partial volumetric reconstruction," *Medical Imaging, IEEE Transactions on*, vol. 23, no. 11, pp. 1404–1416, 2004.

[58] R. Sinkus, M. Tanter, S. Catheline, J. Lorenzen, C. Kuhl, E. Sondermann, and M. Fink, "Imaging anisotropic and viscous properties of breast tissue by Magnetic Resonance-Elastography," *Magnetic Resonance in Medicine*, vol. 53, no. 2, pp. 372–387, 2005.

[59] E. E. W. Van Houten, D. vR. Viviers, M. D. J. McGarry, P. R. Perrinez, I. I. Perreard, J. B. Weaver, and K. D. Paulsen, "Subzone based Magnetic Resonance Elastography using a Rayleigh damped material model," *Medical Physics*, vol. 38, no. 4, pp. 1993–2004, 2011.

[60] T. Lotz, P. D. Simpson, D. Stocker, C. E. Hann, and J. G. Chase, "In vitro evaluation of surface based non-invasive breast cancer screening with Digital Image based Elasto To-

mography (DIET)," *Engineering in Medicine and Biology Society (EMBC), 2010 Annual International Conference of the IEEE*, pp. 3077 – 3080, 2010.

[61] A. Peters, *Digital Image Elasto-Tomography: Mechanical Property Reconstruction from Surface Measured Displacement Data*. PhD thesis, Thesis University of Canterbury, 2007.

[62] E. E. W. Van Houten, A. Peters, and J. G. Chase, "Phantom elasticity reconstruction with Digital Image Elasto-Tomography," *Journal of the Mechanical Behavior of Biomedical Materials*, vol. In Press, Accepted Manuscript, pp. –, 2011.

[63] R. G. Brown, C. E. Hann, and J. G. Chase, "Vision-based 3D surface motion capture for the DIET breast cancer screening system," *International Journal of Computer Applications in Technology*, vol. 39, no. 1, pp. 72–78, 2010.

[64] T. F. Lotz, N. Muller, C. E. Hann, and J. G. Chase, "Minimal elastographic modeling of breast cancer for model based tumour detection in a Digital Image Elasto Tomography (DIET) system," in *Proceedings of SPIE*, vol. 7963, p. 796322, 2011.

[65] H.-U. Berger, C. E. Hann, J. G. Chase, B. Broughton, and E. E. W. Van Houten, "Boundary element methods in elastography a first explorative study," in *Proc SPIE Medical Imaging Conf - Physiology, Function, and Structure from Medical Images, Feb 17-22, San Diego, USA, 12-pages.*, 2007.

[66] H.-U. Berger, *Boundary Element Methods for Inverse Problems in Soft Tissue Elastography*. PhD thesis, University of Canterbury, 2009.

[67] P. E. Barbone and J. C. Bamber, "Quantitative elasticity imaging: what can and cannot be inferred from strain images," *Physics in Medicine and Biology*, vol. 47, no. 12, p. 2147, 2002.

[68] D. J. N. Wall, P. Olsson, and E. E. W. Van Houten, "On an inverse problem from Magnetic Resonance elastic imaging," *SIAM Journal on Applied Mathematics*, vol. 71, p. 1578, 2011.

[69] M. McGarry and E. Van Houten, "Use of a Rayleigh damping model in elastography," *Medical and Biological Engineering and Computing*, vol. 46, pp. 759–766, 2008. 10.1007/s11517-008-0356-5.

[70] N. Naik, R. Beatson, J. Eriksson, and E. E. W. V. Houten, "An implicit radial basis function based reconstruction approach to electromagnetic shape tomography," *Inverse Problems*, vol. 25, 2009.

[71] S. R. Arridge, O. Dorn, V. Kolehmainen, M. Schweiger, and A. Zacharopoulos, "Parameter and structure reconstruction in optical tomography," *Journal of Physics: Conference Series*, vol. 135, no. 1, p. 012001, 2008.

[72] M. Aguilo, W. Aquino, J. Brigham, and M. Fatemi, "An inverse problem approach for elasticity imaging through vibroacoustics," *Medical Imaging, IEEE Transactions on*, vol. 29, no. 4, pp. 1012 – 1021, 2010.

[73] L. G. Olson and R. D. Throne, "Numerical simulation of an inverse method for tumour size and location estimation," *Inverse Problems in Science and Engineering*, vol. 18, no. 6, pp. 813–834, 2010.

[74] E. Garduno and G. T. Herman, "Implicit surface visualization of reconstructed biological molecules," *Theoretical Computer Science*, vol. 346, pp. 281–299, 2005.

[75] J. Blinn, "A generalization of algebraic surface drawing," *ACM Transactions on Graphics*, vol. 1, no. 3, pp. 135–256, 1982.

[76] J. Bloomenthal, *Introduction to Implicit Surfaces*. Morgan Kaufmann Publishers, Inc., 1997.

[77] W. E. Ong, R. Beatson, and C. J. Price, "Reconstruction with blobby shapes," *ANZIAM Journal*, vol. 52, pp. C596–C611, 2011.

[78] S. Osher and J. Sethian, "Fronts propagating with curvature-dependent speed: algorithms based on Hamilton-Jacobi formulations," *Journal of computational physics*, vol. 79, no. 1, pp. 12–49, 1988.

[79] H. Ameur, M. Burger, and B. Hackl, "Level set methods for geometric inverse problems in linear elasticity," *Inverse Problems*, vol. 20, p. 673, 2004.

[80] A. Peters, J. G. Chase, and E. E. W. Van Houten, "Digital Image Elasto-Tomography: Combinatorial and hybrid optimization algorithms for shape-based elastic property reconstruction," *Biomedical Engineering, IEEE Transactions on*, vol. 55, pp. 2575 –2583, nov. 2008.

[81] Y. Zhang, L. Hall, D. Goldgof, and S. Sarkar, "A constrained genetic approach for computing material property of elastic objects," *IEEE Transactions on Evolutionary Computation*, vol. 10, no. 3, pp. 341–357, 2006.

[82] A. S. Khalil, B. E. Bouma, and M. R. Kaazempur Mofrad, "A combined FEM/genetic algorithm for vascular soft tissue elasticity estimation," *Cardiovascular Engineering*, vol. 6, no. 3, pp. 93–102, 2006.

[83] R. Karimi, T. Zhu, B. Bouma, and M. Kaazempur Mofrad, "Estimation of nonlinear mechanical properties of vascular tissues via elastography," *Cardiovascular Engineering*, vol. 8, no. 4, pp. 191–202, 2008.

[84] R. L. Haupt and S. E. Haupt, *Practical Genetic Algorithms*. Wiley Interscience, 2 ed., 2004.

[85] R. Myers, A. Khuri, and W. Carter Jr, "Response surface methodology: 1966-1988," *Technometrics*, pp. 137–157, 1989.

[86] R. Regis and C. Shoemaker, "Constrained global optimization of expensive black box functions using radial basis functions," *Journal of Global Optimization*, vol. 31, no. 1, pp. 153–171, 2005.

[87] D. R. Jones, M. Schonlau, and W. J. Welch, "Efficient global optimization of expensive black-box functions," *Journal of Global Optimization*, vol. 13, no. 4, pp. 455–492, 1998.

[88] M. Sambridge, "Geophysical inversion with a neighbourhood algorithm II. Appraising the ensemble," *Geophysical Journal International*, vol. 138, no. 3, pp. 727–746, 1999.

[89] A. Peters, J. G. Chase, and E. E. W. Van Houten, "Estimating elasticity in heterogeneous phantoms using Digital Image Elasto-Tomography," *Medical and Biological Engineering and Computing*, vol. 47, no. 1, pp. 67–76, 2009.

[90] J. Biehler, "The impact of meshing and boundary conditions on DIET inverse problems," Master's thesis, University of Canterbury, 2008.

[91] Factor II, Incorporated. http://www.factor2.com.

[92] T. Lotz, A. Kashif, S. Feng, P. Biret, Y. Denais, D. Lottin, L. Maillard, T. Tirschler, and J. G. Chase, "A clinical prototype of the Digital Image Elasto Tomography breast cancer screening system," in *Bioinformatics and Biomedical Engineering,(iCBBE) 2011 5th International Conference on*, pp. 1–4, IEEE, 2011.

[93] C. E. Hann, J. G. Chase, X. Q. Chen, C. Berg, R. G. Brown, and R. B. Elliot, "Strobe imaging system for Digital Image-Based Elasto-Tomography breast cancer screening," *Industrial Electronics, IEEE Transactions on*, vol. 56, no. 8, pp. 3195–3202, 2009.

[94] R. G. Brown, C. E. Hann, J. G. Chase, and L. Ray, "Discrete colour-based euclidean-invariant signatures for feature tracking in a DIET breast cancer screening system," in *San Diego, CA, USA: SPIE Medical Imaging Conference-Physiology, Function, and Structure from Medical Images*, pp. 17–22, 2007.

[95] P. Tong and Y. Fung, "The stress-strain relationship for the skin," *Journal of Biomechanics*, vol. 9, no. 10, pp. 649–657, 1976.

[96] A. Samani, J. Bishop, M. Yaffe, and D. Plewes, "Biomechanical 3-d finite element modeling of the human breast using mri data," *Medical Imaging, IEEE Transactions on*, vol. 20, no. 4, pp. 271–279, 2001.

[97] J. Bischoff, E. Arruda, and K. Grosh, "Finite element modeling of human skin using an isotropic, nonlinear elastic constitutive model," *Journal of biomechanics*, vol. 33, no. 6, pp. 645–652, 2000.

[98] E. E. W. Van Houten, M. Doyley, F. Kennedy, J. Weaver, and K. Paulsen, "Initial in vivo experience with steady-state subzone-based mr elastography of the human breast," *Journal of Magnetic Resonance Imaging*, vol. 17, no. 1, pp. 72–85, 2003.

[99] M. Green, L. Bilston, and R. Sinkus, "In vivo brain viscoelastic properties measured by magnetic resonance elastography," *NMR in Biomedicine*, vol. 21, no. 7, pp. 755–764, 2008.

[100] A. Athanasiou, A. Tardivon, M. Tanter, B. Sigal-Zafrani, J. Bercoff, T. Deffieux, J. Gennisson, M. Fink, and S. Neuenschwander, "Breast lesions: Quantitative elastography with supersonic shear imagingpreliminary results1," *Radiology*, vol. 256, no. 1, pp. 297–303, 2010.

[101] J. Ophir, S. Alam, B. Garra, F. Kallel, E. Konofagou, T. KROUSKO, C. Merritt, R. RIGHETT, R. Souchon, S. Srinivasan, *et al.*, "Elastography: imaging the elastic properties of soft tissues with ultrasound," *J. Med*, vol. 29, p. 156, 2002.

[102] FarField Technology, "FastRBF ^{TM} toolbox." `http://www.farfieldtechnology.com`.

[103] A. Samani, J. Bishop, M. Yaffe, and D. Plewes, "Biomechanical 3-d finite element modeling of the human breast using mri data," *Medical Imaging, IEEE Transactions on*, vol. 20, no. 4, pp. 271 – 279, 2001.

[104] S. Bhatti and M. Sridhar-Keralapura, "A novel breast software phantom for biomechanical modeling of elastography," *Medical Physics*, vol. 39, p. 1748, 2012.

[105] V. Rajagopal, A. Lee, J. Chung, R. Warren, R. Highnam, M. Nash, and P. Nielsen, "Creating individual-specific biomechanical models of the breast for medical image analysis.," *Academic radiology*, vol. 15, no. 11, p. 1425, 2008.

[106] C. A. C. Coello, G. B. Lamont, and D. A. V. Veldhuizen, *Evolutionary Algorithms for Solving Multi-Objective Problems*. Springer, second edition ed., 2007.

[107] E. Aarts and J. Lenstra, *Local search in combinatorial optimization*. Princeton University Press, 2003.

[108] J. Kennedy and R. Eberhart, "Particle swarm optimization," in *Neural Networks, 1995. Proceedings., IEEE International Conference on*, vol. 4, pp. 1942–1948, IEEE, 1995.

[109] D. Goldberg, *Genetic algorithms in search, optimization and machine learning*. Addison-Wesley, 1989.

[110] N. N. Schraudolph and R. K. Belew, "Dynamic parameter encoding for genetic algorithms," *Mach. Learn.*, vol. 9, pp. 9–21, June 1992.

[111] S. Kirkpatrick, C. Gelatt, and M. Vecchi, "Optimization by simulated annealing," *science*, vol. 220, no. 4598, p. 671, 1983.

[112] A. Tarantola, *Inverse Problem Theory Methods for Data Fitting and Model Parameter Estimation*. Elsevier, 1987.

[113] K. Mosegaard and A. Tarantola, "Monte carlo sampling of solutions to inverse problems," *Journal of Geophysical Research*, vol. 100, no. B7, pp. 12.431–12.447, 1995.

[114] P. R. Amestoy, I. S. Duff, J. Koster, and J. L'Excellent, "A fully asynchronous multifrontal solver using distributed dynamic scheduling," *SIAM Journal on Matrix Analysis and Applications*, vol. 23, no. 1, pp. 15–41, 2001.

[115] P. R. Amestoy, A. Guermouche, J. L'Excellent, and S. Pralet, "Hybrid scheduling for the parallel solution of linear systems," *Parallel Computing*, vol. 32, no. 2, pp. 136–156, 2006.

[116] J. Quinn, Michael, *Parallel Programming in C with MPI and OpenMP*. New York: McGraw-Hill Press, 2003.

[117] S. Feng, T. Lotz, J. G. Chase, and C. E. Hann, "An image based vibration sensor for soft tissue modal analysis in a Digital Image Elasto Tomography DIET system," *Engineering in Medicine and Biology Society (EMBC), 2010 Annual International Conference of the IEEE*, pp. 25–28, 2010.

[118] R. Brown, *Three-dimensional motion capture for the DIET breast cancer imaging system*. PhD thesis, University of Canterbury, 2008.

[119] J. Wulff, T. Lotz, T. Stehle, T. Aach, and J. Chase, "Correspondence estimation from non-rigid motion information," in *Proceedings of SPIE*, vol. 7962, p. 79621R, 2011.

[120] Blue Phantom Ultrasound Training Models, "http://www.bluephantom.com/product/elastography-ultrasound-breast-phantom.aspx?cid=438."

[121] J. Hebden, H. Veenstra, H. Dehghani, E. Hillman, M. Schweiger, S. Arridge, and D. Delpy, "Three-dimensional time-resolved optical tomography of a conical breast phantom," *Applied optics*, vol. 40, no. 19, pp. 3278–3287, 2001.

[122] A. Bakar, A. Abbosh, P. Sharpe, M. Bialkowski, and Y. Wang, "Heterogeneous breast phantom for ultra wideband microwave imaging," *Microwave and optical technology letters*, vol. 53, no. 7, pp. 1595–1598, 2011.

[123] S. Wu, S. Weinstein, E. Conant, A. Localio, M. Schnall, and D. Kontos, "Fully automated chest wall line segmentation in breast mri by using context information," in *SPIE Medical Imaging*, pp. 831507–831507, International Society for Optics and Photonics, 2012.

[124] H. Mehrabian and A. Samani, "An iterative hyperelastic parameters reconstruction for breast cancer assessment," in *Proc. of SPIE Vol*, vol. 6916, pp. 69161C–1, 2008.

[125] J. O'Hagan and A. Samani, "Measurement of the hyperelastic properties of 44 pathological ex vivo breast tissue samples," *Physics in Medicine and Biology*, vol. 54, p. 2557, 2009.

[126] GE, "Vscan handheld ultrasound." http://www.ge.com/innovation/vscan/index.html.

[127] J. Sanders and E. Kandrot, *CUDA by Example*. Addison-Wesley, 2010.

[128] G. R. Joldes, A. Wittek, and K. Miller, "Real-time nonlinear finite element computations on GPU: Application to neurosurgical simulation," *Computer Methods in Applied Mechanics and Engineering*, vol. 199, no. 49-52, pp. 3305 – 3314, 2010.

[129] K. Bathe and E. Wilson, *Numerical methods in finite element analysis*, vol. 8. Prentice-Hall Englewood Cliffs, NJ, 1976.